

VOLUME 38

DECEMBER 1960

NUMBER 12

Canadian Journal of Physics

Editor: H. E. DUCKWORTH

Associate Editors:

L. G. ELLIOTT, *Atomic Energy of Canada, Ltd., Chalk River*
J. S. FOSTER, *McGill University*
G. HERZBERG, *National Research Council of Canada*
L. LEPRINCE-RINGUET, *Ecole Polytechnique, Paris*
B. W. SARGENT, *Queen's University*
G. M. VOLKOFF, *University of British Columbia*
W. H. WATSON, *University of Toronto*
G. A. WOONTON, *McGill University*

Published by THE NATIONAL RESEARCH COUNCIL
OTTAWA CANADA

CANADIAN JOURNAL OF PHYSICS

Under the authority of the Chairman of the Committee of the Privy Council on Scientific and Industrial Research, the National Research Council issues THE CANADIAN JOURNAL OF PHYSICS and five other journals devoted to the publication, in English or French, of the results of original scientific research. Matters of general policy concerning these journals are the responsibility of a joint Editorial Board consisting of: members representing the National Research Council of Canada; the Editors of the Journals; and members representing the Royal Society of Canada and four other scientific societies.

EDITORIAL BOARD

Representatives of the National Research Council

I. McT. Cowan (Chairman), *University of British Columbia*
Léo Marion, *National Research Council*

H. G. Thode, *McMaster University*
D. L. Thomson, *McGill University*

Editors of the Journals

D. L. Bailey, *University of Toronto*
T. W. M. Cameron, *Macdonald College*
F. E. Chase, *Ontario Agricultural College*
H. E. Duckworth, *McMaster University*

Léo Marion, *National Research Council*
J. F. Morgan, *Department of National Health and Welfare, Ottawa*
J. A. F. Stevenson, *University of Western Ontario*

Representatives of Societies

D. L. Bailey, *University of Toronto*
Royal Society of Canada
T. W. M. Cameron, *Macdonald College*
Royal Society of Canada
H. E. Duckworth, *McMaster University*
Royal Society of Canada
Canadian Association of Physicists
P. R. Gendron, *University of Ottawa*
Chemical Institute of Canada

D. J. Le Roy, *University of Toronto*
Royal Society of Canada
J. F. Morgan, *Department of National Health and Welfare, Ottawa*
Canadian Biochemical Society
R. G. E. Murray, *University of Western Ontario*
Canadian Society of Microbiologists
J. A. F. Stevenson, *University of Western Ontario*
Canadian Physiological Society

Ex officio

Léo Marion (Editor-in-Chief), *National Research Council*
J. B. Marshall (Administration and Awards), *National Research Council*

Manuscripts for publication should be submitted to Dr. H. E. Duckworth, Editor, Canadian Journal of Physics, Hamilton College, McMaster University, Hamilton, Ontario.

For instructions on preparation of copy, see **NOTES TO CONTRIBUTORS** (back cover).

Proof, correspondence concerning proof, and orders for reprints should be sent to the Manager, Editorial Office (Research Journals), Division of Administration and Awards, National Research Council, Ottawa 2, Canada.

Subscriptions, renewals, requests for single or back numbers, and all remittances should be sent to Division of Administration and Awards, National Research Council, Ottawa 2, Canada. Remittances should be made payable to the Receiver General of Canada, credit National Research Council.

The journals published, frequency of publication, and subscription prices are:

Canadian Journal of Biochemistry and Physiology	Monthly	\$9.00 a year
Canadian Journal of Botany	Bimonthly	\$6.00 a year
Canadian Journal of Chemistry	Monthly	\$12.00 a year
Canadian Journal of Microbiology	Bimonthly	\$6.00 a year
Canadian Journal of Physics	Monthly	\$9.00 a year
Canadian Journal of Zoology	Bimonthly	\$5.00 a year

The price of regular single numbers of all journals is \$2.00.

CORRECTIONS

Volume 35, 1957

Page 572. In equation (6), " $+2(a_1+a_2)\{-a_1(a_1+a_2)\}^{-\frac{1}{2}}Ht \sin \chi$ " should read " $+2(a_1+a_2)\{-a_1(a_1+1)\}^{-\frac{1}{2}}Ht \sin \chi$ ".

Volume 38, 1960

Page 229. On page 229, the formula for g (equation (19)) should read

$$g = \frac{1}{2r_e B_e^{1/2} (\omega_e x_e)^{3/2}} \left\{ (4\omega_e x_e U)^{1/2} \left[\alpha_e - \frac{3\omega_e \gamma_e}{4\omega_e x_e} \right] + \left[2\omega_e x_e B_e - \alpha_e \omega_e + \frac{\gamma_e (3\omega_e^2 - 4\omega_e x_e U)}{4\omega_e x_e} \right] \left[\ln \frac{(\omega_e^2 - 4\omega_e x_e U)^{1/2}}{\omega_e - (4\omega_e x_e U)^{1/2}} \right] \right\}.$$

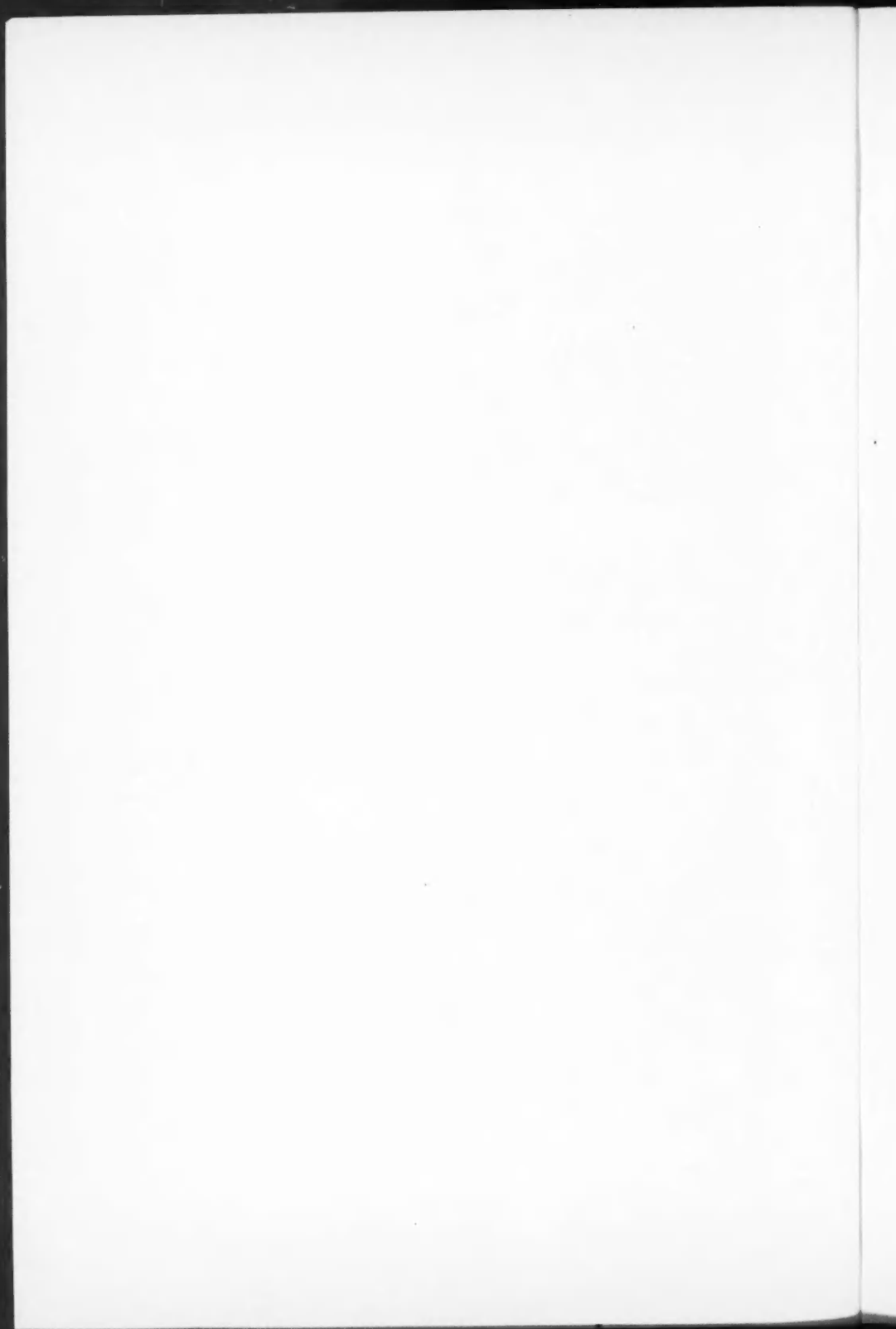
Page 332. In line 15 up "(Wilson, Rose, and Pomerantz 1959)" should read "(Wilson Rose, and Pomerantz 1960)".

Page 333. In line 8 up "Wilson, B. G., Rose, D. C., and Pomerantz, M. A. 1959. Can. J. Phys. 38, 328." should read "Wilson, B. G., Rose, D. C., and Pomerantz, M. A. 1960. Can. J. Phys. 38, 328."

Pages 1114-1133. Two errors in the Appendix have been pointed out to the author of the paper "Scattering of radio waves by an ionized gas in thermal equilibrium". These errors do not occur in the corresponding analysis of Pines and Bohm, which is correct within its range of validity.

The first error consists in the omission of the second order term in the expansion of the logarithm leading to equation (58). The second occurs in the final integration leading to equation (73), where the lack of independence of Fourier components with wave number vectors of equal magnitude and opposite direction was not taken into account.

The corrected forms of equations (6), (7), (73), and (76) are obtained by replacing T in the original equations by $T/2$. The corrected form of equation (8) is obtained by replacing λ^2 in the original equation by $2\lambda^2$. The results obtained for the frequency spectrum of scattered power are not affected.



Canadian Journal of Physics

Issued by THE NATIONAL RESEARCH COUNCIL OF CANADA

VOLUME 38

DECEMBER 1960

NUMBER 12

TE SURFACE WAVES GUIDED BY A DIELECTRIC-COVERED METAL PLANE¹

D. MORRIS AND A. G. MUNGALL

ABSTRACT

Investigations of the phase velocities of *TE* mode surface waves are described. The surface waves were excited over a sand-covered metal plane and the phase velocities of the first three *TE* modes determined as a function of the sand depth, at a frequency of about 9300 Mc/sec. A phase comparison system was used for the measurements. The simultaneous existence of two modes with different velocities, predicted theoretically for certain sand depths, was found experimentally.

The variation of relative surface wave power carried above the dielectric layer with thickness of the layer is also discussed.

INTRODUCTION

A previous paper (Mungall and Morris 1959, subsequently referred to as I) described the determination of the phase velocity of surface waves in the first three *TM* modes propagated over a plane dielectric-covered metal surface. This paper will deal with the determination of the phase velocity of transverse electric modes of surface waves propagated over the same guiding structure. Most other experimental investigations have been confined to the dominant mode of propagation over the dielectric-coated metal plane, which is a *TM* mode. However, Rich (1955) has given the equations for the field components of *TE* modes and diagrams of the field lines associated with the first *TE* mode, and the use of this mode has been suggested in connection with the design of surface wave antennas (Hansen 1957). In I equations relating the phase velocity of the waves to the dielectric depth are given, and the relations are shown graphically for both *TM* and *TE* modes for a particular value of dielectric constant.

The measurements described in this paper serve to check the correctness of the theory of *TE* mode surface wave propagation over a sand-covered metal plane.

Theoretical

The equations defining *TE* surface wave propagation over a perfectly conducting plane covered with a layer of loss-less dielectric, as given in paper I, are as follows:

¹Manuscript received August 24, 1960.

Contribution from the Division of Applied Physics, National Research Council, Ottawa, Canada.

Issued as N.R.C. No. 6014.

Can. J. Phys. Vol. 38 (1960)

$$(1) \quad v = \omega \left[\frac{\omega^2}{c^2} \kappa_2' - \beta_2^2 \right]^{-\frac{1}{2}}$$

and

$$(2) \quad \beta_2 \cot \beta_2 l = - \left[\frac{\omega^2}{c^2} (\kappa_2' - 1) - \beta_2^2 \right]^{\frac{1}{2}}$$

where v = surface wave phase velocity,

ω = angular frequency,

κ_2' = dielectric constant of layer,

β_2 = phase constant of propagation in the dielectric,

c = velocity of electromagnetic waves in free space,

l = thickness of dielectric layer.

The magnetic permeabilities of both the conducting plane and the dielectric layer are taken equal to that of free space.

Equations (1) and (2) can be combined to give a dimensionless relation in terms of relative dielectric thickness and velocity, in the form given by Hansen (1957) or as follows (Mungall and Morris 1960):

$$(3) \quad L = \frac{V}{2\pi(\kappa_2' V^2 - 1)^{\frac{1}{2}}} \cot^{-1} \left[- \left(\frac{1 - V^2}{\kappa_2' V^2 - 1} \right)^{\frac{1}{2}} \right]$$

where $L = l/\lambda_0$,

$V = v/c$,

λ_0 = free space wavelength.

From equation (3) the minimum dielectric depth for TE mode propagation (occurring at $V = 1.0$) is $L = 1/(4(\kappa_2' - 1)^{\frac{1}{2}})$, i.e. corresponding to a cutoff wavelength of $\lambda_c = 4l(\kappa_2' - 1)^{\frac{1}{2}}$.

For a given value of V , there is more than one value of L which will satisfy equation (3). This can be interpreted as indicating the existence of higher order modes. The nomenclature followed in this paper is to describe the n th solution of equation (3) as the TE_n mode. Thus the lowest TE mode is TE_1 . The existence of this mode structure was examined experimentally, and the results are compared with theoretical predictions in Fig. 5.

It is also of interest to consider the power flow in the air above the dielectric for the various modes and also for different velocities within a given mode. For TE modes the proportion of the total surface wave power carried above the dielectric layer can be shown to be

$$(4) \quad \frac{P_a}{P_a + P_d} = \frac{(\kappa_2' V^2 - 1)}{(\kappa_2' - 1) V^2 \left\{ 1 + \left(\frac{1 - V^2}{\kappa_2' V^2 - 1} \right)^{\frac{1}{2}} \cot^{-1} \left[- \left(\frac{1 - V^2}{\kappa_2' V^2 - 1} \right)^{\frac{1}{2}} \right] \right\}}$$

where P_a and P_d are respectively the power carried in the air and in the dielectric. Calculations from (4) for the case $\kappa_2' = 3.0$, representative of dry sand, give the results shown graphically in Fig. 1. The relative power carried above the dielectric falls rapidly with decrease of phase velocity, particularly for the higher order modes. Experiments showing qualitative agreement with this will be described.

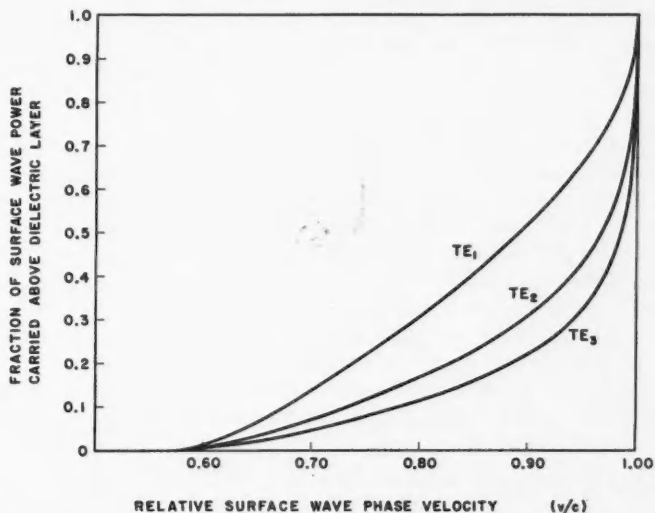


FIG. 1. Fraction of surface wave power carried above dielectric layer as a function of relative phase velocity for first three *TE* modes propagated over a sand-covered metal plane.

EXPERIMENTAL

1. Technique

The experimental method used was similar to that described in I except for the technique of exciting and detecting the surface waves. The method depends on the phase comparison of two signals arriving at two mixers (both powered by the same local oscillator klystron) via two different paths, but both being derived from the same klystron. One path is over the surface wave structure and the other consists of a fixed length of waveguide. The heterodyne outputs from the two mixers are amplified and applied to an oscilloscope, and phase changes are measured by the use of a variable phase shifter in the waveguide path. All measurements were made at a frequency close to 9300 Mc/sec ($\lambda_0 = 3.2$ cm).

The simple technique described in I for exciting and detecting *TM* mode surface waves, i.e. propagation over a metal sheet followed by the surface wave structure, could not be used in the present investigation since it is not possible to propagate a *TE* wave close to a metal sheet. Instead, the equipment shown in Fig. 2 was used. This equipment was contained in a wooden box lined with microwave absorbing panels. The signal path was as follows. Horn 1 transmitted a wave with its electric vector vertically polarized over a metal sheet, path A, at velocity c , to horn 2. The wave received by horn 2 then travelled along a waveguide twist to horn 3 from which it was radiated with horizontal polarization. Part of the energy was launched as a *TE* surface wave and travelled at a velocity v over the dielectric-coated conducting plane, path B, to horn 4. The received signal then entered one of the mixers. The

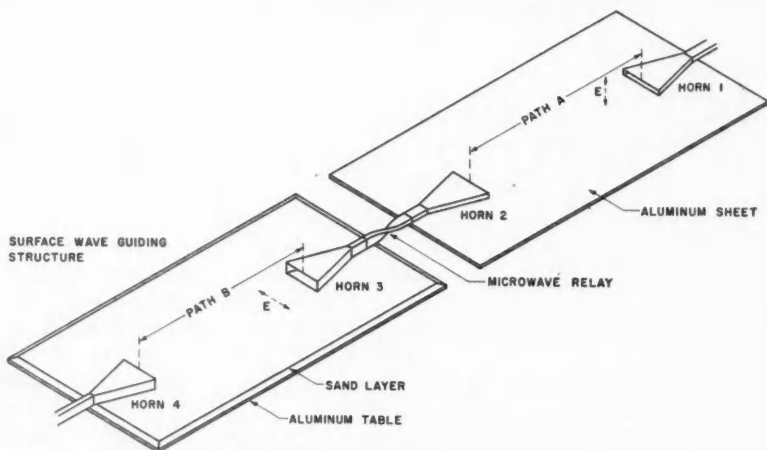


FIG. 2. Schematic diagram of equipment for exciting and detecting TE mode surface waves.

microwave relay assembly, consisting of horns 2 and 3 and the connecting waveguide twist, was mounted on a carriage to facilitate accurate motion in the direction of wave propagation.

The following procedure was then used. The microwave relay was positioned initially at one end of its travel and the setting of the phase shifter in the waveguide path required to bring the phase pattern on the oscilloscope to a straight line was noted. The microwave relay was then moved in 1-cm steps to decrease the path over the guiding structure and the corresponding phase shifter readings noted. A change of phase took place when the carriage was moved if the velocity of the wave propagated over the sand-covered metal sheet was less than that of free space. Direct coupling between the transmitting and receiving horns at the ends of the box was very small, due to the difference in polarization of the transmitted and received waves. It was reduced to negligible proportions by interposing a sheet of microwave absorbing material across the box just above the microwave relay assembly.

The total path length employed was 200 cm. The surface wave guiding structure consisted of a thick aluminum plate, 90 cm long and 60 cm wide, covered with a layer of dry sand. It was found that, to obtain reproducible results, the sand had to be well compacted and possess a smooth surface. A removable scraper was devised to satisfy these requirements. The scraper had a rounded lower surface, and its carriage ran on ball races on rails bolted to the underside of the aluminum plate. The uniformity of the gap between the scraper blade and the table as the scraper was moved from one end to the other was better than ± 0.2 mm, after shimming of the rails. The sand layers produced by this rounded scraper blade were well compacted and had

a smooth surface, and the sand depths were probably uniform to the above accuracy. The dry sand had a dielectric constant of 3.0 at the frequency used, 9300 Mc/sec.

2. Results

Most of the graphs showing phase change as a function of the path length over the guiding structure were similar to those obtained for the *TM* modes and shown in I. With the horns described for exciting the surface waves, an accompanying free-space component was always present to a greater or lesser extent and the graphs usually showed the results of interference between the surface wave and the free-space component. In general, when a surface wave predominates over the free-space wave the plot of phase change as a function of path length is monotonic, approximating a straight line. The interference results in a periodic oscillation of phase about the average slope of the graph. When the surface wave interferes with a much stronger free-space component the phase changes periodically as the path length is varied. The phase velocity of the surface waves can be determined from the average slope of the monotonic curves and from the periodicity of the oscillatory phase curves. Since the proportion of the surface wave power carried in the air above the dielectric decreases with decreasing phase velocity (see Fig. 1), if the receiving horn was positioned above the dielectric it received a very small proportion of the surface wave power mixed with a relatively large amount of the free-space power for the low velocity waves. Hence, for better detection, in this case the receiving horn was lowered until it rested on the metal table and the sand layer was tapered into the mouth of the horn. Even with this technique it was not possible to get the amplitude of a low velocity surface wave greater than that of the free-space component. However, the mouth of the horn extended somewhat above the sand surface and so still received some of the free-space component. Also the launching efficiency of the exciting horn was probably poor. This horn had to be movable and so it could not be positioned below the surface of the sand. Hence, probably only a small proportion of power was launched as a surface wave at the lower wave velocities.

When the sand depth was such that two surface wave modes could propagate, the presence of both could be inferred from the phase change graphs obtained when the receiving horn was first set just above the sand surface, and was then set below the surface and the sand tapered into the mouth of it. Such graphs are shown in Figs. 3 and 4, which were both obtained for the same sand depth, 19.0 mm ($L = 0.59$). Figure 3 shows the phase curve obtained when the horn was above the sand surface. The curve shows only slight variations due to the interfering free-space wave, showing that the amplitude of the latter is much less than that of the surface wave. Hence, the amplitude of the interfering free-space wave was probably even less when the receiving horn was lowered. From the mean slope of the curve in Fig. 3 the derived relative phase velocity is 0.92. This is in good agreement with the theoretical value of 0.93 for the TE_2 mode, computed from equation (3)

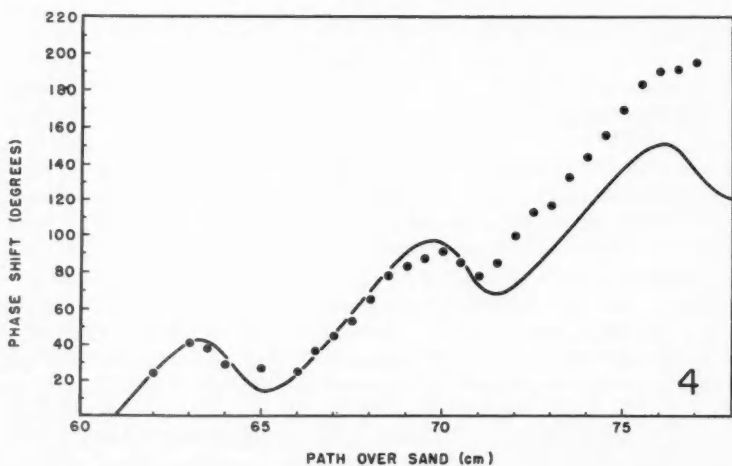
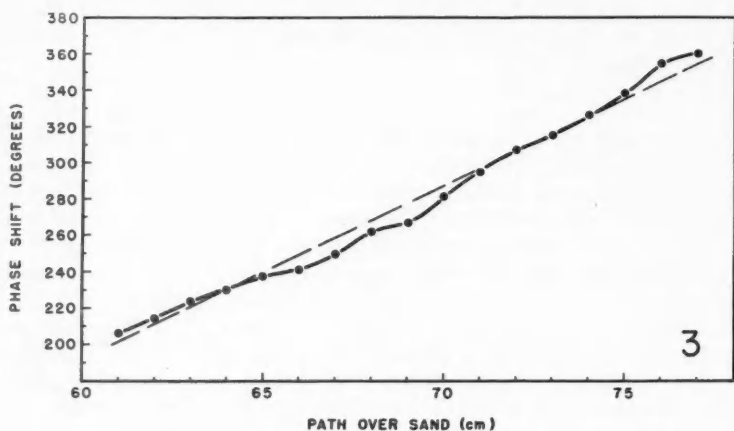


FIG. 3. Phase change as a function of path length at sand depth 19.0 mm with receiving horn above sand surface. TE_2 mode indicated.

FIG. 4. Phase change as a function of path length at sand depth 19.0 mm with receiving horn just below sand surface. Circles indicate experimental points. Theoretical curve obtained for interference between waves in TE_1 and TE_2 modes.

for $L = 0.59$. The theoretical relative phase velocity of the TE_1 wave at this dielectric depth is 0.63. In Fig. 4 the experimental points were obtained with the receiving horn below the sand surface. The points are compared with the solid curve obtained by calculating the phase change as a function of path length when a wave of amplitude unity and velocity $0.93c$ interferes with a wave of amplitude 0.4 and velocity $0.63c$. The actual ratio of the amplitudes of the waves was not known, but the experimental points tend to follow a

curve of the same shape as the theoretical one. Thus, the experimental results shown in Fig. 4 indicate the simultaneous propagation of two TE modes, at different velocities.

Figure 5 shows the experimental variation of phase velocity with dielectric depth for the first three TE modes compared with the theoretical curves computed from equation (3) with $\kappa_2' = 3.0$. The experimental points denoted by circles indicate cases where the phase curves obtained were essentially

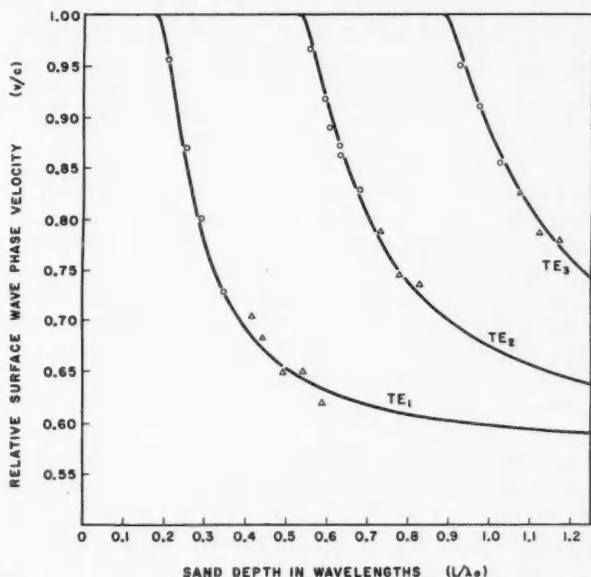


FIG. 5. Comparison of experimental and theoretical TE surface wave phase velocities as a function of sand depth over a conducting plane. Experimental points for $\lambda_0 = 3.2$ cm.

monotonic, i.e. the surface wave component was predominant. The points denoted by triangles represent cases where periodic phase curves were obtained, indicating that the surface waves were weak. The accuracy of the determination of the phase velocity from the periodic curves was usually not better than 2-3%. However, the satisfactory agreement between the experimental points and the theoretical curves appears to be adequate verification of the mode structure described theoretically for TE surface wave propagation over dielectric-covered plane metal surfaces.

REFERENCES

- HANSEN, R. C. 1957. IRE Trans. MTT-5, 115.
 MUNGALL, A. G. and MORRIS, D. 1959. Can. J. Phys. **37**, 1349.
 ——— 1960. Can. J. Phys. **38**, 779.
 RICH, G. J. 1955. Proc. Inst. Elec. Engrs. (London), B, **102**, 237.

A FABRY-PEROT SPECTROMETER FOR AURORAL AND AIRGLOW OBSERVATIONS¹

G. G. SHEPHERD

ABSTRACT

A 1-in. Fabry-Perot interferometric spectrometer employing mechanical scanning has been constructed to operate at low order. Such an instrument gives a resolution similar to that of a grating spectrometer but has, at that resolution, a much higher light gathering power. The spectrometer is capable of resolving the sodium D lines in the twilight airglow, scanning once per minute. Some preliminary results on the variation of D_2/D_1 ratio during twilight are presented. This type of spectrometer should be useful for a number of other applications.

1. INTRODUCTION

The use of the Fabry-Perot interferometer in conjunction with photographic spectrographs for high resolution studies is well known. In recent years, it has been developed into a scanning photoelectric instrument, mainly by Chabbal (1953, 1958*a*, *b*). At the Bellevue Conference on Interferometry* in 1957, more than thirty papers were given on the use of the Fabry-Perot spectrometer, indicating the increasing interest in such a device. In these papers, and elsewhere (Jacquinot 1954) it is made clear that the Fabry-Perot spectrometer has a much higher light gathering power than has a grating spectrometer operating at the same resolution. That is, if G is the light gathering power, A the area of the selective element, Ω the solid angle it will receive, and T the transmission of the instrument, then $G = A\Omega T$. Further, if R is the resolving power of the instrument, then GR is a constant for any spectrometer, but this constant has a much larger value for the Fabry-Perot spectrometer than for a grating spectrometer, if both have the same area, A .

For this reason, instruments of this type would be very useful for observation of faint sources such as the airglow and transient sources such as the aurora. Nevertheless, they have not as yet become very widely used, perhaps because they are considered to be complicated technically. Applications of interferometry to the airglow and aurora have so far consisted mainly of line width measurements at high resolution (Armstrong 1959; Wark 1960). In this paper, the design and construction of a relatively simple 1-in. (2.5 cm diameter) mechanical scanning Fabry-Perot spectrometer is described. An instrumental half width of 2.5 \AA is obtained at an order of 170. The passbands are 36 \AA apart so that an interference filter can be used as a monochromator. This 1-in. instrument was intended as a prototype for a larger one, but the results of some preliminary observations of the sodium twilight airglow which will be described demonstrate that it is itself a useful instrument.

¹Manuscript received August 26, 1960.

Contribution from the Physics Department, University of Saskatchewan, Saskatoon, Saskatchewan. Supported by National Research Council grant No. A-822.

*J. phys. radium, **19**, 13-434 (1958).

2. PRELIMINARY CONSIDERATIONS

Figure 1(a) shows a schematic arrangement of a Fabry-Perot spectrometer. An etalon of spacing t is placed in a gas of refractive index n , followed by a lens L_1 forming a circular fringe pattern at its focus, which is coincident with the diaphragm. A small central portion of the fringe pattern passes through the diaphragm, is collected by the lens L_2 , and falls on a photo-multiplier, or some other detector. The transmission of the etalon is a function

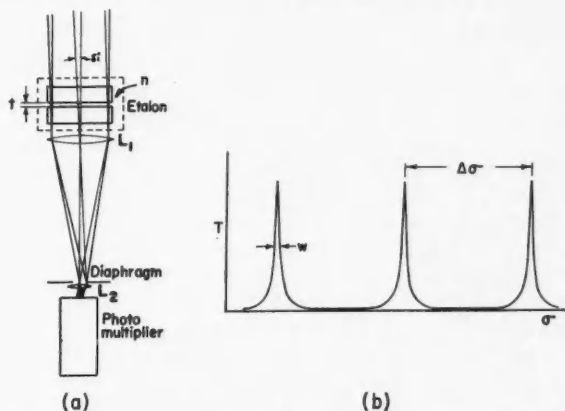


FIG. 1. (a) Schematic arrangement of a Fabry-Perot spectrometer. (b) Passbands of a Fabry-Perot interferometer (Airy function) for a finesse equal to 20.

of t , n , i (the angle of incidence), and σ (the wave number of the radiation). For fixed t , n , and i , the transmission vs. σ graph represents the passbands of the instrument, shown in Fig. 1(b). The separation between passbands will be denoted by $\Delta\sigma$, and is equal to $1/2nt$. The ratio of this quantity to the half width of a single passband, w , is called the finesse, and will be denoted by N . The finesse obtained depends on the quality of the surfaces, the reflectivity of their coatings, and the size of the diaphragm used. Typical values range from 10 to 30.

The multiple passbands of the Fabry-Perot can cause some difficulty. However, if one is studying a simple, isolated spectral feature, a wide passband filter will suffice. In other situations where nearby features are present, or worse still, a continuum, some form of monochromator is essential. At the low orders used here the passbands are 20–40 Å apart and an interference filter will isolate a single passband. At higher resolutions it is necessary to use several etalons in series (Chabbal 1958b).

Two methods of scanning are available. The first is by varying the refractive index of the gas surrounding the plates, and the second is by mechanical motion of one of the plates. There is a third method, tilting the etalon (varying i) but this method has some limitations and will not be considered here. It

can easily be shown that using the refractive index method, the scanning range is independent of the order, and spacing t , and that for one atmosphere pressure variation in air, the scanning range is 1.5 \AA at 5000 \AA . For mechanical scanning, a motion of $\lambda/2$ causes a scan through one order, which for $t = 1 \text{ cm}$ is only equal to 0.2 \AA at 5000 \AA . On the other hand, for $t = 0.1 \text{ mm}$, a motion of $\lambda/2$ gives a scan of 20 \AA . Obviously mechanical scanning is advantageous at low order if a large scanning range is desired.

3. MECHANICAL DESIGN

A cross-sectional view of the mounting is shown in Fig. 2. The Fabry-Perot plates (A) are 1 in. in diameter and $\frac{1}{4}$ in. thick. They are inexpensive plates, intended for use in an undergraduate laboratory, rather than for research purposes. The upper plate is held in the upper holder (B) by a three-point support. Each point consists of an open vee-shaped piece with the two ends touching the etalon plate, and the apex connected through a steel ball to a

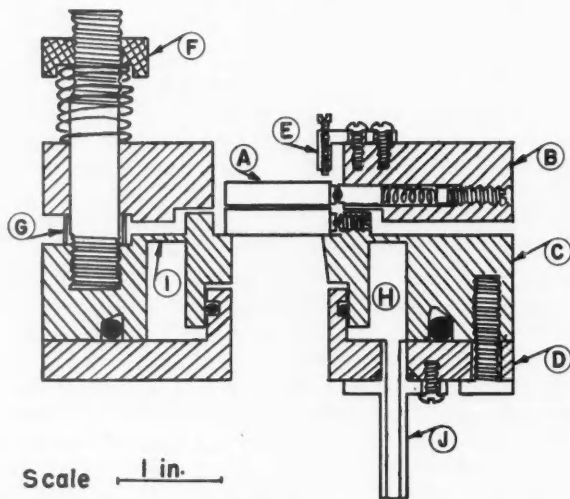


FIG. 2. Cross-sectional view of the mechanical scanning mounting for the 1-in. Fabry-Perot spectrometer. A, Fabry-Perot plates; B, upper (fixed) plate holder; C, lower (movable) plate holder; D, air space cover; E, coarse adjustment screw (3); F, fine adjustment screw (3); G, invar spacer (3); H, air space; I, annular membrane 0.045 in.; J, air inlet.

spring-loaded rod, carefully ground into a reamed hole in B. This support mechanism holds the upper plate firmly in any desired orientation. The three coarse adjustment screws (E) are used to slide the upper plate in its bearing pieces to the desired position and are then withdrawn from contact with the plate. The lower plate is held in a support which is connected to the lower holder (C) through an annular membrane (I), all of which is machined from one piece. A cover plate (D) encloses an air space (H), sealed with two "O"

rings. Air pressure produced in H causes elastic deformation of the membrane, giving a motion to the lower plate which is linear with pressure. The "O" ring connecting the lower plate support to D does not interfere with the deformation of the steel membrane. The required thickness of the membrane was calculated from an equation given by Timoshenko (1930), which served as a guide for the first machining. After initial tests had been made using the etalon, the membrane was further machined to 0.045 in. thick, giving a displacement of $\lambda/2$ for a pressure change of 10 cm Hg. This scanning mechanism is a variation of that used earlier by Chabbal and Soulet (1958) in which the membrane is deformed by a cam and lever arrangement.* B and C are separated by three invar spacers (G), and compression of these by the spring and nut devices (F) provides the fine adjustment of the etalon. The length of G is chosen to give thermal compensation of the etalon spacing. The mounting is machined of SAE 3140 steel, which is a 1.3% nickel alloy, and was chosen for its resistance to creep. The apparatus is considered satisfactory, being relatively easy to adjust, and stable for periods of several hours or more. The scanning motion has been tested over seven orders and the adjustment found to remain good through that range.

This mounting is fixed on teflon supports to the bottom of a cylindrical cast aluminum alloy cell having 1-in. thick walls. Four Chromalox strip heater elements are clamped to the outer wall. The large thermal conductivity of the aluminum gives a reasonably uniform temperature over the inner wall. A temperature-sensitive resistance, consisting of Balco wire wound on a 0.2 in. diameter lucite rod, is inserted in the wall of the casting. A commercial regulator designed for domestic application gives adequate temperature control.

The pressure drive for the Fabry-Perot is a simple arrangement, consisting of a 2.5 in. diameter sylphon bellows, driven through a cam by a synchronous 1 r.p.m. motor. The pressure variation produced by the bellows was surprisingly linear with displacement. Some non-linearity is produced because the change in volume is not negligible compared with the total volume and this was allowed for in the cam design. Unfortunately, it was not possible to locate the sylphon bellows in the temperature-controlled cell. This did not affect the stability unduly, although it was necessary to operate the scanning mechanism for about one hour before the etalon was adjusted.

The detector was an E.M.I. 9502A photomultiplier, cooled with dry ice, and was followed by a preamplifier of the type described by Hunten (1953). A further triode stage provided attenuation and high frequency cutoff, and coupled the preamplifier to a G-10 Varian recorder.

The interference filter was placed in a box above the etalon, outside the cell. (The optical axis of the system is vertical, which is considered to improve the etalon stability.) A tilting mechanism is provided for the interference filter in order to shift the peak of its passband to the desired wavelength.

*During the preparation of this manuscript it was learned that Karandikar (1959) has used a similar mechanism, employing liquid pressure, not applied directly to the steel membrane, but indirectly through another membrane in contact with the plate support itself.

The entire apparatus, with the exception of the electronics, has been located outdoors on the roof of the Physics building. It performed quite satisfactorily here, and runs were taken at temperatures down to -25°C with no great difficulty.

4. OPTICAL CONSIDERATIONS

When a particular diffraction grating has been selected, the manner in which it can be used to study a given spectral feature is quite limited. This is definitely not the case for the Fabry-Perot spectrometer, for which several parameters can be independently varied. For example, the resolving power of a grating is fixed, but that of the Fabry-Perot is variable and can be increased without limit. While the variety of adjustments introduces technical complications, this flexibility gives the Fabry-Perot several advantages.

The first problem chosen to test the instrument was the observation of sodium emission in the twilight. Because of the low brightness of this emission, the highest possible light-gathering-power was desired. Thus the lowest possible resolution which would still separate the D lines was to be used, about 3 \AA . Because of the Rayleigh scattered sunlight accompanying the emission, a monochromator was essential; but the low order permits the use of an interference filter. A filter of 20-\AA half width and 70% transmission was available* and this was considered more useful than a narrower band-pass filter having lower transmission. If the Fabry-Perot passband is to be 3 \AA in width and the finesse is N , the separation between orders is $3N\text{ \AA}$. This determines the etalon spacing that must be used. This also illustrates that even at low resolution, a high finesse is desirable.

To determine the finesse of the etalon, nine-layer dielectric coatings were applied and the localized fringes observed in collimated monochromatic light. By scanning, the contours of the plates can then be observed as described by Chabbal (1958c). Two pairs of 1-in. plates were available and different combinations of these were tried, giving a variety of contours. One combination was definitely superior to the others, showing a spherical curvature of finesse about 20. To investigate the microirregularities of the surfaces a single line was scanned in the usual fashion, but using only a small portion of the etalon and a very small diaphragm. In this way, all other contributions to the line width were negligible, and the observed profile gave the finesse of these defects, again about 20 in this case.

To give GR its maximum value, the finesse associated with the coatings should be similar to that of the defects and so five-layer coatings of ZnS and cryolite, with a finesse of about 23, were applied. Some measurements were made with three-layer coatings, but the gain in transmission was not great enough to warrant the loss of resolution.

The last parameter to be determined is the size of detector diaphragm, but this is readily adjustable and so several can be tried. After some preliminary twilight runs this was left at 1.5 \AA .

*This was kindly supplied by Dr. D. M. Hunten of the Physics Department, University of Saskatchewan.

The final adjustments were at an order of 170, giving passbands 36 \AA apart, an instrumental line width of about 2.5 \AA , and thus a resultant finesse of about 14. Under these conditions it was estimated that the interference filter would allow the secondary passbands a transmission equal to 7% of the primary, and the tertiary passbands 2% each, giving 18% altogether. This was considered a satisfactory compromise with the resolution.

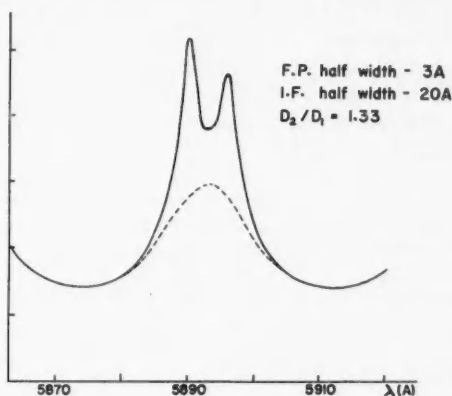
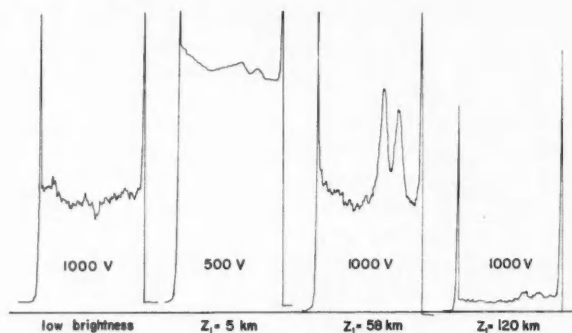


FIG. 3. Synthetic sodium twilight spectrum using Fabry-Perot of half width 3 \AA , and interference filter of half width 20 \AA . Dotted curve: response to white light only; solid curve: white light plus sodium emission.

A synthetic twilight spectrum is shown in Fig. 3, where the white light intensity has been arbitrarily chosen equal to that of D_2 (as seen by a single passband without the interference filter) and the D_2/D_1 ratio fixed at 1.33. An instrumental passband of 3 \AA was used here. It is seen that the intensity drops only to about 50% between orders because of the secondary passbands moving in. The sodium emission lines appear to ride on top of the white light maximum, making them a little difficult to separate. As will be seen, the actual spectra differed somewhat from this.

5. SODIUM TWILIGHT OBSERVATIONS

The first observation with the instrument of twilight sodium was made on January 29, 1960. Following some subsequent adjustments, 13 runs were obtained between February 20 and May 26, 1960. The procedure followed in making a run was similar to that of Hunten and Shepherd (1954) except that only the zenith was observed. Figure 4 shows some selected 1-minute scans from a morning run on February 21. It should be noted that the sodium lines were not well centered in the scan. The first is of a low brightness source (Shepherd 1954) and should give the white light profile of Fig. 3. It does not, in the sense that the peaking effect of the interference filter is not as great as was expected, although it is present. The next scan was taken in early twilight, with the unrefracted shadow line at 5 km , and shows the two



Feb 21, 1960, A.M.

FIG. 4. Selected scans from a sodium twilight run for various heights of unrefracted shadow line. Photomultiplier voltages are indicated for each scan.

Fraunhofer absorption lines. The next scan is taken at 58 km, and shows the emission lines quite well resolved. The last is taken with the shadow line at 120 km, and shows a trace of emission, which must be nightglow. This is the only occasion on which the nightglow was observed.

The procedure used in analysis was also similar to that of Hunten and Shepherd (1954) except that the two D lines were treated separately. In addition to giving the variation of sodium brightness during twilight these results can also give the D_2/D_1 ratio, which has not been extensively measured so far. A summary of the previous results is given by Chamberlain, Hunten, and Mack (1958). In all cases the ratio obtained is an average over one or more evenings. Chamberlain, Hunten, and Mack (1958) have calculated the D_2/D_1 ratio as a function of sodium abundance (atoms/cm² vertical column) for a solar depression of 6.5° and zenith angles of observation of 0° and 75°. Donahue and Stull (1959) have calculated D_2/D_1 as a function of solar depression for several abundances, but only for a zenith angle of 75°.

Only for the later runs was the interference filter adjusted to give equal transmission at D_1 and D_2 . For the earlier runs, a correction factor was applied by noting the wavelength of the maximum in the low brightness source spectrum and using the derived interference filter characteristics. Application of these correction factors gave D_2/D_1 ratios which were much too large. The correction was obviously being overestimated and in fact, the most reasonable values appeared to be the uncorrected ones. Under these circumstances the absolute value of D_2/D_1 for the early runs could not be considered reliable and instead it appeared more useful to concentrate in the analysis on the variation of D_2/D_1 during twilight.

For each run, D_2/D_1 was plotted against Z_1 , the unrefracted shadow height. The scatter of plotted points was disturbing at first, and some smoothing was attempted, including averaging several runs together. But it was concluded that these attempts served only to average out the true variations. On re-examining the original plots, it was seen that they could be grouped into

several characteristic plots. From the calculations of Donahue and Stull (1959) one would associate each of these with a different sodium abundance. For an abundance of 1×10^9 atoms/cm² column their plot from $Z_1 = 30$ km to 80 km is essentially horizontal, showing only a slight maximum at the center. At an abundance of 5×10^9 , the low Z_1 end of the plot has fallen, making the curve unsymmetrical. At 10×10^9 , the high Z_1 end has also fallen, making the curve symmetrical again with a central broad maximum. At 20×10^9 , the high Z_1 end falls even more and for higher abundances, the maximum disappears completely, with D_2/D_1 decreasing with increasing Z_1 through the entire range. Eleven runs had variations which could be included by one of these cases, but the other two runs did not fit at all, with D_2/D_1 increasing rapidly with Z_1 . The grouping of nights that resulted is given in Table I. For each

TABLE I
Grouping of runs according to characteristic D_2/D_1 variation, 1960

Runs	Associated abundance
March 18, May 3, May 5, May 17, May 26	1×10^9 atoms/cm ² column
April 18, May 7	5×10^9 atoms/cm ² column
February 20	10×10^9 atoms/cm ² column
February 21, March 23, April 11	20×10^9 atoms/cm ² column
April 8, May 6	—

group, one run is shown in Fig. 5, along with the calculated curves of Donahue and Stull (1959). This is done for abundances of 1×10^9 , 5×10^9 , 10×10^9 , and 20×10^9 atoms/cm² column. Unfortunately, the calculations are for a zenith angle of 75° and the runs were made at 0° but the difference only becomes important for large abundances. Because of the uncertainty in the absolute value of D_2/D_1 , the calculated curves were shifted to obtain best visual agreement with the results and this shift is indicated by the arrow at the right of each plot. This uncertainty of the absolute D_2/D_1 ratio is not just that introduced by the instrument (as mentioned above), but includes that of the intensities at the bottom of the Fraunhofer lines for D_1 and D_2 . This latter quantity is still not agreed upon to within 10%. Points indicated by a cross are those of Chamberlain, Hunten, and Mack (1958) and have been interpolated from their Table 3. (The results in this table appear to have been shifted from the corresponding plot in their Fig. 3.) Since the differences between the shapes of the curves of different calculated abundances are slight, it is unfortunate that the experimental scatter is so large. This is particularly true for the points at the ends of the curve which have much to do with determining the shape; but nevertheless the experimental variations are considered to be real. However, the accuracy does not warrant the conclusion, for example, that the abundance on March 23 was 20×10^9 and that on February 20 was 10×10^9 . Rather, it merely suggests that the abundance on March 23 was greater than on February 20. Support for this is given by the fact that in Table I the runs near the seasonal maximum, February and March, have been assigned the higher abundances as compared with the runs during May.

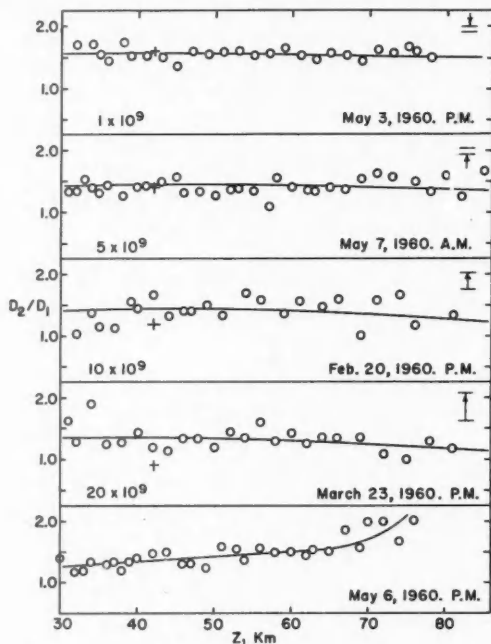


FIG. 5. Variation of D_2/D_1 ratio during twilight for a number of runs. Solid curve is that calculated by Donahue and Stull (1959) for the abundances shown (atoms/cm² column), shifted by the amounts indicated. Crosses are points calculated by Chamberlain, Hunten, and Mack (1958), unshifted.

The plot at the bottom of Fig. 5 is for May 6, which like April 8, could not be fitted into any group. A smooth curve has been sketched through the points. The increase of D_2/D_1 at the end of the run could perhaps be explained as a result of nightglow, which has so far not been considered. One would have to further assume that the ratio of twilightglow to nightglow intensity was much lower on this evening than for the others for which the effect is not seen. The measurements are not adequate to consider this point in detail.

6. CONCLUSIONS

A 1-in. mechanical scanning Fabry-Perot spectrometer has been constructed and operated at low resolution with a free spectral range (between orders) of 36 Å. By using an interference filter as monochromator, sodium twilight spectra have been obtained with an instrumental half width of 2.5 Å. This can be compared with the 10-Å half width for a 4×4 in. grating spectrometer operating at roughly the same light gathering power. It is concluded that such an instrument is very suitable for studies involving a spectral range of about 30 Å or less. With a scanning monochromator this range could be extended considerably.

Observations made of the D_2/D_1 ratio during twilight gave variations which were different from night to night, and which resembled the variations for different sodium abundances as calculated by Donahue and Stull (1959). Two of the 13 runs were exceptions and did not fit into any of the above patterns. Absolute values of D_2/D_1 were not obtained with certainty on all runs, but are in general agreement with what is expected.

Future measurements should have the aim first of eliminating any uncertainty in the absolute value of D_2/D_1 , second of reducing the scatter in the measurements, and third of making simultaneous absolute brightness measurements. This will provide two independent abundance values during the same run and give a crucial test to the calculations. In particular, it should remove the uncertainty in the ratio of residual intensities at the bottom of the Fraunhofer lines. The absolute calibration of a Fabry-Perot is more difficult than that for a grating spectrometer because of the uncertain instrumental profile, but these difficulties can be overcome.

While it would be possible to make these improvements on 1-in. instruments, it has been decided instead to concentrate on a larger 6-cm instrument, for which the 1-in. was intended as a test version. It is anticipated that this new instrument will produce results an order of magnitude better than the present one.

ACKNOWLEDGMENTS

The initial planning of this project, and a preliminary design of the pressure scanning mounting were carried out by Dr. D. M. Hunten and Dr. R. Montalbetti. After the author assumed responsibility for the project, Dr. Hunten continued to give valuable advice, and has made available an evaporation chamber for dielectric coating of the plates, as well as supplying interference filters prepared with the same equipment. The present mounting design, along with other useful ideas, resulted from discussions between the author and Dr. R. Chabbal. Financial support in the early stages was supplied by the Institute of Upper Atmospheric Physics, University of Saskatchewan. The excellent machining of the mounting was done by Mr. F. Rittmann. Mr. H. H. Zwick assisted with some of the observations.

REFERENCES

- ARMSTRONG, E. B. 1959. *J. Atmospheric and Terrest. Phys.* **13**, 205.
CHABBAL, R. 1953. *J. recherches centre natl. recherche sci.* **24**, 138.
——— 1958a. *Thèses. Université de Paris.*
——— 1958b. *J. phys. radium*, **19**, 246.
——— 1958c. *J. phys. radium*, **19**, 295.
CHABBAL, R. and SOULET, M. 1958. *J. phys. radium*, **19**, 274.
CHAMBERLAIN, J. W., HUNTEN, D. M., and MACK, J. E. 1958. *J. Atmospheric and Terrest. Phys.* **12**, 153.
DONAHUE, T. M. and STULL, V. R. 1959. *Ann. geophys.* **15**, 481.
HUNTEN, D. M. 1953. *Can. J. Phys.* **31**, 681.
HUNTEN, D. M. and SHEPHERD, G. G. 1954. *J. Atmospheric and Terrest. Phys.* **5**, 57.
JACQUINOT, P. 1954. *J. Opt. Soc. Am.* **44**, 761.
KARANDIKAR, R. V. 1959. Final Report, Air Force Cambridge Research Center, Contract AF 19(604)-2172.
SHEPHERD, G. G. 1954. Scientific Report No. AR-16, Contract AF 19(122)-152, University of Saskatchewan.
TIMOSHENKO, S. 1930. *Strength of materials, Part II* (D. Van Nostrand Co.).
WARK, D. Q. 1960. *Astrophys. J.* **131**, 491.

ON THE OPTICAL AND ELECTRICAL PROPERTIES OF SEMITRANSSPARENT COPPER FILMS¹

R. S. ADHAV²

ABSTRACT

Simultaneous measurements were made of the optical constants n and k , reflectance R , transmittance T , and of the d-c. conductivity σ , of semitransparent copper films deposited onto quartz by evaporation *in vacuo*. All depositions were carried out at a pressure $p \approx 10^{-5}$ mm Hg and with a deposition rate $D \approx 2$ Å/sec. The optical constants were determined by an ellipsometer with a photomultiplier tube attachment at the wavelengths 435 mμ, 546 mμ, and 630 mμ. The reflectance values were computed from the optical constants. The transmittance values were measured at these wavelengths by a unicam spectrophotometer. The d-c. conductivities were measured by a Kohlrausch bridge. These measurements were carried out in the thickness range 60 Å to 455 Å. The disagreement of the results with the Garnett theory and the Fuchs theory is discussed and conclusions regarding the structure and the degree of porosity are drawn.

Sennett and Scott (1950) have used the Garnett theory to explain the appearance of a maximum in the absorption ' A ' against the thickness curve, and have shown that the agreement between theory and experiment is perfect for silver. Reynolds and Stilwell (1952) have shown that there is a close agreement between theoretical and experimental values of the d-c. conductivity of thin evaporated films above a certain thickness. Givens (1955) has stressed the need of pressure $p < 10^{-5}$ mm Hg during deposition of films of copper. In the present investigation, simultaneous measurements are made of the optical constants n and k , reflectance R , transmittance T , and of the d-c. conductivity σ , of semitransparent copper films deposited onto quartz by evaporation *in vacuo*. The disagreement of the results with the above-mentioned optical and electrical theories is discussed and conclusions regarding the structure and the degree of porosity are drawn.

The semitransparent copper films in the thickness range 60 Å to 455 Å were prepared by vacuum deposition at a pressure $p \approx 10^{-5}$ mm Hg and at a deposition rate $D \approx 2$ Å/sec. The optical constants n and k were determined at the three wavelengths $\lambda_1 = 435$ mμ, $\lambda_2 = 546$ mμ, and $\lambda_3 = 630$ mμ, with the help of an ellipsometer with a photomultiplier tube (RCA 931 A). This wavelength range was selected since pure copper is reported to have an absorption band with its long wavelength limit between the range 550 mμ–600 mμ. The new formulae obtained by Ditchburn (1955) were used for computing the real term n and the phase-shift term k of a complex refractive index. The reflectance R was computed from the values of n and k . The transmittance T in the same wavelength range was directly measured by a spectrophotometer. The absorption A was obtained by assuming $T+R+A$

¹Manuscript received March 8, 1960.

²Contribution from the Physics Department, Gujarat College, Ahmedabad, India.

³Present address: Dominion Observatory, Ottawa, Canada.

= 100%. Hence it includes the light scattered by the films, which is of the order of 1% over the thickness range and the wavelength range under consideration. The d-c. conductivity was measured by means of a Kohlrausch bridge. The method used in measuring the film thickness was essentially that described by Tolansky and his collaborators (1948).

The Garnett theory assumes that (a) the film may be represented by spherical metal crystallites of diameter that is small as compared to the film dimensions; (b) these spherical particles are distributed at random in space and the density of the film is characterized by the volume factor q giving the fractional volume occupied by the metal. A film of metal of optical constants n and k ($= nk$) exhibits apparent optical constants n_1 and k_1 ($= n_1k_1$) related to n , k , and q by the formulae,

$$n_1k_1 = 3qb / [(1-qa)^2 + 4q^2b^2]$$

$$k_1^2 - n_1^2 = 2 - \frac{3(1-qa)}{[(1-qa)^2 + 4q^2b^2]}$$

where q is the volume factor and naturally $0 < q < 1$. The constants a and b are given by

$$a = \frac{(k^2 - n^2 + 1)(k^2 - n^2 - 2) + 4n^2k^2}{(k^2 - n^2 - 2)^2 + 4k^2n^2},$$

$$b = 3nk / [(k^2 - n^2 - 2)^2 + 4k^2n^2].$$

The product n_1k_1 gives a measure of absorption of the film. According to Sennett and Scott (1950), the curve n_1k_1 against q possesses a maximum if $\tilde{K} > 0$ where

$$\tilde{K} = 2(k^2 - n^2)^3 - 9(k^2 - n^2)^2 + (12 + 8n^2k^2)(k^2 - n^2) - 4(3n^2k^2 + 1).$$

For the wavelengths used, the values of \tilde{K} are greater than zero and are shown in Table I.

TABLE I
Theoretical values of n , k , a , b , and \tilde{K} for the three wavelengths

$\lambda = m\mu$	n	k	a	b	\tilde{K}
435	1.15	1.70	0.92	0.38	2.45
546	1.07	2.25	1.21	0.27	137.2
630	0.59	5.78	1.09	0.01	6.5×10^4

Hence the theory expects a maxima for the absorption against the thickness curve for the three wavelengths under consideration. Table II shows the theoretical values of n_1k_1 assuming that q ranges from 0.6 to 1.

The experimental results of transmittance T , reflectance R , and absorption A for these copper films at the three wavelengths, are in the Table III. The absorption A is negative for a film of thickness 60 Å for wavelengths $\lambda_2 = 546$

TABLE II
Theoretical values of $n_1 k_1$ at the three wavelengths for various q values

Volume factor q	$n_1 k_1$		
	$\lambda_1 = 435 \text{ m}\mu$	$\lambda_2 = 546 \text{ m}\mu$	$\lambda_3 = 630 \text{ m}\mu$
0.6	1.66	2.80	0.164
0.7	1.93	5.63	0.375
0.8	2.08	3.47	1.40
0.9	2.06	3.12	33.9
1.0	1.95	2.45	25.0

TABLE III
Transmittance T , reflectance R , and absorption A for thickness range 60 Å to 455 Å, for the three wavelengths

Thickness in Å	$\lambda_1 = 435 \text{ m}\mu$			$\lambda_2 = 546 \text{ m}\mu$			$\lambda_3 = 630 \text{ m}\mu$		
	$T\%$	$R\%$	$A\%$	$T\%$	$R\%$	$A\%$	$T\%$	$R\%$	$A\%$
60	67.0	32.0	1.0	75.0	25.8	-0.8	71.0	31.3	-2.3
105	47.0	29.1	23.9	55.0	27.7	17.3	52.0	28.3	19.7
165	34.2	32.4	33.4	42.0	31.5	26.5	38.0	32.7	29.3
212	24.8	39.5	35.7	31.6	33.0	35.4	26.0	34.8	39.2
286	14.9	42.2	42.9	21.0	37.6	41.4	15.7	43.6	40.7
350	11.4	44.0	44.6	16.2	39.1	44.7	11.0	45.8	43.2
455	6.5	47.6	45.9	10.8	41.5	47.7	6.7	56.2	37.1

$m\mu$, and $\lambda_3 = 630 \text{ m}\mu$, because below the depth of penetration (of about 150 Å) the substrate partly modifies the reflection and also because the film structure becomes more granular.

Fuchs (1938) made an analysis of the problem of electrical conductivity of thin metallic films with the help of the electron theory of metals. He obtained expressions of the form,

$$\sigma/\sigma_0 = 4/3M \log(1/M) \quad \text{for thin films,}$$

where σ = electrical conductivity of film,

σ_0 = electrical conductivity of bulk metal,

$$M = t/l,$$

where t is the thickness and l is the mean free path of electrons in the metal at a given temperature.

In this case, $l = 420 \text{ Å}$,

$$\sigma_0 = 0.5618 \times 10^6 (\text{ohm-cm})^{-1}.$$

Dingle (1950) does not assume that there is a diffuse scattering at the surface of the film, and modifies the formulae by multiplying it by the ratio $(1-p)/(1+p)$ where p is the probability of an electron being scattered elastically at the surface.

The experimental and theoretical results of electrical conductivity of the same films are shown in Table IV.

TABLE IV

Experimental and theoretical values of d-c. conductivity of the same films in the thickness range 60 Å to 455 Å

Thickness in Å	Resistance in:		Experimental		Theoretical	
	Vacuum (ohms)	Air (ohms)	$k = t/l$	$1 + \log (\sigma_0/\sigma)$	$k = t/l$	$1 + \log (\sigma_0/\sigma)$
60	∞	∞	—	—	—	—
105	10,000	10,000	0.25	4.74	0.01	2.42
165	7.00	7.90	0.39	1.78	0.10	1.67
212	4.76	5.60	0.50	1.72	0.20	1.47
286	3.01	3.25	0.68	1.66	0.50	1.27
350	2.39	2.58	0.88	1.64	1.00	1.16
455	1.81	1.89	1.08	1.63	2.00	1.08

The theoretical values of $n_1 k_1$ against volume factor q as given in Table II are plotted in Fig. 1.

The experimental values of absorption A against thickness as given in Table III are plotted in Fig. 2.

Experimentally, therefore, absorption maxima occur for wavelengths above $\lambda = 550 \text{ m}\mu$, while theory suggests maxima above $\lambda = 435 \text{ m}\mu$. The explanation of the differences is to be found in the intrinsic differences in structures of experimental and theoretical films. The results of Sennett and Scott (1950) with silver show that the degree of fit with the theory is better for films deposited at higher rates of evaporation. The results of Krautkramer (1938) show that the degree of fit is better for films deposited at a higher substrate temperature. In the present investigation the rate of deposition is about 2 Å/sec , for all the films and the substrate temperature is about 30°C . Halliday, Rymer, and Wright (1954) have examined thin films of copper obtained by deposition *in vacuo*, by an electron diffraction method. Their results show that thin copper films consist of crystallites in the form of disks, of diameter 90 Å and thickness 15 Å . Electron micrograph of copper films obtained by Sennett and Scott (1950) shows that the aggregation of copper crystallites does not appear as regular and as well defined as in the case of silver.

Figure 2 indicates that the maxima occur at about 320 Å thickness for a wavelength of $\lambda_3 = 630 \text{ m}\mu$. Figure 1 indicates that the maxima occur for the same wavelength at a q value of 0.9. Hence the porosity of a film of thickness 320 Å is of the order of 10%. Again, the absorption A falls to zero at a thickness of about 60 Å for the wavelength under consideration. The indications are that a film of copper of 60 Å in thickness is almost transparent. This could be on account of an oxide film of 60 Å in thickness formed on all the copper films immediately after exposure to air. Garforth (1948) observed that an oxide layer of 70 Å was formed on the copper films even at a pressure of oxygen of 10^{-2} mm Hg in about 7 hours at room temperature.

The above observations were further carried out over a period of 1 day. A typical result at $\lambda_3 = 630 \text{ m}\mu$, over a period of 18 hours is shown by a dotted line (Fig. 2). As the oxidation proceeds, the absorption maxima become less marked and move towards shorter thicknesses. The absorption also falls to zero at a greater thickness, giving a higher intercept on the thickness axis.

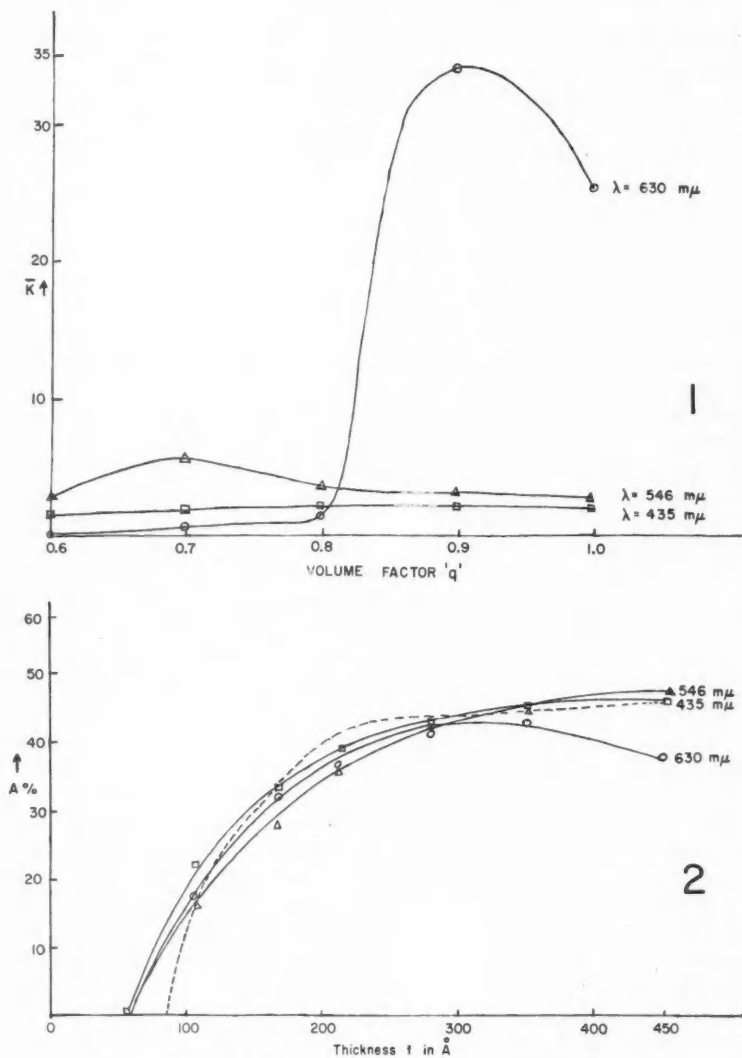


FIG. 1. Theoretical curves of \bar{K} against 'q' for the three wavelengths.
 FIG. 2. Experimental curves of absorption A against thickness t in \AA .

The initial 60 Å intercept moved to 85 Å over a period of 18 hours, indicating that an oxide film of 85 Å is formed over these films. Hence the absorption against thickness curve provides a method of estimating the thickness of overlying oxide film.

In Fig. 3, the experimental and theoretical curves of $(1 + \log(\sigma_0/\sigma))$ do not coincide. Above a certain thickness, they run almost parallel indicating the

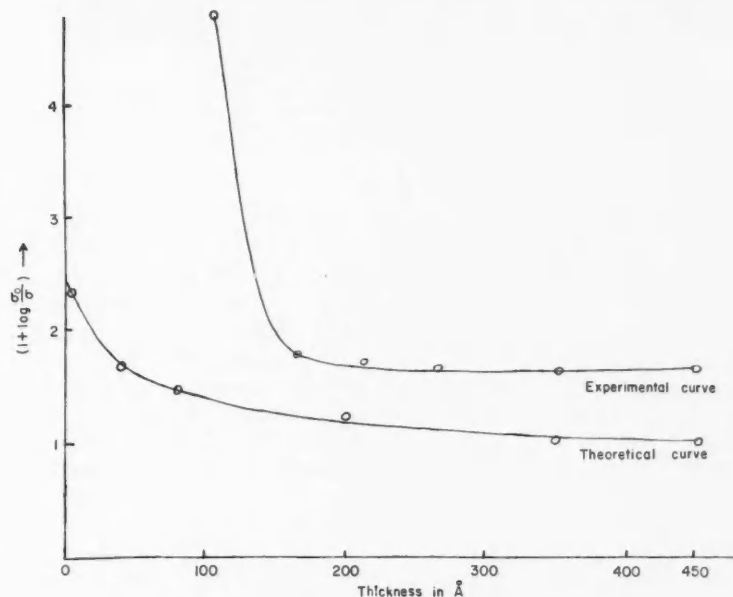


FIG. 3. $(1 + \log(\sigma_0/\sigma))$ against thickness in Å.

porous structure of experimental films, even for thicknesses greater than the mean free path of electrons in metal. Hence any formulae for d-c. conductivity of thin films must take into account the volume factor q . In the present investigation, the critical thickness at which electrical conductivity is almost established is found to be about 120 Å. This is almost double that for silver, as reported by Oppenheim (1956). This again depends upon the crystalline property of bulk metal and upon the numerous conditions of preparation of the film.

The author is very much indebted to Dr. Y. G. Naik for suggesting the problem and to Mr. D. K. Gijare for helping in the techniques of preparation of thin films. Thanks are also due to Dr. D. M. Dennison for many valuable suggestions and encouragement.

REFERENCES

- DINGLE, R. B. 1950. *Proc. Roy. Soc. A*, **201**, 545.
DITCHBURN, R. W. 1955. *J. Opt. Soc. Am.* **45**, 743.
FUCHS, K. 1938. *Proc. Cambridge Phil. Soc.* **34**, 100.
GARFORTH, F. 1948-49. *Repts. Progr. in Phys.* **XII**, p. 174.
GIVENS, M. P. 1955. *J. Opt. Soc. Am.* **45**, 229.
HALLIDAY, J. S., RYMER, T. B., and WRIGHT, K. H. R. 1954. *Proc. Roy. Soc. A*, **225**, 546.
KRAUTKRAMER, J. 1938. *Ann. Physik*, **32**, 537.
OPPENHEIM, U. 1956. *J. Opt. Soc. Am.* **46**, 628.
REYNOLDS, F. W. and STILWELL, G. R. 1952. *Phys. Rev.* **88**, 418.
SENNETT, R. S. and SCOTT, G. D. 1950. *J. Opt. Soc. Am.* **40**, 203.
TOLANSKY, S. 1948. *Multiple beam interferometry* (Oxford University Press, London).

THE DECAY OF Pm^{149}

AGDA ARTNA AND MARGARET E. LAW

ABSTRACT

The 52.8-hour activity of Pm^{149} has been investigated using a high resolution beta spectrometer, a lens type coincidence spectrometer, and a scintillation spectrometer in conjunction with a multichannel analyzer. The beta spectrum was found to consist of two groups with maximum energies of 1.072 ± 0.002 Mev and 0.786 ± 0.004 Mev, and intensities of $97.1 \pm 0.4\%$ and $2.9 \pm 0.4\%$ respectively. A gamma ray of energy 285.7 ± 0.3 kev was found to be in coincidence with the 0.786-Mev beta group. No other gamma rays with intensities greater than 0.1% were found. The K conversion coefficient for the 286-kev transition was measured to be 0.075 ± 0.008 . This together with the values of 6.5 ± 0.7 and 4 ± 1 obtained for the K/L and L/M conversion ratios respectively indicate that this transition is $M1$ in character with less than 10% $E2$ admixture.

INTRODUCTION

The 52-hour activity of Pm^{149} has been investigated previously by Rutledge, Cork, and Burson (1952), and by Kondaiah (1952). Rutledge *et al.* reported a strong 285-kev gamma ray in coincidence with a 1.05-Mev beta group, and a weak 1300-kev gamma ray. However, Kondaiah found that the decay consisted of a single beta group of end point 1.05 Mev leading to the ground state of Sm^{149} . More recently, Chapman, Grace, Gregory, and Sowter (1960) have carried out nuclear alignment studies on Pm^{149} . They also detected a 285-kev gamma ray associated with the 52-hour activity, but found it to be in coincidence with a weak beta group of end point 0.770 Mev. Since there is obvious disagreement between these three reports it was decided to investigate this decay scheme further.

Pm^{149} is the product of the 2-hour negatron decay of Nd^{149} . Neodymium oxide enriched to 82% in Nd^{148} was irradiated for 15 hours in the high flux reactor at Oak Ridge, and was received some 30 hours after removal from the reactor. The sample also contained 4% Nd^{146} and 7% Nd^{160} , producing the 11-day Nd^{147} and 27-hour Pm^{151} activities. In addition, a small amount of samarium was present, giving the 47-hour Sm^{153} activity.

EXPERIMENTAL

A. Gamma-ray Spectrum

The gamma-ray spectrum of the sample was investigated using a scintillation spectrometer consisting of a DuMont 6363 photomultiplier and a 3-in. NaI crystal, in conjunction with a RCL 256 channel analyzer. Figure 1 shows a typical spectrum taken 7 days after removal of the sample from the reactor. No higher energy radiations were seen with intensities greater than 10% of the 540-kev gamma ray.

¹Manuscript received August 8, 1960.

Contribution from the Department of Physics, McMaster University, Hamilton, Ontario.

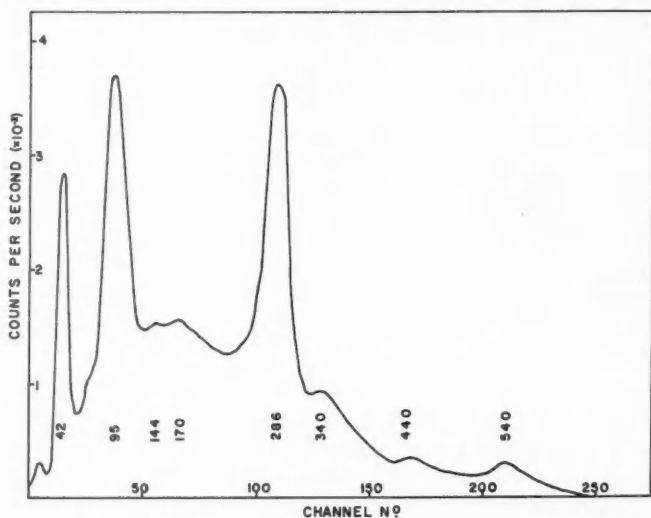


FIG. 1. Gamma-ray spectrum taken 7 days after removal of the sample from the reactor. The energies of the peaks are given in kev.

The spectrum was followed over a period of 20 days to obtain the half lives of the various peaks. The majority of these could be accounted for by the known gamma rays resulting from either Nd^{147} , Pm^{151} , or Sm^{153} decay. The 286-kev gamma ray was found to have a half life of 54 ± 2 hours and is therefore associated with the Pm^{149} decay. No other gamma rays were found to decay with this half life.

B. The 286-kev Transition

(i) Coincidence Experiments

The beta spectrum in coincidence with the 286-kev gamma ray was investigated with a double long-lens coincidence spectrometer of the Gerholm type (Gerholm 1955). One spectrometer (No. 1) was set on the 286-kev K conversion line and the beta spectrum scanned with the other (No. 2). A Bell, Graham, and Petch (1952) fast-slow coincidence circuit was used, set at 8 μsec resolving time. The sources were prepared by dissolving the neodymium oxide in nitric acid, and evaporating to dryness a small droplet of the solution on a backing of V.Y.N.S. film. The resulting sources were approximately 2 mm in diameter and $300 \mu\text{g}/\text{cm}^2$ thick.

In all, three complete experiments were done. Each experiment lasted 4 days, during which time the beta spectrum was scanned approximately 20 times. Figure 2 shows the Fermi plot of the coincidence spectrum obtained from one of the experiments. The mean end point of the beta spectrum in coincidence with the 286-kev K line was found to be 0.788 ± 0.009 Mev.

From the singles counting rate in spectrometer No. 1, set on the 286-kev K peak, it was possible to obtain an accurate determination of the half life

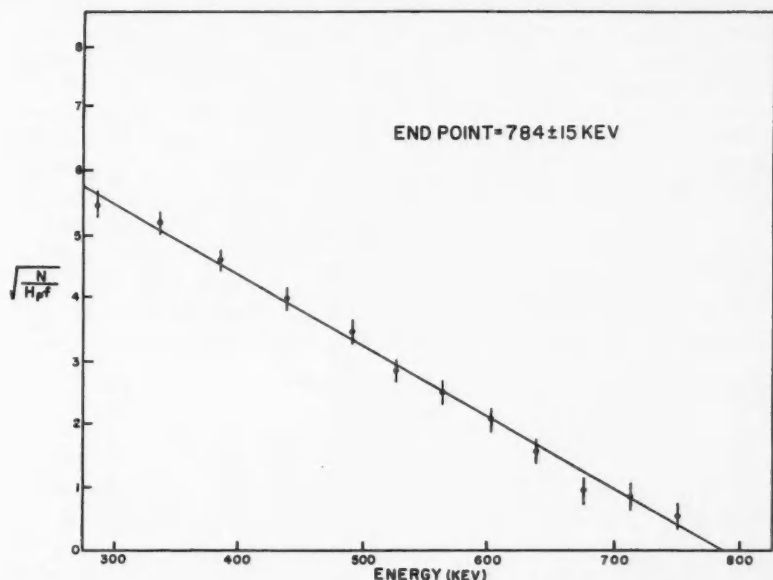


FIG. 2. Fermi plot of the beta spectrum in coincidence with the 286-keV K conversion line.

of the Pm^{149} activity. The counting rate obtained had to be corrected for the 27-hour Pm^{151} and the 11-day Nd^{147} contributions. The latter was measured after all the shorter-lived activities had died, while the former was estimated from the intensity of the gamma rays associated with Pm^{151} as measured with the scintillation spectrometer. Neither correction amounted to more than 5% of the total. In addition, it was estimated from the internal conversion spectrum that $1.5 \pm 1.0\%$ of the activity was due to 47-hour Sm^{153} . However, because of the similar half lives of Sm^{153} and Pm^{149} , the half-life plot was insensitive to this small amount of impurity, and over a period of 4 days the correction for this was negligible compared to the statistical errors. The resulting half life of Pm^{149} is 52.8 ± 0.3 hours.

(ii) *External and Internal Conversion Experiments*

The internal and external conversion lines of the 286-keV transition were studied using a 50-cm Siegbahn type beta-ray spectrometer (Johns *et al.* 1953). Line sources for this instrument were prepared as described above ($B(i)$), the source backing in this case being aluminum-coated mylar. These sources were 2.5 cm long and had varying widths and thicknesses depending on the resolution and counting rates desired.

The K internal conversion coefficient, α_K , was measured directly by comparing the number of K conversion electrons with the gamma-ray intensity from the same source. The number of gamma rays was obtained from the external conversion peak according to the equation $N_\gamma = N_{p.e.} \times f \times k$ where

$N_{p.e.}$ is the photoelectron peak height, f is the photoelectric yield for a given gamma-ray energy and for a given radiator material and thickness (this factor has been discussed by Johns *et al.* 1954), and k is a factor depending on the source radiator geometry. α_K is then given by

$$\alpha_K = N_{eK}/N_\gamma = N_{eK}/N_{p.e.} \times f \times k.$$

The source radiator geometry factor, k , was measured by repeating the experiment in the same geometry with the 412-keV Au^{198} transition, for which $\alpha_K = 0.028$ (Wapstra *et al.* 1958). Figure 3 shows the internal and external conversion peaks for both these transitions. The gold source consisted of $0.5 \times 2.5 \text{ cm}^2$ rectangle of gold-coated mylar ($30 \mu\text{g}/\text{cm}^2 \text{ Au}$). The promethium source of the same dimensions had an approximate thickness of $500 \mu\text{g}/\text{cm}^2$. The continuum underlying the external conversion peaks is mainly due to

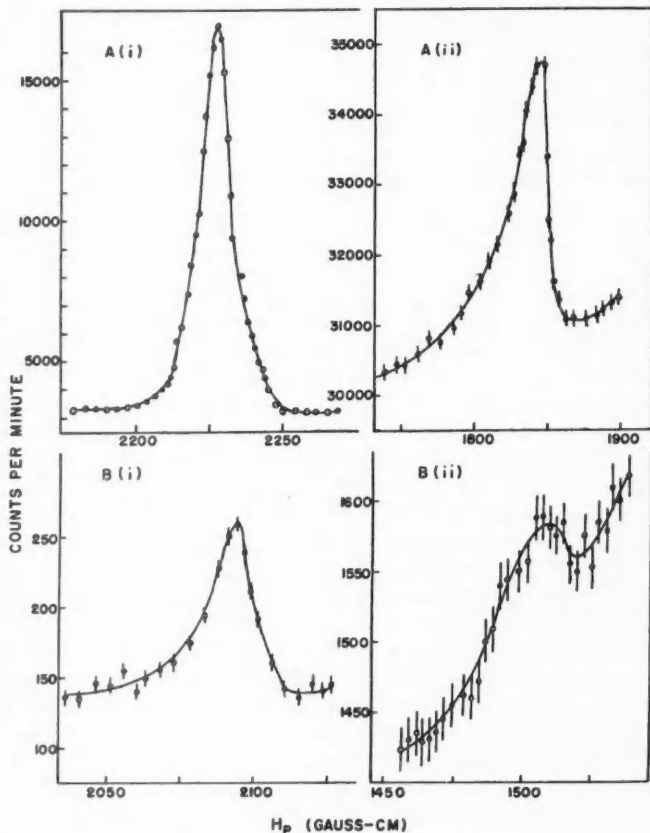


FIG. 3. The internal (A) and external (B) conversion lines of the 412-keV gamma ray of Au^{198} (i) and the 286-keV gamma ray of Pm^{149} (ii).

high energy betas which have penetrated the radiator backing used as the beta stopper. In the case of the promethium peak, some of the continuum is also due to Compton electrons accompanying the higher energy gamma rays of Pm^{151} . In order to check the reproducibility of the geometry, the experiment was carried out with two different radiators of 2.2 mg/cm^2 and 2.9 mg/cm^2 uranium. The K conversion coefficient was found to be 0.075 ± 0.008 , the error being mainly due to the uncertainty in the 286-keV external conversion peak height. The photoelectric yield factor for this instrument, f , is known to better than $\pm 5\%$.

The internal conversion lines were studied using a $0.2 \times 2.5 \text{ cm}^2$ beta source, approximately $50 \text{ } \mu\text{g/cm}^2$ thick. The spectrometer resolution under these conditions was 0.5% . Figure 4 shows the K , L , and M peaks. The K/L and

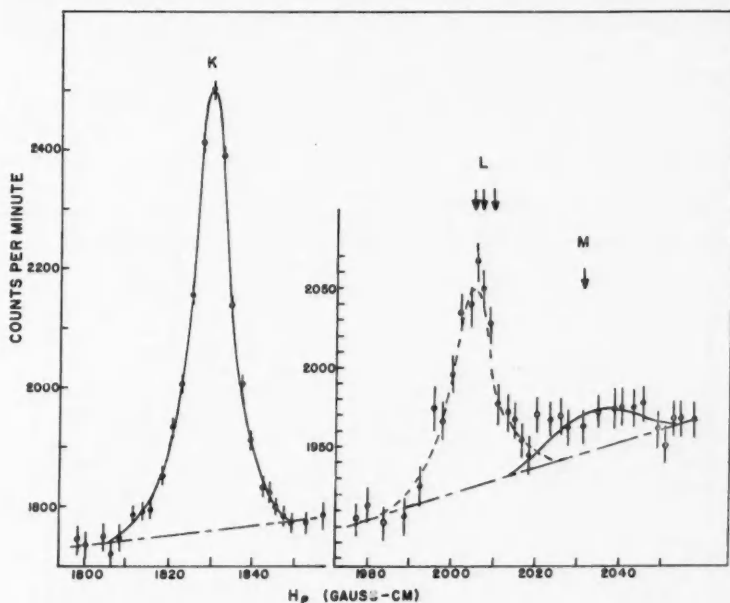


FIG. 4. Internal conversion peaks of the 286-keV transition. Superimposed on the L peaks is the normalized outline of the K peak.

L/M ratios obtained from these were 6.5 ± 0.7 and 4.0 ± 1.0 respectively. In addition, from a comparison of the profiles of the K and L lines it could be concluded that the L peak consisted mainly of the L_1 component. An upper limit of 0.1 could be set for the $L_1 + L_2/L_3$ ratio.

The energy of the transition as measured in both external and internal conversion experiments is $285.7 \pm 0.3 \text{ keV}$. The standards used for this measurement were the thorium F line and the 411.77-keV gamma ray of Au^{198} for internal conversion, and the 316.46 line of Ir^{192} , and the 411.77 line of Au^{198} for external conversion.

C. Beta-ray Spectrum

The beta continuum was scanned with the high resolution spectrometer. The end point of the spectrum as obtained from a Fermi plot is 1.073 ± 0.002 Mev. Subtracting from this the energy of the gamma ray, the end point of the second group is 0.786 ± 0.002 Mev. Since only one gamma ray was found to belong to this decay the beta spectrum was assumed to consist of only these two groups.

The method of Fermi analysis normally used to obtain branching ratios could not be used here because of the presence of impurities, in particular Sm^{153} , which have end points similar to that of the inner group. This type of analysis is very sensitive to such small corrections. Instead, the intensity of the 0.786-Mev beta group (b_1) was calculated in terms of the number of conversion electrons (N_{eK}), and either the number of betas in the ground state transition ($N_{\beta 0}$), or the total number of betas ($N_{\beta T}$), according to the equations

$$b_1 = N_{eK}(1 + \alpha_T) / \alpha_K N_{\beta 0} + \alpha_K N_{eK}(1 + \alpha_T), \quad (\text{i})$$

$$b_1 = N_{eK}(1 + \alpha_T) / \alpha_K N_{\beta T}. \quad (\text{ii})$$

Figure 5 shows a Fermi plot of the total spectrum. The number of ground state betas could be found by reconstructing the spectrum as shown in the insert (curve B). The second curve in the insert (curve A) shows the total beta spectrum after the Nd^{147} , Pm^{151} , and Sm^{153} contributions had been

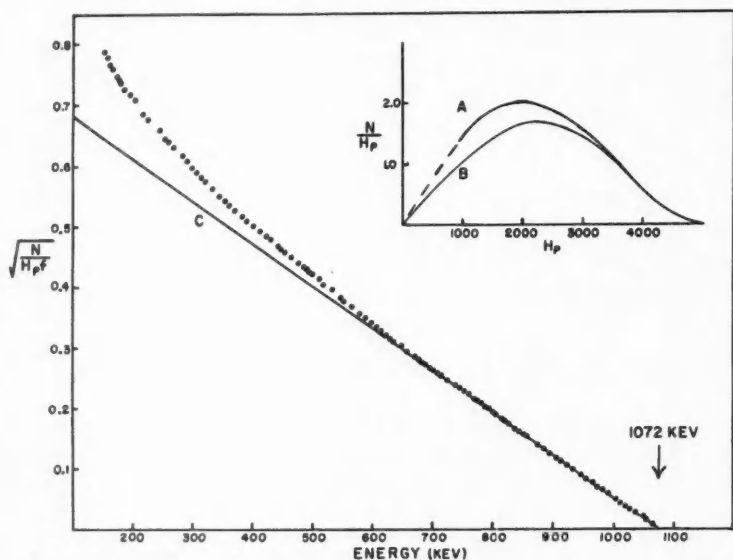


FIG. 5. Fermi plot of the total beta spectrum. The insert shows the total beta spectrum (A), and the spectrum of the high energy beta group (B) reconstructed from the straight line of the Fermi plot (C).

subtracted. Since curve B is an ideal spectrum with no source thickness effects, equation (i) gives an upper limit for b_1 . The spectrum was scanned three times. The mean value of b_1 obtained from equation (i) was 0.033 ± 0.004 , and from equation (ii) 0.028 ± 0.003 . A similar analysis of the singles spectrum measured in spectrometer No. 2 of the coincidence spectrometer gave results in agreement with these.

In addition, the relative intensity b_1 could also be calculated from the data of the coincidence experiments, using the following equation:

$$b_1 = A_{\text{coinc}(2)} / A_{\text{total}(2)} \times (1 + \alpha_T) / \alpha_K \cdot w(1)$$

where $A_{\text{coinc}(2)}$ is the area under the beta continuum in coincidence with the 286-keV K peak; $A_{\text{total}(2)}$ is the area under the total beta continuum, and $w(1)$ is the transmission of spectrometer No. 1 set on the 286-keV K peak. Using values of $\alpha_T = 0.089 \pm 0.009$, $\alpha_K = 0.075 \pm 0.008$, and $w(1) = 0.017 \pm 0.002$, a mean value of 0.029 ± 0.006 was obtained for b_1 .

From these results the intensities of the 1.072-MeV and 0.786-MeV beta groups were found to be $97.1 \pm 0.4\%$ and $2.9 \pm 0.4\%$ respectively, leading to ft values of 7.1 and 8.1.

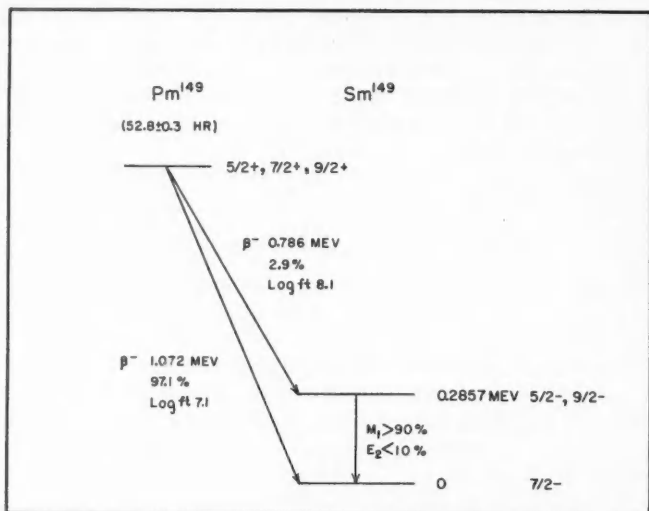
SUMMARY

Table I compares the measured values of the conversion coefficients and ratios for the 286-keV transition with the theoretical predictions for several multipolarities. From these results it was deduced that the gamma ray is $>90\%$ $M1$ with possible $E2$ admixture.

TABLE I
Conversion data for the 286-keV transition

	Theoretical conversion coefficients and ratios ($k = 0.56$, $Z = 62$)					Experimental values
	$E1$	$E2$	$E3$	$M1$	$M2$	
α_K	0.014	0.050	0.16	0.078	0.33	0.075 ± 0.008
α_L	0.0018	0.011	0.084	0.010	0.058	0.011 ± 0.002
$K:L$	7.8	4.4	2.1	7.9	5.7	6.5 ± 0.7
$L_1:L_2:L_3$	11:1:1	2:1.5:1	1:2.5:1.5	77:5:1	17:1.7:1	$L_1 \gg L_2 + L_3$
$L:M$	3.0	2.8	2.8	2.8	3.0	4 ± 1

Figure 6 shows the proposed decay scheme for Pm^{149} , which is essentially in agreement with that of Chapman *et al.* (1960). The only discrepancy is in the branching ratio of the beta groups. The value of $1.8 \pm 0.3\%$ obtained by Chapman *et al.* for the relative intensity of the inner group, is lower than the value measured in this work. The spin of the ground state of Sm^{149} is known to be $7/2$ (Bogle and Scovil 1952). From the $M1$ character of the 286-keV transition it can be deduced that the excited state has negative parity with spin $5/2$, $7/2$, or $9/2$. Chapman *et al.* (1960) have ruled out the $7/2$ possibility from their alignment studies. There is no evidence from Coulomb excitation experiments (Heydenburg and Temmer 1955) for collective motion in this nucleus. It would therefore seem most likely that the 286-keV

FIG. 6. The decay scheme of Pm^{149} .

level is due to particle excitation with spin $5/2^-$. The $\log ft$ values and the allowed shapes of the two beta spectra (Figs. 2 and 5) indicate that these are both first forbidden non-unique. This leads to a positive parity for the ground state of Pm^{149} . The possible spin assignments are $5/2$, and $7/2$ if the spin of the 286-kev level is $5/2$, and $7/2$, or $9/2$ if the excited level has spin $9/2$. The shell model prediction for the spin of Pm^{149} is $5/2$. However, recent unpublished work at Berkeley (quoted by Chapman *et al.* 1960) has shown that the spin is $7/2$.

In comparing this decay scheme with those of neighboring odd neutron nuclei one might expect a level at approximately 100 kev. Sm^{147}_{85} , Gd^{151}_{87} , and Sm^{153}_{89} have levels at 121 kev, 108 kev, and 66 kev respectively. Since no evidence was found for a gamma ray of this energy with intensity comparable to that of the 286-kev transition, this level, if it exists in Sm^{149} , must be very weakly fed.

ACKNOWLEDGMENTS

The sources used in this experiment were obtained through the courtesy of the United States Atomic Energy Commission and the Oak Ridge National Laboratory.

We are indebted to the Canadian National Research Council and the Ontario Research Foundation for financial assistance in the form of research grants. One of the authors (M.E.L.) was a recipient of a National Research Council Fellowship during this work.

We should also like to thank Professors M. W. Johns and M. A. Preston of this laboratory for helpful discussions, and Chapman *et al.* of Oxford for sending details of their work prior to publication. Finally the assistance of R. Goodman and D. MacArthur in recording data is gratefully acknowledged.

REFERENCES

- BELL, R. E., GRAHAM, R. L., and PETCH, H. E. 1952. *Can. J. Phys.* **30**, 35.
BOGLE, G. S. and SCOVIL, H. E. D. 1952. *Proc. Phys. Soc. A*, **65**, 368.
CHAPMAN, C. J. S., GRACE, M. A., GREGORY, J. M., and SOWTER, D. V. 1960. *Proc. Roy. Soc.* To be published.
GERHOLM, T. R. 1955. *Rev. Sci. Instr.* **26**, 1069.
HEYDENBURG, N. P. and TEMMER, G. M. 1955. *Phys. Rev.* **100**, 150.
JOHNS, M. W., WATERMAN, H., MACASKILL, D., and COX, C. D. 1953. *Can. J. Phys.* **31**, 225.
JOHNS, M. W. and NABLO, S. V. 1954. *Phys. Rev.* **96**, 1599.
KONDALAH, E. 1952. *Phys. Rev.* **81**, 1056.
RUTLEDGE, W. C., CORK, J. M., and BURSON, S. B. 1952. *Phys. Rev.* **86**, 775.
WAPSTRA, A. H., NIJGH, G. J., SALOMONS-GROBBEN, N., and ORNSTEIN, L. TH. M. 1958. *Nuclear Phys.* **9**, 538.

PROPAGATION OF ELECTROMAGNETIC WAVES ALONG A THIN PLASMA SHEET¹

JAMES R. WAIT

ABSTRACT

It is shown that a thin ionized sheet will support a trapped surface wave. The effect of a constant and uniform magnetic field is to modify the phase velocity and polarization of the surface wave. The essential features are illustrated by numerical results for selected values of the electron density, collision frequency, and gyro frequency. The effect of locating the plasma sheet near and parallel to a conducting plane is also considered. In this situation other modes of a waveguide type are possible in addition to the surface wave.

INTRODUCTION

The propagation of electromagnetic waves in a plasma medium is currently receiving a great deal of attention. In the theoretical approach to such problems, it is usually assumed that the medium is infinite in extent and homogeneous in its macroscopic electrical properties. The complications which arise when the medium is inhomogeneous are considerable. Nevertheless, it is desirable to consider the influence of boundaries if experimental data are to be interpreted. In particular, such boundaries or interfaces can support surface waves which propagate in a manner very different from that in homogeneous media. It is the purpose of this paper to consider the surface waves which may exist in a thin ionized (plasma) sheet in the presence of a steady magnetic field. Following Poeverlein (1958), the thickness, δ , of the sheet is taken to be very small so that the currents, \mathbf{J} , flowing in the sheet are purely transverse.

FORMULATION OF BOUNDARY CONDITIONS

Starting with the relevant equations (Ratcliffe 1959) for an electron plasma and harmonic time dependence, the (boundary) conditions relating the fields just above and just below the sheet can readily be obtained. If the sheet is contained in the plane $z = 0$, the equations of motion may be written

$$(1) \quad \begin{aligned} (\nu + i\omega)J_x - \omega_z J_y &= \omega_0^2 \epsilon E_x \\ \omega_z J_x + (\nu + i\omega)J_y &= \omega_0^2 \epsilon E_y \end{aligned}$$

where ν is the (constant) collisional frequency of the electrons with the ions, ω_0^2 is the electron plasma frequency, ω_z is the z component of the (electron) gyro frequency, and ϵ is the dielectric constant of free space. Using a subscript 1 to denote the region above the sheet and a subscript 2 to denote the region below the sheet, the boundary conditions

$$(2) \quad \left. \begin{aligned} H_{1y} - H_{2y} &= -J_x \delta \\ H_{1x} - H_{2x} &= J_y \delta \end{aligned} \right\} \text{ for } z = 0$$

¹Manuscript received August 22, 1960.

Contribution from the National Bureau of Standards, Boulder, Colorado, U.S.A. and the Laboratory for Electromagnetic Theory, Technical University, Copenhagen, Denmark.

Can. J. Phys. Vol. 38 (1960)

immediately follow from Ampere's law. To within the same approximation

$$(3) \quad \left. \begin{aligned} E_y &= E_{1y} = E_{2y} \\ E_z &= E_{1z} = E_{2z} \end{aligned} \right\} \text{for } z = 0.$$

Using equations (1) and (2), the boundary conditions may be written in the form

$$(4) \quad \begin{aligned} \eta[H_{1y} - H_{2y}] &= -ME_x - NE_y \\ \eta[H_{1x} - H_{2x}] &= -NE_x + ME_y \end{aligned}$$

where

$$(5) \quad M = \frac{\epsilon\omega_0^2 \delta (\nu + i\omega)}{(\nu + i\omega)^2 + \omega_z^2} \eta,$$

and

$$(6) \quad N = \frac{\epsilon\omega_0^2 \delta \omega_z}{(\nu + i\omega)^2 + \omega_z^2} \eta,$$

and $\eta = (\mu/\epsilon)^{\frac{1}{2}} = 120 \pi$.

The boundary conditions as developed above must be met by any form of the electromagnetic waves which can exist in the presence of the sheet. The restrictions are that the sheet thickness is infinitesimally small. As a consequence, only the component of the steady magnetic field perpendicular to the sheet is important. This is the reason the transverse components of the gyro frequencies do not appear in the expressions for M and N .

THE SURFACE WAVE SOLUTION

We shall now show that such a sheet can support a surface wave. Whether such a wave can be excited by a physical source has been discussed elsewhere (Wait 1960). The properties of such a wave will be discussed here without consideration of the source. Furthermore, the wave is assumed to propagate in the x direction parallel to the sheet. The variation in the y direction is taken to be zero, so that the disturbance is purely two-dimensional in nature.

To facilitate the solution of the problem, electric and magnetic Hertz vectors are introduced. As will be shown, it is only necessary that these have z components which are denoted Π and Π^* , respectively. Sometimes these are called Hertz potentials. The field components are expressed in terms of these two scalar functions by

$$(7a) \quad E_x = \frac{\partial^2}{\partial x \partial z} \Pi$$

$$(7b) \quad E_y = i\mu\omega \frac{\partial \Pi^*}{\partial x}$$

$$(7c) \quad E_z = \left(k^2 + \frac{\partial^2}{\partial z^2}\right) \Pi$$

$$(8a) \quad H_z = \frac{\partial^2}{\partial x \partial z} \Pi^*$$

$$(8b) \quad H_y = -i\epsilon\omega \frac{\partial \Pi}{\partial x}$$

$$(8c) \quad H_z = \left(k^2 + \frac{\partial^2}{\partial z^2}\right) \Pi.$$

The boundary conditions at the sheet (i.e., $z = 0$) are then given by

$$(9a) \quad ik(\Pi_1 - \Pi_2) = M \frac{\partial \Pi_1}{\partial z} + N ik \eta \Pi_1^*$$

$$(9b) \quad \eta \left[\frac{\partial \Pi_1^*}{\partial z} - \frac{\partial \Pi_2^*}{\partial z} \right] = -N \frac{\partial \Pi_1}{\partial z} + M ik \eta \Pi_1^*$$

$$(9c) \quad \Pi_1^* = \Pi_2^*$$

$$(9d) \quad \frac{\partial \Pi_1}{\partial z} = \frac{\partial \Pi_2}{\partial z}.$$

We now assume the following form of the solutions

$$(10a) \quad \Pi_1 = a e^{-ikCz} e^{-ikSz}$$

$$(10b) \quad \Pi_2 = a' e^{+ikCz} e^{-ikSz}$$

$$(10c) \quad \eta \Pi_1^* = b e^{-ikCz} e^{-ikSz}$$

$$(10d) \quad \eta \Pi_2^* = b' e^{+ikCz} e^{-ikSz}.$$

Since these are to be solutions of the wave equation

$$C^2 + S^2 = 1.$$

Furthermore, if the fields are to be positively damped for directions away from the sheet

$$\text{Im } C < 0.$$

The latter two boundary equations, (9c) and (9d), immediately indicate that

$$a' = -a \quad \text{and} \quad b' = b.$$

The first two boundary equations, (9a) and (9b), then give

$$(11a) \quad \frac{b}{a} = \frac{MC+2}{N}$$

and

$$(11b) \quad \frac{b}{a} = \frac{NC}{M+2C}.$$

In order that the wave be a solution to our problem, the right-hand side of these two equations should be equal. This leads to the following equation for C

$$(12) \quad (M+2C)(MC+2)+N^2C=0.$$

Solutions are

$$(13) \quad C = C_0 = \frac{-(M^2+N^2+4) \pm [(M^2+N^2+4)^2 - 16M^2]^{\frac{1}{2}}}{4M}.$$

Normally only one of these solutions satisfies the condition $\text{Im } C < 0$. This root is denoted C_0 ; it corresponds to the trapped surface wave which propagates in the direction of the positive x -axis. The corresponding value of S is given by

$$(14) \quad S_0 = (1 - C_0^2)^{\frac{1}{2}}.$$

PROPERTIES OF THE SURFACE WAVE

To present the results in a graphical form, certain dimensionless parameters are now introduced. They are

$$B = \frac{\delta\omega_0^2}{c\omega}, \quad Q = \frac{\omega_z}{\omega}, \quad Z = \frac{\nu}{\omega}$$

and therefore

$$(15) \quad M = iB \frac{1-iZ}{Q^2 - (1-iZ)^2},$$

$$(16) \quad N = B \frac{Q}{Q^2 - (1-iZ)^2}.$$

Since the surface-wave fields vary as $\exp(-ikS_0x)$, the phase velocity parallel to the sheet is $1/\text{Re } S_0$ relative to the velocity of light c . This quantity is plotted in Fig. 1 as a function of B which is proportional to the thickness of the sheet. Values of Q , which are proportional to the gyro frequency, are shown on the curve. The case $Q = 0$ corresponds, of course, to zero gyro frequency or no magnetic field. Two values of Z are shown. $Z = 0$ corresponds to a vanishing collision frequency. The influence of collisions, shown by the curves for $Z = 0.2$, is not great. In general it is seen that the phase velocity is less than the velocity of light. It is also seen that an interesting transition region occurs near $Q = 1$.

The attenuation of the waves in the x direction is $-\text{Im } kS_0$ in nepers per meter. Thus $-\text{Im } S_0$ is a measure of the damping of the wave. If $Z = 0$ this quantity is zero since S_0 is a real quantity. In Fig. 2 this "horizontal attenuation" is plotted as a function of B for three values of Z . As expected, the damping of the surface wave increases as Z becomes larger. Again there is a transition effect for Q near 1. In fact, as Q becomes greater than 1 the horizontal attenuation becomes very small even when collisions are considered.

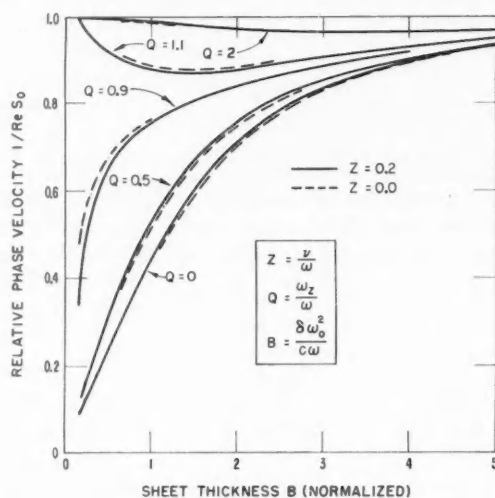


FIG. 1. The phase velocity of the surface wave relative to c , as a function of the normalized thickness of the thin plasma sheet.

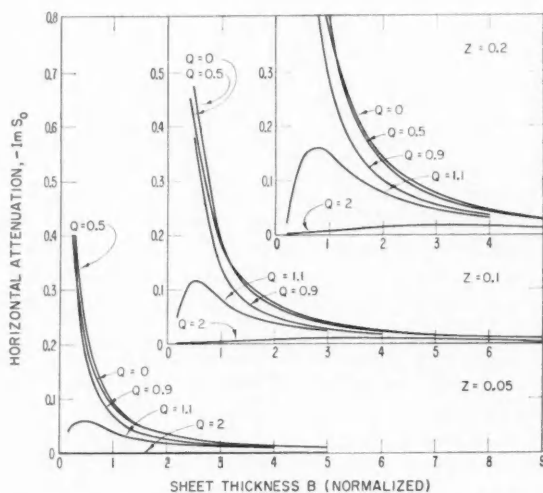


FIG. 2. The horizontal attenuation of the surface wave as a function of the normalized thickness of the thin plasma sheet.

Some further light is shed on the problem when the vertical attenuation is considered. Since the fields vary in the vertical direction according to $\exp(-ikC|z|)$ it is seen that a measure of the decay of the surface wave is $-\text{Im } C_0$. This quantity is plotted in Fig. 3 as a function of B . It appears that

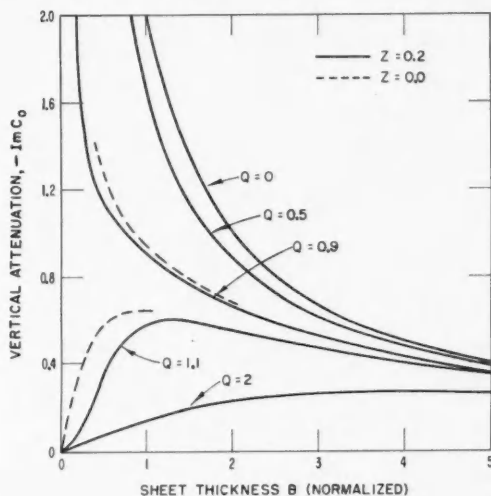


FIG. 3. The vertical attenuation of the surface wave as a function of the normalized thickness of the thin plasma sheet.

the wave is highly trapped when Q is small. As Q increases to values somewhat greater than 1, the wave spreads out on both sides of the sheet. In fact, in the limiting case of $Q \rightarrow \infty$, the surface wave degenerates into a plane wave travelling along the sheet. In this situation the sheet is effectively a perfect magnetic conductor.

The wave polarization, P , is conveniently defined as the ratio of the component of the electric field parallel to the sheet to the component perpendicular to the sheet. That is

$$(17) \quad P = \frac{E_{1y}}{E_{1x}} = -\frac{E_{2y}}{E_{2x}} = \frac{MC_0 + 2}{SN_0}.$$

This quantity is plotted in Fig. 4 as a function of B for the case $Z = 0$. The curves for small finite values of Z would not be very different from those shown. It may be observed that for small values of Q the field is almost vertically polarized. When Q becomes greater than 1 there is a tendency for the polarization to change to horizontal. This change in polarization is quite abrupt for small values of B as indicated in Fig. 4.

These results could indicate that surface waves propagating along air-plasma interfaces may be profoundly influenced by the presence of an impressed

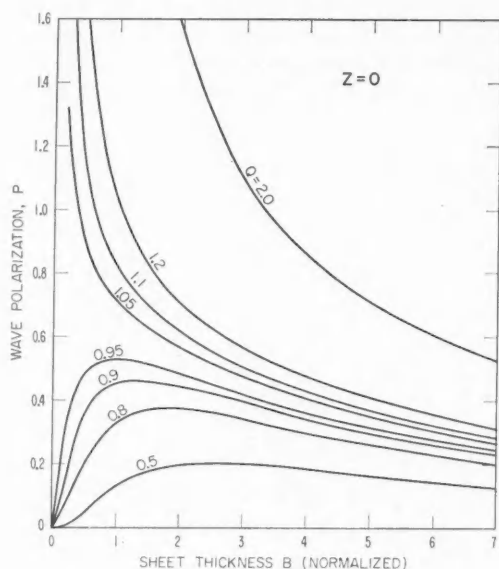


FIG. 4. The polarization of the surface wave in a plane normal to the direction of propagation.

magnetic field. In fact, this behavior may find application in microwave diagnostics of plasma. It is admitted, however, that the model chosen is highly idealized.

AN EXTENSION OF THE PROBLEM

As emphasized, the previous analysis was restricted to a thin plasma sheet with unbounded media on both sides. It would seem to be worth while to investigate the case where the plasma sheet is located above a conducting plane. Intuitively one would feel that the surface wave of the kind discussed above should not be influenced by the presence of the conducting plane if the separation was reasonably large, say of the order of a wavelength. On the other hand, the space contained by the plasma sheet and the conducting plane could be expected to support waveguide type modes. The following analysis supports these contentions.

With reference to the usual Cartesian co-ordinate system, the thin plasma sheet is again taken to be located in the plane $z = 0$. Now, however, there is assumed to be a conducting plane boundary at $z = -d$. As far as the harmonically varying fields are concerned, this boundary is assumed to be perfectly conducting. The steady or d-c. magnetic field which is applied is considered not to be affected by the presence of the conducting medium occupying the space $z < -d$.

The boundary conditions at the sheet are unchanged, but now an additional

boundary condition at $z = -d$ must be met. This latter condition is that the tangential components of the electric field should be zero on the plane. This suggests writing the Hertz potentials in the following form

$$(18) \quad \Pi_1 = ae^{-ikCz}e^{-ikSz} \quad \text{for } z > 0,$$

$$(19) \quad \Pi_2 = a'(e^{ikCz} + e^{-ikC(z+2d)})e^{-ikSz} \quad \text{for } -d < z < 0,$$

$$(20) \quad \eta\Pi_1^* = be^{-ikCz}e^{-ikSz} \quad \text{for } z > 0,$$

$$(21) \quad \eta\Pi_2^* = b'(e^{ikCz} - e^{-ikC(z+2d)})e^{-ikSz} \quad \text{for } -d < z < 0.$$

Since $\partial\Pi_2/\partial z$ and Π_2^* vanish at $z = -d$, the boundary condition $E_x = E_y = 0$ at $z = -d$ is met. Application of equations (9a) to (9d) now leads readily to four linear equations involving the coefficients a , a' , b , and b' . Setting the determinant of these equal to zero gives

$$(22) \quad [(1+V)+MC][(1+V)C+M]+N^2C=0$$

where

$$(23) \quad V = \frac{1+e^{-2ikCd}}{1-e^{-2ikCd}},$$

It is seen that when

$$-\text{Im } kCd \gg 1$$

V may be replaced by unity as the equation reduces to equation (12) of the previous section. A surface wave does indeed satisfy this condition if d is of the order of a wavelength or greater. Thus, a conducting plane at a reasonable distance from the plasma sheet has little influence on the surface wave on the structure.

A first-order correction to the surface wave solution to account for the presence of the conducting plane can be obtained by perturbation. For example, in equation (22), V is replaced by V_0 , where

$$(24) \quad V_0 = \frac{1+e^{-2ikC_0d}}{1-e^{-2ikC_0d}}$$

and C_0 is given by equation (13). Solving the resulting quadratic in C leads to the first-order solution \hat{C}_0 given by

$$(25) \quad \hat{C}_0 = \frac{-[M^2+N^2+(1+V_0)^2] \pm \{[M^2+N^2+(1+V_0)^2]^2 - 4(1+V_0)^2 M\}^{\frac{1}{2}}}{2(1+V_0)M}.$$

When $-\text{Im } kC_0d \gg 1$, V_0 may be replaced by unity and the previous solution is obtained.

In addition to a modification of the surface wave solution, equation (22) has other solutions. These are the waveguide modes. To illustrate their behavior, N is set equal to zero. The equation breaks into two independent parts. These may be written in the form

$$(26) \quad 1-e^{-i2kCd} = -2/(MC), \quad \text{and} \quad 1+e^{-i2kCd} = -2C/M.$$

The first of these equations corresponds to the TM (transverse magnetic) modes while the second corresponds to the TE (transverse electric) modes. In general, it appears these transcendental equations must be solved by numerical or graphical means. However, if $|M|$ is sufficiently large a simple perturbation method may be used to solve for the modes.

The following substitutions are now made

$$2kCd = 2n\pi + \Delta \quad (n = 0, 1, 2, 3, \dots)$$

for the TM modes, and

$$2kCd = (2m-1)\pi + \Delta' \quad (m = 1, 2, 3, \dots)$$

for the TE modes. Then under the condition that Δ and $\Delta' \ll 1$, it is readily found that

$$(27a) \quad \Delta \cong \frac{\epsilon_n i k d}{n \pi M}; \quad \epsilon_0 = 1, \quad \epsilon_n = 2 \quad \text{for } n = 1, 2, 3, \dots$$

and

$$(27b) \quad \Delta' \cong \frac{i(2m-1)\pi}{Mkd}, \quad \text{for } m = 1, 2, 3, \dots$$

Thus

$$(28a) \quad S_n \cong \left[1 - \left(\frac{\pi n}{kd} \right)^2 - \frac{\epsilon_n i}{Mkd} \right]^{\frac{1}{2}} \quad \text{for the } TM \text{ modes } (n = 0, 1, 2, \dots)$$

and

$$(28b) \quad S_m \cong \left\{ 1 - \left[\frac{(m-\frac{1}{2})\pi}{kd} \right]^2 \left(1 + \frac{2i}{Mkd} \right) \right\}^{\frac{1}{2}} \quad \text{for the } TE \text{ modes } (m = 1, 2, 3, \dots).$$

These relatively simple expressions are valid if

$$|Mkd| \gg 1.$$

The corresponding results for $N \neq 0$ are somewhat more involved. Then coupling between TE and TM modes takes place.

It can be concluded that a thin plasma sheet parallel to a conducting plane will support a strongly trapped surface wave whose propagation characteristics depend mainly on the electrical properties of the sheet. However, in addition there are waveguide modes which have to be considered.

ACKNOWLEDGMENT

I would like to thank Mrs. Alyce Conda and Mrs. Nancy Carter for carrying out the computations.

REFERENCES

- POEVERLEIN, H. 1958. J. Atmospheric and Terrest. Phys. **12**, 126.
 RATCLIFFE, J. A. 1959. Magneto-ionic theory (Cambridge University Press).
 WAIT, J. R. 1960. Scientific Report No. 8, Contract AF 19(604)-CSO and A 58-40, to the U.S. Air Force Cambridge Research Center, Bedford, Mass.

A MAGNETIC SUSCEPTIBILITY BALANCE AND THE TEMPERATURE DEPENDENCE OF THE MAGNETIC SUSCEPTIBILITY OF COPPER, SILVER, AND GOLD, 295°-975° K¹

M. GARBER,² W. G. HENRY, AND H. G. HOEVE³

ABSTRACT

A magnetic susceptibility balance is described which has a reproducibility of better than $\pm 0.15\%$. The temperature dependence of the magnetic susceptibility of copper, silver, and gold from 295° to 975° K is reported.

1. INTRODUCTION

In an earlier paper, referred to hereinafter as I (Henry and Rogers 1956), an apparatus was described which is suitable for making measurements at room temperature of the magnetic susceptibility of weakly dia- and para-magnetic, machinable alloys with a precision of approximately $\pm 0.2\%$. It was pointed out that serious errors may arise in the measurement of the magnetic susceptibility of metal specimens containing ferromagnetic impurities if any part of the specimen is in a field in which the ferromagnetic impurities are not reasonably saturated. The minimum allowable field for silver specimens was found to be about 6500 gauss. Phases other than solid solutions are in general not readily machinable. For this reason a magnetic susceptibility balance capable of making precise measurements on cast specimens, cut roughly to length, was felt desirable. Some solid solutions such as those formed by the metals of the first transition series in copper are unstable at room temperature. As it was planned to measure the temperature dependence of some of these alloys to determine the effective Bohr magneton value of the solute, an apparatus which would make measurements above room temperature was required. In this paper an apparatus is described which meets all these requirements and which has a reproducibility of better than $\pm 0.15\%$. With a suitable Dewar the apparatus could be used for low-temperature measurements.

The basic components of the apparatus are: a modified Varian Associates electromagnet with pole pieces 12 in. in diameter; a Varian Associates power supply; a combined mechanical and electronic balance which is a modified version of that suggested by Mauer (1954). In order to avoid the necessity of accurately machined specimens the pole pieces were designed using the electrolytic tank technique to produce a volume of approximately constant $B_z \partial B_z / \partial x$ where x is the vertical direction. The furnace consists of two globars inside a silver shield.

¹Manuscript received September 21, 1960.

Contribution from the Division of Applied Chemistry, National Research Council, Ottawa, Canada.

Issued as N.R.C. No. 6027.

²Present address: Michigan State University, Department of Physics, East Lansing, Michigan, U.S.A.

³Present address: E. I. Du Pont de Nemours and Company, Central Research Department, Wilmington, Delaware, U.S.A.

There have been numerous magnetic susceptibility devices described in the literature. In general the investigators have been interested in either results of much lower precision or only in reasonably high precision relative to, say, a room temperature measurement. Stevens, Cleland, Crawford, and Schweinler (1955), who measured the susceptibility of germanium at low temperatures, have recently described an apparatus capable of a degree of precision similar to that of the present apparatus. The problem of irregularly shaped specimens was avoided by making the measurements relative to oxygen. This method, which is satisfactory at low temperatures, would not be satisfactory at temperatures at which oxidation would take place. Also the method loses precision as the temperature increases because of the decrease in the susceptibility of oxygen. The specimens were placed in the fringing field of an electromagnet and no attempt was made to shape the pole pieces.

In the present paper the results of the measurement of the variation of the magnetic susceptibility of copper, silver, and gold from room temperature to 975° K are presented. There have been only three previous investigations in which all three metals were measured (Honda 1910; Owen 1912; Shimizu 1937). The materials used by Honda and Owen were sufficiently impure to cast doubt on their results and, further, no numerical values were given. Ross (1934) and Bitter, Kaufmann, Starr, and Pan (1941) found that copper becomes less diamagnetic as the temperature increases, whereas Shimizu found the reverse. The present work confirms the results of Ross and Bitter *et al.* regarding the sign and magnitude of the temperature dependence. The absolute value of the diamagnetic susceptibility of silver is found to go through a minimum at approximately 750° K. Up to 750° K the silver becomes less diamagnetic; Shimizu found that silver becomes more diamagnetic in that temperature range. Rao and Savithri (1942) found the temperature dependence of the susceptibility of silver to be less than their limit of error, which was approximately $\pm 1.0\%$. The sign of the temperature dependence of gold is found to differ from those found by Shih (1931) and Shimizu. The present work appears to agree with that of Vogt and Gerstensberg (1959) but they give no data and hence a good comparison cannot be made. The differences are probably due to the differences in purity of the materials, and in the method of handling ferromagnetic impurities.

2. POLE PIECE DESIGN, CALIBRATION AND CORRECTION FOR FERROMAGNETIC IMPURITIES

(a) Pole Piece Design

The pole pieces were designed by the method of electrical analogy (Malavard 1947). Eight electrostatic models were investigated, the best of which is described here. References to other pole piece designs are given by Bates (1951).

Assuming the pole faces to be magnetostatic equipotentials, profiles are sought in the $x-z$ plane such that along the vertical symmetry axis (x -axis)

$$(2.1) \quad B_z \partial B_z / \partial x = \text{constant.}$$

Since the pole pieces are long in the y direction (horizontal and parallel to the faces), $B_y = 0$ and $\partial/\partial y = 0$. Equation (2.1) represents the condition that all elements of the sample lying in the x - y plane experience the same vertical force per cc, provided the magnetization is a linear function of the field. A discussion of the more general case in which ferromagnetic impurities are present is given in I. For elements of the sample which are not in the x - y plane, the complete expression must be used in place of (2.1) (I),

$$(2.2) \quad -B_x \partial B_z / \partial z + B_z \partial B_x / \partial x = \text{constant}.$$

As a first approximation the variations with respect to z are neglected and attention is confined to (2.1). The relationship between $B_z(x,0)$ and x is thus given by

$$(2.3) \quad B_z = (ax+b)^{\frac{1}{2}}$$

In order to obtain a relationship between the gap width and x , it is assumed that $B_z(x,0)$ varies inversely with the gap width and is given by

$$(2.4) \quad B_z = d/2z,$$

where d is a constant and $2z$ is the gap width. On combining (2.3) and (2.4), it is found that

$$(2.5) \quad 2z = d/(ax+b)^{\frac{1}{2}}.$$

Equation (2.5) represents the trial equipotential surface which was used as a starting point for the electrostatic tank experiments. The constants a and b were determined by applying the following conditions: at the base of the specimen ($x = 0$ cm) the gap width is 5.0 cm; at the top of the specimen ($x = 2$ cm) the field is half that at $x = 0$ cm. The latter condition ensures that for the lowest magnet current used the field will be strong enough (6500 gauss) everywhere over the sample to saturate ferromagnetic impurities and yet allow for a sufficiently strong force per unit volume. The relation between z and x is

$$(2.6) \quad z^2 = 50/(8-3x).$$

In the electrostatic model, the gap was allowed to narrow to 3.1 cm, being limited by furnace design, and below this point the pole pieces were tapered apart at an angle of 60° in order to provide a stronger field. The model showed that the above design led to a nearly constant force density over the desired working length of about 2 cm; that the tapering did not adversely affect the desired field over this length, and that replacing the curved shape by straight line segments, in order to facilitate machining, would have no significant influence.

A cross section and plan view of the pole piece are shown in Fig. 1. The pole pieces were made from castings kindly supplied by the Bureau of Mines, Ottawa, Canada. The analysis of the material is: C, 0.016; Mn, 0.20; Si, 0.03; S, 0.023; P, 0.015; Cr, 0.03; Ni, 0.06; Mo, <0.01; V, 0.003; Al, 0.035; Cu, 0.15; Sn, 0.01; Co, 0.003 wt. %.

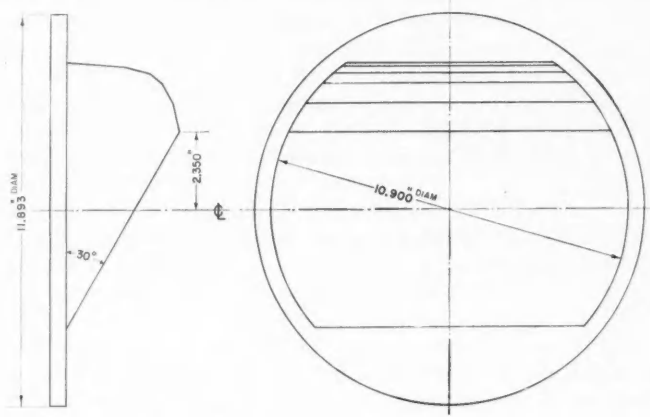


FIG. 1. A cross section and plan view of a pole piece.

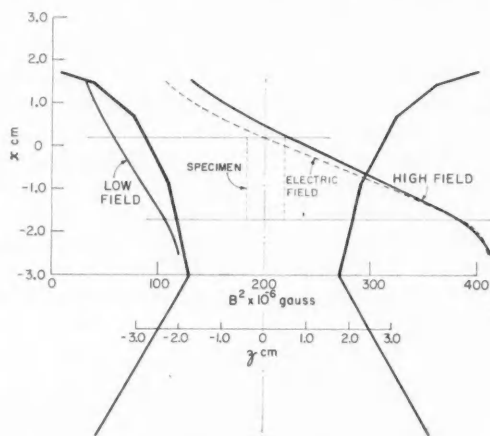


FIG. 2. The low and high fields and the specimen position.

As in 1, two fields were used; the lowest was determined by the condition that no part of the specimen should be in a field of less than 7000 gauss. In Fig. 2, the variation of the square of both the low and high fields with x is shown. The mean values of the slope of the squares of the fields over the 2-cm length are -84.0×10^6 and -25.4×10^6 gauss² per cm. The dotted curve was that found by the method of electrical analogy. The constant of proportionality between the electric field and the field of magnetic induction was found by fitting the two curves in the high field region.

The relationship between the field strength and the gap width is better

approximated by $B_z = d/(2z)^{0.85}$ than by equation (2.4). The pole pieces were not redesigned using this information because the degree of the success of the method was not known beforehand. This does suggest, however, a self-consistent method for designing pole pieces. Thus as a first step an approximation such as (2.4) would be used, then the actual relationship between B_z and z would be determined experimentally in the tank. The design expression would then be reformulated using the experimentally determined counterpart to equation (2.4).

(b) Field Calibration

The calibration was made using copper specimens free from interfering ferromagnetic contamination, of constant diameter, and varying length (1.6 to 2.0 cm). The absolute mass susceptibility of the copper had been determined earlier (1) to be -0.0859×10^{-6} c.g.s. e.m.u. The force F_z in the vertical direction is given by

$$(2.7) \quad F_z = (m/\alpha')(\chi - \kappa/\rho)$$

where m is the mass of the specimen, $1/\alpha'$ is the mean value of (2.2) over the specimen. The mass susceptibility of the specimen is χ ; κ is the volume susceptibility of the atmosphere and ρ is the density of the specimen. All the experiments were done in helium and hence κ/ρ could be neglected in comparison with the mass susceptibility of copper.

To determine the constants of the apparatus, the bottoms of the copper specimens were located in a fixed position relative to a fixed mark on the pole pieces, approximately 1.3 cm above the minimum gap. The constants for the low and the high field, shown in Fig. 3, for the copper specimens of various lengths were calculated from the relationship

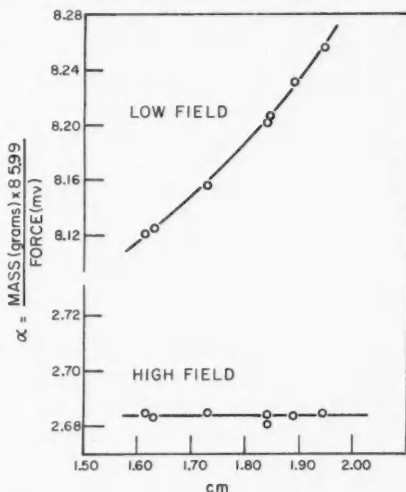


FIG. 3. The low and high field calibration.

$$(2.8) \quad \alpha = \frac{\text{mass(gram)} \times 85.99}{\text{force (mv)}}.$$

The constant α is related to α' of equation (2.7); $\alpha = -\alpha'g \text{ (mg/mv)} \times 10^6$, where (mg/mv) is the constant, milligrams per millivolts, of the balance discussed in Section 3 and g is the gravitational constant. The α for the high field is constant to within $\pm 0.1\%$ for specimens with lengths between 1.6 and 2.0 cm.

(c) *Ferromagnetic Impurities*

When (2.2) is a constant, the extrapolation for ferromagnetic impurities should be made against $1/(B_{\max} + B_{\min})$, where B_{\max} and B_{\min} are the maximum and minimum fields acting on the base and the top of the specimen at the particular setting of the magnet current. This result follows from an argument very similar to that given for the short specimen Gouy method, in I.

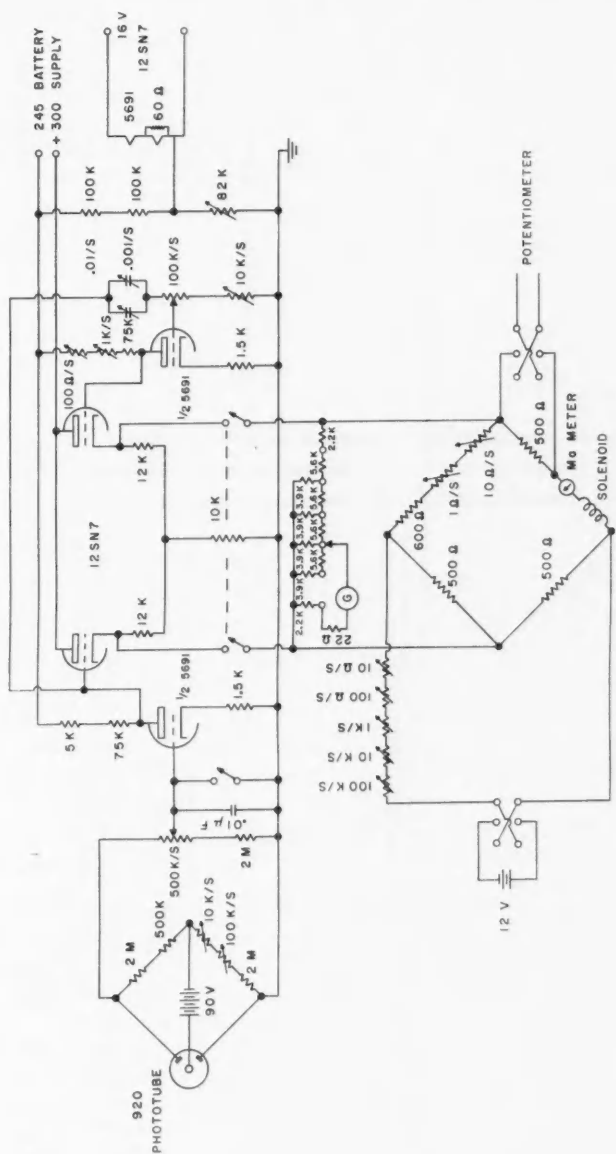
3. BALANCE POWER SUPPLIES, AND OPERATION

The combination mechanical and electronic balance with electronic velocity damping is very similar to that described by Mauer (1954). The major modification consists of the addition of a balancing bridge circuit to the output which converts the instrument to a null-type balance. By making other minor modifications the sensitivity of the device has been increased by a factor of about 20.

The modified circuit is shown in Fig. 4. In order to improve the stability of the circuit, all the resistors are the manganin wire-wound type, except those in the bridge galvanometer sensitivity circuit. The high voltage is supplied by batteries; power supplies using voltage regulating tubes were found unsatisfactory. The filament current is supplied by a separate, transistorized power supply with a stabilization factor of about 2000.

The light source is operated by a well-shielded, battery-stabilized, d-c. supply. The light source and split phototube are completely shielded from the room lights. Separate shielded cables from the Mauer circuit to the mechanical balance are used, one for the phototube output and supply and one for the solenoid and light source. This was necessary to remove pickup in the phototube bridge circuit of both the 60-cycle ripple in the light source supply and the irregular variations of the current in the solenoid.

A general view of the apparatus is shown in Fig. 5. The balance is a Sartorius SM10, semimicro balance with a sensitivity of 0.01 mg and a capacity of 100 g on each pan. The balance is operated at constant load by adjusting the weights on the pan to compensate for the weight of the specimen. The solenoid, 9.5×2.2 cm, which consists of two layers of 0.01-cm enameled wire, is enclosed in a Pyrex case with tungsten leads to facilitate the evacuation of the system. The electrical connections to the solenoid are made through loosely coiled vertical springs. The balancing bridge circuit eliminates the influence of the springs. The cylindrical Alnico magnet 12.5×0.9 cm is fastened to the base of the chamber. The radioactive sources were found essential to eliminate electrostatic forces. To insert a specimen the pin is withdrawn and



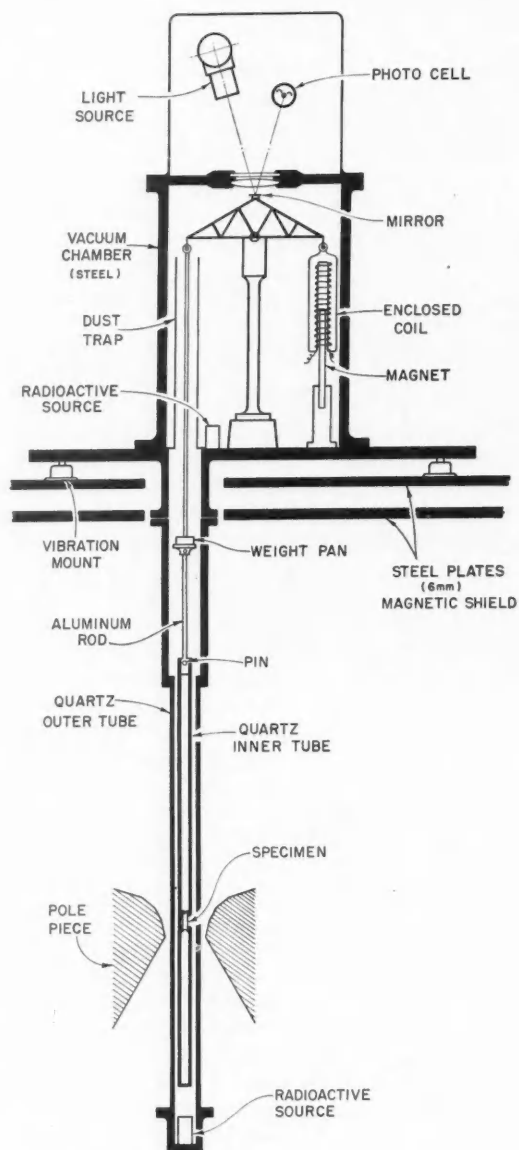


FIG. 5. A general view of the apparatus.

the inner quartz tube removed through the open end at the bottom of the outer quartz tube. Access to the weight pan is through a port.

The solenoid, Alnico magnet system has a sensitivity of about 50 mg per ma. Without the bridge circuit a deflection of the end of the balance arm of about 0.25 mm is required to produce a current of 2 ma. The use of the balancing bridge circuit reduces the deflection to the limit of the reproducibility of the cathetometer, ± 0.01 mm. This feature is important in applications where the rate of change of B_z , $\partial B_z / \partial x$ is significant (see Section 5). In Fig. 6 the millivolt, force relationships are shown with and without the

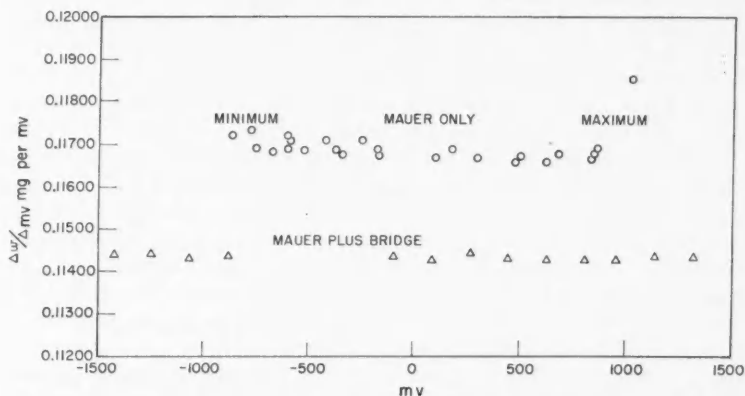


FIG. 6. A comparison of the Mauer (1954) circuit, with and without the addition of the balancing bridge circuit.

bridge circuit. It is seen that with the bridge circuit the milligrams per millivolt are more constant and the useful range is extended. The variation of $\Delta w / \Delta mv$ without the bridge circuit is presumably due to the change of position of the magnet in the coil. Some of the scatter in both cases may be due to the disturbing of the system when weights were either added or subtracted. The results with the bridge circuit were reproduced within experimental error after an interval of one year.

The method of operation is as follows. The balancing bridge circuit is isolated from the Mauer circuit and the former is balanced. This is not altered again. With the balancing bridge circuit connected, the input grid of the 5691 is grounded and the output of the 12SN7 is balanced. With the input grid not grounded and with the beam clamped near the reference position, the phototube bridge is balanced. The maximum deflection on the Cambridge galvanometer (1765 ohms, 20 mv full scale) in the balancing bridge circuit, as the beam passes through the point of maximum lift, is called the reference deflection. The beam is then released and the resistance in the battery leg of the bridge circuit is adjusted to bring the galvanometer back to the reference deflection. The voltage drop across a 500-ohm resistor in the balancing bridge circuit is then read with a Cambridge Vernier-type potentiometer.

The magnet is a model V-4012A water-cooled (closed system) electromagnet made by Varian Associates with a 30.5 cm diameter pole piece. The magnet was supplied with a widened yoke and correspondingly increased coil box separation to accommodate the pole pieces. The number of ampere turns at maximum current is 80,000. The field is set by setting the current. The magnet is demagnetized by reversing the current to a value that was found experimentally to result in an effectively zero field when the current is returned to zero. The magnet power supply is a model V-2100, self-regulating power supply made by Varian Associates which maintains the current constant to $\pm 0.001\%$ at 0.8 amp but requires a small amount of manual adjustment at 2.0 amp. The voltage drop across a Leeds and Northrup 0.1-ohm, 15-amp capacity, standard resistance in series with the magnet current is read continuously during a measurement.

The influence of the magnetic field on the operation of the balance is minimized by the following features. The balance is placed about 1 meter above the center line of the pole pieces and separated from the magnet by two steel plates 1×1 m and 6 mm thick. The balance is enclosed in a steel cylinder which forms part of the vacuum system; the solenoid, contrary to Mauer's design, is fastened to the balance arm. The two sources of spurious forces which might lead to errors are the possible solenoid, magnet interaction, and a weight, magnet interaction. Regarding the solenoid, magnet interaction, it is found that the current through the solenoid required to balance the force on a standard copper specimen, at maximum field strength, is independent of the initial current through the solenoid. The initial current may be varied in either direction by suitably loading the pan. Regarding the weight, magnet interaction, it is found that when a 100-g weight of the same material as the other weights is added to both sides of the balance, one on the pan and the other inside the steel cylinder surrounding the balance, there is no change in the force on the specimen holder at maximum field.

To maintain precision, it is necessary to take some care in making the measurements. The magnet is always cycled in the same way. The zero field reading is interpolated to take account of drift. The sample holder is measured regularly and boiled if necessary in aqua regia to free it from ferromagnetic dust.

4. FURNACE AND TEMPERATURE CALIBRATION

A section and a plan view of the furnace are shown in Fig. 7. The heaters for the furnace are two globars, manufactured by the Carborundum Company, with an active length of 10 cm and a diameter of 0.8 cm. These are operated on a-c. current. The globars are rubber-mounted and mechanically isolated from the furnace assembly; the vibration which does occur does not influence adversely the operation of the apparatus. The globars are operated in series, and the power consumed at 500°C is about 200 watts.

The temperature control system is very similar to that described by Berry, Henry, and Raynor (1951) and it controls the temperature in the absence of the field to $\pm 0.5^\circ\text{C}$. Two chromel-constantan thermocouples in series drive the temperature control circuit. As the magnet field is changed an e.m.f. is

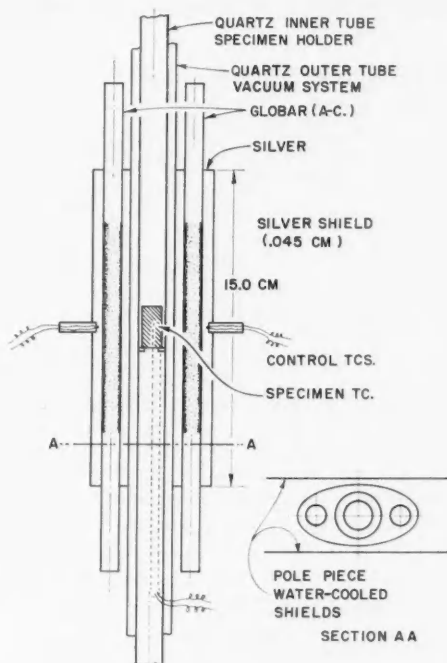


FIG. 7. The globar furnace.

induced in the control thermocouples and some manual anticipation is required to maintain the temperature within the limits of $\pm 1.0^\circ \text{C}$. The e.m.f. of the calibrated, platinum-rhodium, specimen thermocouple is read continuously during a measurement on a Rubicon portable potentiometer. The maximum temperature difference between any two parts of the specimen, as measured by a probe thermocouple inserted in a hole along the axis of the specimen occurs at 400°C and is 4°C .

The temperature calibration of the specimen thermocouple was checked by observing the change in the susceptibility of tin, lead, zinc, and antimony on melting. These metals all showed an abrupt change at their melting points. The melting points were taken to be 232 , 327.5 , 419.5 , and 630.5°C respectively. It is estimated that the absolute error in the mean temperature of the specimen is not greater than $\pm 1.5^\circ \text{C}$.

5. ERRORS

In this section the errors resulting from the specimen not occupying the same volume as the calibrating specimen are considered. Other sources of error are also considered. The expression for the lateral force is given.

It is convenient to let $B_z(x,0) = B$ where $B = B(x)$. The errors are expressed in terms of B^2 only and its derivatives.

(a) *Positioning Error in the x Direction*

The force F_x in the x direction on a specimen in the calibrating position is approximately equal to $m\chi_t/2l\Delta B^2$, where χ_t is the true mass susceptibility, m is the mass; l is the length, and ΔB^2 is the difference in the squares of the fields at the top and the base of the calibrating specimen. If the specimen is now displaced by an amount δx cm, the apparent susceptibility χ_a is given by

$$(4.1) \quad \chi_a = 2lF_x/m\Delta B^2$$

where F_x is now the new force. It follows that the true susceptibility is given by

$$(4.2) \quad \chi_t = \chi_a \left(1 - \frac{\Delta dB^2/dx}{\Delta B^2} \delta x \right).$$

For the low and the high field $(\Delta dB^2/dx)/\Delta B^2$ is approximately 0.03 per cm. At 975° K there is an error approximately equal to or less than the experimental error which arises because of the increase in length of the specimen holder. No correction, however, has been made to take account of this effect.

As indicated in Section 3, the bridge circuit reduces the deflection of the balance under load to ± 0.01 mm. The Mauer circuit, if used alone, could result in errors of the order of 0.1%.

(b) *Positioning Error in the z Direction*

Following the method of paper I, the expressions for $B_z(x,z)$ and $B_z(x,z)$ are given by

$$(4.3) \quad \begin{aligned} B_z(x,z) &= \left(\frac{dB}{dx} \right) z - \frac{1}{6} \left(\frac{d^2B}{dx^2} \right) z^3, \\ B_z(x,z) &= B - \frac{1}{2} \left(\frac{d^2B}{dx^2} \right) z^2 \end{aligned}$$

where $B = B_z(x,0)$ as before. In equation (4.3) the coefficients of the various powers of z are functions of x which are determined by the requirement that $\text{curl } B = 0$, and $\text{div } B = 0$.

The force in the x direction, on an element of volume is given by, keeping terms up to z^2 only,

$$(4.4) \quad \frac{dF_x}{dxdydz} = \frac{\kappa}{2} \frac{dB^2}{dx} + \frac{\kappa}{2} \left[-\frac{1}{2} \frac{d^3B^2}{dx^3} + \frac{1}{B^2} \left(\frac{dB^2}{dx} \right) \left(\frac{d^2B^2}{dx^2} \right) - \frac{1}{2B^4} \left(\frac{dB^2}{dx} \right)^3 \right] z^2$$

where κ is the volume susceptibility. Let the part in the square bracket be denoted by $f(x)$. Then if the center of the specimen is displaced in the z direction from the x -axis by an amount q cm, the force on a circular slice of thickness dx and diameter d is given by

$$(4.5) \quad \left(\frac{dF_x}{dx} \right)_q = \frac{\pi}{8} d^2 \kappa \left(\frac{dB^2}{dx} \right) + \frac{\pi}{8} \left(\frac{d^4}{16} + q^2 d^2 \right) \kappa f(x).$$

It follows that the true susceptibility of a slice, provided the correction is small, is given by

$$(4.6) \quad \chi_t = \chi_a[1 - q^2 f(x)/(dB^2/dx)].$$

The mean value of the second term in the square bracket over the length of the specimen is approximately $0.1 q^2$ for both the low and the high fields. No correction was made to take account of a z positioning error. Displacements of the order of 0.1 cm may have occurred.

(c) *Diameter Error*

If the specimen diameter is larger by an amount Δd cm than that of the calibrating specimens, then it may be shown by (4.5) with $q = 0$, that for a slice of thickness dx

$$(4.7) \quad \chi_t = \chi_a[1 - d(\Delta d)f(x)/(8dB^2/dx)].$$

No correction to the measured results was necessary since the maximum value of Δd was 0.05 cm.

(d) *Force in the z Direction*

If it is desired to know the maximum susceptibility which may be measured before trouble through, for example, contact with the walls, is liable to arise from the horizontal displacement of the specimen by the field, the force in the z direction must be known as a function of q . It may be shown that the force in the z direction on a slice of thickness dx is given by

$$(4.8) \quad \left(\frac{dF_z}{dx}\right)_q = \frac{\pi}{8} q d^2 \kappa \left[-\frac{d^2 B^2}{dx^2} + \frac{1}{B^2} \left(\frac{dB^2}{dx}\right)^2 \right].$$

This effect is considerably more noticeable in the high field. For the present pole pieces, the force in the z direction on a specimen 1 cm in diameter and 2 cm long is approximately $-10 \times 10^6 \kappa q$ mg/cm.

The error in the measurement of the mass is negligible. Reference to the α curves, Fig. 3, shows that the length of the specimen need only be determined to within 1 mm to obtain α to better than 0.05%.

The $\Delta w/\Delta mv$ curve shown in Fig. 6 has a scatter of about $\pm 0.05\%$ but as noted in Section 3 some of this scatter was probably due to opening and closing the system to either add or remove weights for each point. The reproducibility of the force during an actual experiment is much better than 0.1%.

As an indication of the long term stability and the reproducibility of the apparatus the results obtained on a single specimen, which was made as a standard, may be quoted. A silver-cadmium alloy containing approximately 30 at.% cadmium was measured three times with an interval of about 6 months between the measurements. The maximum deviation from the mean susceptibility was 0.1%.

The limiting feature of the apparatus appears at present to be the provision for positioning the specimen in the z direction. Further improvements are probably not worth while, however, until the purity of the specimens is improved.

6. TEMPERATURE DEPENDENCE OF THE MAGNETIC SUSCEPTIBILITIES

(a) *Copper*

The susceptibility results in this and following sections are all c.g.s. e.m.u. per gram $\times 10^6$.

Seven specimens were measured. The specimens were made from four separate lots of copper purchased from the American Smelting and Refining Company (A.S. and R.) and analysis of which, according to the manufacturer is: Fe < 0.00007 , Sb < 0.0001 , Pb < 0.0001 , Sn < 0.0001 , Ni < 0.0001 , Bi < 0.00001 , Ag < 0.00003 , As < 0.0002 , Cr < 0.00005 , Si < 0.00001 , Te < 0.0002 , Se < 0.0001 , S < 0.0001 , O₂ < 0.0001 wt.%. The iron analysis has been checked in our laboratory and found to vary from 0.0001 to 0.00002 wt.%. An oxygen and hydrogen analysis was made by the Department of Mines and Technical Surveys and found to be: oxygen, 0.0001 ± 0.00003 ; hydrogen, 0.00004 wt.%. The specimens were cut to length on a lathe from the "as received" rod; they were then etched heavily with 10 *N* nitric acid to remove ferromagnetic contamination. The specimens were annealed at 575° C for 5 days and air-cooled. It was found in I that this annealing treatment did not alter the susceptibility; it was done in the present work to help put into solution any small amounts of ferromagnetic material not removed by etching.

The α curves (Fig. 3) were determined from a number of specimens of varying length which were not necessarily used to determine the high temperature results. It was necessary to assume that there were negligible amounts of ferromagnetic impurities in these specimens; some selection of specimens was made.

In the high temperature experiments the α curves were used even for the room temperature susceptibility determinations. The average of the room temperature susceptibilities of the seven specimens is -0.0860 , which is essentially the same as the calibrating value of -0.0859 . These room temperature results lend strong support to the assumption regarding negligible amounts of ferromagnetic impurities in the calibrating specimens. There was no indication of ferromagnetic impurity in the specimens used; the low and the high field determinations agreed within experimental error. There was no indication of contamination as a result of being at an elevated temperature; the subsequent room temperature values agreed within experimental error.

The temperature dependence of the susceptibility of the seven copper specimens is shown in Fig. 8 along with the data of Ross (1934), and Bitter, Kaufmann, Starr, and Pan (1941). Ross used electrolytic copper of unknown purity; the specimens were prepared in a hydrogen atmosphere. A paramagnetic impurity such as iron in solution causes the slope to be smaller and hence this does not explain the difference in slope. Bitter *et al.* extrapolated the results of copper-iron alloys of higher concentrations to zero concentration to obtain their data for pure copper. Their specimens were melted in a hydrogen atmosphere and chill-cast in vacuum. They also checked their results against a specimen of A.S. and R. copper. They were not attempting to make an absolute measurement on copper but were interested in relative results

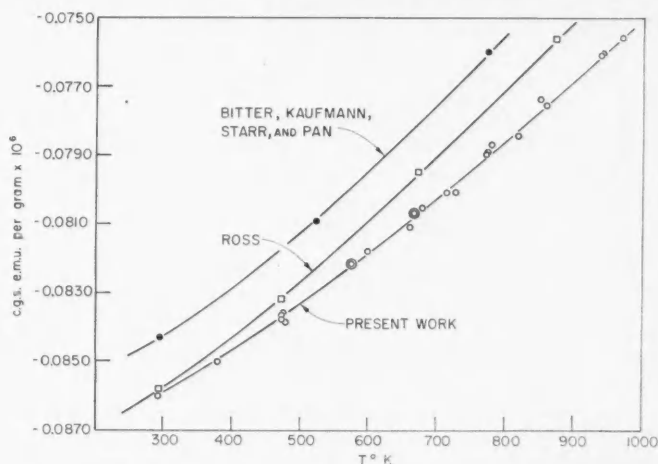


FIG. 8. The temperature dependence of the magnetic susceptibility of copper, 295°–975° K.

(Bitter and Kaufmann 1939) and hence the difference in absolute value between their work and the present work is perhaps not significant.

In order to estimate the error in an individual measurement, a smooth curve was drawn through the data on a large graph such that the sum of the deviations was about 0.0001₀. The mean error was then calculated as $(\sum v^2/n)^{1/2}$, where v is the deviation and n is the number of points. The mean error is found to be $\pm 0.0001_4$. Some of the error is due to the inclusion of some early results in which the temperature was not regulated as well as later on. The values in Table I were taken from the smooth curve.

TABLE I
Magnetic susceptibilities per gram of copper, silver,
and gold $\times 10^6$

Temp., ° K	Copper	Silver	Gold
295	0.0859 ₉	0.1807 ₂	0.1430 ₂
400	0.0846 ₈	0.1792 ₉	
500	0.0833 ₃	0.1780 ₄	0.1428 ₉
600	0.0818 ₈	0.1769 ₆	
700	0.0802 ₉	0.1763 ₉	0.1424 ₉
800	0.0785 ₈	0.1760 ₃	
900	0.0767 ₈	0.1776 ₃	0.1419 ₈
975	0.0753 ₈	0.1786 ₉	0.1417 ₈

In Fig. 9 the low temperature data of Ross (1934), Bitter, Kaufmann, Starr, and Pan (1941), Bowers (1956), and Pugh, Coles, Arrott, and Goldman (1957) are shown with the present high temperature data. The last three investigators have used the same copper (A.S. and R.). The data is presented

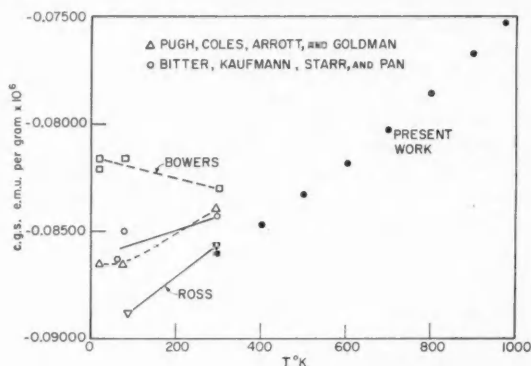


FIG. 9. The temperature dependence of the magnetic susceptibility of copper above and below room temperature.

as a check on the room temperature value of the slope of the susceptibility curve for copper and to show the degree of agreement between the investigators. The present work agrees moderately well with that of Ross, Bitter *et al.*, Pugh *et al.*, but not with Bowers.

(b) Silver

Three specimens were measured. The specimens were made from twice-electrolyzed silver (Harrow and Henry), the analysis of which is: Fe 0.0002, Si 0.0002, Pb <0.0005, Cu 0.0001, Mg <0.0001, Cd <0.0002, Mn <0.0001 wt.%. The specimens were melted under vacuum in quartz crucibles and chill-cast (Craw and Henry 1956). After casting the Si content was found to be 0.0004 wt.%. The specimens were cut to length and then given a 2-minute treatment with concentrated nitric acid. They were then sealed in Pyrex, in vacuum, and annealed for 7 days at 575° C, and then air-cooled. It was found in I that the room temperature susceptibility was not influenced by this procedure.

There was no evidence of ferromagnetic impurity; the low and high field measurements agreed within experimental error.

The temperature dependence of the susceptibility of the three specimens is shown in Fig. 10. The same procedure was followed as for copper to determine the error in an individual measurement. The mean error is $\pm 0.0001_2$. The values in Table I were taken from the smooth curve.

The minimum in the absolute value of the susceptibility at about 750° K was unexpected and further work was done to rule out the possibility of oxygen contamination being the cause. Steacie and Johnson (1926) found that the solubility of oxygen in silver is a maximum at about this temperature. The vacuum-cast specimens were found earlier (I) to have the same susceptibility as degassed specimens. It was possible, however, that some oxygen con-

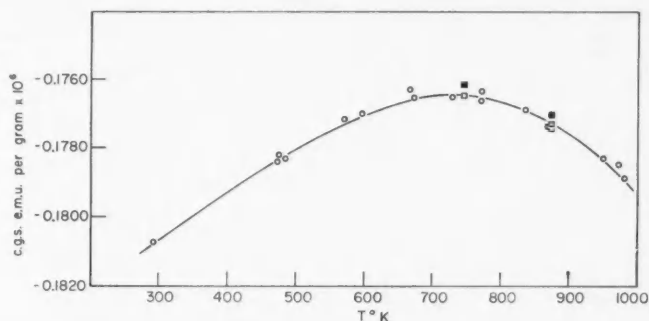


FIG. 10. The temperature dependence of the magnetic susceptibility of silver, 295°–975° K. ○ normal specimens; ■ 12 hours in air at this temperature; □ degassed specimens.

tamination of the specimen occurred during the measurement. The specimens marked in Fig. 10 were held overnight *in situ*, at the temperatures indicated in air and then measured. The specimen was then degassed overnight, in a vacuum of approximately 5×10^{-5} mm, at 875° K and measured. It was held a further 24 hours at 875° K in vacuum and measured again. The two squares which almost superimpose represent these latter measurements. The lower square at about 750° K represents the result of the measurement at that temperature after the degassing at 875° K. The magnitude of the change as a result of the contamination indicates that the minimum could not be the result of oxygen contamination. The additional fact that indicates that there was little or no contamination during the experiments on the other specimens is that the room temperature values before and after being at temperature agreed within experimental error.

Pugh and Ryan (1958) found the susceptibility of silver to vary from -0.183 to -0.181 from 20.4 to 295° K. The slope has the same sign as in the present work.

(c) Gold

Three specimens were measured. The specimens were made from twice-electrolyzed gold (Harrow and Henry), the analysis of which is: Mg <0.0001 , Fe <0.0001 , Si <0.0001 , Cu <0.0001 , Pb (estimate) 0.0001 , Ca 0.0001 , Ni <0.0001 , Ag 0.0001 wt.%. The gold was melted under argon in quartz crucibles and chill-cast. The specimens were cut to length and then given a heavy etch with hot (60° C), concentrated aqua regia. They were then sealed in Pyrex, in vacuum, and annealed for 7 days at 575° C.

There was no evidence of ferromagnetic impurities; the low and high field determinations agreed within experimental error.

The results of the measurements on the three specimens are shown in Fig. 11. The error in an individual measurement was found to be ± 0.00007 . The values in Table I were taken from the smooth curve.

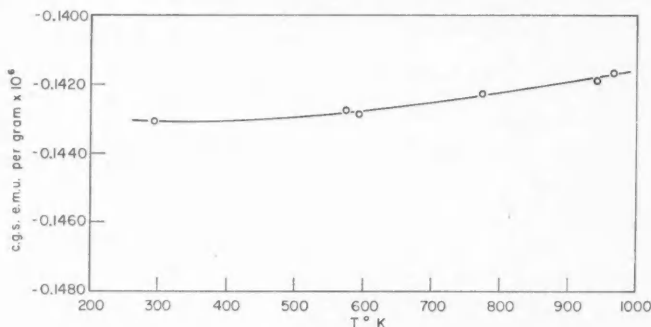


FIG. 11. The temperature dependence of the magnetic susceptibility of gold, 295°–975° K.

7. DISCUSSION OF RESULTS

In the present work the mean susceptibilities of the silver and gold specimens at 295° K are found to be $-0.1807_2 \pm 0.0000_4$ and $-0.1430_3 \pm 0.0000_6$ respectively where the errors are the root mean square errors relative to copper determined from the measured values at 295° K. The fact that the silver value has decreased and the gold value has increased compared to I suggests that the differences are not due to some systematic error in making the measurement. In I, one specimen of twice-electrolyzed silver was included among the pure specimens. This specimen had the lowest absolute value of the group (-0.1810_0) but was not considered a "wild" one. A measurement on another specimen of twice-electrolyzed silver made after the publication of I on the apparatus used in I yielded a value of -0.1807_8 . These latter measurements taken in conjunction with the results of the present work suggest that the increased purity of the specimens is somehow responsible for the difference between the value for silver in I and the present value. The difference in the values for gold is also probably due again to increased purity. The specimen of highest purity in I, made from proof plate, gave a value of -0.1429_0 in good agreement with the present value. Although the susceptibilities of the other three specimens were corrected in I for an iron content of 1.2 p.p.m. by weight, the presence of additional transition metal impurities at this level could account for the difference.

ACKNOWLEDGMENTS

The authors wish to thank Mr. D. S. Russell for the chemical analyses and Mr. S. L. Gertsman of the Department of Mines and Technical Surveys, Ottawa, Canada, for the oxygen and hydrogen analyses of the A.S. and R. copper. We also wish to thank Mr. L. L. T. Bradley for valuable assistance in the design and construction of the power supplies.

REFERENCES

- BATES, L. F. 1951. Modern magnetism, 3rd ed. (Cambridge Univ. Press), p. 109.
BERRY, R. L., HENRY, W. G., and RAYNOR, G. V. 1951. J. Inst. Metals, **78**, 643.
BITTER, F. and KAUFMANN, A. R. 1939. Phys. Rev. **56**, 1044.
BITTER, F. and KAUFMANN, A. R., STARR, C., PAN, S. T. 1941. Phys. Rev. **60**, 134.
BOWERS, R. 1956. Phys. Rev. **102**, 1486.
CRAW, D. A. and HENRY, W. G. 1956. J. Sci. Instr. **33**, 22.
HARROW, G. A. and HENRY, W. G. To be published.
HENRY, W. G. and ROGERS, J. L. 1956. Phil. Mag. **1**, 223.
HONDA, K. 1910. Ann. Physik, **32**, 1027.
MALAVARD, L. 1947. Roy. Aeronaut. Soc. **51**, 739.
MAUER, F. A. 1954. Rev. Sci. Instr. **25**, 598.
OWEN, M. 1912. Ann. Physik, **37**, 657.
PUGH, E. W., COLES, B. R., ARROTT, A., and GOLDMAN, J. E. 1957. Phys. Rev. **105**, 814.
PUGH, E. W. and RYAN, F. M. 1958. Phys. Rev. **111**, 1038.
RAO, S. R. and SAVITHRI, K. 1942. Proc. Indian Acad. Sci. **16**, 207.
ROSS, W. H. 1934. Phys. Rev. **46**, 46.
SHIH, J. W. 1931. Phys. Rev. **38**, 2051.
SHIMIZU, Y. 1937. Sci. Repts. Tôhoku Univ. **25**, 921.
STEACIE, E. W. R. and JOHNSON, F. M. G. 1926. Proc. Roy. Soc. A, **112**, 542.
STEVENS, D. K., CLELAND, J. W., CRAWFORD, J. H., JR., and SCHWEINLER, H. C. 1955. Phys. Rev. **100**, 1084.
VOGT, E. and GERSTENBERG, D. 1959. Ann. Phys. **4**, 145.

THE IDENTIFICATION AND HALF LIVES OF FISSION-PRODUCT Rb^{92} AND Rb^{93} ¹

K. FRITZE AND T. J. KENNETT

ABSTRACT

The existence of two new rubidium isotopes, Rb^{92} and Rb^{93} , has been established and their half lives measured. The half lives of these short-lived fission products were determined using a technique of timed precipitations. The values obtained for Rb^{92} and Rb^{93} were 5.3 ± 0.5 sec and 5.6 ± 0.5 sec respectively. The half lives of the strontium and yttrium daughters were also determined. The strontium isotopes were studied by observing the decay rate of a characteristic γ -ray peak. For Sr^{92} , the decay of the 1.37-Mev line gave a value of 2.71 ± 0.02 hr. A γ -ray peak at 590 kev, which was found to be associated with Sr^{93} , decayed with a half life of 7.54 ± 0.06 min. The half lives of the yttrium daughters were determined by β counting. The values found for Y^{92} and Y^{93} were 3.53 ± 0.02 hr and 10.1 ± 0.1 hr respectively.

(A) Rb^{92} AND Rb^{93}

The existence of Rb^{92} and Rb^{93} was implied by the discovery of their respective parents Kr^{92} and Kr^{93} . The latter were established to be fission products through gas sweeping experiments carried out with irradiated uranium solutions by Dillard *et al.* (1951). Hahn and Strassmann (1940) reported an 80-sec activity associated with rubidium fission products which has been assigned to Rb^{92} in recent nuclear data compilations.

To investigate the half lives of Rb^{92} and Rb^{93} , a method similar to that described by Sugarman (1949) was used. This technique consists of dividing a sample of fission products into portions from which certain elements are precipitated. The precipitations are carried out serially with a time separation between each. At a later time, a daughter product is extracted from the precipitate, purified, and counted. Since the quantity of the daughter found in each sample is proportional to the amount of the parent present at the time of precipitation, one has a method of determining the half life of the parent. This method has the distinct advantage of unique mass assignment, a virtue not shared by direct measurements of the half life.

The usefulness of the timed-precipitation technique depends strongly upon the nature of the precipitation reaction. This reaction must be fast in comparison to the intervals between successive precipitations in order to minimize timing uncertainties. Also, and of greater importance, the precipitate must not carry any daughter activities. For this work it was found that the precipitation of rubidium perchlorate fulfills both requirements, provided that a sufficient quantity of rubidium carrier is used. The co-precipitation of the carrier-free daughter products which was determined by using Sr^{90} and Y^{90} , was found to be of the order of $10^{-4}\%$.

To determine the half lives of Rb^{92} and Rb^{93} , the rubidium perchlorate precipitate can be analyzed for the strontium ($2.7\text{-hr } \text{Sr}^{92}$, $7.5\text{-min } \text{Sr}^{93}$) or

¹Manuscript received September 2, 1960.

Contribution from the Department of Physics, McMaster University, Hamilton, Ont.

yttrium (3.5-hr Y^{92} , 10.1-hr Y^{93}) daughters. The yttrium daughters are the obvious choice because of their convenient half lives and the uncomplicated decay to stable or long-lived zirconium isotopes. To obtain the maximum activity of Y^{92} , the first strontium-yttrium separation should be performed 4.5 hours after the irradiation. The decay curve of the purified yttrium samples will then be composed of the 3.5-hr Y^{92} and 10.1-hr Y^{93} plus a contribution from the 91 mass chain (50-min Y^{91m} and 58-day Y^{91}). By unravelling the Y^{92} and Y^{93} components in the decay curves and correcting for chemical yields, the half lives of Rb^{92} and Rb^{93} can be easily calculated from the time schedule of the successive precipitations.

Preliminary measurements conducted for Rb^{92} and Rb^{93} indicated that both half lives were less than 10 seconds. Since the krypton precursors (3-sec Kr^{92} , 2-sec Kr^{93}) should be allowed to decay almost completely, the time available for the rubidium perchlorate precipitations ranges from 15 to 30 seconds after the irradiation. Because of this rather short time interval only two precipitations were performed for each run.

Procedure

Samples containing 2 ml of uranyl nitrate solution (93% enriched in U^{235}) were irradiated in sealed polyethylene bottles using the rabbit system of the McMaster reactor. Immediately after delivery the irradiated solution was mixed with 400 mg of rubidium carrier contained in 18 ml of 2 *M* HCl. The resulting solution was divided into two parts and the first one added to approximately 10 ml of 20% HClO_4 contained in a large millipore-filter apparatus of the type normally used in radiochemical work. Immediately after precipitating the rubidium perchlorate, the liquid was drawn through the filter. Exactly the same procedure was then used approximately 10 seconds later for the second part of the sample. Both precipitates were washed with 10% HClO_4 . The two precipitates were then rinsed into 100-ml volumetric flasks, each of which contained 20 mg of strontium and 10 mg of yttrium carrier in 9 ml of 9 *M* HCl. After the rubidium perchlorate had dissolved, one 10-ml aliquot was taken from each sample for chemical-yield determinations. The remaining solutions were then quantitatively transferred into beakers and after evaporation to near dryness, analyzed for yttrium in the following steps: $\text{Y}(\text{OH})_3$ precipitation 4.5 hours after the end of the irradiation, tributylphosphate-solvent extraction of the dissolved $\text{Y}(\text{OH})_3$ (Stanley 1954), $\text{Y}(\text{OH})_3$ precipitation from the back-extracted yttrium solution, passage of the redissolved yttrium in 10 *M* HCl over Dowex 1, $\text{Y}(\text{OH})_3$ precipitation of the eluant, and finally an yttrium oxalate precipitation. The yttrium oxalate was filtered over Whatman No. 42 paper, washed with 50% $\text{C}_2\text{H}_5\text{OH}$, dried, and mounted on a turntable for automatic counting of two samples. Here the samples were alternately counted for 10-minute periods each followed by a 0.3-minute changing interval. The counting was done using either a β -scintillation detector or an end-window proportional counter. Figure 1 shows a typical decay curve as obtained in this way. After the counting was finished, the yttrium oxalate samples were ashed and weighed as Y_2O_3 . The chemical

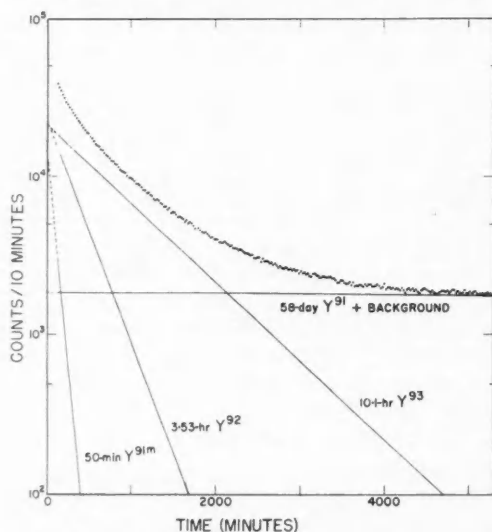


FIG. 1. A typical decay curve for the yttrium daughters of a fast precipitation of fission-product rubidium. The solid lines indicate the components obtained from a least-squares analysis of the data.

yields of the initial rubidium precipitations were determined as rubidium perchlorate. Each initial rubidium perchlorate precipitate usually contained slightly more than 40% of the total rubidium (= 80–90% yield for the individual rubidium perchlorate precipitations) whereas the yttrium yields were always around 60%.

Results

The decay curves were analyzed with a least-squares program using a Bendix G-15 digital computer. The data, which were accumulated for at least 70 hours for each run, were analyzed into four exponential components. The components sought for from the decay curve were 50-min Y^{91m} , 3.5-hr Y^{92} , 10.1-hr Y^{93} , and a combination of 58-day Y^{91} and a constant background. The least-squares program was designed to yield the counting rate and associated error for each component at the time when counting began. A simple calculation was then used to find the counting rate at the time of the first strontium–yttrium separation. Figure 1 shows a decay curve with the components found using the least-squares analysis.

Table I gives the irradiation conditions and half lives obtained for Rb^{92} and Rb^{93} . The errors quoted with each measurement are only those arising from the least-squares analysis of the decay curves. Errors associated with uncertainties in the timing of the precipitations can be inferred by the reproducibility between runs. The largest uncertainty in any half-life determination of this kind arises from the fact that the washing of the precipitate removes

TABLE I

Run	U ²³⁵ (μg)	Flux (neutrons cm ⁻² sec ⁻¹)	Duration of irradiation (sec)	RbClO ₄ precipitation times (sec)		Rb ⁹² half life (sec)	Rb ⁹³ half life (sec)
				1st ppt.	2nd ppt.		
1	100	3×10 ¹²	30	23	33	5.8±.3*	5.7±.1*
2	200	3×10 ¹²	20	20	28	5.6±.2	5.7±.1
3	200	4×10 ¹²	20	19	33	4.8±.1	5.8±.1
4	200	4×10 ¹²	20	17.5	28.5	5.1±.1	5.4±.1
					Average	5.3	5.6

*Quoted errors are only those obtained from the least-squares analysis.

some of the daughter atoms which have grown in since the time of the initial precipitation. In order to estimate the magnitude of this effect, rubidium perchlorate was precipitated 1 minute after the end of an irradiation and then washed very carefully with 10% HClO₄. It was left on the membrane filter in order to let the Rb⁹¹ decay. The precipitate was then washed again with 10 ml of HClO₄ for a contact time of approximately 5 seconds. Both the precipitate and filtrate were analyzed for Sr⁹¹. It was found that for even this short a contact time, 40% of the strontium was washed out of the precipitate.* However, the relatively small scattering of the results in Table I indicates that the errors due to these effects cancel out to a large extent, particularly in view of the fact that in runs 1 and 2 the washing was done after both precipitations were performed whereas in runs 3 and 4, the washing was done after each precipitation. Consideration of the small number of measurements and the difficulty of assigning errors to some aspects of the experiment lead us to suggest the following half lives:

$$\text{Rb}^{92} = 5.3 \pm 0.5 \text{ sec}$$

$$\text{Rb}^{93} = 5.6 \pm 0.5 \text{ sec.}$$

Finally, it should be mentioned that in one of the preliminary experiments, four precipitations of rubidium perchlorate were carried out at intervals of approximately 2 minutes, starting 1 minute after the end of the irradiation. The resulting yttrium samples showed only the 50-min Y^{91m} and the 58-day Y⁹¹. It must therefore be concluded that the 80-sec rubidium isotope observed by Hahn and Strassmann (1940) is not connected with either the Rb⁹² or the Rb⁹³. A possible explanation is that this activity is the 1.67-min isomer of Rb⁹¹ (Kofoed-Hansen and Nielsen 1951).

(B) Sr⁹³

Two determinations of the Sr⁹³ half life have been reported in the literature. An early value of 7 minutes was obtained by direct measurement (Lieber 1939) while a more recent value deduced from yttrium milking yielded 8.2 minutes (Knight *et al.* 1959). The convenient half life of Sr⁹³ favors a direct measurement. However, since this nuclide is obtained as a fission product the

*Since cesium is co-precipitated with the RbClO₄, the precipitate and filtrate were also analyzed for Ba¹⁴⁰. The result was the same as for the case of Sr⁹¹.

complexity arising from the presence of other strontium isotopes and the ingrowth of their respective yttrium daughters presents a disadvantage. The irradiation time and subsequent separation times can be optimized in order to reduce the yield of other isotopes. If this is done the only activities which contribute to any measurable degree are the ingrowing 10.1-hr Y^{93} daughter and the 2.7-hr $Sr^{92} \rightarrow 3.5$ -hr Y^{92} system. Even then it would appear that any measurement involving the decay rate of gross β or γ radiation would be somewhat ambiguous because of the uncertainty in the nature of the background. In order to circumvent this background uncertainty it was decided to investigate the γ rays associated with the decay of Sr^{93} in the hope that more favorable conditions could be found.

A series of measurements were conducted to determine the γ rays emitted in the decay of Sr^{93} . This study revealed the presence of strong γ rays at 150, 250, 590, 720, and 900 keV* (see insert in Fig. 2). Since the decay of Sr^{92} , Y^{92} , and Y^{93} yield no γ rays at 590 keV it was decided to use this line for a half-life determination.

The Sr^{93} samples were prepared by irradiating samples containing 100 μ g of U^{235} for 10 seconds in a pneumatic rabbit where the flux was 5×10^{12} neutrons $cm^{-2} sec^{-1}$. The irradiated solution was then mixed with 10 mg each of strontium and barium carrier and, 30 seconds after the irradiation, strontium nitrate was precipitated. The strontium was then purified by several barium chromate and yttrium hydroxide precipitations, and finally obtained as strontium nitrate about 15 minutes after the irradiation.

The system used for following the decay of the 590-keV line consisted of a good quality 3×3 in. NaI(Tl) scintillator, a single channel analyzer, and a 256-channel analyzer. The multichannel analyzer was modified to operate as a multichannel scaler. The address was advanced by an external time-scaling system, which in this case stepped channels at a rate of 0.4 min/channel. The only events accepted for storage were those whose pulse height fell within a 4% window centered about the 590-keV line. Typical data obtained in this way are shown in Fig. 2. After the analysis was completed (101.6 min) a strontium-yttrium separation was performed and the strontium fraction again counted for the same period. This technique is quite useful since it gives the shape of the background caused by the Sr^{92} - Y^{92} system. Thus it is possible to reconstruct the background which is associated with the original measurement. These background components contributed less than 2% to the initial counting rate. It was also found that the contribution from ingrowing 10.1-hr Y^{93} was negligible. Two such experiments were conducted and the data were analyzed using a least-squares program. The results obtained were:

Sample 1: 7.58

Sample 2: 7.50

Average: $7.54 \pm .06$ min.

(C) Sr^{92}

A measurement of the Sr^{92} half life was carried out using the same technique as described for Sr^{93} . The γ spectrum of Sr^{92} contains a strong line at 1.37 MeV

*Details on the decay scheme of Sr^{93} will be published elsewhere.

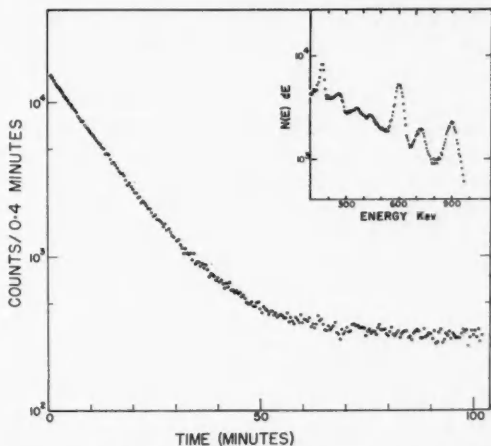


FIG. 2. A decay curve obtained for Sr^{92} . The only events recorded were those whose pulse height fell within a 4% window centered about the 590-kev γ -ray line. The γ -ray spectrum associated with the decay of Sr^{92} is shown as an insert. A least-squares analysis of the decay curve gave a half life of 7.58 ± 0.06 min.

(Heath 1957a) which is not greatly influenced by the decay of the ingrowing Y^{92} and was therefore ideally suited for this measurement.

The Sr^{92} source was prepared by precipitating strontium nitrate from an irradiated uranyl nitrate solution. Following this several barium chromate and yttrium hydroxide precipitations were used to purify the sample. About 75 minutes after the end of the irradiation strontium nitrate was precipitated and counted. The equipment employed was identical with that used for the Sr^{93} half-life measurement.

A least-squares analysis of the data gave a half life of 2.71 ± 0.02 hr. This value is in good agreement with published results (Götte 1941; Herrmann and Strassmann 1956) which were done using other techniques.

(D) Y^{92} AND Y^{93}

Although a number of well-agreeing half lives have been reported for Y^{92} (Lieber 1939; Ames *et al.* 1952) and Y^{93} (Hahn and Strassmann 1943; Ballou *et al.* 1951; Heath 1957b) a remeasurement seemed desirable because of the important role these half lives play in the Rb⁹² and Rb⁹³ calculations.

For the half-life determination of Y^{92} , samples were prepared using two different techniques. This approach was undertaken in order to check the possibility of contamination. The first sample was precipitated as strontium nitrate 30 seconds after the end of the irradiation. The strontium nitrate was purified by several barium chromate and yttrium hydroxide precipitations. The last yttrium hydroxide precipitation was performed 2 hours after the irradiation to ensure the complete removal of Y^{93} . The Y^{92} was then allowed to grow in from Sr^{92} for 4.3 hours during which time the strontium solution, in 9 M HCl, was passed over Dowex 1. After this, yttrium hydroxide was successively precipitated a total of three times, each time in the presence of

20 mg of strontium holdback carrier. The final precipitate was dissolved and reprecipitated as the oxalate. This was then counted after drying.

The second sample was precipitated as strontium nitrate 30 seconds after the end of the irradiation. The strontium nitrate was then dissolved in 9 *M* HCl, passed over Dowex 1, and reprecipitated as strontium nitrate a total of three times, the last being 3.5 hours after the irradiation (to remove the Y^{93}). Four hours later the strontium nitrate was dissolved in water, 0.2 mg of iron added and ferric hydroxide precipitated. The ferric hydroxide was dissolved in 0.3 ml of concentrated HCl and passed over a 0.1 ml Dowex 1 column. After it was washed with 0.1 ml of 9 *M* HCl, the eluant was diluted with H_2O to about 12 ml and the carrier-free yttrium absorbed on a few milligrams of Dowex 50. This resin was then transferred to the top of a Dowex 50 column maintained at 65° C. The yttrium was eluted with a 0.2 *M* solution of α -hydroxy-iso-butyric acid adjusted to a pH of 4.2 (Choppin and Silva 1956). The elution was monitored with a Geiger counter in order to determine the position of the yttrium peak. The carrier-free yttrium, which was eluted in less than 15 minutes, was mixed with 20 mg of yttrium carrier, and precipitated as the oxalate for counting.

Both samples were counted using a β -scintillation detector. Typical data which were accumulated for the half-life measurement are shown in Fig. 3. A

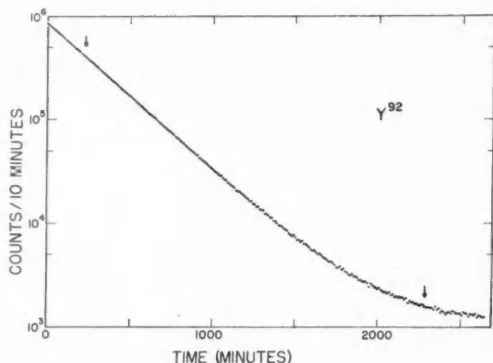


FIG. 3. The decay curve obtained for Y^{92} by gross β counting. The least-squares analysis was conducted using the data between the two arrows. This yields a half life of 3.53 ± 0.02 hr.

least-squares analysis which was carried out for both samples gave the following results:

Sample 1: 212.4 min
 Sample 2: 210.8 min
 Average: 211.6 ± 0.8 min
 $= 3.53 \pm 0.02$ hr.

The value obtained is in good agreement with previous measurements.

A remeasurement of the Y^{93} half life was also carried out. In this case, the objective was to obtain a sample of nearly pure Y^{93} with a minimum amount of 3.53-hr Y^{92} . To achieve this condition, a precipitation of fission product strontium was done 15 seconds after the irradiation. The strontium was allowed to decay for about one half life of the Sr^{93} and the resulting yttrium separated. This yttrium is highly enriched in Y^{93} and, at least at the beginning of the counting, in Y^{94} and Y^{95} . The yttrium was purified in a manner similar to the second Y^{92} sample.

The counting of the Y^{93} was done in exactly the same manner as described for Y^{92} . Figure 4 shows the decay curve obtained. The presence of 20-min Y^{94} and 10-min Y^{95} are indicated at the beginning of counting and a small

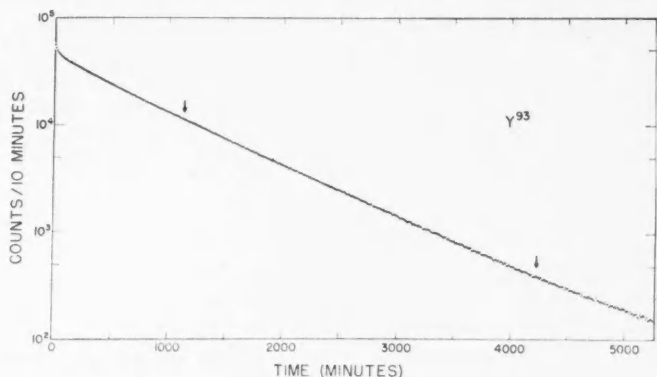
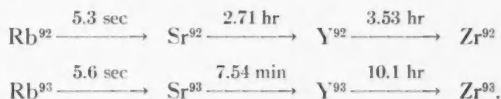


FIG. 4. The decay curve obtained for Y^{93} by gross β counting. The arrows enclose the region used for the least-squares analysis. The half life was found to be 10.1 ± 0.1 hr.

contribution of 3.53-hr Y^{92} may possibly exist over the first 100 points (16.7 hours). To avoid any influence of the Y^{92} the data were analyzed from 1100 to 4100 minutes. A least-squares fit over this region yielded a half life of 604 ± 1 min = 10.08 ± 0.02 hr.

(E) CONCLUSION

The work reported here can be summarized as follows:



The techniques described in this paper are, of course, useful to determine the half lives of other nuclides. In particular they have been applied to show the existence of the hitherto unknown fission products: Rb^{94} , Cs^{141} , Cs^{142} , and Ba^{143} . Experiments are in progress to determine their respective half lives.

ACKNOWLEDGMENTS

The authors gratefully acknowledge the financial support given by the National Research Council. They also appreciate the help received from J. Hallam and the McMaster reactor staff.

REFERENCES

- AMES, D., BUNKER, M., and STARNER, J. 1952. LASL Classified Report WASH-66.
BALLOU, N. E., NOVEY, T. B., ENGELKEMEIR, D. W., BRADY, E. L., and SEILER, J. A. 1951. Natl. Nuclear Energy Ser. Div. IV. **9**, 675.
CHOPPIN, G. R. and SILVA, R. J. 1956. J. Inorg. & Nuclear Chem. **3**, 153.
DILLARD, C. R., ADAMS, R. M., FINSTON, H., and TURKVICH, A. 1951. Natl. Nuclear Energy Ser. Div. IV. **9**, 624.
GÖTTE, H. 1941. Naturwiss. **29**, 496.
HAHN, O. and STRASSMANN, F. 1940. Naturwiss. **28**, 54.
——— 1943. Naturwiss. **31**, 249.
HEATH, R. L. 1957a. Phys. Rev. **105**, 1011.
——— 1957b. Bull. Am. Phys. Soc. Ser. II, **2**, 230.
HERRMANN, G. and STRASSMANN, F. 1956. Z. Naturforsch. **11a**, 946.
KNIGHT, J. D., HOFFMAN, D. C., FRASCO, D. L., and DROPECKY, B. V. 1959. J. Inorg. & Nuclear Chem. **10**, 183.
KOFOED-HANSEN, O. and NIELSEN, K. O. 1951. Phys. Rev. **82**, 96.
LIEBER, C. 1939. Naturwiss. **27**, 421.
STANLEY, C. W. 1954. A.E.C. Report LA-1721, p. 104.
SUGARMAN, N. 1949. J. Chem. Phys. **17**, 11.

SCATTERING BY A NARROW UNIDIRECTIONALLY CONDUCTING INFINITE STRIP¹

S. R. SESHADRI²

ABSTRACT

The scattering of a plane electromagnetic wave of wave number k by a unidirectionally conducting infinite strip of width $2a$ is investigated. The problem is formulated in terms of an integral equation whose solution is obtained by a well-known procedure in the form of a series in powers of ka . Expressions for the far-zone fields and the first two terms in the series for the total scattering cross section are obtained.

INTRODUCTION

A unidirectionally conducting screen is one which is perfectly conducting in a given direction and is insulating in the perpendicular direction. It is an idealization of a screen composed of fine parallel wires. Consider a unidirectionally conducting infinite strip of width $2a$, illuminated by a plane electromagnetic wave of wave number k . It is desired to obtain a solution of this scattering problem for the width of the strip much smaller compared to wavelength, i.e. $ka \ll 1$. The problem is formulated in terms of an integral equation which specifies the current induced on the strip. The integral equation is solved for $ka \ll 1$ and explicit expressions for the diffraction pattern in the far field and the first two terms in the series for the total scattering cross section are obtained. The method employed in the solution of the integral equation is similar to that used by Bouwkamp (1953) in the solution of the corresponding problem of scattering by a perfectly conducting strip.

FORMULATION OF THE PROBLEM

A unidirectionally conducting infinite strip occupies the region $|x| < a$, $-\infty < y < \infty$, and $z = 0$, where x , y , and z form a right-hand rectangular co-ordinate system. It is convenient to introduce also a rotated system of co-ordinates ξ , η , z where

$$\begin{aligned} \xi &= x \cos \alpha + y \sin \alpha, \\ \eta &= -x \sin \alpha + y \cos \alpha, \\ z &= z, \end{aligned} \quad (1)$$

and $0 \leq \alpha < \pi/2$. The strip is assumed to be conducting in the ξ direction only. When a field $\mathbf{E}^i(\mathbf{r})$, $\mathbf{H}^i(\mathbf{r})$ is incident on the strip, there arise the scattered fields $\mathbf{E}^s(\mathbf{r})$, $\mathbf{H}^s(\mathbf{r})$. The total fields $\mathbf{E}^i(\mathbf{r}) + \mathbf{E}^s(\mathbf{r})$, $\mathbf{H}^i(\mathbf{r}) + \mathbf{H}^s(\mathbf{r})$ denoted by $\mathbf{E}(\mathbf{r})$, $\mathbf{H}(\mathbf{r})$ respectively satisfy the time harmonic Maxwell's equations

$$\begin{aligned} \nabla \times \mathbf{E}(\mathbf{r}) &= ik\mathbf{H}(\mathbf{r}), \\ \nabla \times \mathbf{H}(\mathbf{r}) &= -ik\mathbf{E}(\mathbf{r}) \end{aligned} \quad (2)$$

¹Manuscript received August 5, 1960.

Contribution from the Gordon McKay Laboratory, Harvard University, U.S.A.

²Present address: Electronics Research and Development Establishment, Bangalore 1, India.

in the exterior of the strip. The harmonic time dependence $e^{-i\omega t}$ is implied for all the field components. The unidirectional conductivity of the strip is taken into account by imposing the following boundary conditions on the strip, i.e. $|x| < a$,

$$(3) \quad E_{\xi}(x, y, 0) = 0,$$

$$(4) \quad [H_{\xi}(x, y)] \equiv H_{\xi}(x, y, 0^+) - H_{\xi}(x, y, 0^-) = 0,$$

$$(5) \quad [E_{\eta}(x, y)] = 0.$$

Further, the scattered fields are required to be outgoing at infinity. In order to have a unique solution, it is necessary to guarantee quadratic integrability of $\mathbf{E}(\mathbf{r})$, $\mathbf{H}(\mathbf{r})$ at the edges of the strip and to assume the condition

$$(6) \quad [H_{\eta}(x, y)] = 0, \quad \text{for } x = \pm a.$$

On account of the unidirectional conductivity of the strip, the current induced on the strip and hence the vector potential $\mathbf{A}(\mathbf{r})$ has only a ξ component. It therefore follows that $H_{\xi}^s(\mathbf{r}) = 0$. It is evident (see Karp 1957) that when $E_{\xi}^i(\mathbf{r}) = 0$, the incident field is undisturbed by the strip. Hence it is possible to decompose the total field into two components: one component has the magnetic vector and the other the electric vector transverse to the direction in which the strip is conducting. It is obvious that for the second component of the incident wave, the strip has no effect and therefore it is enough to consider only that component of the incident wave which has its magnetic vector in η - z plane. The incident wave may therefore be taken as

$$(7) \quad \begin{aligned} \mathbf{E}^i(\mathbf{r}) &= [(q^2 + n^2)\hat{\xi} - pq\hat{\eta} - pn\hat{z}]e^{ik(p\xi + q\eta + nz)}, \\ \mathbf{H}^i(\mathbf{r}) &= [n\hat{\eta} - q\hat{z}]e^{ik(p\xi + q\eta + nz)}, \end{aligned}$$

where

$$(8) \quad \begin{aligned} p &= l \cos \alpha + m \sin \alpha, \\ q &= -l \sin \alpha + m \cos \alpha, \end{aligned}$$

and l , m , n are the direction cosines of the direction of propagation of the incident wave.

The scattered fields are derived from $\mathbf{A}(\mathbf{r})$ with the help of (2) and the relation

$$(9) \quad \mathbf{H}^{(s)}(\mathbf{r}) = \nabla \times \mathbf{A}(\mathbf{r}).$$

Since $H_{\xi}^s(\mathbf{r}) = 0$, condition (4) is satisfied. Further it follows from considerations of symmetry with respect to the plane $z = 0$ that

$$(10) \quad \begin{aligned} H_{\xi, \eta}^{(s)}(z) &= -H_{\xi, \eta}^{(s)}(-z), \\ E_{\xi, \eta}^{(s)}(z) &= E_{\xi, \eta}^{(s)}(-z). \end{aligned}$$

As a consequence of (10), condition (5) is satisfied. The vector potential is obtained from the current distribution on the strip by the relation

$$(11) \quad A_{\xi}(\mathbf{r}) = \int_{-a}^a \int_{-\infty}^{\infty} J(x', y') \frac{e^{ik|\mathbf{r}-\mathbf{r}'|}}{4\pi|\mathbf{r}-\mathbf{r}'|} dx' dy'$$

where \mathbf{r} , \mathbf{r}' denote the position vector of a point in space and in the x - y plane respectively. It is obvious from the geometry of the problem that all the field components depend on y only through the phase factor e^{ikmy} . Hence (11) becomes

$$(12) \quad A_{\xi}(\mathbf{r}) = \frac{i}{4} e^{ikmy} \int_{-a}^a J(x') H_0^{(1)}[k_0 \sqrt{(x-x')^2 + z^2}] dx'$$

where

$$k_0 = k\sqrt{(1-m^2)} = km_1.$$

Together with (1), (2), and (9), (12) gives

$$(14) \quad E_{\xi}^2(x, z) = -\frac{1}{4k} \left[k^2 + \left(\cos \alpha \frac{d}{dx} + ikm \sin \alpha \right)^2 \right] \int_{-a}^a J(x') H_0^{(1)}[k_0 \sqrt{(x-x')^2 + z^2}] dx'.$$

With the help of (3) and (7), (14) gives the following integral equation

$$(15) \quad \left[k^2 + \left(\cos \alpha \frac{d}{dx} + ikm \sin \alpha \right)^2 \right] \int_{-a}^a J(x') H_0^{(1)}[k_0 |x-x'|] dx' = 4k(q^2 + n^2) e^{iklz}.$$

By solving the differential equation (15) for the integral it is easily obtained that

$$(16) \quad \int_{-a}^a k J(x') H_0^{(1)}(km_1 |x-x'|) dx' = 4e^{iklz} + Ce^{ikc_1 z} + De^{-ikc_2 z}$$

where

$$(17) \quad c_1 = \sec \alpha - m \tan \alpha,$$

$$(18) \quad c_2 = \sec \alpha + m \tan \alpha.$$

The two arbitrary constants of integration C and D are determined in terms of the unknown function by consideration of the integral and its x derivative. For $0 \leq \alpha < \pi/2$, $J(\pm a) = 0$ by virtue of (6). Hence (16) can be reduced to

$$(19) \quad \int_{-a}^a k J(x') \left[H_0^{(1)}(km_1 |x-x'|) - \left\{ \frac{c_2 e^{ikc_1 z}}{c_1 + c_2} + \frac{c_1 e^{ikc_2 z}}{c_1 + c_2} \right\} H_0^{(1)}(km_1 |x'|) \right. \\ \left. + \left\{ \frac{e^{ikc_1 z}}{ik(c_1 + c_2)} - \frac{e^{-ikc_2 z}}{ik(c_1 + c_2)} \right\} \frac{d}{dx'} H_0^{(1)}(km_1 |x'|) \right] dx' \\ = 4e^{iklz} - \frac{(l+c_2)}{c_1 + c_2} 4e^{ikc_1 z} + \frac{(l-c_1)}{c_1 + c_2} 4e^{-ikc_2 z}.$$

SOLUTION OF THE INTEGRAL EQUATION FOR $ka \ll 1$

With the substitutions $x = a \cos u$, $x' = a \cos v$, $\epsilon = ka$, (19) becomes

$$(20) \quad \int_0^\pi \epsilon^2 F_1(v) \left[H_0^{(1)}(\epsilon m_1 |\cos u - \cos v|) - \frac{1}{c_1 + c_2} \left\{ c_2 e^{i\epsilon c_1 \cos u} + c_1 e^{-i\epsilon c_2 \cos u} \right\} \right. \\ \left. H_0^{(1)}(\epsilon m_1 |\cos v|) - \frac{1}{i\epsilon(c_1 + c_2) \sin v} \left\{ e^{i\epsilon c_1 \cos u} - e^{-i\epsilon c_2 \cos u} \right\} \frac{d}{dv} H_0^{(1)}(\epsilon m_1 |\cos v|) \right] \sin v \, dv \\ = 4e^{i\epsilon l \cos u} - \frac{(l+c_2)}{c_1+c_2} 4e^{i\epsilon c_1 \cos u} + \frac{(l-c_1)}{c_1+c_2} 4e^{-i\epsilon c_2 \cos u}$$

where $0 \leq u \leq \pi$ and

$$(21) \quad \epsilon F_1(v) = J(a \cos v).$$

For small ϵ , it can be shown that

$$(22) \quad H_0^{(1)}(\epsilon m_1 |\cos u - \cos v|) = \frac{2i}{\pi} (g_0 + g_1 m_1^2 \epsilon^2 + g_2 m_1^4 \epsilon^4 + \dots)$$

where

$$(23) \quad g_0 = p + \log |2(\cos u - \cos v)| = p - 2 \sum_{m=1}^{\infty} \frac{\cos mu \cos mv}{m}, \\ g_n = \frac{(-1)^n}{2^{2n} (n!)^2} (\cos u - \cos v)^{2n} \left[p - 1 - \frac{1}{2} \dots \frac{1}{n} - 2 \sum_1^{\infty} \frac{\cos mu \cos mv}{m} \right]$$

for $n \geq 1$ and

$$(24) \quad p = \log \frac{\gamma \epsilon m_1}{4} - \frac{1}{2} \pi i,$$

$\log \gamma = 0.5772157$ is Euler's constant,

$$(25) \quad H_0^{(1)}(\epsilon m_1 |\cos v|) = \frac{2i}{\pi} [g_{00} + g_{01} m_1^2 \epsilon^2 + g_{02} m_1^4 \epsilon^4 + \dots]$$

where

$$(26) \quad g_{00} = p - \sum_1^{\infty} \frac{(-1)^m \cos 2mv}{m}, \\ g_{0n} = \frac{(-1)^n}{2^{2n} (n!)^2} (\cos v)^{2n} \left[p - 1 - \frac{1}{2} \dots \frac{1}{n} - \sum_1^{\infty} \frac{(-1)^m \cos 2mv}{m} \right],$$

and

$$(27) \quad \frac{d}{dv} H_0^{(1)}(\epsilon m_1 |\cos v|) = \frac{2i}{\pi} (h_0 + h_1 m_1^2 \epsilon^2 + h_2 m_1^4 \epsilon^4 + \dots)$$

where

$$h_0 = 2 \sum_1^{\infty} (-1)^m \sin 2mv,$$

$$(28) \quad h_n = \frac{(-1)^{n+1} n}{2^{2n-1} (n!)^2} (\cos v)^{2n-1} \sin v \left[p - 1 - \frac{1}{2} \dots \frac{1}{n} - \sum_1^m \frac{(-1)^m \cos 2mv}{m} \right] \\ + \frac{(-1)^n (\cos v)^{2n}}{2^{2n-1} (n!)^2} \sum_1^\infty (-1)^m \sin 2mv.$$

A solution is assumed in the form

$$(29) \quad F_1(v) = f_0 + f_1 \epsilon + f_2 \epsilon^2 + f_3 \epsilon^3 + f_4 \epsilon^4 + \dots$$

where f_n depend only on v , l , m , and $\log \epsilon$. The above expansions are inserted in (20), the exponentials are expanded into their power series, and the coefficients of like powers of ϵ on both sides of (20) are equated. The result is the following infinite set of integral equations which enable the determination of f_n 's iteratively.

$$\begin{aligned} \int_0^\pi dv \sin v f_0 K_0 &= i \beta_0 \cos^2 u, \\ \int_0^\pi dv \sin v f_1 K_0 &= -\beta_1 \cos^3 u - \int_0^\pi dv \sin v f_0 K_1, \\ \int_0^\pi dv \sin v f_2 K_0 &= -i \beta_2 \cos^4 u - \int_0^\pi dv \sin v f_1 K_1 - \int_0^\pi dv \sin v f_0 K_2, \\ (30) \quad \int_0^\pi dv \sin v f_3 K_0 &= \beta_3 \cos^5 u - \int_0^\pi dv \sin v f_2 K_1 - \int_0^\pi dv \sin v f_1 K_2 \\ &\quad - \int_0^\pi dv \sin v f_0 K_3, \\ \int_0^\pi dv \sin v f_4 K_0 &= i \beta_4 \cos^6 u - \int_0^\pi dv \sin v f_3 K_1 - \int_0^\pi dv \sin v f_2 K_2 \\ &\quad - \int_0^\pi dv \sin v f_1 K_3 - \int_0^\pi dv \sin v f_0 K_4 \dots \\ &\dots \dots \dots \end{aligned}$$

where

$$\begin{aligned} K_0 &= g_0 - g_{00} - \frac{\cos u}{\sin v} \delta_0 h_0, \\ K_1 &= -i \frac{\cos^2 u}{\sin v} \delta_1 h_0, \\ (31) \quad K_2 &= g_1 m_1^2 - g_{01} m_1^2 + \gamma_2 \cos^2 u g_{00} - \frac{\cos u}{\sin v} \delta_0 h_1 m_1^2 + \frac{\cos^3 u}{\sin v} \delta_2 h_0, \\ K_3 &= i \gamma_3 \cos^3 u g_{00} - i \frac{\cos^2 u}{\sin v} \delta_1 h_1 m_1^2 + i \frac{\cos^4 u}{\sin v} \delta_3 h_0, \\ K_4 &= g_2 m_1^4 - g_{02} m_1^4 + \gamma_2 \cos^2 u g_{01} m_1^2 - \gamma_4 g_{00} \cos^4 u \\ &\quad - \frac{\cos u}{\sin v} \delta_0 h_2 m_1^4 + \frac{\cos^3 u}{\sin v} \delta_2 h_1 m_1^2 - \frac{\cos^5 u}{\sin v} \delta_4 h_0, \end{aligned}$$

and

$$\begin{aligned}
 \delta_n &= \frac{c_1^{n+1} - (-c_2)^{n+1}}{(n+1)!(c_1+c_2)}, \\
 \gamma_n &= \frac{c_1 c_2 [c_1^{n-1} - (-c_2)^{n-1}]}{n!(c_1+c_2)}, \\
 \beta_n &= \frac{2\pi}{(n+2)!} \left[l^{n+2} - c_1^{n+2} \frac{(l+c_2)}{c_1+c_2} + (-c_2)^{n+2} \frac{(l-c_1)}{c_1+c_2} \right].
 \end{aligned}
 \tag{32}$$

On account of (6) $f_n(v) = 0$ for $v = 0, \pi$. Hence f_n may be expressed in a Fourier sine series and the coefficients of the various terms in the series can be determined with the help of the integral equations (30). It is found that the solution of (30) is readily obtained in the form

$$\begin{aligned}
 f_{2n} &= \sum_{r=0}^n a_{2n,r} \sin(2r+1)v \\
 f_{2n+1} &= \sum_{r=0}^n a_{2n+1,r} \sin(2r+2)v \quad n = 0, 1, 2, \dots
 \end{aligned}
 \tag{33}$$

where

$$\begin{aligned}
 a_{00} &= \frac{2i\beta_0}{\pi}, \\
 a_{10} &= -\frac{3\beta_1}{2\pi}, \\
 a_{20} &= \frac{3i\beta_1\delta_1}{\pi} - \frac{2i\beta_0\gamma_2 p}{\pi} + \frac{i\beta_0\gamma_2}{\pi} + \frac{i\beta_0 m_1^2 p}{2\pi} + \frac{i\beta_0 m_1^2}{8\pi} - \frac{3i\beta_2}{\pi}, \\
 a_{21} &= \frac{i\beta_0 m_1^2}{24\pi} - \frac{i\beta_2}{\pi}, \\
 a_{30} &= \frac{\beta_1 m_1^2}{8\pi} - \frac{9\beta_1\delta_2}{4\pi} + \frac{3\beta_0\gamma_3(p - \frac{1}{2})}{2\pi} + \frac{5\beta_3}{2\pi}, \\
 a_{31} &= \frac{5\beta_3}{8\pi} - \frac{\beta_1 m_1^2}{64\pi}, \\
 a_{40} &= \frac{15i\beta_4}{4\pi} - \frac{15i\beta_3\delta_1}{4\pi} - \frac{3i\beta_2 m_1^2 p}{4\pi} - \frac{i\beta_2 m_1^2}{4\pi} + \frac{3i\beta_2\gamma_2 p}{\pi} \\
 &\quad - \frac{3i\beta_2\gamma_2}{4\pi} + \frac{9i\beta_1\delta_1\delta_2}{2\pi} + \frac{3i\beta_1\delta_1 m_1^2 p}{8\pi} - \frac{3i\beta_1\delta_1\gamma_2 p}{\pi} \\
 &\quad + \frac{3i\beta_1\delta_1\gamma_2}{2\pi} - \frac{9i\beta_1\delta_3}{2\pi} + \frac{13i\beta_0 m_1^4}{384\pi} + \frac{3i\beta_0\gamma_2 m_1^2 p}{8\pi} \\
 &\quad - \frac{i\beta_0 m_1^4 p}{32\pi} - \frac{3i\beta_0\gamma_2\delta_1 p}{\pi} + \frac{3i\beta_0\gamma_2\delta_1}{2\pi} - \frac{i\beta_0\gamma_2 p^2 m_1^2}{\pi}
 \end{aligned}
 \tag{34}$$

$$\begin{aligned}
 & -\frac{2i\beta_0\gamma_2^2\rho}{\pi} + \frac{2i\beta_0\gamma_2^2\rho^2}{\pi} + \frac{i\beta_0\gamma_2^2}{2\pi} + \frac{i\beta_0m_1^2\gamma_2}{16\pi} \\
 & + \frac{i\beta_0m_1^4\rho^2}{8\pi} + \frac{3i\beta_0\gamma_4\rho}{\pi} - \frac{3i\beta_0\gamma_4}{2\pi}, \\
 a_{41} = & \frac{15i\beta_4}{8\pi} - \frac{i\beta_2m_1^2}{32\pi} + \frac{i\beta_1\delta_1m_1^2}{16\pi} - \frac{3i\beta_1\delta_3}{2\pi} + \frac{i\beta_0\gamma_4\rho}{\pi} \\
 & - \frac{i\beta_0\gamma_4}{2\pi} - \frac{i\beta_0\gamma_2\rho m_1^2}{24\pi} + \frac{i\beta_0\gamma_2m_1^2}{48\pi} - \frac{i\beta_0m_1^4\rho}{192\pi} - \frac{i\beta_0m_1^4}{512\pi}, \\
 a_{42} = & \frac{3i\beta_4}{8\pi} - \frac{i\beta_2m_1^2}{160\pi} - \frac{i\beta_0m_1^4}{7680\pi}.
 \end{aligned}$$

TOTAL SCATTERING COEFFICIENT

The total scattering cross section σ per unit length of the strip is the total scattered power per unit length of the strip divided by the incident power flow through unit area normal to the direction of the incident wave. The ratio of σ to the area $2a$ per unit length of the strip is a dimensionless quantity called the total scattering coefficient t . By integrating the real part of $\nabla \cdot E^{**} \times H^*$ throughout the volume bounded by the two sides of the strip and a cylindrical surface at infinity, it can be easily shown that

$$(35) \quad t = \frac{1}{2a} \operatorname{Re} \int_{-a}^a e^{-ikx'} J(x') dx'.$$

With the substitution $x' = a \cos v$, $\epsilon = ka$ in (35), and the relations (21), (29), and (33), it can be easily derived that the first few terms in the power series of t are given as

$$(36) \quad t = \frac{\pi}{4} \operatorname{Re} \sum_{n=0}^{\infty} t_{2n+1} \epsilon^{2n+1},$$

where

$$\begin{aligned}
 (37) \quad t_1 &= a_{00}, \\
 t_3 &= a_{20} - \frac{ila_{10}}{2} - \frac{l^2 a_{00}}{8}, \\
 t_5 &= a_{40} - \frac{ila_{30}}{2} - \frac{l^2}{8} (a_{20} + a_{21}) + \frac{il^3}{24} a_{10} + \frac{l^4}{192} a_{00}.
 \end{aligned}$$

The substitution of (34) and (37) in (36) together with the use of (32), gives the first two terms in the total scattering coefficient as

$$\begin{aligned}
 (38) \quad t = & \frac{\pi \epsilon^3}{4} \left(\frac{\beta_0 m_1^2}{4} - \beta_0 \gamma_2 \right) \\
 & + \frac{\pi \epsilon^5}{4} \left[m_1^4 \left(-\frac{\beta_0}{64} + \frac{\beta_0 d}{8} \right) + m_1^2 \left(-\frac{\beta_0 d^2}{32} + \frac{3\beta_0 \gamma_2}{16} - \beta_0 \gamma_2 d + \frac{3\beta_1 \delta_1}{16} - \frac{3\beta_2}{8} \right) \right. \\
 & \left. + \left(\frac{\beta_0 \gamma_2 d^2}{8} - \frac{3l}{8} \beta_0 \gamma_2 - \frac{3\beta_0 \gamma_2 \delta_1}{2} - \beta_0 \gamma_2^2 + \frac{3\beta_0 \gamma_4}{2} + 2\beta_0 \gamma_2^2 d - \frac{3\beta_1 \delta_1 \gamma_2}{2} + \frac{3\beta_2 \gamma_2^2}{2} \right) \right]
 \end{aligned}$$

where

$$d = \log \gamma \epsilon m_1.$$

For the case when the direction of propagation of the incident wave lies in a plane perpendicular to the plane of the infinite strip, i.e. $m = 0$ and when $\alpha = 0$, the total scattering coefficient becomes

$$(39) \quad t = \frac{\pi^2 \epsilon^3}{16} (1 - l^2) \left[1 + \frac{5\epsilon^2}{16} \left(1 - \frac{8}{5} d - \frac{4}{5} l^2 \right) \right].$$

For $\alpha = 0$, the strip is conducting in the direction perpendicular to its edges and the present problem is easily seen to be identical with that of scattering by a perfectly conducting infinite strip of a plane wave which has no component of the magnetic field in the direction perpendicular to the edges of the strip. This problem has been extensively treated in the literature (for example, Millar 1960) for the particular case $m = 0$, which corresponds to the propagation vector of the incident wave lying in a plane perpendicular to the plane of the strip. The first two terms in the total scattering coefficient for this special case are in complete agreement with (39).

SCATTERED FIELDS IN THE FAR ZONE

It is desired to give the expressions for the scattered fields in the far zone. Setting $x = \rho \sin \theta$, $z = \rho \cos \theta$ in (12) and taking only the leading term in the asymptotic expression of the Hankel function for large ρ , it is obtained that

$$(40) \quad \mathbf{A}(\mathbf{r}) = \frac{i}{4} a e^{ikmy} \sqrt{\frac{\pi}{2km_1\rho}} e^{i(km_1\rho - \pi/4)} \sum_0^\infty T_{2n+1} \epsilon^{2n+1}$$

where T_{2n+1} is the same as t_{2n+1} with l replaced by $m_1 \sin \theta$. With the help of (1), (2), (9), and (40) the far-zone scattered fields for $z > 0$ are obtained as

$$(41) \quad \begin{aligned} H_\xi^s(\mathbf{r}) &= 0, \\ H_\eta^s(\mathbf{r}) &= -m_1 \cos \theta \cdot A, \\ H_z^s(\mathbf{r}) &= (m \cos \alpha - m_1 \sin \theta \sin \alpha) A, \\ E_\xi^s(\mathbf{r}) &= -[1 - (m \sin \alpha + m_1 \sin \theta \cos \alpha)^2] A, \\ E_\eta^s(\mathbf{r}) &= (m \cos \alpha - m_1 \sin \theta \sin \alpha) (m \sin \alpha + m_1 \sin \theta \cos \alpha) A, \\ E_z^s(\mathbf{r}) &= m_1 \cos \theta (m \sin \alpha + m_1 \sin \theta \cos \alpha) A \end{aligned}$$

where

$$(42) \quad A = \frac{1}{4} \sqrt{\frac{\pi}{2km_1\rho}} e^{ikmy} e^{i(km_1\rho - \pi/4)} \sum_{n=0}^\infty T_{2n+1} \epsilon^{2n+2}.$$

ACKNOWLEDGMENTS

The author is indebted to Professor Ronold W. P. King and Dr. Tai Tsun Wu for their help and encouragement.

REFERENCES

- BOUWKAMP, C. J. 1953. Diffraction theory, a critique of some recent developments, New York University, Institute of Mathematical Sciences, Research Report No. EM-50.
- KARP, S. N. 1957. Diffraction of a plane wave by a unidirectionally conducting half-plane, New York University, Institute of Mathematical Sciences, Research Report No. EM-108.
- MILLAR, R. F. 1960. *Can. J. Phys.* **38**, 38.

SCALAR DIFFRACTION BY A PROLATE SPHEROID AT LOW FREQUENCIES¹

T. B. A. SENIOR

ABSTRACT

For the scalar problem of the diffraction of a plane wave by a prolate spheroid the exact solution is known, and by expanding this in ascending powers of ka , where k is the wave number and $2a$ is the interfocal distance, the Rayleigh series for both the "soft" and "hard" bodies are obtained up to and including terms in $(ka)^6$. The corresponding results for an oblate spheroid can be deduced by a trivial change of parameters. Some particular cases are examined.

1. INTRODUCTION

It is well known that the scalar problem of diffraction by a perfectly conducting prolate or oblate spheroid can be solved exactly. The solution is obtained as an infinite series of spheroidal functions with specified coefficients, but because of the difficulties associated with the computation of these functions very few calculations have been carried out based on this solution. This is particularly true at the shorter wavelengths since the slow convergence of the series requires a large number of terms to be considered.

At the other end of the frequency spectrum the task is more simple, and it is a relatively straightforward matter either to compute the exact solution or to deduce a sequence of terms in the Rayleigh series. Rather surprisingly, the Rayleigh series for the scalar problem seems to have been neglected, and apart from the work of Sleator (1957) for the 'hard' body, a search of the literature has failed to produce anything beyond the first term. Although the Rayleigh series has a limited radius of convergence, a significant number of terms are required in order to obtain an insight into the way in which the scattered field is generated at low frequencies, and in the present paper the terms are calculated up to and including $(ka)^6$, where k is the wave number and $2a$ is the interfocal distance.

2. THE EXACT SOLUTION

The solutions for prolate and oblate spheroids can be deduced from one another by a trivial change of parameters, and for this reason the analysis will be given for only the first type of body. Consider, therefore, a prolate spheroid which is defined in terms of the prolate spheroidal co-ordinates (ξ, η, ϕ) by the equation $\xi = \xi_0$. Incident upon the body is a plane wave travelling in the (x, z) plane of a Cartesian co-ordinate system (x, y, z) where

$$x = a[(1 - \eta^2)(\xi^2 - 1)]^{\frac{1}{2}} \cos \phi,$$

$$y = a[(1 - \eta^2)(\xi^2 - 1)]^{\frac{1}{2}} \sin \phi,$$

$$z = a\eta\xi,$$

¹Manuscript received August 12, 1960.

Contribution from the Radiation Laboratory, University of Michigan, Ann Arbor, Michigan, U.S.A.

and if the direction of incidence makes an angle ζ with the positive z axis, the field can be written as

$$V^i = e^{ik(z \sin \zeta + z \cos \zeta)}.$$

A time factor $e^{-i\omega t}$ is employed and suppressed.

The incident field can also be expanded in an infinite series of spheroidal functions in the form*

$$(1) \quad V^i = \sum_{m=0}^{\infty} \sum_{n=m}^{\infty} \gamma_{mn}(c, \zeta) \psi_{emn}^{(1)}(c; \eta, \xi, \phi)$$

where $c = ka$ and

$$(2) \quad \gamma_{mn}(c, \zeta) = 2(2 - \delta_{0m}) i^n N_{mn}^{-1} S_{mn}(c, \cos \zeta),$$

$$(3) \quad \psi_{emn}^{(j)} = S_{mn}(c, \eta) R_{mn}^{(j)}(c, \xi) \cos m\phi.$$

$S_{mn}(c, \eta)$ and $R_{mn}^{(j)}(c, \xi)$ are the angular and radial functions respectively, and it will be observed that in equation (1) the radial function is of the first kind. For the scattered field V^s a similar expansion is assumed, and this is

$$(4) \quad V^s = \sum_{m=0}^{\infty} \sum_{n=m}^{\infty} A_{mn} \psi_{emn}^{(3)}(c; \eta, \xi, \phi)$$

where the amplitudes A_{mn} are to be determined from the boundary condition at $\xi = \xi_0$.

If the body is 'soft' so that the boundary condition at $\xi = \xi_0$ is

$$V^i + V^s = 0$$

(Dirichlet condition), the orthogonality of the $\cos m\phi$ and the angular functions gives immediately

$$(5) \quad A_{mn} = -\gamma_{mn}(c, \zeta) \frac{R_{mn}^{(1)}(c, \xi_0)}{R_{mn}^{(3)}(c, \xi_0)}.$$

In the 'hard' case for which the Neumann boundary condition applies (vanishing normal derivative of $V^i + V^s$ at $\xi = \xi_0$), the corresponding amplitudes differ from equation (5) in that each radial function is replaced by its first derivative with respect to ξ_0 . It follows that by differentiation it is possible to deduce the results for the Neumann problem from those for the Dirichlet, and we shall therefore restrict attention to the latter problem. It is noted in passing that this similarity enables us to deduce the Rayleigh series for the hard body from the Rayleigh series for the soft body by differentiating each radial function (and hence, each Legendre function in terms of which the $R_{mn}^{(j)}(c, \xi_0)$ are expanded) with respect to ξ_0 , and although this might suggest that the two series are similar in form, we shall see later that the differentiation serves to remove some of the powers of c .

*The notation is that of Flammer (1957), and the reader is referred to this book for the definitions of the symbols and functions here used.

For the sake of simplicity we shall now particularize the problem to the case of a field which is incident in the direction of the negative z axis, so that

$$V^i = e^{-ikz}$$

(corresponding to $\zeta = \pi$). Since

$$\lim_{\zeta \rightarrow \pi} S_{mn}(c, \cos \zeta) = 0, \quad n \neq 0,$$

γ_{mn} is zero unless $m = 0$, and the summation over m in equations (1) and (4) produces only the first term. Hence

$$(6) \quad V^s = \sum_{n=0}^{\infty} A_{0n} S_{0n}(c, \eta) R_{0n}^{(3)}(c, \xi)$$

with

$$(7) \quad A_{0n} = -\gamma_{0n}(c, \pi) \frac{R_{0n}^{(1)}(c, \xi_0)}{R_{0n}^{(3)}(c, \xi_0)},$$

and both V^i and V^s are now independent of ϕ .

In the far field $c\xi \sim kR$, where R is the distance from the center of the spheroid. For large values of $c\xi$,

$$R_{0n}^{(3)}(c, \xi) \sim \frac{1}{c\xi} e^{i[c\xi - \frac{1}{2}(n+1)\pi]},$$

and if this is inserted into equation (6) the coefficient of e^{ikR}/kR is the far-field amplitude and is

$$(8) \quad f(\eta) = 2i \sum_{n=0}^{\infty} \frac{S_{0n}(c, -1)}{N_{0n}} \frac{R_{0n}^{(1)}(c, \xi_0)}{R_{0n}^{(3)}(c, \xi_0)} S_{0n}(c, \eta).$$

For sufficiently small values of c , $f(\eta)$ can be expanded in a convergent series of positive increasing powers of c with coefficients which are functions of ξ_0 and η . This is the Rayleigh series for the body, and it is the purpose of the paper to calculate the first few terms.

3. THE RAYLEIGH SERIES

The angular spheroidal function $S_{0n}(c, \eta)$ is defined as

$$S_{0n}(c, \eta) = \sum_{r=0,1}^{\infty} d_r^{0n}(c) P_r(\eta)$$

where $P_r(\eta)$ is the Legendre polynomial of order r and argument η , and the summation extends over even or odd values of r according as n is even or odd. This is denoted by a prime attached to the summation sign. The radial functions $R_{0n}^{(j)}(c, \xi)$ are similarly defined in terms of Legendre functions of the first and/or second kind of argument ξ , and the coefficients are either the same d_r^{0n} , or can be determined from them. The d_r^{0n} themselves are given by a recurrence relation coupled with a normalizing equation, and since each coefficient can be expanded in a series of powers of c , it is only necessary to

insert the appropriate expansions to obtain the required Rayleigh series for $f(\eta)$. Moreover, a trivial calculation shows that the first three terms in equation (8) are sufficient to specify the terms in the Rayleigh series up to and including c^6 , and this is as far as the analysis will be carried.

Using the expansions given in the Appendix it now follows that*

$$(9) \quad f(\eta) = -c \sum_{n=0}^{\infty} a_n(\xi_0) \frac{P_n}{Q_n} S_{0n}(c, \eta)$$

where

$$(10) \quad \begin{aligned} a_0(\xi_0) = & 1 - ic \frac{P_0}{Q_0} - c^2 \left\{ \frac{1}{9} \left(\frac{P_2}{P_0} - \frac{Q_2}{Q_0} \right) - \frac{1}{2} \frac{P_1}{Q_0} + \left(\frac{P_0}{Q_0} \right)^2 + \frac{1}{6} \right\} \\ & + ic^3 \frac{P_0}{Q_0} \left\{ \frac{2}{9} \left(\frac{P_2}{P_0} - \frac{Q_2}{Q_0} \right) - \frac{P_1}{Q_0} + \left(\frac{P_0}{Q_0} \right)^2 + \frac{5}{18} \right\} \\ & + c^4 \left[\frac{1}{525} \left(\frac{P_4}{P_0} - \frac{Q_4}{Q_0} \right) - \frac{1}{60} \frac{P_3}{Q_0} + \frac{1}{3} \left(\frac{P_2}{P_0} - \frac{Q_2}{Q_0} \right) \right. \\ & \quad \cdot \left\{ \left(\frac{P_0}{Q_0} \right)^2 - \frac{1}{27} \frac{Q_2}{Q_0} - \frac{1}{6} \frac{P_1}{Q_0} + \frac{25}{378} \right\} \\ & \quad - \frac{3}{2} \frac{P_1}{Q_0} \left\{ \left(\frac{P_0}{Q_0} \right)^2 - \frac{1}{27} \frac{Q_2}{Q_0} - \frac{1}{6} \frac{P_1}{Q_0} + \frac{1}{10} \right\} \\ & \quad \left. + \left(\frac{P_0}{Q_0} \right)^4 + \frac{7}{18} \left(\frac{P_0}{Q_0} \right)^2 + \frac{43}{3240} \right] \\ & - ic^5 \frac{P_0}{Q_0} \left[\frac{2}{525} \left(\frac{P_4}{P_0} - \frac{Q_4}{Q_0} \right) - \frac{1}{30} \frac{P_3}{Q_0} + \frac{4}{9} \left(\frac{P_2}{P_0} - \frac{Q_2}{Q_0} \right) \right. \\ & \quad \cdot \left\{ \left(\frac{P_0}{Q_0} \right)^2 + \frac{1}{36} \frac{P_2}{P_0} - \frac{1}{12} \frac{Q_2}{Q_0} - \frac{1}{2} \frac{P_1}{Q_0} + \frac{13}{84} \right\} \\ & \quad - 2 \frac{P_1}{Q_0} \left\{ \left(\frac{P_0}{Q_0} \right)^2 - \frac{1}{18} \frac{Q_2}{Q_0} - \frac{3}{8} \frac{P_1}{Q_0} + \frac{37}{180} \right\} \\ & \quad \left. + \left(\frac{P_0}{Q_0} \right)^4 + \frac{1}{2} \left(\frac{P_0}{Q_0} \right)^2 + \frac{233}{5400} \right] + O(c^6), \end{aligned}$$

$$(11) \quad a_1(\xi_0) = -\frac{1}{3} c^2 + \frac{1}{3} c^4 \left\{ \frac{1}{25} \left(\frac{P_3}{P_1} - \frac{Q_3}{Q_1} \right) + \frac{1}{6} \frac{P_0}{Q_1} + \frac{1}{10} \right\} + \frac{1}{27} ic^5 \frac{P_1}{Q_1} + O(c^6),$$

$$(12) \quad a_2(\xi_0) = \frac{4}{405} c^4 + O(c^6),$$

and $a_n(\xi_0) = O(c^6)$, $n \geq 3$. The corresponding expansion for the hard body can be obtained by replacing each Legendre function of argument ξ_0 by its first derivative, and to preserve this feature no attempt was made to use Legendre function identities in simplifying the above expressions.

*Unless otherwise shown, the Legendre functions have argument ξ_0 .

To complete the expansion of $f(\eta)$ it is necessary to expand the angular spheroidal functions $S_{0n}(c, \eta)$, and to achieve the simplest possible form for the final results we shall now sacrifice the symmetry property referred to above. Taking first the solution $f(\eta) = f_s(\eta)$ for the soft body, and using the Legendre function identities

$$P_2 \frac{Q_0}{P_0} - Q_2 = \frac{3}{2} P_1,$$

$$P_4 \frac{Q_0}{P_0} - Q_4 = \frac{7}{4} P_3 + \frac{1}{3} P_1,$$

we have

$$(13) \quad f_s(\eta) = -c \sum_{n=0}^{\infty} u_n(\eta) (-ic)^n$$

where

$$u_0 = \frac{P_0}{Q_0} P_0(\eta),$$

$$u_1 = \left(\frac{P_0}{Q_0}\right)^2 P_0(\eta),$$

$$u_2 = \frac{1}{9} \frac{P_0}{Q_0} P_2(\eta) + \frac{1}{3} \frac{P_1}{Q_1} P_1(\eta) + \frac{P_0}{Q_0} \left\{ \left(\frac{P_0}{Q_0}\right)^2 - \frac{1}{3} \frac{P_1}{Q_0} + \frac{2}{9} \right\} P_0(\eta),$$

$$u_3 = \frac{1}{9} \left(\frac{P_0}{Q_0}\right)^2 P_2(\eta) + \left(\frac{P_0}{Q_0}\right)^2 \left\{ \left(\frac{P_0}{Q_0}\right)^2 - \frac{2}{3} \frac{P_1}{Q_0} + \frac{1}{3} \right\} P_0(\eta),$$

$$\begin{aligned} u_4 = & \frac{1}{525} \frac{P_0}{Q_0} P_4(\eta) + \frac{1}{75} \frac{P_1}{Q_1} P_3(\eta) + \frac{1}{9} \left[\frac{4}{45} \frac{P_2}{Q_2} + \frac{P_0}{Q_0} \left\{ \left(\frac{P_0}{Q_0}\right)^2 - \frac{1}{3} \frac{P_1}{Q_0} + \frac{16}{63} \right\} \right] P_2(\eta) \\ & + \frac{1}{3} \frac{P_1}{Q_1} \left\{ \frac{1}{25} \left(\frac{P_3}{P_1} - \frac{Q_3}{Q_1}\right) + \frac{1}{6} \frac{P_0}{Q_1} + \frac{4}{25} \right\} P_1(\eta) \\ & - \frac{P_0}{Q_0} \left[\frac{1}{75} \frac{P_3}{Q_0} + \frac{P_1}{Q_0} \left\{ \left(\frac{P_0}{Q_0}\right)^2 + \frac{1}{27} \frac{Q_2}{Q_0} - \frac{1}{6} \frac{P_1}{Q_0} + \frac{91}{675} \right\} - \left(\frac{P_0}{Q_0}\right)^4 - \frac{4}{9} \left(\frac{P_0}{Q_0}\right)^2 - \frac{2}{75} \right] P_0(\eta), \\ u_5 = & \frac{1}{525} \left(\frac{P_0}{Q_0}\right)^2 P_4(\eta) + \frac{1}{9} \left(\frac{P_0}{Q_0}\right)^2 \left\{ \left(\frac{P_0}{Q_0}\right)^2 - \frac{2}{3} \frac{P_1}{Q_0} + \frac{23}{63} \right\} P_2(\eta) \\ & - \frac{1}{27} \left(\frac{P_1}{Q_1}\right)^2 P_1(\eta) - \left(\frac{P_0}{Q_0}\right)^2 \left[\frac{2}{75} \frac{P_3}{Q_0} + \frac{4}{3} \frac{P_1}{Q_0} \left\{ \left(\frac{P_0}{Q_0}\right)^2 \right. \right. \\ & \left. \left. - \frac{1}{18} \frac{Q_2}{Q_0} - \frac{1}{3} \frac{P_1}{Q_0} + \frac{58}{225} \right\} - \left(\frac{P_0}{Q_0}\right)^4 - \frac{5}{9} \left(\frac{P_0}{Q_0}\right)^2 - \frac{127}{2025} \right] P_0(\eta). \end{aligned}$$

For the hard body the expansion for the far-field amplitude $f(\eta) = f_h(\eta)$ is of somewhat simpler form. Since $P_0'(\xi_0) \equiv 0$, where the prime denotes differentiation with respect to ξ_0 , the expression for $a_0(\xi_0)$ deduced from equation (10) contains only terms in c^2 and c^4 , and if

$$(14) \quad f_h(\eta) = -c \sum_{n=0}^{\infty} v_n(\eta) (-ic)^n,$$

then

$$v_0 = v_1 = 0,$$

$$v_2 = \frac{1}{3} \frac{P_1'}{Q_1'} P_1(\eta) + \frac{1}{9} \frac{P_2'}{Q_0'} P_0(\eta),$$

$$v_3 = 0,$$

$$v_4 = \frac{1}{75} \frac{P_1'}{Q_1'} P_3(\eta) + \frac{1}{81} \left\{ \frac{4}{5} \frac{P_2'}{Q_2'} + \frac{P_2'}{Q_0'} \right\} P_2(\eta) \\ + \frac{1}{75} \frac{P_1'}{Q_1'} \left\{ \frac{P_3'}{P_1'} - \frac{Q_3'}{Q_1'} + 4 \right\} P_1(\eta) \\ + \frac{1}{3} \left[\frac{1}{175} \frac{P_4'}{Q_0'} - \frac{1}{27} \frac{P_2'}{Q_0'} \left\{ \frac{Q_2'}{Q_0'} + \frac{9}{2} \frac{P_1'}{Q_0'} + \frac{16}{7} \right\} \right] P_0(\eta),$$

$$v_5 = -\frac{1}{27} \left(\frac{P_1'}{Q_1'} \right)^2 P_1(\eta) + \frac{1}{81} \left(\frac{P_2'}{Q_0'} \right)^2 P_0(\eta).$$

The differences between the Rayleigh series for the hard and soft bodies are now apparent, and whereas $f_s(\eta)$ contains all powers of c starting with the first, $f_h(\eta)$ begins with c^3 and has no term in c^4 . In this respect the expansion for $f_h(\eta)$ is similar to the Rayleigh series for the vector problem (see, for example, Stevenson 1953), and the agreement is further strengthened by the fact that the first imaginary term in $f_h(\eta)$ is provided by v_5 (and is therefore of order c^6). A comparison between the actual coefficients will be given at a later date.

For the oblate spheroid the appropriate expansions can be obtained from equations (13) and (14) by replacing c by $-ic$ and ξ_0 by $i\xi_0$.

4. PARTICULAR CASES

We shall conclude by examining the form taken by the above expansions when the spheroid degenerates into either a sphere or a disk.

If $\xi_0 \rightarrow \infty$ and $a \rightarrow 0$ in such a way that $a\xi_0$ tends to a finite limit ρ/k , the spheroid reduces to a sphere of this radius. The Legendre functions in the expressions for the $u_n(\eta)$ and $v_n(\eta)$ can now be replaced by the leading terms in their asymptotic developments for large ξ_0 , and in the limit $c\xi_0 = \rho$ the Rayleigh series for the soft and hard spheres are found to be

$$(15) \quad f_s(\eta) = -\rho \left[\left\{ 1 - i\rho - \frac{2}{3} \rho^2 + \frac{1}{3} i\rho^3 + \frac{2}{15} \rho^4 - \frac{2}{45} i\rho^5 \right\} P_0(\eta) \right. \\ \left. - \rho^2 \left\{ 1 - \frac{3}{5} \rho^2 - \frac{1}{3} i\rho^3 \right\} P_1(\eta) + \frac{1}{9} \rho^4 P_2(\eta) + O(\rho^6) \right],$$

$$(16) \quad f_h(\eta) = -\rho \left[\frac{1}{3} \rho^2 \left\{ 1 - \frac{3}{5} \rho^2 - \frac{1}{3} i \rho^3 \right\} P_0(\eta) \right. \\ \left. + \frac{1}{2} \rho^2 \left\{ 1 - \frac{3}{10} \rho^2 + \frac{1}{6} i \rho^3 \right\} P_1(\eta) - \frac{2}{27} \rho^4 P_2(\eta) + O(\rho^6) \right],$$

respectively. These are in agreement with the results obtained by expanding the Bessel function ratios in the known scalar solutions for a sphere.

The second case to be considered is the disk, and for this purpose it is necessary to go over to oblate spheroidal co-ordinates. Replacing c by $-ic$ and ξ_0 by $i\xi_0$ and then letting $\xi_0 \rightarrow 0$, the (oblate) spheroid reduces to a disk of radius a , and the Rayleigh series for this body can therefore be deduced from equations (13) and (14). Putting $\xi_0 = 0$ in these equations with $-ic$ instead of c , we have

$$(17) \quad f_s(\eta) = -\frac{2c}{\pi} \left[\left\{ 1 - \frac{2ic}{\pi} - c^2 \left(\frac{4}{\pi^2} - \frac{2}{9} \right) + \frac{2ic^3}{\pi} \left(\frac{4}{\pi^2} - \frac{1}{3} \right) \right. \right. \\ \left. \left. + c^4 \left(\frac{16}{\pi^4} - \frac{16}{9\pi^2} + \frac{2}{75} \right) - \frac{2ic^5}{\pi} \left(\frac{16}{\pi^4} - \frac{20}{9\pi^2} + \frac{127}{2025} \right) \right\} P_0(\eta) \right. \\ \left. + \frac{c^2}{9} \left\{ 1 - \frac{2ic}{\pi} - c^2 \left(\frac{4}{\pi^2} - \frac{12}{35} \right) + \frac{2ic^3}{\pi} \left(\frac{4}{\pi^2} - \frac{23}{63} \right) \right\} P_2(\eta) \right. \\ \left. + \frac{1}{525} c^4 \left\{ 1 - \frac{2ic}{\pi} \right\} P_4(\eta) + O(c^6) \right],$$

$$(18) \quad f_h(\eta) = -\frac{2c}{\pi} \left[\frac{1}{3} c^2 \left\{ 1 + \frac{4}{25} c^2 + \frac{2i}{9\pi} c^3 \right\} P_1(\eta) + \frac{1}{75} c^4 P_3(\eta) + O(c^6) \right].$$

In equation (17) the terms up to and including c^5 can be compared with those obtained by Bouwkamp (1954) for a circular aperture in a hard screen and if account is taken of the difference in sign implied by Babinet's principle, the expansions are seen to be in agreement.

5. ACKNOWLEDGMENT

The author is indebted to Mrs. B. Ullman for checking the calculations in this paper.

This work was carried out for the Air Force Cambridge Research Center under Contract AF 19(604)-6655.

REFERENCES

- BOUWKAMP, C. J. 1954. Phys. Soc. Repts. Progr. in Phys. **17**, 35.
 FLAMMER, C. 1957. Spheroidal wave functions (Stanford Univ. Press).
 SLEATOR, F. B. 1957. University of Michigan Report No. 2591-1-T.
 STEVENSON, A. F. 1953. J. Appl. Phys. **24**, 1134, 1143.

APPENDIX

The required coefficients d_r^{0n} for $n \leq 2$ are

$$d_0^{00} = 1 - \frac{1}{18} c^2 + \frac{67}{16200} c^4 + O(c^6),$$

$$d_2^{00} = -\frac{1}{9} c^2 + \frac{11}{1134} c^4 + O(c^6),$$

$$d_4^{00} = \frac{1}{525} c^4 + O(c^6);$$

$$d_1^{01} = 1 - \frac{3}{50} c^2 + O(c^4),$$

$$d_3^{01} = -\frac{1}{25} c^2 + O(c^4);$$

$$d_0^{02} = \frac{1}{45} c^2 + O(c^4),$$

$$d_2^{02} = 1 + O(c^2).$$

The function $S_{0n}(c, -1)$ has the value

$$S_{0n}(c, -1) = (-1)^n \sum_{r=0,1}^{\infty} d_r^{0n};$$

hence

$$S_{00}(c, -1) = 1 - \frac{1}{6} c^2 + \frac{17}{1080} c^4 + O(c^6),$$

$$S_{01}(c, -1) = -\left\{1 - \frac{1}{10} c^2 + O(c^4)\right\},$$

$$S_{02}(c, -1) = 1 + O(c^2).$$

The normalizing constant N_{0n} is

$$N_{0n} = 2 \sum_{r=0,1}^{\infty} \frac{(d_r^{0n})^2}{2r+1},$$

so that

$$N_{00} = 2 \left\{ 1 - \frac{1}{9} c^2 + \frac{28}{2025} c^4 + O(c^6) \right\},$$

$$N_{01} = \frac{2}{3} \left\{ 1 - \frac{3}{25} c^2 + O(c^4) \right\},$$

$$N_{02} = \frac{2}{5} \left\{ 1 + O(c^2) \right\}.$$

The radial function of the first kind, $R_{0n}^{(1)}(c, \xi)$ is defined as

$$R_{0n}^{(1)}(c, \xi) = \frac{1}{k_{0n}^{(1)}(c)} S_{0n}(c, \xi),$$

where

$$k_{0n}^{(1)}(c) = \frac{n!}{2^n \frac{n}{2}! \frac{n}{2}! d_0^{0n}} \sum_{r=0}^{\infty} d_r^{0n}, \quad (n \text{ even})$$

$$= \frac{3(n+1)!}{2^n \left(\frac{n-1}{2}\right)! \left(\frac{n+1}{2}\right)! c d_1^{0n}} \sum_{r=1}^{\infty} d_r^{0n}. \quad (n \text{ odd})$$

Hence

$$\frac{1}{k_{00}^{(1)}} = 1 + \frac{1}{9} c^2 + \frac{14}{2025} c^4 + O(c^6),$$

$$\frac{1}{k_{01}^{(1)}} = \frac{c}{3} \left\{ 1 + \frac{1}{25} c^2 + O(c^4) \right\},$$

$$\frac{1}{k_{02}^{(1)}} = \frac{2}{45} c^2 \left\{ 1 + O(c^2) \right\}.$$

The radial function of the third kind, $R_{0n}^{(3)}(c, \xi)$, is

$$R_{0n}^{(3)}(c, \xi) = R_{0n}^{(1)}(c, \xi) + i R_{0n}^{(2)}(c, \xi)$$

where

$$R_{0n}^{(2)}(c, \xi) = \frac{1}{k_{0n}^{(2)}(c)} \left\{ \sum_{r=0,1}^{\infty} d_r^{0n} Q_r(\xi) + \sum_{r=2,1}^{\infty} d_{\rho|r}^{0n} P_{r-1}(\xi) \right\}$$

with

$$d_{\rho|r}^{0n} = \lim_{\rho \rightarrow 0} \frac{1}{\rho} d_{-r+\rho}^{0n}$$

and

$$k_{0n}^{(2)}(c) = - \frac{2^n \frac{n}{2}! \frac{n}{2}! c^2 d_0^{0n}}{n!} \sum_{r=0}^{\infty} d_r^{0n}, \quad (n \text{ even})$$

$$= - \frac{2^n \left(\frac{n-1}{2}\right)! \left(\frac{n+1}{2}\right)! c^2 d_1^{0n}}{3(n+1)!} \sum_{r=1}^{\infty} d_r^{0n}. \quad (n \text{ odd})$$

The required $d_{\rho|r}^{0n}$ are

$$d_{\rho|2}^{00} = -\frac{1}{2} c^2 \left\{ 1 - \frac{17}{90} c^2 + O(c^4) \right\},$$

$$d_{\rho 14}^{00} = \frac{1}{60} c^4 \left\{ 1 + O(c^2) \right\},$$

$$d_{\rho 11}^{01} = \frac{1}{6} c^2 \left\{ 1 + O(c^2) \right\};$$

and

$$\frac{1}{k_{00}^{(2)}} = -\frac{1}{c} \left\{ 1 + \frac{2}{9} c^2 + \frac{41}{2025} c^4 + O(c^6) \right\},$$

$$\frac{1}{k_{01}^{(2)}} = -\frac{3}{c^2} \left\{ 1 + \frac{4}{25} c^2 + O(c^4) \right\},$$

$$\frac{1}{k_{02}^{(2)}} = -\frac{45}{2c^3} \left\{ 1 + O(c^2) \right\}.$$

These expansions are sufficient to give the far-field amplitude correct to c^6 .

THE HYDROGEN ION EFFECT IN WHISTLER DISPERSION¹

R. E. BARRINGTON AND T. NISHIZAKI

ABSTRACT

Four low-altitude whistlers have been carefully analyzed by a specially developed filtering technique. In each case the low-frequency portions of the resulting dispersion curves show similar departures from the simple $tf^{\frac{1}{2}} = \text{const.}$ law developed by Eckersley. The departures are found to be of the form and magnitude predicted by Storey on the assumption that the propagation is partly supported by the light hydrogen ions of the exosphere. If it is assumed that the observed deviations are due only to hydrogen ions, and that above some transitional level the positive ions are mostly hydrogen, an estimate of 1000 km for the height of the transitional level is obtained.

1. INTRODUCTION

Whistlers are electromagnetic radiations of natural origin found in the audio-frequency band of the radio spectrum where they normally appear as quasi-musical tones of descending pitch. Their interpretation as provided by Storey (1953) implies a much greater extent to the earth's outer ionosphere, its exosphere, than was believed a decade ago, and presents the problem of the origin, composition, and abundance of the ionization thus revealed. Whistlers have provided considerable information on the exospheric electron density, but an understanding of its origin requires a knowledge of the positive ions and their distribution. Some authors (for example, Chapman 1957) have suggested that solar protons, injected into the earth's magnetic field, provide the bulk of the positive ions. Others (for example, Johnson 1960) consider the exosphere to be populated by hydrogen which has diffused from the lower ionosphere, has been ionized by charge exchange or some other process, and has been trapped in the earth's magnetic field. These conflicting ideas only emphasize the need of measurements of the positive-ion constituents of the exosphere.

Storey (1956) has shown that the relationship between the instantaneous frequency f of a whistler, and the time t taken by this frequency to travel from source to observer, should provide information about the presence of hydrogen ions along the whistler path. This relationship may be conveniently studied by determining the variation of the whistler 'dispersion', which will be defined here as $tf^{\frac{1}{2}}$, with frequency. To a first approximation the dispersion is constant although at frequencies approaching the electron gyro-frequency it increases and gives rise to the well-known 'nose' effect in whistlers. There is a similar but smaller increase in dispersion for frequencies near the gyro-frequency of any abundant positive ion of the medium, and it is this variation which is of particular interest in the present paper. Of all the positive ions likely to be present in appreciable quantities in the exosphere, only hydrogen

¹Manuscript received July 15, 1960.

Contribution from the Radio Physics Laboratory, Defence Research Telecommunications Establishment, Defence Research Board, Ottawa, Canada.

has a gyro-frequency of sufficient magnitude to produce a measurable effect on whistler dispersion, in the frequency range of observation. Thus whistler dispersion is a potential source of information about the protons of the high ionosphere.

In the work reported here, the dispersion of four selected whistlers observed in Japan was measured. The analysis was carried out with high accuracy since the maximum effect due to the hydrogen ions was 2 or 3% of the total dispersion at most. The method by which this was achieved is outlined in Section 2 and the results are presented in Section 3. A model exosphere is employed in Section 4 to derive dispersion curves, which are then compared with the observed results for the two best whistlers. In the final section the implications of this analysis in terms of the hydrogen ion component of the exosphere are discussed.

2. METHOD OF DISPERSION MEASUREMENT

Whistlers from Wakkanai, geomagnetic latitude 35.3° N., and Toyokawa, geomagnetic latitude 24.5° N., were chosen for analysis primarily because the protons of the exosphere are expected to account for a greater percentage of the dispersion at these stations than at higher latitudes. It has also been found that the whistlers recorded at these stations have a greater purity of tone than those observed at higher latitudes. Since the analysis is slow and tedious, only a few of the best samples were used. The examples chosen were well defined over a frequency range greater than 5 kc/s and extended down to at least 1 kc/s.

A preliminary study of the whistler recordings was made with a sonograph. This provided the approximate rate of change of frequency in various parts of the whistler spectrum. It also gave an indication of those individual whistlers which offered some possibility for the identification of their initiating spheric. In a similar investigation Iwai and Otsu (1959) used a sonograph to measure the relative arrival times of the frequency components of the whistler. This complicates the analysis. The filtering technique used in the sonograph is such that its response to a gliding tone is asymmetric in time, reaching its maximum somewhat after resonance. This time delay is a function of filter bandwidth and rate of change of frequency in the gliding tone. The net result is to introduce an error into the measurement of the whistler dispersion which has the same variation with frequency as the hydrogen ion effect.

Storey and Grierson (1958) analyzed the response of various filters to a gliding tone, and developed a filtering technique which gives a response symmetrical in time and centered on the instant of resonance. This obviates the need for any correction to the time of maximum filter response, and was used here in all cases to measure the relative time delays of the frequency components of the whistler. The method utilizes a parallel tuned narrow-band filter and time-reversal tape recording. The filter output is rectified and time marker pulses are added to it at intervals of 10 msec by a combined adding and switching circuit (Grierson 1958) which suppresses the filter output during the marker pulses. When displayed on an oscilloscope, displacement of the

trace in one direction from a fixed base line shows the envelope of the filter response, and displacement in the opposite direction, the timing marks. The waveform appearing on the oscilloscope was recorded on moving 35-mm film. Figure 1 shows a sample of the results obtained in this manner.

The maximum of the filter response can usually be determined with an accuracy of about ± 1 millisecond. The resonant frequency of the filter was measured with a signal generator and counter, and is accurate to ± 1 cycle/sec. The bandwidth of the filter was set for optimum signal-to-noise by the criterion

$$4\pi W^2 = |df/dt|$$

where W = bandwidth of filter between 3-db points,
and df/dt = rate of change of frequency in the gliding tone.

To convert the relative time delays of the whistler frequency components to dispersion, the time of the initiating spheric must be known. To determine this, the whistler and a few seconds of the record preceding it was played through a 10 kc/s bandwidth filter, and displayed as before. This procedure makes the spherics stand out above the noise as sharp spikes. The approximate time of the initiating spheric was determined by extrapolating linearly from the mid-frequencies of a plot of relative time delays against f^{-1} . Allowance was made for the time delay introduced by the propagation of the spheric to the observer on the assumption that the spheric occurred at the conjugate point. In three of the four cases studied here there was only one spheric within 10 msec of the approximate time origin determined in this manner. This spheric was taken to be the initiating spheric and all times were measured from it in calculating the dispersion. The error involved in measuring the time of this spheric is less than 1 msec. In the case of the fourth whistler there were three spherics fairly close to the approximate time origin. Hence in computing the dispersion the approximate time was used, and the resulting dispersion probably has a time error.

3. EXPERIMENTAL RESULTS

Figures 2-5 show the dispersion of the four whistlers (denoted by numerals 1-4 respectively) which were analyzed, as a function of frequency. Comparison of the event observed at Toyokawa, for which the time origin is not accurately known, with the other three examples seems to indicate that the ion effect is about the same size at both stations. This may be due to a small time error associated with the Toyokawa results. The important feature of these curves is their similarity for whistlers observed in different seasons, and at different times of day. This indicates that the observed variation of dispersion with frequency is due to some constant properties of the path. It has been established that the electronic constituent of the exosphere can only cause the dispersion to increase with increasing frequency. Thus it seems likely that the increase of dispersion at low frequencies which is observed in all cases studied, and is of the form predicted by Storey from considerations of the effects of protons on the propagation of whistlers, is indeed a hydrogen ion effect.

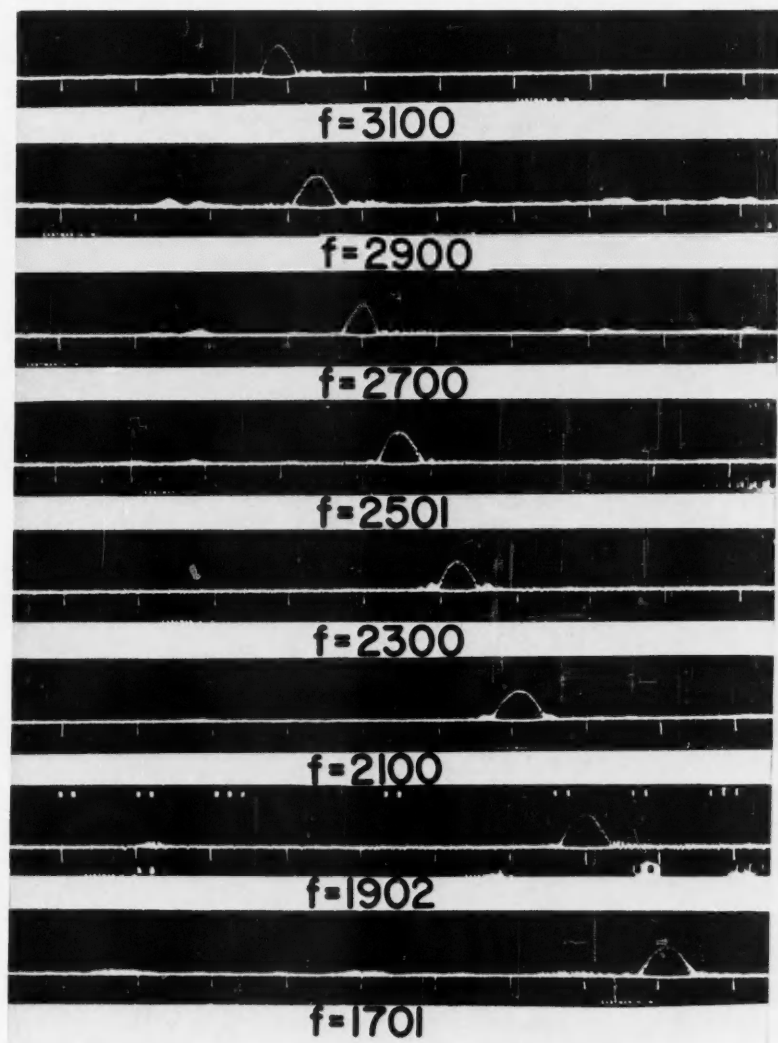
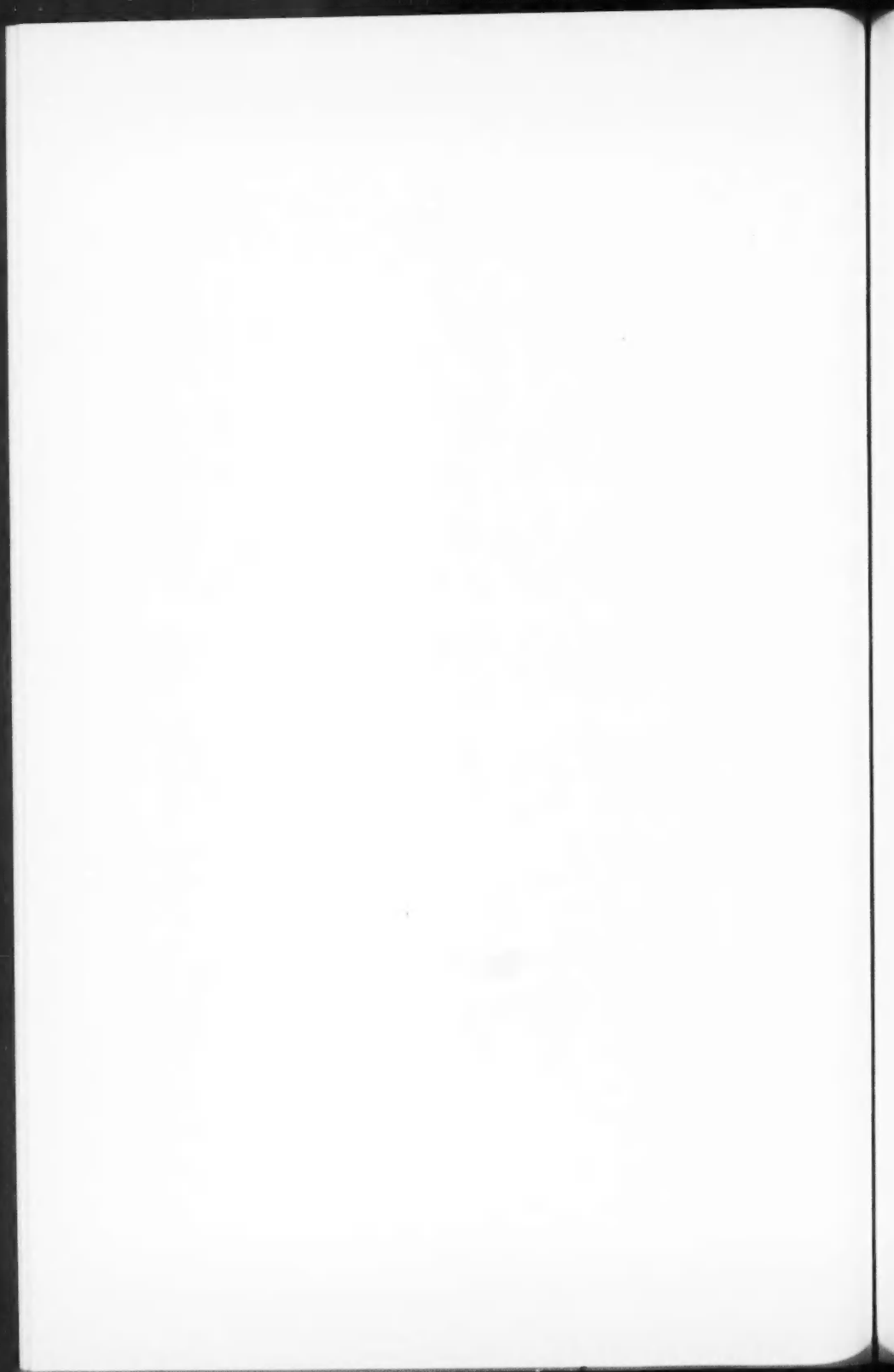


FIG. 1. Filter response to a whistler at various frequencies as a function of time. The large time markers are at 50-msec intervals.



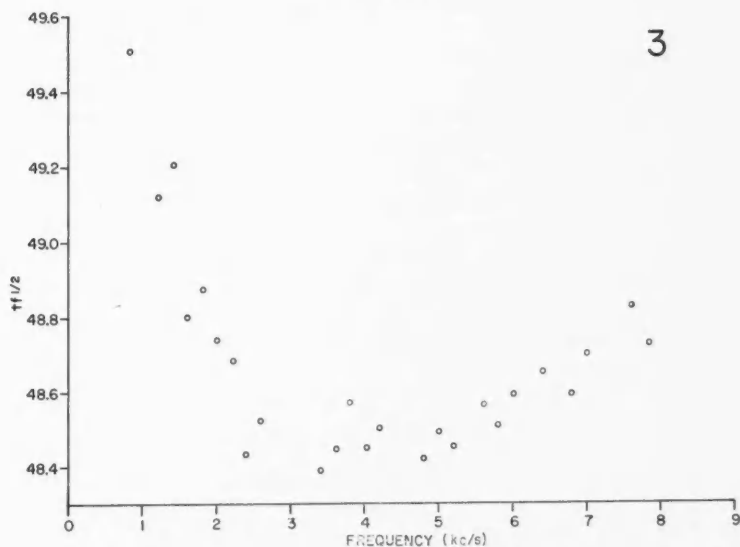
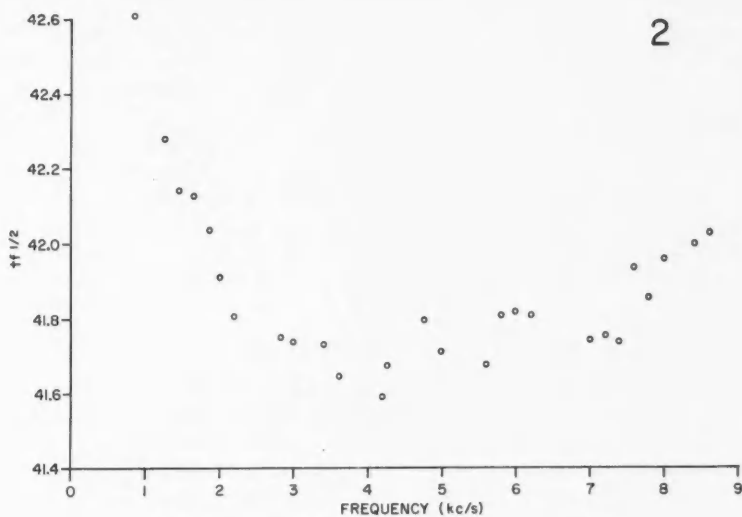


FIG. 2. Dispersion of whistler No. 1 observed at Wakkanai, geomagnetic latitude 35.3, March 9, 1958, 2-5 hr JST.

FIG. 3. Dispersion of whistler No. 2 observed at Wakkanai, geomagnetic latitude 35.3, Dec. 24, 1957, 1600 JST.

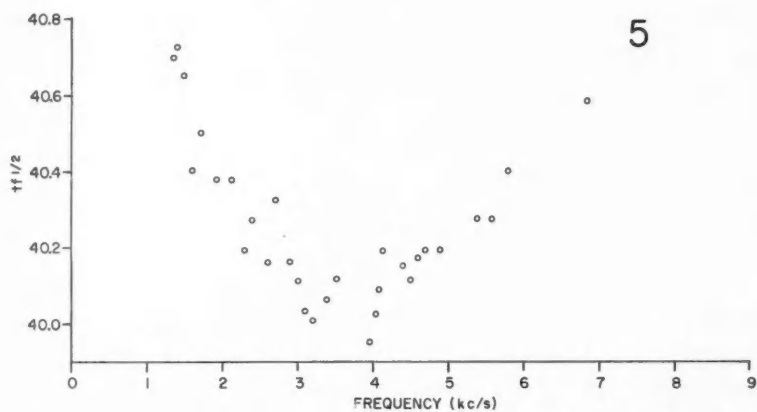
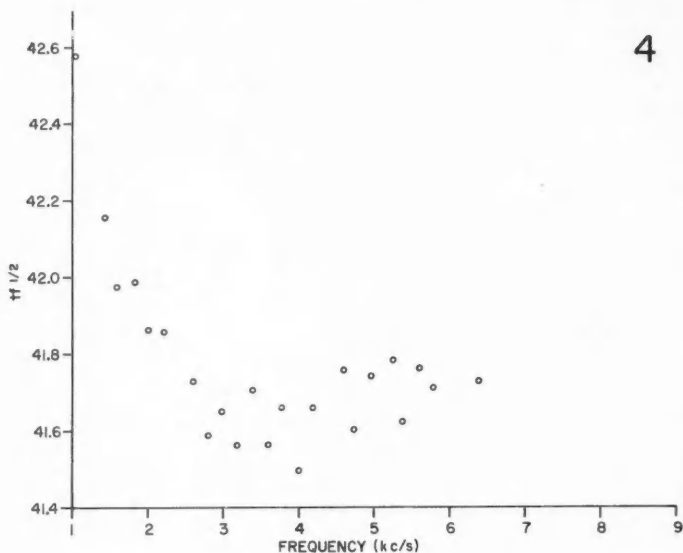


FIG. 4. Dispersion of whistler No. 3 observed at Wakkanai, geomagnetic latitude 35.3, March 9, 1958, 2-5 hr JST.

FIG. 5. Dispersion of whistler No. 4 observed at Toyokawa, geomagnetic latitude 24.5, Feb. 23, 1956, 1700 JST.

The scatter of the experimental points appears to be due largely to a residual multipath effect, rather than to errors introduced by the method of analysis. In some cases the scatter represents errors in time measurements of 5 msec. This is much greater than the error involved in estimating the time of maximum of the filter response. It was also noticed that occasionally the filter response was asymmetric or had a two-humped shape. This is suggestive of interference effects due to signals which have propagated by slightly different paths. Further support for such a conclusion comes from the fact that sometimes several of the experimental points show a systematic trend of a finer scale than the over-all frequency dependence of the dispersion. Such a multipath effect is not unexpected, since for whistlers observed at higher geomagnetic latitudes the errors introduced by this effect are so large that they mask the ion effect entirely.

4. COMPARISON OF EXPERIMENTAL AND CALCULATED DISPERSIONS

It is possible that ducts or inhomogeneities of the medium might have effects on whistler dispersion similar to those predicted for protons. In order to provide additional support for the view that the observed effects are due to protons, and also to provide some indication of the proton distribution and abundance, a plausible model of the exosphere was used to calculate the variation of dispersion with frequency. Such curves are not found to be critically dependent on the electron-density model chosen, and do fit the observed dispersion curves surprisingly well.

In making such a test, several plausible assumptions which cannot be entirely justified are necessary. It is assumed that the whistler propagated along the line of force on which it was observed. The gyro-frequencies along this path are considered to be adequately described by the centered-dipole approximation. The longitudinal refractive index is used to calculate the dispersion. This is a good approximation if propagation is by a magneto-ionic duct as suggested by Helliwell (1960). The purity of tone of the whistlers studied here supports the idea of propagation by such a duct.

The dispersion of a whistler when the motion of the positive ions is taken into account can be approximated by combining the asymptotic expressions given by Storey (1956) to form the equation

$$(1) \quad tf^{1/2} \simeq \frac{1}{2c} \int_{\text{path}} \frac{f_0}{f_H^{1/2}} \left\{ \frac{1}{(1-f/f_H)^{3/2}} + \frac{1+2f_{IH}/f}{[1+f_{IH}/f]^{3/2}} - 1 \right\} ds$$

where f_0 = plasma frequency,

f_H = electron gyro-frequency,

f_{IH} = proton gyro-frequency,

f = wave frequency.

This applies only for a medium in which the numbers of protons and electrons are equal. If the medium contains more than one type of positive ion, of which

only the protons have a gyro-frequency of sufficient magnitude to affect the observed dispersion, equation (1) must be replaced by,

$$(2) \quad tf^{1/2} \simeq \frac{1}{2c} \int_{\text{path}} \frac{f_0}{f_H^{1/2}} \left\{ \frac{1}{(1-f/f_H)^{3/2}} + \frac{1-\epsilon \left[\frac{f_{iH}}{f_{iH}+f} \right]^2}{\left[1-\epsilon \frac{f_{iH}}{f_{iH}+f} \right]^{1/2}} - 1 \right\} ds$$

where ϵ = ratio of number of protons to number of electrons.

The first term within the brackets of equation (2) is due to the electrons along the whistler path, and may be expanded as a binomial series in f/f_H . Since the whistlers examined in the present study originate in low geomagnetic latitudes, the ratio f/f_H was always much less than unity along the whole length of the path even for the highest frequencies observed. The terms in the power series above that in f/f_H are negligible and the dispersion due to the electrons may be written

$$(3) \quad D_{el} = \frac{1}{2c} \int_{\text{path}} \frac{f_0}{f_H^{1/2}} ds + \left[\frac{3}{4c} \int_{\text{path}} \frac{f_0}{f_H^{3/2}} ds \right] f \equiv D_0 + D_1 f$$

say. The first term here is independent of frequency and approximately equal to the mean whistler dispersion. The second term is small and shows that in the frequency interval of interest, the electrons of the medium cause the dispersion to increase linearly with frequency.

The frequency dependence of the other terms in equation (2), due to the protons on the path of propagation, is not as simply expressed as that due to the electrons. Over most of the whistler path, $\epsilon f_{iH}/(f_{iH} + f)$ is small compared with unity. Under these circumstances the contribution of the protons to the observed dispersion is given approximately by

$$(4) \quad \frac{1}{2c} \int_{\text{path}} \frac{\epsilon f_0}{f_H^{1/2}} \left\{ \frac{f_{iH}(f-f_{iH})}{2[f_{iH}+f]^2} \right\} ds.$$

The bracketed part of the integrand of this expression is plotted as a function of f_{iH}/f in Fig. 6. Since this curve passes through the origin and is a single-valued function of f_{iH}/f with a single broad maximum in the interval $0 < f_{iH}/f < .6$ it can be approximated in this range by a function of the form

$$(5) \quad D_{-2}f^{-2} + D_{-1}f^{-1}.$$

Thus the frequency dependence of the dispersion of a whistler may then be approximated by

$$(6) \quad tf^{1/2} \simeq D_{-2}f^{-2} + D_{-1}f^{-1} + D_0 + D_1 f.$$

In this expression D_0 and D_1 depend on the electron distribution along the path while D_{-2} and D_{-1} depend on the proton and electron distribution. The values of these constants for whistlers 1 and 2 were determined by a least-squares fit of the experimental points to a function of the form (6). In such a fit D_0 is determined with the greatest accuracy, while D_{-2} and D_{-1} have the greatest errors.

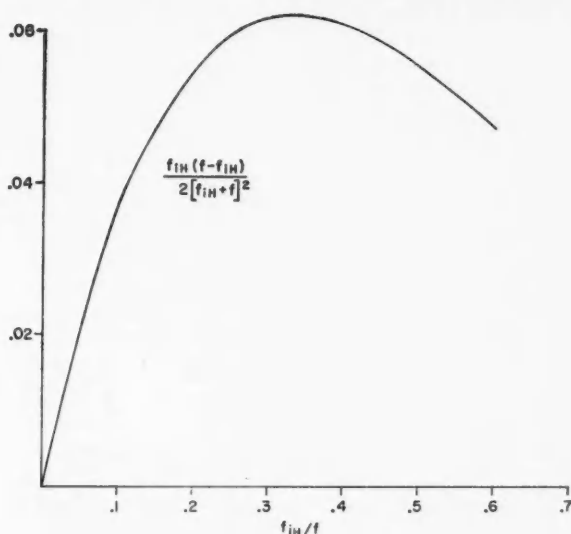


FIG. 6. Plot of $\frac{1}{2} f_{IH}(f - f_{IH}) / (f_{IH} + f)^2$ as a function of f_{IH}/f .

The ratio of D_0/D_1 has been shown by Storey (1957) to provide a limit to the range of latitudes over which the whistler might have entered the ionosphere, and also information about the electron distribution along the path. It was found to be much more sensitive to the path of propagation than to the electron distribution so it was not employed as a check on the latter. Instead, it was used to confirm the assumption that the whistlers studied here actually propagated along the line of force on which the observing station is situated. In the case of whistlers 1 and 2 the ratio D_0/D_1 was determined fairly accurately, and in both cases showed that the whistler emerged from the ionosphere within 2 or 3 degrees of the observing station.

The electron distribution was determined by using the value of D_0 to normalize models of the exosphere suggested by other workers. Johnson (1960), from theoretical considerations, has arrived at an electron density distribution given by

$$(7) \quad N(h) = N_0 \exp [g_0 R_0^2 m / (R_0 + h) K T] \exp [m \Omega^2 (R + h)^2 \cos^2 \theta / 2 K T]$$

where $N(h)$ = number density at altitude h ,

N_0 = normalization constant,

g_0 = acceleration of gravity at the earth's surface,

R_0 = radius of the earth,

m = half the ion mass,

Ω = the earth's rotational velocity,

θ = the latitude of the point under consideration.

At the Naval Research Laboratory a model ionosphere has been derived by a compilation of sounding, rocket, satellite, and whistler data. These two models were adjusted by the choice of an arbitrary factor to give the observed values of D_0 and are compared in Fig. 7. While the derived distributions differ somewhat, the discrepancies are not large compared with the errors of measure-

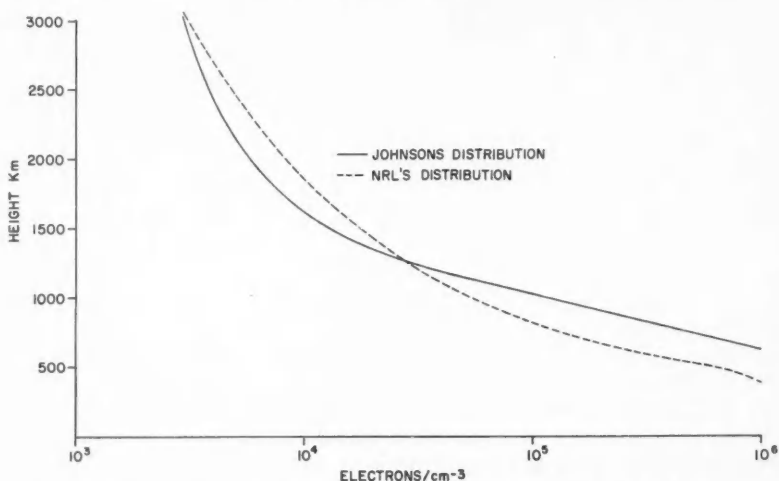


FIG. 7. Comparison of electron densities derived for Johnson's model and the Naval Research Laboratory model.

ment encountered elsewhere in this work. (The differences are somewhat larger at greater heights.) In subsequent calculations the Naval Research Laboratory's model is used, although Johnson's model of electron densities leads to essentially the same results.

D_{-2} and D_{-1} contain information about the number and distribution of protons along the whistler path, but they are not sufficient to determine the distribution. They also have errors of measurement associated with them, as well as inaccuracies due to the assumption that equation (2) can be approximated by equation (6). Rather than employ these quantities to determine something about the proton distribution, an idealized model of the exosphere was used. In the absence of any measurements of the proton distribution it was assumed that, from the top of the whistler path down to some transition level h_T , the number of protons and electrons is equal. Below this level the number of protons is assumed to be zero. On this basis the approximations of equations (2) and (3) can be avoided, and (1) applied with the aid of the electron-density distribution described previously to calculate dispersion curves for various heights of the transition level. The relationship

$$(8) \quad t f^{1/2} = \frac{1}{c} \int_0^{h_T} \frac{f_0}{f_H^{1/2}} ds + \frac{1}{c} \int_{h_T}^{h_m} \frac{f_0}{f_H^{1/2}} \left\{ \frac{1}{(1-f/f_H)^{1/2}} + \frac{1+2f_{\infty}/f}{[1+f_{\infty}/f]^{3/2}} - 1 \right\} ds$$

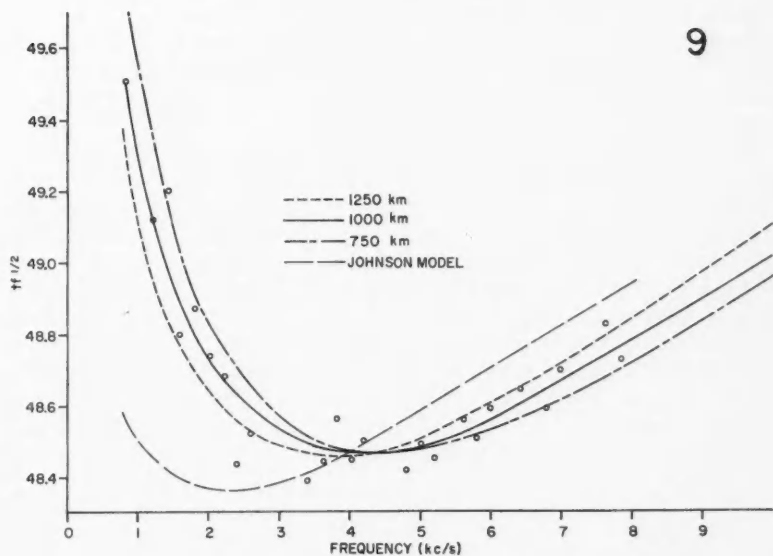
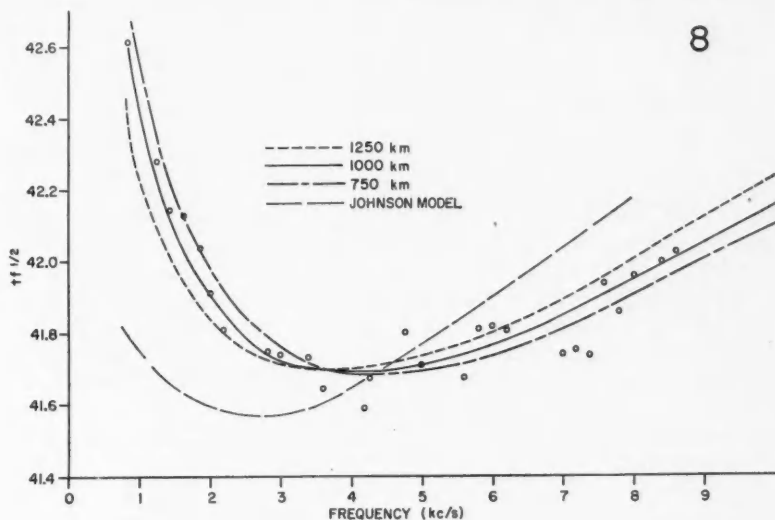


FIG. 8. Comparison of experimental points with calculated dispersion curves for whistler No. 1. Dispersion curves are shown for transition heights of 750, 1000, and 1250 km, and for Johnson's model of the exosphere.

FIG. 9. Comparison of experimental points with calculated dispersion curves for whistler No. 2. Dispersion curves are shown for transition heights of 750, 1000, and 1250 km, and for Johnson's model of the exosphere.

with h_m = greatest height of whistler path, was calculated for various values of h_T the assumed transition height and the experimental points were then fitted to the calculated curves as shown in Figs. 8 and 9 for whistlers 1 and 2. Also shown on these figures are dispersion curves calculated from Johnson's predicted proton and electron distributions.

5. DISCUSSION AND CONCLUSIONS

On comparing the experimental points with the curves calculated on the basis of the preceding assumptions, the agreement is found to be quite good, especially in the case of the curves calculated for a transition level of 1000 km. The fact that the analysis of two whistlers observed at different times and seasons leads to the same transition level for the protons, even though the values of D_0 and hence the electron densities of the exosphere are quite different at the times of observation, lends further support to the conclusion that the observed behavior of the dispersion at low frequencies is due to protons.

The proton distribution used in calculating the dispersion is at best a gross approximation to the actual distribution. It is useful in demonstrating that the ion effects observed under different conditions fit a single model for the proton distribution. Johnson's model of this distribution, which is derived from considerations of the escape and ionization of hydrogen diffusing from the lower atmosphere, does not fit the observations as well. While observations of the ion effect in whistler dispersion do not make it possible at present to derive a unique model of the exospheric ionization, they do provide an observational test for any model which is suggested by other considerations. Whistler dispersion does show that protons form a major constituent of the exosphere, down to heights of 1000 km or below.

More accurate information about the path of propagation and the electron densities of the ionosphere could be obtained if the dispersion were measured at higher frequencies (Storey 1957). This would increase the accuracy with which the dispersion due to the electrons of the medium could be separated from that due to the ions. Any further increase in accuracy of measurements of the ion dispersion requires a reduction in the multipath effects. Some progress in this direction might be made by more careful selection of the whistlers used in the analysis. Satellite observations of whistlers offer the possibility of a much greater reduction of this effect as well as better information on the path of propagation. Probably the largest uncertainty of this work is in the location of the initiating spheric. This could be overcome by timing and direction-finding equipment near the point conjugate to that at which a satellite observed a whistler.

ACKNOWLEDGMENTS

The authors wish to thank Dr. L. R. O. Storey for initiating this investigation, and for his advice during its course. The equipment was designed and built for this work by L. R. O. Storey and J. K. Grierson. Thanks also are due to A. Iwai of the Research Institute of Atmospheres of Nagoya University for providing the whistler recordings used in this study.

REFERENCES

- CHAPMAN, S. 1957. *Smithsonian Contrib. to Astrophysics*, **2**, 1.
GRIERSON, J. K. 1958. *Electronic Eng.* **30**, 506.
HELLIWELL, R. A. 1960. *Proceedings of the Symposium on Physical Processes in the Sun-earth Environment*, DRTE publication No. 1025, p. 165.
IWAI, A. and OUTSU, J. 1959. *Proceedings Research Inst. Atmospheric, Nagoya University* **6**, 44.
JOHNSON, F. S. 1960. *J. Geophys. Research*, **65**, 577.
STOREY, L. R. O. 1953. *Phil. Trans. Roy. Soc. A*, **246**, 113.
——— 1956. *Can. J. Phys.* **34**, 1154.
——— 1957. *Can. J. Phys.* **35**, 1107.
STOREY, L. R. O. and GRIERSON, J. K. 1958. *Electronic Eng.* **30**, 586, 648.

ELECTRON-HYDROGEN ATOM SCATTERING IN BORN APPROXIMATION¹

TA-YOU WU

ABSTRACT

The elastic (1s-1s) and the inelastic (1s-2s, 1s-2p) scattering cross sections in the Born approximation at energies of 1, 4, 9, 16 rydbergs have been calculated exactly from the closed formulas of the matrix elements for these transitions. Both the differential and the total cross sections are given here.

The theory of the scattering of an electron by a hydrogen atom in the Born approximation has been known since 1926, and with exchange, since 1928. The fact remains, however, that no *exact* calculations of this approximation for even such simple transitions as 1s-2s, 1s-2p have been carried out. The only calculation in the literature seems to be the early work of Massey and Mohr (1931), in which the "exchange" scattering amplitude is evaluated by means of some approximations (namely, the neglect of higher order terms in an infinite series and the replacement of Bessel functions in the integrals by its asymptotic forms). Some years ago, such matrix elements as those occurring in the Born approximation have been evaluated in this laboratory in closed analytic forms (Corinaldesi and Trainor 1952). The actual calculations have now been carried out and the results are presented below.

In atomic units (length in Bohr radius a_B , and energy in rydbergs), the scattering amplitudes $f(\theta)$, $g(\theta)$ for "direct" and "exchange" scattering are, for the transition $k, \phi_0 \rightarrow k_n', \phi_n$,

$$(1) \quad f(\theta) = \frac{1}{4\pi} \iint e^{-ik_n' \cdot r_1} \phi_n(r_2) \left[-\frac{2}{r_1} + \frac{2}{|r_1 - r_2|} \right] e^{ik \cdot r_1} \phi_0(r_2) dr_1 dr_2,$$

$$(2) \quad g(\theta) = \frac{1}{4\pi} \iint e^{-ik' \cdot r_2} \phi_n(r_1) \left[-\frac{2}{r_2} + \frac{2}{|r_1 - r_2|} \right] e^{ik \cdot r_1} \phi_0(r_2) dr_1 dr_2.$$

The total cross section is given by

$$(3) \quad \begin{aligned} \sigma &= 2\pi \frac{k_n'}{k} \int \left\{ \frac{1}{4} |f(\theta) + g(\theta)|^2 + \frac{3}{4} |f(\theta) - g(\theta)|^2 \right\} \sin \theta d\theta \\ &= 2\pi \frac{k_n'}{k} \int \left\{ f^2(\theta) + g^2(\theta) - g(\theta)f(\theta) \right\} \sin \theta d\theta. \end{aligned}$$

(A). 1s \rightarrow 1s (ELASTIC SCATTERING)

$$(4) \quad \begin{aligned} f(\theta) &= \frac{1}{2P^2} - \frac{1}{2P^2(1+P^2)^2}, \\ g(\theta) &= \frac{16}{(1+k^2)^3} - \frac{4}{(1+k^2)^3 P^2} \left[\frac{1}{(1+P^2)^2} \left\{ P^4 + \frac{1}{2} (3+k^4) P^2 - k^2 \right\} \right. \\ &\quad \left. + \frac{1}{P} (k^2 + P^2) \sin^{-1} \frac{P}{\sqrt{1+P^2}} \right], \end{aligned}$$

¹Manuscript received September 12, 1960.

Contribution from the Division of Pure Physics, National Research Council, Ottawa.
Issued as N.R.C. No. 5945.

where k^2 is the energy of the incident electron in units of rydbergs, and

$$P = k \sin (\theta/2).$$

From these expressions, one obtains, in the forward direction,

$$(5) \quad f(0) = 1, \quad g(0) = \frac{1}{(1+k^2)^3} \left[3 - \frac{10}{3} k^2 - k^4 \right].$$

(B). $1s \rightarrow 2s$ (INELASTIC SCATTERING)

Let

$$t^2 = 8k^2 - 3 - 4xk\sqrt{4k^2 - 3},$$

$$x = \cos \theta,$$

$$X = \sin^{-1} \left[\frac{t^2 + 3}{\sqrt{(t^2 + 1)(t^2 + 9)}} \right] + \sin^{-1} \left[\frac{t^2 - 3}{\sqrt{(t^2 + 1)(t^2 + 9)}} \right],$$

$$\kappa = 1 + 4k^2,$$

$$B_1 = \frac{64}{(t^2 + 9)^2}, \quad B_2 = -\frac{48}{t^2(t^2 + 9)} + \frac{8}{t^3} X,$$

$$B_3 = \frac{6(t^2 + 3)}{t^4} + \frac{(t^4 - 10t^2 - 27)}{t^5} X,$$

$$C_1 = \frac{512}{3} \cdot \frac{t^2 + 27}{(t^2 + 9)^3}, \quad C_2 = \frac{128}{(t^2 + 9)^2},$$

$$C_3 = -\frac{8}{t^4} \cdot \frac{t^2 - 27}{t^2 + 9} + \frac{4}{t^5} (t^2 - 9) X,$$

$$C_4 = \frac{1}{3t^6} (9t^4 - 58t^2 - 135) + \frac{1}{2t^7} (t^6 - 7t^4 + 63t^2 + 135) X,$$

then

$$(6) \quad \begin{aligned} f(\theta) &= -512\sqrt{2} \frac{1}{(t^2 + 9)^3}, \\ g(\theta) &= \frac{256\sqrt{2}(4k^2 - 1)}{\kappa^4} - \frac{4\sqrt{2}}{\kappa^3} [3\kappa^2 B_1 + 16\kappa B_2 + 32B_3] \\ &\quad + \frac{3}{\sqrt{2}\kappa^4} [\kappa^3 C_1 + 8\kappa^2 C_2 + 128\kappa C_3 + 256C_4]. \end{aligned}$$

(C). $1s \rightarrow 2p$, $\Delta m = 0$ (INELASTIC SCATTERING)

Let

$$D_1 = \frac{1024}{5} \frac{1}{(t^2 + 9)^3},$$

$$D_2 = -\frac{64}{t^4(t^2 + 9)^2} (5t^2 + 27) + \frac{32}{t^5} X,$$

$$D_3 = \frac{6}{t^6(t^2 + 9)} (t^4 + 40t^2 + 135) + \frac{1}{t^7} (t^4 - 30t^2 - 135) X,$$

then

$$(7) \quad \begin{aligned} f(\theta) &= -\frac{1536\sqrt{2}}{t^2(t^2+9)^3} [2k-x\sqrt{4k^2-1}], \\ g(\theta) &= \frac{1024}{\kappa^4} \frac{\sqrt{2}}{k} - \frac{8\sqrt{2}k}{\kappa^4} [\kappa^2 C_2 + 32\kappa C_3 + 96C_4] \\ &\quad - \frac{2k-x\sqrt{4k^2-3}}{\sqrt{2}\kappa^3} [15\kappa^2 D_1 + 48\kappa D_2 + 128D_3]. \end{aligned}$$

(D). $1s \rightarrow 2p$ ($\Delta m = \pm 1$) (INELASTIC SCATTERING)

$$(8) \quad \begin{aligned} f(\theta) &= 1536\sqrt{(1-x^2)} \frac{1}{t^2(t^2+9)^3} \sqrt{(4k^2-3)} e^{im\phi}, \\ g(\theta) &= 0. \end{aligned}$$

The differential cross sections $f^2 + g^2 - fg$ for the $1s-1s$, $1s-2s$, $1s-2p$ ($\Delta m = 0$), $1s-2p$ ($\Delta m = \pm 1$) transitions at energies 1, 4, 9, 16 rydb ergs (13.6, 54.4, 122.4, 217.6 ev respectively) are shown in logarithmic scale in Figs. 1-4. (The ordinates in Figs. 1-4 give the differential cross section $f^2 + g^2 - fg$ as defined in eqs. (1)-(3) in the text, in a_B^2 . $k = 1, 2, 3, 4$ correspond to incident electron energy of 1, 4, 9, 16 rydb ergs respectively.) The total cross sections are given below.

Energy in rydb ergs	1s-1s	1s-2s	1s-2p $\Delta m = 0$	1s-2p $\Delta m = \pm 1$
1	2.104	1.486	1.351	0.0748
4	0.574	0.0862	0.3981	0.2549
9	0.256	0.0406	0.2039	0.1945
16	0.144	0.0236	0.1197	0.1437

Total cross sections in units of πa_B^2 .

There are very meager data with which these *exact* Born approximation results can be compared. The total cross sections of elastic scattering at $k^2 = 1, 4$ can be compared with the variational calculations of Massey and Moiseiwitsch (1951). Those for the inelastic scatterings $1s-2s$, $1s-2p$ can be compared with the approximate values obtained by Massey and Mohr (1931). The comparison is shown below.

	k^2 energy in rydb ergs	Born approx'n here calc.	Born approx'n Massey-Mohr (from their Fig. 4)	Variational Massey- Moiseiwitsch
1s-1s	1	6.60		10.5
	4	1.80		1.55
1s-2s	1	4.65	~ 5.3	
	3.5		~ 2.1	
	4	0.27		
1s-2p	1	4.71*	~ 6.2	
	3.5		~ 2.8	
	4	2.83*		

Total cross sections in a_B^2 . The values * are the sums of the cross sections for $\Delta m = 0, \pm 1$.

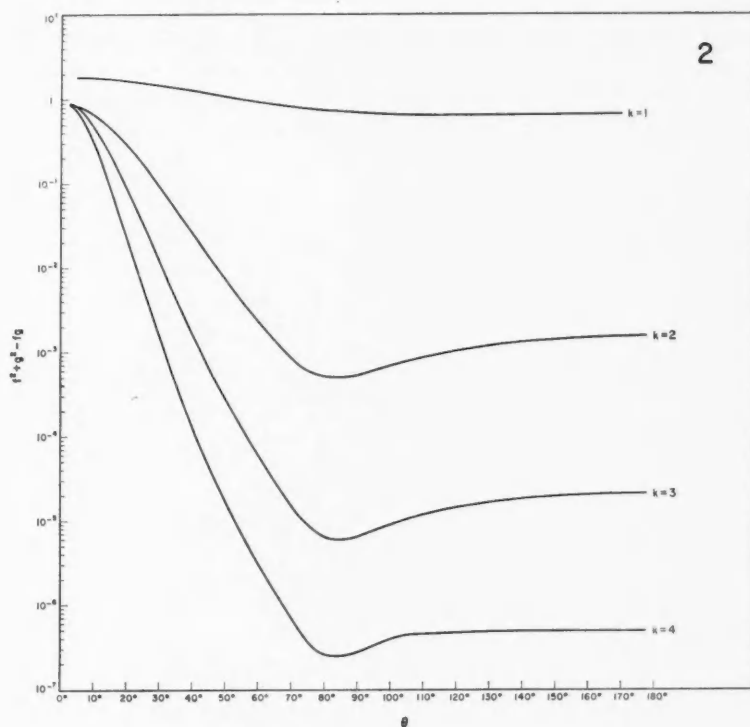
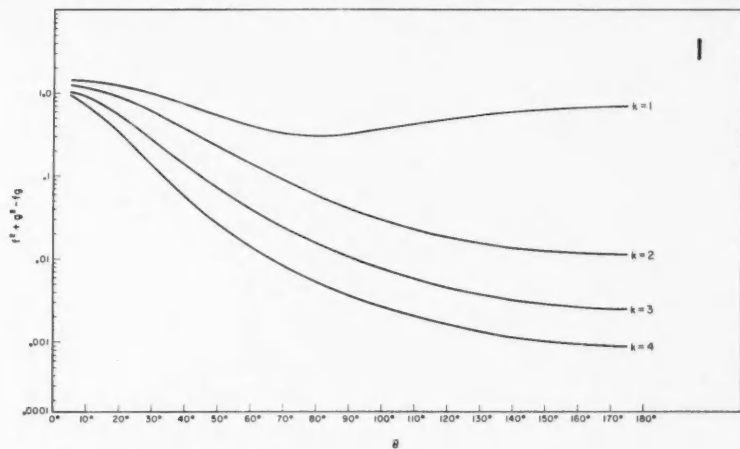
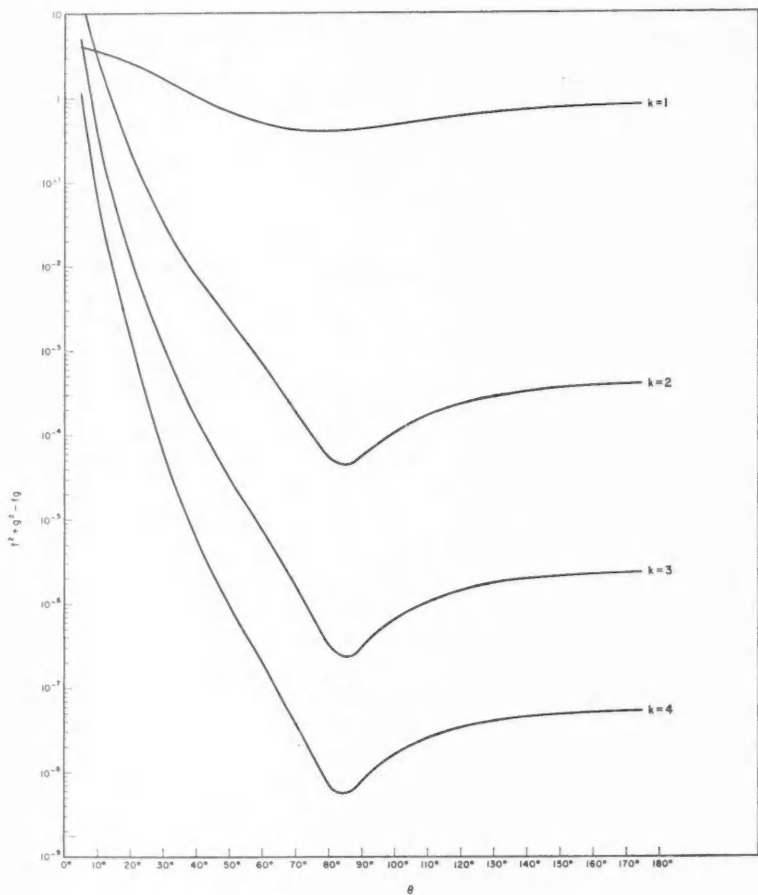
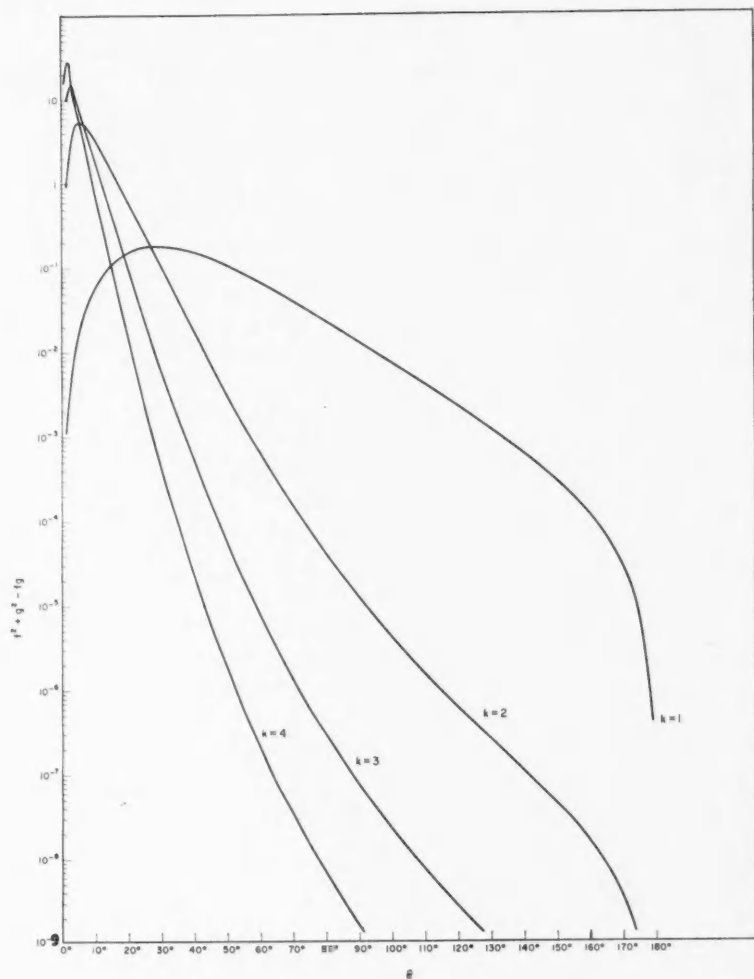


FIG. 1. Elastic scattering $1s \rightarrow 1s$.
FIG. 2. Inelastic scattering $1s \rightarrow 2s$.

FIG. 3. Inelastic scattering $1s \rightarrow 2p$, $m = 0$.

FIG. 4. Inelastic scattering $1s \rightarrow 2p, m = \pm 1$.

It is seen that at 13 ev, the Born approximation for $1s-1s$ is not satisfactory, as expected, but at 54 ev, it is in quite satisfactory agreement with the variational calculations of Massey and Moiseiwitsch, which is the "best" theoretical result available at present.

The writer appreciates the help of Mrs. M. Helfenstein in the computations involved.

REFERENCES

- CORINALDESI, E. and TRAINOR, L. 1952. *Nuovo Cimento*, **9**, 940.
MASSEY, H. S. W. and MOHR, C. B. O. 1931. *Proc. Roy. Soc. London, A*, **132**, 605.
MASSEY, H. S. W. and MOISEWITSCH, B. L. 1951. *Proc. Roy. Soc. London, A*, **205**, 483.

A SOLUTION OF THE EINSTEIN FIELD EQUATIONS¹

PETER RASTALL

ABSTRACT

An exact, cylindrically symmetric, time-dependent solution of the Einstein gravitational field equations for empty space is derived. A particular case of the solution has singularities only on the axis of symmetry and may represent a number of particles in an otherwise empty universe.

INTRODUCTION

Static, cylindrically symmetric solutions of the Einstein gravitational field equations for empty space were considered by Weyl (1917) and Levi-Civita (1919). They showed that no such solutions exist which are pseudo-Euclidean at infinity and which have more than one singularity on the axis of symmetry. This must be so if the singularities are interpreted as the positions of particles and the field equations are to imply the proper equations of motion. Later work on cylindrically symmetric solutions is summarized by Marder (1958, 1959).

We shall look for a class of solutions which are cylindrically symmetric but not static. We assume a line element of the form

$$(1) \quad ds^2 = h(x^0) \{ \mu(x^1, x^2) (dx^1{}^2 + dx^2{}^2) + \nu(x^1, x^2) dx^3{}^2 \} + \lambda(x^1, x^2) dx^0{}^2,$$

where h is not a constant.

SOLUTION OF THE FIELD EQUATIONS

When the metric tensor is diagonal, $g_{\pi\rho} = 0$ for $\pi \neq \rho$, the most convenient form for the contracted curvature tensor $R_{\pi\rho}$ is

$$(2) \quad R_{\pi\pi} = (1/4) \sum_{\tau \neq \pi} \left\{ 2(g_{\tau\tau,\pi}/g_{\tau\tau})_{,\pi} + 2(g_{\pi\pi,\tau}/g_{\tau\tau})_{,\tau} \right. \\ \left. - (g_{\pi\pi,\pi}/g_{\pi\pi})(g_{\tau\tau,\pi}/g_{\tau\tau}) + (g_{\tau\tau,\pi}^2/g_{\tau\tau}^2) \right. \\ \left. - (g_{\pi\pi,\tau}^2/g_{\tau\tau}g_{\pi\pi}) + \sum_{\sigma \neq \pi} (g_{\pi\pi,\tau}/g_{\tau\tau})(g_{\sigma\sigma,\tau}/g_{\sigma\sigma}) \right\},$$

$$(3) \quad R_{\pi\rho} = (1/4) \sum_{\tau \neq \pi, \rho} \left\{ 2(g_{\tau\tau,\pi}/g_{\tau\tau})_{,\rho} - (g_{\pi\pi,\rho}/g_{\pi\pi})(g_{\tau\tau,\pi}/g_{\tau\tau}) \right. \\ \left. - (g_{\rho\rho,\pi}/g_{\rho\rho})(g_{\tau\tau,\rho}/g_{\tau\tau}) + (g_{\tau\tau,\pi}/g_{\tau\tau})(g_{\tau\tau,\rho}/g_{\tau\tau}) \right\}.$$

In these two equations the summation convention has been suspended and $\pi \neq \rho$.

¹Manuscript received June 10, 1960.

Contribution from the Department of Physics, University of British Columbia, Vancouver 8, B.C.

Substitute the metric tensor of (1) into (3). The field equations $R_{10} = 0$ and $R_{20} = 0$ imply

$$\lambda_1 h_0 / \lambda h = 0, \quad \lambda_2 h_0 / \lambda h = 0,$$

where to save writing commas we put $h_0 \equiv dh/dx^0$, $\lambda_1 \equiv \partial\lambda/\partial x^1$, etc. Since $h_0 \neq 0$, except perhaps at certain instants, it follows that λ is a constant, and we may take $\lambda = -1$.

One can separate variables in the remaining equations $R_{\tau\rho} = 0$ and find for h the two equations

$$2hh_{00} - h^2 = 0, \quad 2hh_{00} + h^2 = 2Ah.$$

A is a separation constant. The solution, provided that the origin of time be suitably chosen, is

$$(4) \quad h = (A/4)x^{0^2}.$$

The assumption that h is not constant implies $A \neq 0$.

μ and ν must satisfy the four equations

$$(5) \quad 2(\mu_{11} + \mu_{22})/\mu - 2(\mu_1^2 + \mu_2^2)/\mu^2 = \mu A,$$

$$(6) \quad (\nu_{11} - \nu_{22})/\nu - (\nu_1^2 - \nu_2^2)/2\nu^2 - (\mu_1\nu_1 - \mu_2\nu_2)/\mu\nu = 0,$$

$$(7) \quad 2\nu_{12}/\nu - (\mu_1\nu_2 + \mu_2\nu_1)/\mu\nu - \nu_1\nu_2/\nu^2 = 0,$$

$$(8) \quad (\nu_{11} + \nu_{22})/\nu - (\nu_1^2 + \nu_2^2)/2\nu^2 = \mu A.$$

Equation (5) involves only μ and is of a type which has been discussed by the mathematicians. It is best to introduce new dependent variables u and v by

$$\mu = 1/v^2, \quad \nu = u^2/v^2,$$

and new independent variables ξ and η by

$$\xi = (x^1 - ix^2)/2, \quad \eta = (x^1 + ix^2)/2.$$

The set of equations (5), (6), (7), (8), is then equivalent to

$$(9) \quad -v v_{\eta\xi} + v_{\eta} v_{\xi} = A/4,$$

$$(10) \quad u_{\eta\eta}/u = v_{\eta\eta}/v,$$

$$(11) \quad u_{\xi\xi}/u = v_{\xi\xi}/v,$$

$$(12) \quad v u_{\eta\xi} + u v_{\eta\xi} - u_{\xi} v_{\eta} - u_{\eta} v_{\xi} = 0.$$

The solution of (9) is

$$(13) \quad v = K_{\eta}^{-1}(\eta) L_{\xi}^{-1}(\xi) \{ k K(\eta) L(\xi) + l + m K(\eta) + n L(\xi) \},$$

where K and L are arbitrary analytic functions, and k, l, m, n are constants satisfying

$$(14) \quad mn - kl = A/4.$$

The constant $A/4$ which appears in ds^2 through the h of equation (4) may be absorbed into the arbitrary function v . One then finds, without any loss of generality,

$$(4)' \quad h = x^{0^2},$$

$$(14)' \quad mn - kl = 1.$$

Equations (10) and (11) are satisfied by a u of the same form as v ,

$$(15) \quad u = K_{\eta}^{-\frac{1}{2}}(\eta)L_{\xi}^{-\frac{1}{2}}(\xi)\{pK(\eta)L(\xi) + q + rK(\eta) + sL(\xi)\}.$$

The K and L are the same as in (13). The constants p, q, r, s are not restricted by a relation like (14), but (12) is satisfied if and only if one has

$$(16) \quad ms + nr = kq + lp.$$

If the line element is to be real and to have the correct signature, u^2 and v^2 must both be real and positive. Thus u and v must be real, and we take

$$K(\eta) = L^*(\xi), \quad m = n^*, \quad r = s^*,$$

and assume k, l, p, q to be real.

Provided that $k \neq 0$, one can write μ and ν in simpler forms. Define a new function H by

$$(17) \quad H = k(K + n/k).$$

Then substituting in (13) and (15),

$$(18) \quad \mu = 1/v^2 = H_{\eta}H_{\xi}^*/[HH^* - 1]^2,$$

$$(19) \quad \nu = u^2/v^2 = [P(HH^* + 1) + QH + Q^*H^*]^2/[HH^* - 1]^2.$$

P is an arbitrary real and Q an arbitrary complex constant. Restrictive conditions like (14) and (16) are no longer necessary. The solution (18) is given by Forsyth (1906, Art. 225).

A PARTICULAR SOLUTION

Now interpret x^1 as the radial co-ordinate, x^2 as the z co-ordinate, and x^3 as the angular co-ordinate of a system of cylindrical polar co-ordinates. Choose the H in (18) and (19) to be

$$(20) \quad H = \sum_{j=1}^N a_j/(2\eta - ib_j),$$

where a_j and b_j are real constants, and take $P = 0, Q = 1$. The resulting μ and ν are singular only at the points $x^1 = 0, x^2 = b_j$, and on the surfaces where $HH^* = 1$ which surround each of these points. One should compare this with the spherically symmetric Schwarzschild solution, where, too, a point singularity is surrounded by a singular surface.

CONCLUSION

It is possible that the solution given in the last section describes a set of N particles alone in an otherwise empty universe. It satisfies the correct

boundary condition: at great distances from the particles both μ and ν tend to zero, which is what one expects if Mach's principle is valid. However, it is arguable that Mach's principle would imply that displacements in the x^3 direction should make no sense ($\nu \equiv 0$). This is a difficult point which will perhaps be discussed in a later paper.

The distances between the singularities of the solution increase or decrease linearly with time. If we do interpret the singularities as representing particles, then in Newtonian language we must say that they exert no forces on one another. The usual gravitational attraction depends on the existence of matter off the line joining the attracting particles.

REFERENCES

- FORSYTH, A. R. 1906. *Theory of differential equations*, Part IV (Cambridge).
LEVI-CIVITA, T. 1919. *Atti accad. naz. Lincei*, **28**, 3.
MARDER, L. 1958. *Proc. Roy. Soc. A*, **244**, 524.
——— 1959. *Proc. Cambridge Phil. Soc.* **55**, 82.
WEYL, H. 1917. *Ann. Phys. (Leipzig)*, **54**, 117.

BACKSCATTERING FROM A CONDUCTING CYLINDER WITH A SURROUNDING SHELL¹

M. A. PLONUS

ABSTRACT

Far-field backscattering from a perfectly conducting cylinder with a surrounding shell has been investigated. The spacing of the shell from the cylinder and thickness of the shell are arbitrary. The material in the shell is also arbitrary and is characterized by the propagation constant h . The incident plane wave is at right angles to the cylinder, and is either horizontally or perpendicularly polarized. When the shell is thin in units of wavelength a much simpler expression for the backscattered field coefficient is obtained. It was possible to express this coefficient in a form which resembles the coefficient from the conducting cylinder alone plus a perturbation term due to the shell. Another simplification resulted when the propagation constant h of the shell is much larger than the free-space propagation constant k .

It was desirable to see what scattering properties a cylinder with a surrounding shell exhibits. The cylinder was chosen to be large with respect to wavelength and the shell spaced a resonant distance from the cylinder. The scattering cross section, for this particular combination of parameters was then given by a slowly converging series which proved too lengthy for hand-computation, and was then programmed for and computed by the IBM 704. The scattering cross section versus shell spacing is shown in graphical form.

FORMULATION OF THE PROBLEM

The problem is a two-dimensional one, and can best be carried out in cylindrical co-ordinates. Figure 1 shows a cross section of the cylindrical structure.

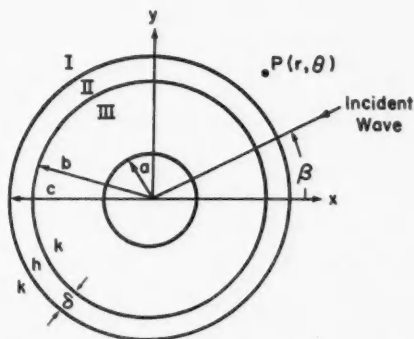


FIG. 1. Cross section of the cylindrical structure.

A cylindrical shell surrounds a perfectly conducting cylinder of radius a . The lossy shell which is assumed to be thin is spaced a distance $b-a$ from

¹Manuscript received August 26, 1960.

Contribution from the Radiation Laboratory, Department of Electrical Engineering, The University of Michigan, Ann Arbor, Michigan. This work was sponsored in part by Contract AF 19(604)-6655 with Electronics Research Directorate, Cambridge Research Laboratories, Air Force Research Division.

the conducting cylinder. Region I is free space with a propagation constant k , region II which is the shell has a propagation constant h , and region III has the same propagation constant as free space. The propagation constant h can have a loss component and arbitrary permittivity ϵ , however, μ in region I and region II are identical.

INCIDENT E VECTOR PARALLEL TO AXIS OF CYLINDER

The solution of this problem is carried out by matching the solutions of the various regions at the boundaries. When the time dependence is $e^{+i\omega t}$, the direction of incidence is normal to the axis, and the E vector of the incident field is parallel to the axis of the cylinder the solutions in the three regions are:

$$E_z^I = e^{ikr \cos(\beta-\theta)} + \sum_{n=-\infty}^{\infty} A_n H_n^{(2)}(kr) e^{in\theta},$$

$$E_z^{II} = \sum_{n=-\infty}^{\infty} (B_n H_n^{(2)}(hr) + C_n J_n(hr)) e^{in\theta},$$

$$E_z^{III} = \sum_{n=-\infty}^{\infty} (D_n H_n^{(2)}(kr) + E_n J_n(kr)) e^{in\theta}.$$

The incident field can now be expanded in terms of Bessel functions, thus

$$e^{ikr \cos(\beta-\theta)} = \sum_{n=-\infty}^{\infty} i^n J_n(kr) e^{in(\beta-\theta)}.$$

The angle of incidence β can be chosen as zero without loss of generality. At the boundaries of the various regions the electric and magnetic fields must be continuous and the electric field must vanish on the surface of the perfectly conducting cylinder. These boundary conditions will provide enough equations to solve for the unknown coefficients in the various regions. The two-dimensional scattering cross section is usually stated as

$$\sigma = \lim_{r \rightarrow \infty} 2\pi r \left| \frac{E^s}{E^I} \right|^2.$$

Thus the scattering cross section for this problem can be written as

$$\sigma = \frac{2\lambda}{\pi} \left| \sum_{n=-\infty}^{\infty} i^n A_n \right|^2.$$

The scattered far field will be known if the coefficient A_n is determined. The boundary condition at $r = a$ is

$$E_z^{III}(a, \theta) = 0.$$

Continuity of fields at $r = b$ yields

$$E_z^{III}(b, \theta) = E_z^{II}(b, \theta)$$

$$H_\theta^{III}(b, \theta) = H_\theta^{II}(b, \theta) \quad \text{or} \quad \frac{\partial E_z^{III}(b, \theta)}{\partial r} = \frac{\partial E_z^{II}(b, \theta)}{\partial r}.$$

Continuity of fields at $r = c$ yields

$$E_z^I(c, \theta) = E_z^{II}(c, \theta)$$

$$H_\theta^I(c, \theta) = H_\theta^{II}(c, \theta) \quad \text{or} \quad \frac{\partial E_z^I(c, \theta)}{\partial r} = \frac{\partial E_z^{II}(c, \theta)}{\partial r}.$$

This gives five equations in five unknowns. After considerable manipulations these can be solved for the coefficient A_n . The above shorthand notations should be interpreted as

$$\frac{\partial E(c, \theta)}{\partial r} \equiv \frac{\partial E(r, \theta)}{\partial r} \bigg|_{r=c}.$$

Further abbreviations that will be used are

$$J'(kr) \equiv \frac{\partial J_n(kr)}{\partial r}$$

$$H'(hc) \equiv \frac{\partial H_n^{(2)}(hr)}{\partial r} \bigg|_{r=c}$$

$$A_n \equiv A$$

i.e. all subscripts n will be left off. The resulting five simultaneous equations are thus:

$$DH(ka) + EJ(ka) = 0,$$

$$DH(kb) + EJ(kb) = BH(hb) + CJ(hb),$$

$$i^n J(kc) + AH(kc) = BH(hc) + CJ(hc),$$

$$DH'(kb) + EJ'(kb) = BH'(hb) + CH'(hb),$$

$$i^n J'(kc) + AH'(kc) = BH'(hc) + CJ'(hc).$$

When these are solved for A we get the following result

$$(1) \quad A = -i^n \frac{J(kc)J'(hc) - J'(kc)J(hc) + \xi[H(hc)J'(kc) - H'(hc)J(kc)]}{H(kc)J'(hc) - H'(kc)J(hc) + \xi[H(hc)H'(kc) - H'(hc)H(kc)]}$$

where ξ is

$$(2) \quad \xi = \frac{J(ka)[J'(hb)H(kb) - J(hb)H'(kb)] + H(ka)[J(hb)J'(kb) - J'(hb)J(kb)]}{J(ka)[H(kb)H'(hb) - H(hb)H'(kb)] + H(ka)[H(hb)J'(kb) - H(hb)J(kb)]}.$$

Since the lossy shell was assumed to be thin, i.e.

$$h\delta = h(c-b) < 1$$

we can expand all functions with argument c about b . Thus to a first approximation we can write

$$(3) \quad J(hc) = J(hb) - h(b-c) \frac{\partial J(hb)}{\partial hb} = J(hb) + \delta J'(hb)$$

$$H'(kc) = H'(kb) + \delta H''(kb).$$

These are then substituted in the expressions for A and ξ . The complicated expressions which result can be simplified when the various terms are identified with the Wronskian and the derivative of the Wronskian, i.e.

$$J(kx)H'(kx) - J'(kx)H(kx) = \frac{-2i}{\pi x},$$

$$J(kx)H''(kx) - J''(kx)H(kx) = \frac{2i}{\pi x^2},$$

$$J'(kx)H''(kx) - J''(kx)H'(kx) = -\left(k^2 - \frac{n^2}{x^2}\right) \frac{2i}{\pi x}.$$

The last expression can be derived from Bessel's equation

$$x^2 J''(kx) + x J'(kx) + [(kx)^2 - n^2] J(kx) = 0.$$

The final result for A is then

$$(4) \quad A = -i^n \frac{J(ka) + \delta \frac{\pi b}{2i} [(hj)J(ka) - (jj)H(ka)]}{H(ka) + \delta \frac{\pi b}{2i} [(hh)J(ka) - (jh)H(ka)]}$$

where

$$(hj) = H(kb)J''(kb) + J(kb)H'(kb) \frac{1}{b} + J(kb)H(kb) \left(h^2 - \frac{n^2}{b^2}\right),$$

$$(jj) = J(kb)J''(kb) + J(kb)J'(kb) \frac{1}{b} + J^2(kb) \left(h^2 - \frac{n^2}{b^2}\right),$$

$$(hh) = H(kb)H''(kb) + H(kb)H'(kb) \frac{1}{b} + H^2(kb) \left(h^2 - \frac{n^2}{b^2}\right),$$

$$(jh) = J(kb)H''(kb) + H(kb)J'(kb) \frac{1}{b} + J(kb)H(kb) \left(h^2 - \frac{n^2}{b^2}\right).$$

The answer which has been obtained for A can be easily checked. When the thickness of the lossy layer goes to zero, i.e. δ goes to zero, or when the propagation constant h of the lossy layer approaches the free-space propagation constant k , A should approach the scattered field coefficient for a perfectly conducting cylinder of radius a in free space. Indeed when letting $\delta = 0$, or $h = k$ the above A simplifies to

$$A = -i^n \frac{J(ka)}{H(ka)},$$

which is the scattering coefficient for a perfectly conducting cylinder above. A different kind of check can be performed by letting the propagation constant h of the shell approach infinity (short wavelength limit), thus making the shell a dielectric with an infinite dielectric constant which is a perfect

reflector and should behave like a perfectly conducting cylinder of radius b . Again, when the limit operation is performed A simplifies to

$$A = -i^n \frac{J(kb)}{H(kb)}.$$

If the free-space scattering coefficients A are to be computed it would be desirable to avoid Bessel and Hankel function terms which have to be differentiated. When the coefficients in A are re-expressed using Bessel's equation and the Wronskian of argument kb a further simplification results

$$(hj) = -\frac{2i}{\pi b^2} + J(kb)H(kb)(h^2 - k^2),$$

$$(jj) = J^2(kb)(h^2 - k^2),$$

$$(hh) = H^2(kb)(h^2 - k^2),$$

$$(jh) = \frac{2i}{\pi b^2} + J(kb)H(kb)(h^2 - k^2).$$

Dividing the numerator of A by its denominator and neglecting terms of order higher than δ one obtains

$$(5) \quad A = -i^n \frac{J(ka)}{H(ka)} \left(1 - \delta \frac{\pi b}{2i} \frac{h^2 - k^2}{J(ka)H(ka)} [J(kb)H(ka) - J(ka)H(kb)]^2 \right).$$

This is a simple enough result which would lend itself easily for computation.

The material of the thin shell was assumed to be non-magnetic, of arbitrary dielectric constant ϵ , and conductivity σ , i.e.

$$\mu_k = \mu_h$$

$$k = \omega \sqrt{(\mu_0 \epsilon_0)}$$

$$h = \omega \sqrt{(\mu \epsilon^*)}$$

where

$$\epsilon^* = \epsilon_h - (i\sigma/\omega).$$

An interesting observation can be made now. In the above expression for A_n , when $b = a$, the thin shell is in contact with the surface of the perfectly conducting cylinder. The terms that multiply δ vanish now. Thus, when the E vector of the incident field is parallel to the axis of the cylinder one can say that to a first-order correction the scattered field of a perfectly conducting cylinder coated with a thin dielectric or lossy shell is the same as the scattered field of a perfectly conducting cylinder alone.

INCIDENT E VECTOR PERPENDICULAR TO AXIS OF CYLINDER

The mathematical manipulations for this polarization are even more involved than in the previous case. The initial equations in the various regions are now

$$\begin{aligned}
 H_z^I &= \sum_{n=-\infty}^{\infty} i^n J_n(kr) e^{in\theta} + \sum_{n=-\infty}^{\infty} A_n H_n^{(2)}(kr) e^{in\theta}, \\
 H_z^{II} &= \sum_{n=-\infty}^{\infty} (B_n H_n^{(2)}(hr) + C_n J_n(hr)) e^{in\theta}, \\
 H_z^{III} &= \sum_{n=-\infty}^{\infty} (D_n H_n^{(2)}(kr) + E_n J_n(kr)) e^{in\theta}.
 \end{aligned}$$

The boundary condition on the surface of the perfectly conducting cylinder is

$$E_{\theta}^{III}(ka, \theta) = 0.$$

Matching the fields at $r = b$

$$H_z^{III}(kb, \theta) = H_z^{II}(hb, \theta)$$

$$E_{\theta}^{III}(kb, \theta) = E_{\theta}^{II}(hb, \theta) \quad \text{or} \quad \frac{1}{k^2} \frac{\partial H_z^{III}(kb, \theta)}{\partial r} = \frac{1}{h^2} \frac{\partial H_z^{II}(hb, \theta)}{\partial r}.$$

Matching at $r = c$

$$H_z^I(kc, \theta) = H_z^{II}(hc, \theta)$$

$$E_{\theta}^I(kc, \theta) = E_{\theta}^{II}(hc, \theta) \quad \text{or} \quad \frac{1}{k^2} \frac{\partial H_z^I(kc, \theta)}{\partial r} = \frac{1}{h^2} \frac{\partial H_z^{II}(hc, \theta)}{\partial r}.$$

This again gives five equations in five unknowns, which are

$$DH'(ka) + EJ'(ka) = 0,$$

$$DH(kb) + EJ(kb) = BH(hb) + CJ(hb),$$

$$i^n J(kc) + AH(kc) = BH(hc) + CJ(hc),$$

$$\frac{1}{k^2} (DH'(kb) + EJ'(kb)) = \frac{1}{h^2} (BH'(hb) + CJ'(hb)),$$

$$\frac{1}{k^2} (i^n J'(kc) + AH'(kc)) = \frac{1}{h^2} (BH'(hc) + CJ'(hc)).$$

Solving these for A we get

$$(6) \quad A = -i^n \frac{k^2 J(kc) J'(hc) - h^2 J'(kc) J(hc) + \xi [h^2 H(hc) J'(kc) - k^2 J(kc) H'(hc)]}{k^2 H(kc) J'(hc) - h^2 H'(kc) J(hc) + \xi [h^2 H(hc) H'(kc) - k^2 H(kc) H'(hc)]}$$

where ξ is

$$(7) \quad \xi =$$

$$\begin{aligned}
 & \frac{J'(ka) [k^2 J'(hb) H(kb) - h^2 J(hb) H'(kb)] + H'(ka) [h^2 J(hb) J'(kb) - k^2 J'(hb) J(kb)]}{J'(ka) [k^2 H(kb) H'(hb) - h^2 H(hb) H'(kb)] + H'(ka) [h^2 H(hb) J'(kb) - k^2 H'(hb) J(kb)]}
 \end{aligned}$$

All functions of argument c will again be expanded in a Taylor series about b . Since

$$k\delta = k(c-b) < 1$$

only the first two terms in the expansion are kept and substituted in the above expression for A . Simplifying the resulting expression, we get the following result for the scattered magnetic field coefficient

$$(8) \quad A = -i^n \frac{J'(ka) + \delta[(hj)J'(ka) - (jj)H'(ka)]}{H'(ka) + \delta[(hh)J'(ka) - (jh)H'(ka)]}$$

where

$$(hj) = -\frac{1}{b} + \frac{i}{(kh)^2} \frac{\pi b}{2} (k^2 - h^2) \left(h^2 J'(kb) H'(kb) + k^2 \frac{n^2}{b^2} H(kb) J(kb) \right),$$

$$(jj) = \frac{i}{(kh)^2} \frac{\pi b}{2} (k^2 - h^2) \left(h^2 J'^2(kb) + k^2 \frac{n^2}{b^2} J^2(kb) \right),$$

$$(hh) = \frac{i}{(kh)^2} \frac{\pi b}{2} (k^2 - h^2) \left(h^2 H'^2(kb) + k^2 \frac{n^2}{b^2} H^2(kb) \right),$$

$$(jh) = \frac{1}{b} + \frac{i}{(kh)^2} \frac{\pi b}{2} (k^2 - h^2) \left(h^2 J'(kb) H'(kb) + k^2 \frac{n^2}{b^2} J(kb) H(kb) \right).$$

Dividing the numerator of A by its denominator and neglecting terms of order higher than δ one obtains

$$(9) \quad A = -i^n \frac{J'(ka)}{H'(ka)} \left(1 - \delta \frac{\pi b}{2i} \frac{h^2 - k^2}{(kh)^2 J'(ka) H'(ka)} \right. \\ \left. \cdot \left[h^2 (H'(ka) J'(kb) - J'(ka) H'(kb))^2 + k^2 \frac{n^2}{b^2} (H'(ka) J(kb) - J'(ka) H(kb))^2 \right] \right).$$

This expression is more complicated than the corresponding one for the other polarization, but still adaptable for hand computation, at least for properly chosen ka and kb .

When the corresponding expressions for the two different polarizations are compared, one finds that for the perpendicular polarization, A has an additional term which does not vanish when the shell is in contact with the surface of the cylinder. Letting $b = a$, we get the scattered field coefficient for a coated cylinder

$$(10) \quad A = -i^n \frac{J'(ka)}{H'(ka)} \left(1 + \delta \frac{2in^2(h^2 - k^2)}{\pi a^3 h^2 J'(ka) H'(ka)} \right).$$

Thus for perpendicular polarization one should expect different scattered fields for a coated cylinder and a bare cylinder, whereas for the case of parallel polarization the scattered fields are the same to a first-order approximation. However, if second-order approximations would have been considered even the parallel polarization case would have yielded a second-order correction

term. This should be expected since a coated cylinder and a bare cylinder are different physically and this difference must show up in the mathematics eventually, even if only as high-order correction terms.

Another expression for A which might be useful is obtained when eqs. (6) and (7) are so rearranged that terms which contain the propagation constant h and terms which contain the propagation constant k are grouped together. Such an arrangement might prove to be useful when one of the propagation constants is much larger than the other one and asymptotic expressions are to be used. Thus, eqs. (6) and (7) for perpendicular polarization can be written

$$(11) \quad A = -i^n \frac{J(kc)\alpha + J'(kc)\beta + \rho(J(kc)\gamma + J'(kc)\tau)}{H(kc)\alpha + H'(kc)\beta + \rho(H(kc)\gamma + H'(kc)\tau)}$$

where

$$\begin{aligned} \rho &= \frac{h^2(J'(ka)H'(kb) - J'(kb)H'(ka))}{k^2(J(kb)H'(ka) - H(kb)H'(ka))}, \\ \alpha &= k^2(J'(hb)H'(hc) - J'(hc)H'(hb)), \\ \beta &= h^2(J'(hc)H'(hb) - H(hc)J'(hb)), \\ \gamma &= k^2(J(hb)H'(hc) - J'(hc)H(hb)), \\ \tau &= h^2(J(hc)H(hb) - J(hb)H(hc)). \end{aligned}$$

When

$$h > k$$

and

$$ka > 1$$

we can use asymptotic expressions for the Bessel and Hankel functions of argument hb and hc . If we substitute

$$\begin{aligned} J_n(hb) &= \sqrt{\frac{2}{\pi hb}} \cos\left(hb - n\frac{\pi}{2} - \frac{\pi}{4}\right) \\ H_n^{(2)}(hc) &= \sqrt{\frac{2}{\pi hc}} e^{i(-hc + n\frac{\pi}{2} + \frac{\pi}{4})} \end{aligned}$$

in the above expression we obtain

$$(12) \quad A = i^n \frac{k^2 h^2 J(kc) \sin h\delta + h^3 J'(kc) \cos h\delta + \rho[k^2 h J(kc) \cos h\delta - h^2 J'(kc) \sin h\delta]}{k^2 h^2 H(kc) \sin h\delta + h^3 H'(kc) \cos h\delta + \rho[k^2 h H(kc) \cos h\delta - h^2 H'(kc) \sin h\delta]}$$

where

$$h\delta = hc - hb.$$

AN APPLICATION

It was desirable to see what scattering properties a cylinder with a surrounding shell exhibits. To make a sample calculation for a particular cylinder the defining parameters are chosen as

$$\text{reflection coefficient } |R|^2 = .8,$$

$$\text{dielectric constant for shell } (\epsilon/\epsilon_0) = 100,$$

$$ka = 12.$$

The shell was spaced at distances $\lambda/2$, λ , $3\lambda/2$, but to catch any resonance effects a few [increments] were taken on each side of the spacing distances.

Stratton gives formulas which relate the reflection coefficients R to the thickness δ of the shell. He considers a thin plane dielectric sheet separating two semi-infinite dielectric media.

The reflection coefficient R for the shell is then given as

$$R = \frac{(r_{12} + r_{23})^2 - 4r_{12}r_{23} \sin^2 k_2 \delta}{(1 + r_{12}r_{23})^2 - 4r_{12}r_{23} \sin^2 k_2 \delta}$$

where the small lettered r 's are the reflection coefficients at each boundary. When the specified values of R and (ϵ/ϵ_0) are substituted in the above expression one can solve for the thickness δ of the shell in units of wavelength, thus

$$h\delta = .416$$

and since

$$h = 10k$$

then also

$$k\delta = .0416.$$

Since for the particular value of ka chosen, hand-computation proved too lengthy, the problem was programmed for the IBM 704. The computer calculated eq. (5) as two sums, i.e.

$$(13) \quad \sum_{n=-\infty}^{\infty} i^n A_n = - \sum_{n=-\infty}^{\infty} (-1)^n \frac{J_n(ka)}{H_n(ka)} [1 + \delta_1(\dots)].$$

The advantage of this calculation is that the thickness and material of the shell could be specified after the calculation by the constant δ_1 , where δ_1 is given by eq. (16).

For perpendicular polarization the computer calculated eq. (9) as three sums, i.e.

$$(14) \quad \sum_{n=-\infty}^{\infty} i^n A_n = - \sum_{n=-\infty}^{\infty} (-1)^n \frac{J_n(ka)}{H_n(ka)} [1 + \delta_1(\dots) + \delta_2(\dots)]$$

where δ_2 is given by eq. (19).

For parallel polarization eq. (5) the result was presented in the form

$$(15) \quad a + ib + \delta_1(c + id)$$

where

$$(16) \quad \delta_1 = \frac{\delta \pi b}{2i} (h^2 - k^2) = \frac{99\pi}{2i} (k\delta)(kb).$$

We are interested in the scattering cross section, which now becomes

$$\sigma = \frac{2\lambda}{\pi} |a + ib + \delta_1(c + id)|^2.$$

Carrying out this operation and dropping terms of order δ_1^2 we get

$$\sigma = \frac{2\lambda}{\pi} (a^2 + b^2 + 2\delta_1(ac + bd)).$$

This result can then be interpreted as the cross section of a perfectly conducting cylinder alone and the contribution to the total cross section from the shell, thus

$$(17) \quad \sigma = \sigma_{\text{cyl}} + \sigma_{\text{shell}} = \frac{2\lambda}{\pi} (a^2 + b^2) + \frac{2\lambda}{\pi} 2\delta_1(ac + bd)$$

where σ_{cyl} is well known, i.e.

$$\sigma_{\text{cyl}} = \frac{2\lambda}{\pi} (a^2 + b^2) = \frac{2\lambda}{\pi} \left| \sum_{n=-\infty}^{\infty} (-1)^n \frac{J_n(ka)}{H_n^{(2)}(ka)} \right|^2.$$

For perpendicular polarization, eq. (9), the results are given as

$$(18) \quad a + ib + \delta_1(c + id) + \delta_2(e + if)$$

where

$$\delta_1 = \delta \frac{\pi b}{2i} (h^2 - k^2) = \frac{99\pi}{2i} (k\delta)(kb)$$

and

$$(19) \quad \delta_2 = \delta \frac{\pi}{2i} \frac{h^2 - k^2}{bh^2} = \frac{99}{100} \frac{\pi k\delta}{2i kb}.$$

The cross section is then again given as

$$(20) \quad \sigma = \frac{2\lambda}{\pi} (a^2 + b^2 + 2\delta_1(ad - bc) + 2\delta_2(af - be))$$

here

$$\sigma_{\text{cyl}} = \frac{2\lambda}{\pi} (a^2 + b^2) = \frac{2\lambda}{\pi} \left| \sum_{n=-\infty}^{\infty} (-1)^n \frac{J'_n(ka)}{H'_n(ka)} \right|^2.$$

No significance could be attached to the cross section obtained by this method when

$$h\delta = .416.$$

Equations (5) and (9) were obtained by expanding the exact expressions in powers of $h\delta$ and retaining terms of order $h\delta$ only. For $h\delta = .416$ this would clearly not be valid. However, after the computer calculated eqs. (13) and (14) and presented the results in the form of eqs. (15) and (18) a significant conclusion could be drawn: the constants c and d in eq. (15) and the constants c , d , e , and f in eq. (18) were comparable in magnitude to the constants a and b , in most cases smaller by three or four magnitudes. Thus, when the shell is thin (i.e. $h\delta \ll 1$) the backscattering cross section for either polarization is approximately equal to that from the perfectly conducting cylinder alone, the shell having only a small perturbation effect.

To calculate the cross section when

$$h\delta = .416$$

and $((\epsilon/\epsilon_0) = 100)$ the IBM 704 was programmed to calculate eq. (12). Equation (12) demands only that

$$h > k.$$

In this calculation $h = 10k$. The computer calculated a set of values for shells spaced from $.46\lambda$ to $.64\lambda$ from the perfectly conducting cylinder. The results are shown in Fig. 2 in graphical form. This can be compared to a

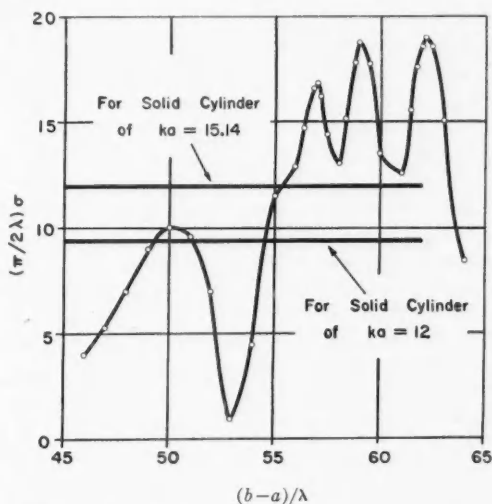


FIG. 2. Variation of the radar cross section as a function of the shell spacing from the cylinder.

perfectly conducting cylinder of $ka = 12$ with a perpendicularly polarized incident wave which is

$$\left| \sum_{n=-\infty}^{\infty} (-1)^n \frac{J'_n(12)}{H'_n(12)} \right|^2 \approx 9.4$$

and to a perfectly conducting cylinder which is as large as the shell, i.e. $kb = 15.2$ which gives

$$\left| \sum_{n=-\infty}^{\infty} (-1)^n \frac{J'_n(15.2)}{H'_n(15.2)} \right|^2 \approx 11.9.$$

This particular set of parameters shows some resonance phenomena which Fig. 2 displays. The average gain of the shell plus cylinder combination over a cylinder of the size of the shell alone is approximately

$$10 \log \frac{15}{11.9} = 1 \text{ db}$$

whereas the peak gain is

$$10 \log \frac{18.97}{11.9} = 2.02 \text{ db}.$$

The values computed by the IBM 704 are tabulated in Table I.

TABLE I

Shell spacing ($b-a$)/ λ	($\pi/2\lambda$) σ	Shell spacing ($b-a$)/ λ	($\pi/2\lambda$) σ
.46	3.923	.58	13.06
.47	5.31	.584	15.26
.48	7.21	.588	17.907
.49	8.98	.59	18.769
.50	10.01	.592	18.97
.51	9.65	.595	17.92
.52	7.02	.60	13.516
.53	1.057	.61	12.62
.54	4.405	.615	15.66
.55	11.52	.618	17.57
.56	12.885	.62	18.62
.564	14.72	.622	19.22
.568	16.73	.625	18.84
.57	16.88	.63	15.102
.572	16.25	.64	8.427
.575	14.385		

ACKNOWLEDGMENTS

The author wishes to thank Professor K. M. Siegel for the advice and support of this problem and Professor R. H. Dicke for suggesting it. The discussions with R. F. Goodrich and T. B. A. Senior proved an invaluable aid in completing this report. Their assistance is gratefully acknowledged.

The author also wishes to thank Miss Suzanne Dinga and Larry Evans for programming the IBM 704.

REFERENCES

- STRATTON, J. A. 1941. Electromagnetic theory (McGraw-Hill, New York).

THE CANADIAN STANDARD FREE-AIR CHAMBER FOR MEDIUM QUALITY X-RAYS¹

W. H. HENRY AND C. GARRETT

ABSTRACT

A description is given of the Canadian standard free-air chamber for measurement of medium quality X-rays, including measurements of the contribution from radiation scattered from the air and from the diaphragm, and a method for the accurate alignment of the chamber and X-ray source.

INTRODUCTION

The free-air ionization chamber to be described is the Canadian standard instrument for measuring X-radiation of medium quality, and forms part of the X-ray standardization equipment at the National Research Council Laboratories.

The use of X-rays in such fields as medicine and biology requires measurements of exposure dose. Exposure dose is essentially a measure of the ionizing ability of X-radiation in air. The practical measurement of exposure dose is complicated by the fact that one is required to collect all the ion pairs produced by the electrons which are themselves released in a known mass of air through the interaction of X-radiation in that mass. In the range of X-ray qualities below 500 kv the best instrument for the absolute measurement of exposure dose is the free-air chamber. This is essentially an ionization chamber with air walls of a thickness roughly equal to the range of the electrons released by the X-radiation. Owing to its large size it is usually used only in the laboratory, and as the standard against which more portable instruments can be calibrated.

The accuracy of a free-air chamber depends upon the fulfillment of a number of requirements. Data relevant to the design of a chamber have been published by Attix and DeLaVergne (1954*a*, *b*) and Wyckoff and Attix (1957). Briefly, the chamber must permit an accurate knowledge of the mass of air from which the electrons are released by the X-radiation, ensure the collection of ions equal in number to the total number produced by these electrons, and have a means of accurately measuring the resulting ionization current. The volume of the mass of air is defined by the effective area of the entrant aperture and by the limiting lines of the electric field ending on the edges of the collecting plate. The electric field in the collecting region must therefore be uniform. Its uniformity depends upon the smoothness and alignment of the collector, guard and high potential plates, and in a parallel plate chamber it is increased by the use of some system of guard loops surrounding the space between the plates. The electric field must also be of sufficient strength to reduce ion recombination

¹Manuscript received September 20, 1960.

Contribution from the Division of Applied Physics, National Research Council, Ottawa, Canada.

Issued as N.R.C. No. 6031.

to a low value. The dimensions of the chamber at right angles to the beam must be sufficiently large for most of the energy of the released electrons to be expended within the air before striking the plates or the guard loops. The ionization produced by radiation scattered out of the main beam should be low, and radiation other than that passing through the entrant aperture must be reduced to a negligible value by adequate shielding around the chamber.

GENERAL ARRANGEMENT

The X-ray standardization equipment is housed in an air-conditioned room where the temperature variations have been reduced to about $\pm 0.5^\circ \text{C}$. Figure 1 is a general view of the setup. One side wall of the standard air chamber

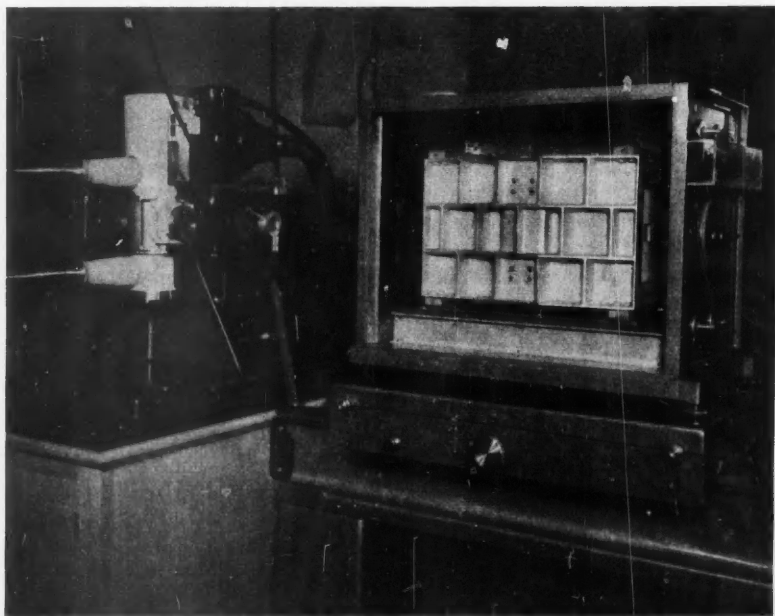


FIG. 1. General view of X-ray standardization setup, showing the standard chamber near one end of the lathe bed and the two X-ray tubeheads mounted on rails perpendicular to the lathe bed.

has been removed, exposing the rear surface of the guard plate. The mounting of the chamber and its supporting carriage on a lathe bed parallel to the X-ray beam permits accurately reproducible positioning of the chamber at distances of 50 to 300 cm from the focal spot. Adjustments are available for varying the vertical position and angular alignment of the chamber. The standard chamber can be moved off the carriage, out of the beam, and onto a table at the end of the lathe bed. Secondary chambers to be calibrated can then be

mounted on the same carriage and placed at the position occupied previously by the standard chamber diaphragm. A removable micrometer pointer assists in accurate positioning.

The box enclosing the plate system is lined with $\frac{5}{16}$ -in. lead sheet to attenuate stray radiation. On the front wall a thickness of $\frac{1}{2}$ in. of lead has proved adequate under all normal conditions to reduce ionization due to primary beam penetration to a few hundredths of one per cent of the total ion current. The inside dimensions of the box give a clearance of at least 10 cm between the open sides of the plate system and the box.

Two interchangeable sources of X-rays are available: a 250-kv constant potential generator, and a 100-kv unit with a beryllium-windowed tube for which half-wave or full-wave rectification or constant potential operation can be chosen. The nominal focal spot sizes of the tubes are respectively 3.5 mm square and 3.5 mm by 1.5 mm. The two tubeheads are mounted on rails at right angles to the lathe bed so that either source can be placed in position. In order to facilitate alignment, the tubeheads are adjustable within the supporting framework.

In an X-ray standardization setup, either the exposure dose rate of the X-ray beam must be very well stabilized, or the fluctuations in it must be measured and suitable corrections made. In the present equipment each X-ray generator incorporates a tube current stabilizer and a line voltage stabilizer which reduce fluctuations and drift in the X-ray exposure dose rate to few tenths of one per cent. Greater stabilization than this would be costly and is made unnecessary by the use of a monitoring ionization chamber, permanently mounted in the path of the X-ray beam at the end of the lathe bed near the tubehead. The chamber consists of three parallel plates perpendicular to the beam: two outer, 1 mm thick, beryllium plates at a potential of 300 v, separated about 1 cm from the central collector of aluminized mylar film. This adds very little extra filtration to the X-ray beam. The fluctuations in the ratio of the standard chamber ionization current to monitoring chamber ionization current are of the order of 0.1%.

PLATE SYSTEM

Figure 2 is a horizontal sectional schematic view of the chamber, showing the main dimensions of the parallel plate system. The 26-cm separation of the plates, which are 35 cm in height, maintains the loss of ionization due to inadequate size of the chamber at generally less than 0.25%, depending upon the quality of the X-radiation. Each plate is made from a ribbed aluminum casting which has been aged by heat treating and machined smooth and plane to within 0.001 in. The central collector plate is supported in the well of the guard plate and co-planar with it by polystyrene insulators. The gaps between the edges of the collector and guard plates are approximately 0.25 mm wide and were made as narrow as possible to reduce uncertainties in the collector length, consistent with the retention of high insulation. Since the plates have a thickness through the strengthening ribs at the edges of about 4 cm, the gaps have been tapered a few degrees toward the outer surface of

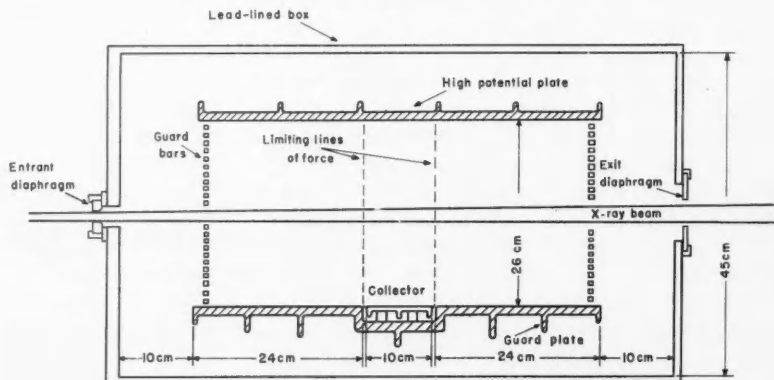


FIG. 2. Schematic horizontal sectional view of standard chamber.

the plates. This enabled conducting dust particles present after assembly to be removed easily.

Since the effective collector length, being determined by the limiting lines of force ending on the collector, will be altered by any distortion of the electric field, the collector and guard plates have been made co-planar by aligning the adjacent edges to within 0.0005 in. along their entire lengths. In the central region where most of the ions are collected the alignment along the edges is within 0.0001 in. The high potential plate is parallel to the guard and collector plates to within 0.001 in. The high potential and guard plates are held in this fixed relative position by four micalex insulators located at the corners. In this way the three plates form an independent assembly, shown in Fig. 3, whose mechanical stability has proved to be excellent.

The plate system as first constructed had two separate guard plates. This required four additional micalex supporting insulators, between the high potential plate and the corners of the guard plates adjacent to the collector. The movement of charges within these insulators induced currents in the collector which were not greatly reduced by guard wires, but which were very nearly eliminated by the guard bar system described below. In order to remove not only the remainder of this effect, but also the possibility of field distortion in the collecting region due to charge distribution on the insulators, the present plate system was constructed with the single guard plate casting, thus eliminating the four insulators nearest the collecting region. A comparison of the ionization currents measured with the two plate systems showed no actual difference greater than 0.1%, the limit of accuracy of the measurements.

The chamber has normally been operated with an electric field of 192 v cm^{-1} , supplied by a highly stable, 5000-v source. An estimate of the loss of ions due to lack of voltage saturation has been made by plotting the reciprocal of the measured ionization current versus the reciprocal of the electric field strength, for fields up to 346 v cm^{-1} . The curve becomes nearly linear for

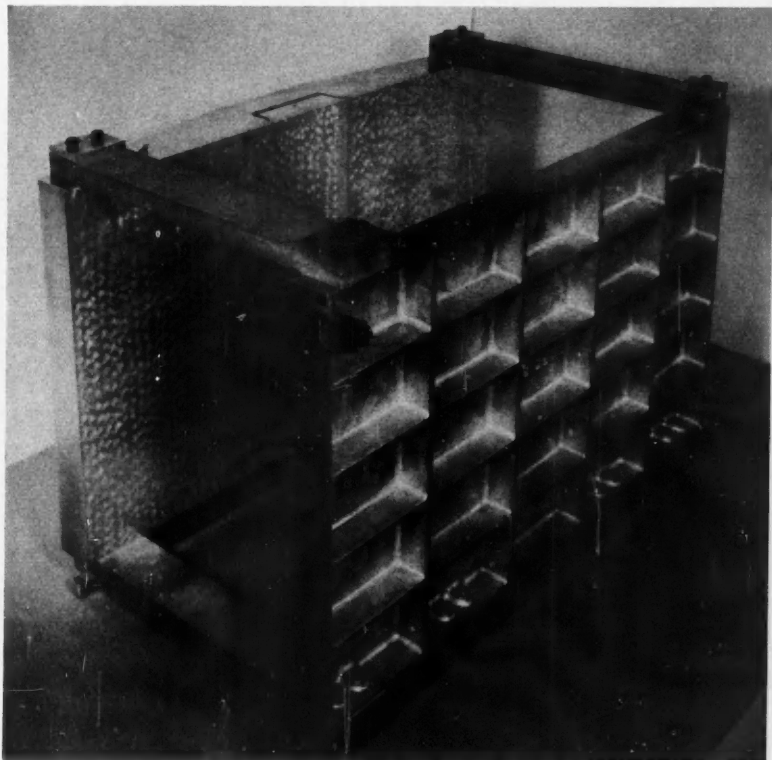


FIG. 3. Photograph of the parallel plate system.

fields above 100 v cm^{-1} , and an extrapolation to infinite field strength indicates a loss in collected ions at 192 v cm^{-1} of 0.2% for an exposure dose rate of 20 r min^{-1} .

GUARDING

In order to make the electric field uniform and perpendicular to the collector, a system of guard bars surrounds the volume within the plate system. A photograph of the guard bars in place within the plate system is shown in Fig. 4. Wires (Taylor and Singer 1930) and strips (Wyckoff and Kirn 1957) are commonly employed, and Failla and Marinelli (1937) used thin rods. Bars offer the twofold advantage of high electrostatic shielding from the effects of external disturbances, while requiring a minimum use of insulating spacers. Twenty-four parallel rectangular loops, made from $\frac{3}{8}$ -in. square aluminum stock, are equally spaced at approximately 1.1 cm, center line to center line. This leaves a small gap of approximately 0.13 cm between adjacent

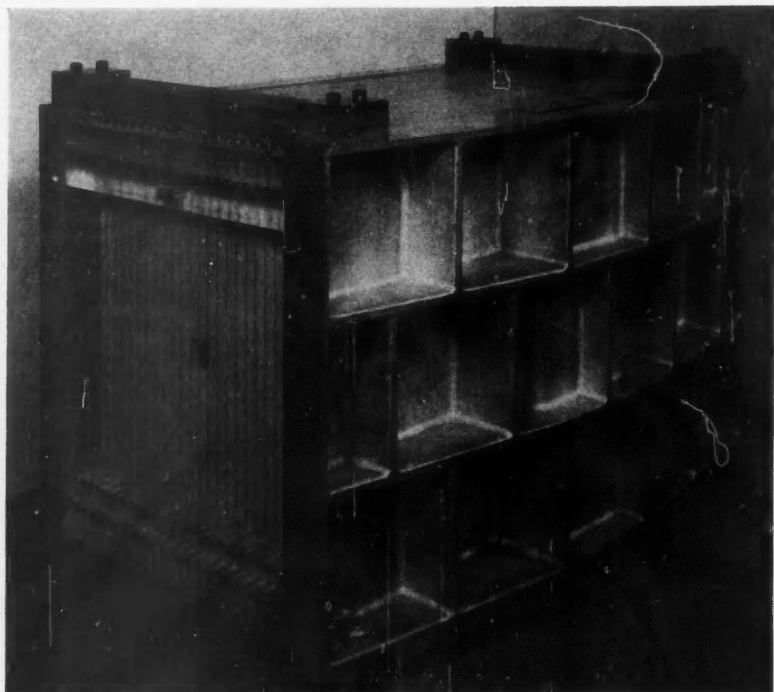


FIG. 4. Guard bar system mounted within the plate system.

bars. The inherent stiffness of the bars allows the use of supports and insulating spacers only at the four corners of the system. This forms an independent assembly, shown in Fig. 5, which is easily removed as a unit from the plate system, making possible the insertion of other trial systems of guarding.

Holes have been made in the guard bars at the front and rear to allow passage of the X-ray beam, while electrical continuity is maintained by offset wires shunting the holes. The possibility of the holes distorting the electric field in the collecting region was investigated by making comparison measurements of charge collected with fine aluminum wires stretched across the larger exit gap. No effect could be detected. A potential divider sets the potentials of the guard bar loops to give a linear gradient between the plates. Since the spacing of the center line of each outside loop from the surface of the plate is one-half the spacing between center lines of adjacent loops, the potential difference between each outside loop and plate is made one-half the potential difference between loops. The wire-wound resistors of the potential divider chain are mounted outside the chamber to avoid heating of the chamber air.

The electric field close to the guard bars is, of course, distorted by the presence of the bars. If the distortion extends into the collecting volume, then

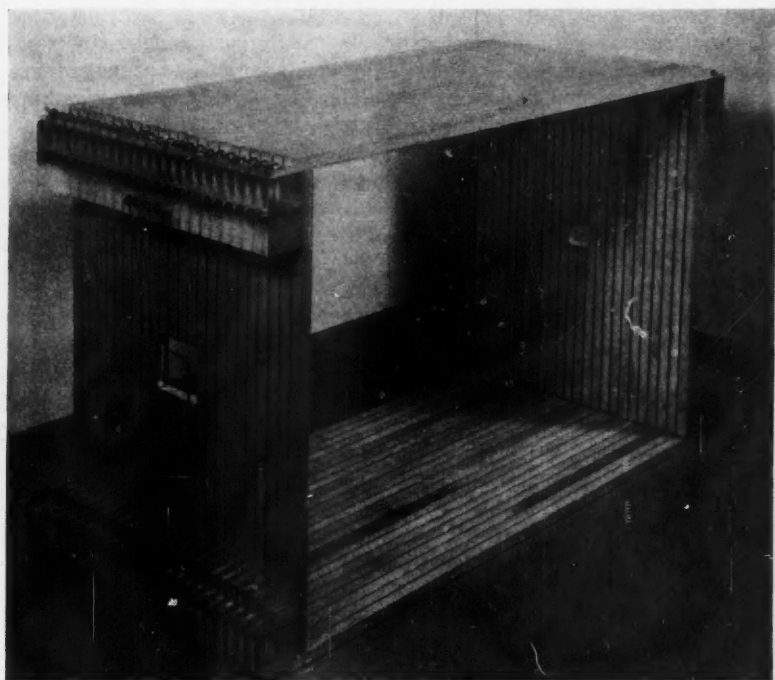


FIG. 5. Guard bar system.

the length from which ions are collected will be unknown. Measurements of ion current were made with the guard bars connected in a way that would considerably increase this distortion. In the first case, loops were shorted together in pairs, thus effectively forming half as many loops of approximately twice the width. In the second case, groups of four were shorted together, effectively forming only six guard loops, each of about four times the width. Table I shows the values of the measured ion current, normalized to a fixed

TABLE I
Ion current with different guard loop arrangements

Guard loop arrangement	Measured ion current, arbitrary units
Normal, connected singly	7.851 ± 0.002
Shorted in pairs	7.852 ± 0.002
Shorted in groups of four	7.855 ± 0.002

X-ray exposure dose rate by means of a monitoring chamber. It is evident that the error due to field distortion from the bars themselves is probably considerably less than 0.1%.

The proximity of the grounded outer box also can cause field distortion. The resulting error in collecting volume is usually measured by comparing the ion currents collected with the box at ground potential and at the potential of the high voltage supply. One-half the difference is taken as the error. Since it was not convenient in this case to operate the box at high potential, the same purpose was accomplished by temporarily mounting aluminum sheets on insulators inside the box about 1 in. from the wall. The sheets could be set at either ground or high potential, and the indicated error from this type of field distortion was less than 0.05%.

DIAPHRAGMS

The volume of the mass of air in which X-ray interactions take place is determined not only by the length of the collector but also by the area of the entrant diaphragm. Cylindrical apertures of 7 mm and 10 mm diameter have been machined in an alloy of tungsten (General Electric Hevimet), that are round and smooth within 0.5μ throughout their lengths. The diameters have been measured within 1.5μ by the Electricity and Mechanics Section of the National Research Council.

The cylindrical bore of each diaphragm was initially 10 mm long, followed by a 3-mm section at the rear (i.e. away from the X-ray source) tapered by 45° . In order to remove slight unevenness in the bore of the 7-mm diaphragm, No. 7A, shown in Fig. 6(a), the front section was tapered by about 3.5° , leaving only a short cylindrical bore of satisfactory roundness and smoothness about 1 mm in length. An added advantage of a short cylindrical bore is the greatly eased problem of alignment (Aitken 1958), since the error introduced by a misalignment is approximately proportional to the length of bore.

Scattered and fluorescent photons from this diaphragm contributed significantly to the total ion current. Such a possibility has been pointed out by

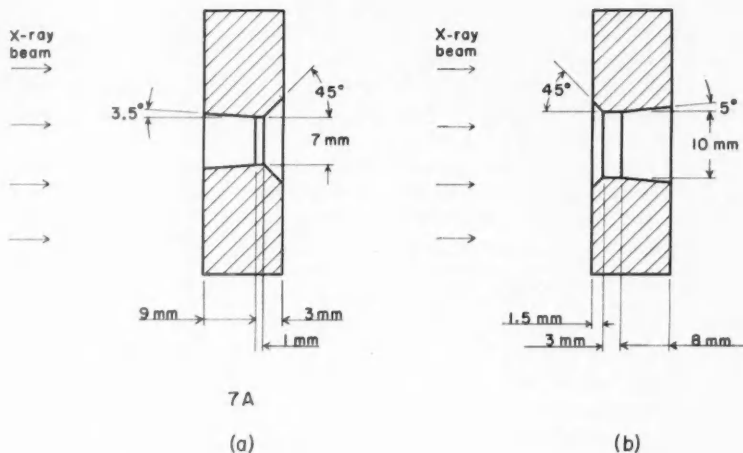


FIG. 6. (a) Shape of diaphragm No. 7A. (b) Shape of a low scattering diaphragm.

Greening (1960), and the measurement of this contribution is described in the next section. To reduce this effect to a negligibly low value, the diaphragm design has since been improved following König (1939), as shown in Fig. 6(b). The cylindrical bore of only several millimeters length is preceded on the side toward the X-ray source by a short section tapered at 45° , and followed by a section of about 8-mm length tapered at 5° . Five degrees is sufficient to avoid incidence of the X-ray beam on the rear conical surface at the smallest used source to chamber distance. The surface of the 45° tapered section can not "see" into the chamber and so secondary photons from this surface are attenuated by the walls of the diaphragm. This leaves only the short cylindrical section as a possible source of scattered radiation. The rear conical section and the cylindrical bore are concentric within $3\ \mu$ and blend with a radius no greater than 0.7 mm, thus giving a well-defined plane of definition.

Although diaphragm 7A itself, when reversed, is similar to the low scattering diaphragm, it is not used in that position owing to the intersection of the cylindrical bore and the added 3.5° taper not giving a well-known defining plane.

A diaphragm on the tube housing limits the emerging X-ray beam to a convenient size. The larger the beam cross section, the greater is the contribution from penetration of the front wall. On the other hand, an aperture smaller than the focal spot would shade part, or all, of the entrant diaphragm from some points on the focal spot. The resulting change in effective area of the entrant diaphragm would not be in proportion to the change in exposure dose rate at its center.

MEASUREMENT OF SCATTERED AND FLUORESCENT PHOTONS

The contribution to the total ion current from scattered and fluorescent photons was measured by a method described by Attix and DeLaVergne (1954a, b). A plastic tube was mounted inside the chamber, between the entrant and exit diaphragms, and of such diameter to just clear the X-ray beam. The tube was coated with graphite and operated at one-half the potential of the high tension plate in order to minimize distortion of the electric field. The wall was sufficiently thick to stop all secondary electrons ejected from the air within the tube. Using entrant diaphragm 7A the observed ionization, due only to scattered and fluorescent photons and corrected for the shadowing effect of the tube and for the estimated attenuation of the photons in the walls of the tube, is shown in the third column of Table II.

TABLE II
Scattered and fluorescent radiation

Constant potential (kv)	H.V.L. (mm)	Contribution from scattered and fluorescent photons, % of total ion current		
		Measured	Calculated	Measured contribution from diaphragm 7A
80	1.6 Al	0.72	0.59	0.03
140	0.7 Cu	0.83	0.46	0.18
250	2.0 Cu	0.75	0.40	0.19

The calculated values in the fourth column of Table II are based on the data of Wyckoff and Attix (1957) for the contribution from secondary photons arising from the interaction of the X-ray beam and the air within the chamber. Their X-ray qualities differed slightly from those in Table II, but since the contribution varies slowly with quality, the necessary interpolation introduces only a small error. Part of the difference between the measured and calculated values is due to scattered and fluorescent photons from the entrant diaphragm, 7A, and also to the length of the chamber differing from that used by Wyckoff and Attix.

The scattered radiation was further investigated by studying its variation along the length of the chamber. Lead sleeves, of 10- to 12-cm length and 1.6-mm wall thickness, were fitted over the entire length of the plastic tube except for a 2-cm gap at the front guard bars where there was not sufficient available space. The removal of a sleeve allowed unattenuated passage of the scattered photons through that particular section. Figure 7 shows the results

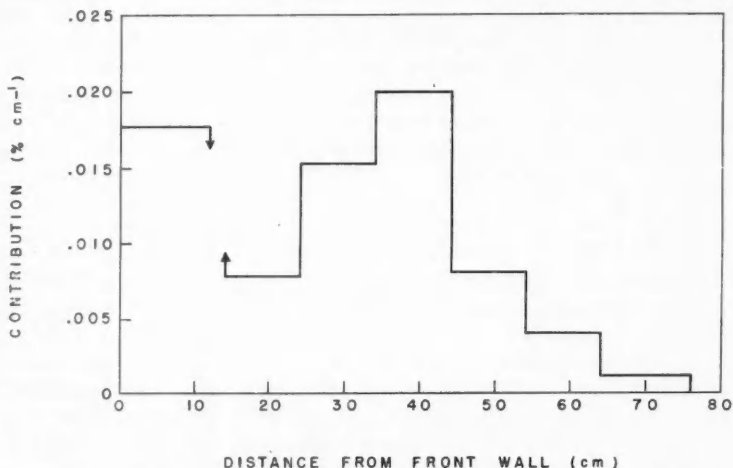


FIG. 7. Contribution to total ion current from scattered and fluorescent radiation passing through sections of the plastic tube along the chamber length; at 140 kv, 0.7 mm Cu H.V.L., with entrant diaphragm 7A. The gap between 12 and 14 cm corresponds to the position of the front guard bars, and the position of the collector is from 34 to 44 cm.

obtained at 140 kv. As expected, the contribution of scattered photons is largest from the central region, opposite the collector, and falls off toward each end of the chamber. The large increase at the front of the chamber is due to the scattered and fluorescent radiation from entrant diaphragm 7A.

An estimate of the scattered radiation (including the fluorescent radiation) from the diaphragm can be made from Fig. 7 by subtracting the extrapolated contribution from the air. However, more accuracy is obtained by comparing the total scattered radiation, from the air and diaphragm, measured with

diaphragm 7A, with the total when measured using a low scattering diaphragm of the type described above. The difference is then equal to the difference in scattered radiation from the diaphragms, and so approximately equal to that from 7A. Column 5 of Table II shows the values so obtained, representing the contribution from scattered radiation from diaphragm 7A transmitted through the front of the guard bar system. This transmission has been estimated to be a few per cent at 80 kv and 60 to 70% at the higher kilovoltages.

The scattered radiation from a cylindrical diaphragm would be approximately proportional to the length of the bore. A low scattering diaphragm was compared with a diaphragm having a cylindrical bore of the same diameter but of about six times the length, loaned by the National Bureau of Standards. The difference was below the limit of measurement at all X-ray qualities, indicating that the contribution from scattered and fluorescent photons from either diaphragm is no greater than a few hundredths of one per cent of the total ion current.

CURRENT MEASUREMENT

The ionization current is measured by a standard Townsend balance type of circuit in which the charge is collected on a capacitor, the resulting voltage balanced by a compensating potential, and the null indicated by a vibrating reed electrometer. The capacitor is a specially designed, air dielectric, quartz-insulated, three terminal type of about 2000- μf capacitance. Precise measurements by the Electricity and Mechanics Section of the National Research Council have shown that the capacitance has not changed by more than 0.01% over many months. The compensating potential is supplied by dry cells and measured with a differential voltmeter calibrated against a built-in standard cell. The feedback of the electrometer maintains the input at very nearly ground potential, thus reducing to a negligible value loss of charge by leakage from the input circuit to ground through the capacitor insulators and the supporting insulators of the collector. The input being held near ground potential by the feedback also reduces distortion in the electric field due to the collector and guard plates not being at the same potential, and eliminates the necessity of continuously maintaining a null. The capacitor and electrometer preamplifier are located on top of the standard chamber inside a $\frac{1}{4}$ -in. lead shield which was found necessary to reduce ionization from stray radiation.

The ionization current from the monitor chamber is measured in the same way. The much larger current, however, necessitates a much larger capacitance. A commercial solid dielectric capacitor of about 1- μf capacitance is used and is entirely satisfactory since the resistance is adequately high, dielectric absorption effects are not noticeable, and long term stability is not a consideration.

ALIGNMENT

The alignment of the standard air chamber requires the placement of the center of the focal spot of the X-ray tube on the axis of the entrant diaphragm, and the maintenance of this condition for all positions of the chamber along the lathe bed.

The latter requirement is conveniently satisfied first. As the chamber moves along the lathe bed, the locus of the center of the defining plane of the entrant diaphragm is, of course, a straight line, and the focal spot must be positioned on this locus. Using a short entrant diaphragm of 1-mm diameter, a film is placed over the exit diaphragm and a double exposure made, one with the chamber at each limit of travel on the lathe bed. The exposure times are adjusted to give a small dark image within a larger, less dense image. From the relative positions of the images and the known geometry, the displacement can easily be calculated by which the focal spot is off the locus. When correctly positioned, the double exposure gives two concentric images.

The axis of the entrant diaphragm must then be made to pass as nearly as possible through the center of the focal spot. A misalignment of a few minutes of arc can produce an error of 0.1% (Wyckoff and Attix 1957). The angular alignment is most easily accomplished by installing a long, narrow entrant diaphragm in order to exaggerate the error for any particular angular misalignment. The diaphragm used has a length of 17 cm and a diameter of 1 mm, made by accurately aligning small holes at the ends of a tube of larger diameter. The radiation transmitted by this diaphragm is conveniently measured with a survey meter mounted at the exit diaphragm. From a plot of the meter reading against angular rotation of the entrant diaphragm, the correct alignment is readily determined within 1 to 2 minutes of arc. Since it is not possible in this chamber to rotate the entrant diaphragm independently, the same purpose is accomplished by moving the focal spot. This gives an effective angular rotation of the diaphragm, and in Fig. 8 is shown the measured variation in transmitted radiation. Then, having determined the angle by which the diaphragm is out of alignment, the entire chamber can be rotated by the indicated amount.

The X-ray beam within the chamber is parallel to the plane of the collector and perpendicular to the plane of the electric lines of force ending on the collector edge, within 10-20 minutes of arc. Hence, cosine errors from this misalignment are less than 0.01%.

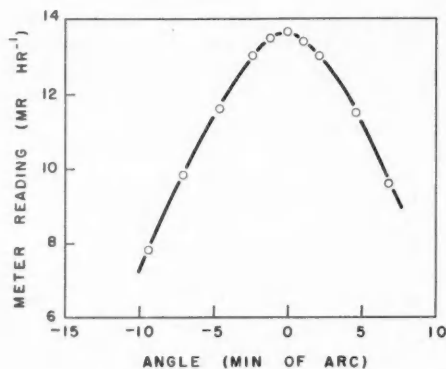


FIG. 8. Transmitted radiation versus effective angular rotation about the aligned position of the 1-mm diameter aperture, of 17-cm length.

ACCURACY

The maximum error in the determination of exposure dose by means of a standard free-air chamber has been estimated in the Report of the International Commission on Radiological Units and Measurements (1956) to be likely no greater than 1.1%. This is the sum of the estimated maximum errors in the individual quantities involved.

In an intercomparison between two standard chambers, since some of the quantities are common to both chambers, it is estimated in the same report that the agreement should be within 0.9%. When the Canadian standard chamber and the standard chamber of the National Bureau of Standards were intercompared, the agreement was well within the estimated 0.9%. A forthcoming paper will describe this intercomparison.

ACKNOWLEDGMENTS

The authors are indebted to Mr. E. Green of the Electricity and Mechanics Section for making the metrological measurements on the diaphragms, to Dr. A. F. Dunn of the same section for the capacitance measurements, and to Mr. J. H. Aitken for his part in developing the monitoring chamber and for many helpful discussions.

REFERENCES

- AITKEN, J. H. 1958. *Phys. in Med. Biol.* **3**, 27.
ATTIX, F. H. and DELAVERGNE, L. 1954a. *Radiology*, **63**, 853.
——— 1954b. *J. Research Natl. Bur. Standards*, **53**, 393.
FAILLA, G. and MARINELLI, L. D. 1937. *Am. J. Roentgenol. Radium Therapy*, **38**, 312.
GREENING, J. R. 1960. *Brit. J. Radiol.* **33**, 178.
KÖNIG, C. 1939. *Physik. Z.* **40**, 46.
REPORT OF THE INTERNATIONAL COMMISSION ON RADIOLOGICAL UNITS AND MEASUREMENTS. 1956. *National Bureau of Standards Handbook 62* (Superintendent of Documents, U.S. Government Printing Office, Washington).
TAYLOR, L. S. and SINGER, G. 1930. *Radiology*, **15**, 637.
WYCKOFF, H. O. and ATTIX, F. H. 1957. *Design of free-air ionization chambers. National Bureau of Standards Handbook 64* (Superintendent of Documents, U.S. Government Printing Office, Washington).
WYCKOFF, H. O. and KIRN, F. S. 1957. *J. Research Natl. Bur. Standards*, **58**, 111.

THE "REACTOR" NEUTRON CAPTURE CROSS SECTION OF Y^{91}

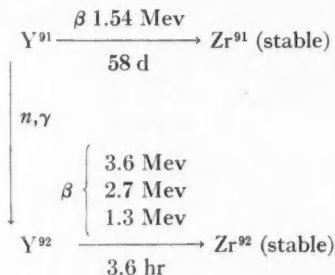
GWEN M. MILTON AND W. E. GRUMMITT

ABSTRACT

A high specific activity source of Y^{91} , freed from natural uranium and rare earths, was irradiated in a high flux position in the NRX reactor. After further chemical purification, 3.6-hour Y^{92} was identified in the sample by measurement of the 3.6-Mev β -particle associated with its decay, using a scintillation spectrometer. Two such measurements have established the reactor neutron capture cross section of Y^{91} to be 1.4 ± 0.3 barns.

INTRODUCTION

As a result of its relatively high fission yield (5.8%) 58-day Y^{91} is a potential reactor poison of some importance, and hence the measurement of its thermal neutron cross section is of more than routine interest. A study of the nuclear reactions involved suggests a possible method for this measurement:



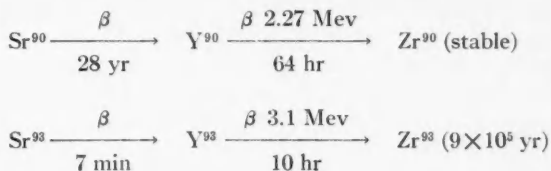
Assuming that a reasonable fraction of the disintegrations of Y^{92} proceeds by emission of the 3.6-Mev β , a small quantity of this nuclide should be easily identifiable in the presence of much larger amounts of Y^{91} by using a scintillation spectrometer to select those β -energies above 3.1 Mev (thus eliminating chance coincidences of two Y^{91} β -particles being counted as a single 3.1-Mev particle).

Preliminary experiments indicated, however, that this cross section is < 10 barns (Eastwood *et al.* 1958) and that with the available counting equipment it could not be measured in the presence of appreciable amounts of uranium and natural rare earth contamination. Thermal neutron fission in uranium produces three yttrium isotopes which could interfere with this experiment, Y^{90} , Y^{93} , and the 3.6-hr Y^{92} under study. (See top of p. 1691.) Also, Y^{90} and Dy^{165} are formed by neutron capture in stable rare earths present in the irradiated sample of Y^{91} . These nuclides can interfere with

¹Manuscript received September 12, 1960.

Contribution from the Research Chemistry Branch, Atomic Energy of Canada Limited, Chalk River, Ontario.

Issued as A.E.C.L. No. 1135.



the determination if the energy discrimination is poor, or if the coincidence rate is sufficiently high to produce "pile-up". This latter effect is caused by the numerical addition of the energy of two β -particles within the amplifier and is a function of the disintegration rate of Y^{91} , of the contaminants, and the resolving time of the instrument (1 μ sec).

In the initial experiments, using carrier-free Y^{91} (4×10^{-12} g = 10^6 d.p.m.) prepared from fission product Sr^{91} , a limit of <7 barns was set for the Y^{91} cross section. As Y^{92} and Y^{93} from fission, and Dy^{165} from capture were limiting the measurement, a considerable effort was required to reduce the quantity of uranium and rare earths present in the sample prior to the irradiation.

EXPERIMENTAL

Chemical

(a) Preparation of a High Specific Activity Source of Y^{91}

Carrier-free Y^{91} can be prepared in a radiochemically pure state by milking it from Sr^{91} . Unfortunately, Sr^{91} obtained by separation from irradiated uranium necessarily contains small amounts of other strontium activities and hence two other yttrium isotopes are collected in this milking process, Y^{90} (stable) and Y^{90} . However, the amounts are very small if the irradiation time is short (<1 day), and the time allowed for growth of Y^{91} from the separated strontium is a minimum. Y^{90} contamination can be reduced further by decay, as its half-life is short relative to that of Y^{91} .

Approximately 25 millicuries (5.6×10^{10} d.p.m.) of carrier-free Sr^{91} were separated from 50 mg of natural uranium and mixed fission products immediately after irradiation in the NRX reactor. The first step in the separation was the removal of anion complexes by their adsorption on Dowex 1 from 10 M HCl, or on a second column, from 0.5 M HCl. The cations which had passed freely through both these columns were adsorbed on a Dowex 50 column in the acid form and subjected to chromatographic elution with 1.5 M ammonium lactate pH 7. The strontium fraction was identified by its radiation characteristics and by its position in the elution sequence. It was found necessary first to purify all reagents by redistilling, or by pouring them through a resin column at a pH suitable for the removal of rare earths. Ammonium lactate was chosen as eluant because of the relative ease of purification.

The separated strontium was set aside overnight to allow the 9.7-hr Sr^{91} to decay to Y^{91} , which was subsequently recovered free from strontium and rare earths by elution with 0.4 M , pH 4 ammonium isobutyrate from Dowex 50. From this step onwards all procedures were carried out in polythene,

avoiding glass as a possible source of natural rare earths. Yttrium was recovered from the ammonium isobutyrate by metathesis to the chloride on a very small Dowex 50 column in the acid form. By washing this column carefully with water all traces of the isobutyrate were removed before the Y was eluted with 6 M HCl. This Y eluate was evaporated to dryness in a platinum boat and ignited; the residue was then taken up in 3 M HCl. The uranium content was further reduced by selective adsorption on a 1/10th ml Dowex 1 column. This was repeated in a glove box to minimize contamination, and the final eluant was stored in polythene for several weeks to allow Y^{90} to decay.

(b) Preparation of the Sample for Irradiation

A preliminary study was made of the fission product contamination resulting from the irradiation of empty nylon, quartz, and polythene containers of roughly equal size. This study indicated that the activity to be expected as contamination in future irradiations would be least if polythene were used, the activities produced in the quartz and nylon containers being 3.5 and 6.5 times as high respectively. From the absolute magnitude of the contamination, it was estimated that a cross section of 1 barn could be measured by the irradiation of 3.5×10^5 d.p.m. Y^{91} in polythene. However, the polythene did not withstand irradiation satisfactorily and it was decided to use very fine quartz tubing, reducing the surface area 10-fold and the contamination contribution below that of the polythene.

Samples were prepared for irradiation as follows: A 10 λ sample of HCl solution containing $\sim 3 \times 10^5$ d.p.m. Y^{91} was drawn into a warmed capillary vial and centrifuged to transfer all the solution to the sealed end. The open end was sealed in a flame and the capillary heated for several hours at 110° C to check that it was leak-free. The tube, wrapped in superpure aluminum, was then put in an iron irradiation capsule along with a cobalt wire flux monitor (diameter = 0.005 in.), similarly sealed and wrapped, and sent by pneumatic carrier to a high flux position in the NRX reactor for 3 hours.

(c) Procedures Following Irradiation

Immediately on delivery from the reactor the quartz sample tube was washed in boiling aqua regia, broken into a beaker containing 5 mg of yttrium carrier in concentrated HCl, and boiled to facilitate solution and exchange. Radioactive contamination was removed from the Y by the following treatment: passage through a column of Dowex 1 with 10 M HCl as complexing agent, three hydroxide precipitations alternated with three fluoride precipitations, and elution from Dowex 50 with 0.3 M isobutyrate, pH 4.0. The separated yttrium was recovered as oxalate, washed with water, alcohol and ether, mounted on an aluminum counting tray, and covered with a mylar film.

In several preliminary runs a search was made for such nuclides as Np^{239} , Ba^{139} , and Sr^{91} , in an effort to set an upper limit on fission contamination present (i.e. a measure of the total uranium in the sample plus capsule).

(d) Preparation of a Source of Yttrium-92

In order to standardize the counting equipment, and also to estimate the relative abundances of the three β -particles associated with Y^{92} decay, it was

necessary to prepare a relatively pure source of this isotope. This was obtained from the decay of 2.7-hr Sr^{92} during the preparation of Sr^{91} (see Chemical (a)), by milking yttrium from the cation column following a 1-hour growth period, after the removal of gross rare earth activities, and before the strontium elution.

Counting

An anthracene crystal 5 cm in diameter and 1 cm thick, attached to a 6342 RCA photomultiplier tube, was used for this measurement. The crystal and tube, wrapped with aluminized mylar film, rested in a lucite ring to the underside of which a slide holder was attached. This was connected through a transistor preamplifier (AEP 1403) to a fast high gain amplifier (AEP 1440, the Moody amplifier). An anticoincidence shield was provided by a layer of nine 12-in. long, 1-in. diameter Geiger counters directly under the sample holder and along two sides of the crystal. Outer shielding consisted of 8 inches of iron plate on the sides and underneath, with 2 inches of lead surrounding the photomultiplier.

Two methods of data collection were utilized during the experiment:

(1) Pulses from the amplifier were fed through a discriminator before entering the anticoincidence circuit and scaler. By suitable adjustment of the discriminator, counting efficiencies of 7% for Ru^{106} - Rh^{106} β -spectrum (end-point energy 3.5 Mev) were obtained at bias settings of about 3 Mev, for which the efficiency of counting Y^{91} was 10-30%. Background readings at these settings averaged 0.2 counts per minute.

(2) Pulses from the Moody amplifier were fed through a 1- μ sec delay line to a 100-channel pulse height analyzer (AEP 2230) gated by the anticoincident circuit. By preparation of a Fermi-Kurie plot to establish the cutoff channels for the various β -energies present, and by comparison with similar data collected for a relatively pure source of Y^{92} , it was possible to determine the contribution of the 3.6-Mev component and plot its decay.

A standard Ru^{106} - Rh^{106} source was used to estimate efficiencies for both methods.

RESULTS

A. Calibration of the Counter

The spectrometer was calibrated for these experiments by the preparation of a standard Fermi-Kurie plot of the spectrum of a Ru^{106} - Rh^{106} source. Substituting the approximation $\sqrt{[N(\epsilon)]/\epsilon}$ for the quantity $[N(\epsilon)]^{1/2}f(Z, \epsilon)\epsilon(\epsilon^2 - 1)^{-1/2}$ (where $N(\epsilon)$ is the total counts per unit time in an energy interval ϵ , ϵ is the total energy in units of mc^2 , and $f(Z, \epsilon)$ is the fermi function) and using the known end-point energy (the 3.53-Mev β of Rh^{106}) plus an estimated cutoff, it was possible by iteration of this plot to determine the cutoff channel for this energy. The error introduced by equating the electron momentum to the electron energy and neglecting the charge on the Rh nucleus (i.e. putting $f(Z, \epsilon) \equiv 1$) and by using a thin crystal probably totalled <3% in deviations from the straight line plot and is negligible in determining the end point.

The energy/channel value obtained from the Rh^{106} cutoff was then used in the preparation of similar plots for Y^{91} , and in an estimation of the cutoff

for Y^{90} . In the case of the Y^{91} the source used was the sample itself, immediately prior to irradiation. Figures 1(a) and 4(a) show the Rh^{106} cutoff at the start of the two experiments outlined in Sections C and D; Figs. 1(b) and 4(b) show the Y^{91} cutoff on the same dates. Using the allowed shape for the Y^{91} first-forbidden transition also introduced a negligible error into that calibration. Using the end-point energy of 1.54 Mev quoted in the most recent

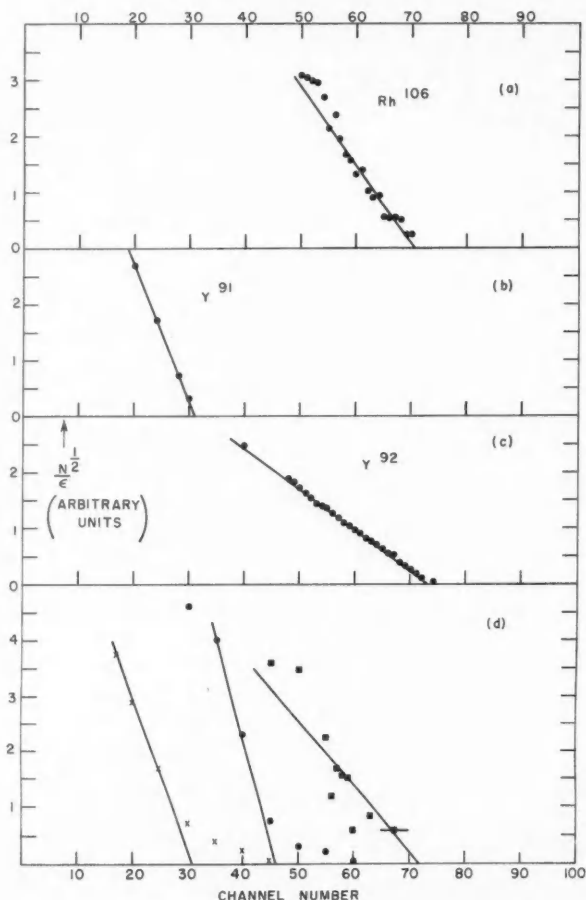


FIG. 1. (a) ● Rh^{106} spectrum at time of first expt.; cutoff channel 70.8; energy/channel = 50 kev. (b) ● Y^{91} spectrum prior to first expt.; cutoff channel 31; energy/channel = 49.7 kev (estimated cutoff for Y^{90} = 45.7). (c) ● Scan of Y^{92} prior to first expt. with instrumental background subtracted; Y^{92} cutoff channel 73; energy/channel = 49.4 kev. (d) First expt.: X original scan, Y^{91} cutoff channel 31, energy/channel = 50 kev; ● original scan $\times 10$, minus Y^{91} contribution, Y^{90} cutoff channel 46; ■ original scan $\times 100$, minus Y^{91} and Y^{90} contributions, Y^{92} cutoff channel 72.

table of isotopes (Strominger *et al.* 1958) the energy/channel values obtained for the Y and Rh plots are seen to be in good agreement.

The preparation of a sample of Y^{92} for calibration purposes has already been described, and Fig. 2 substantiates the purification procedures. The half-life of the decay observed in channels 46-60 over a 3-day period was 3.5

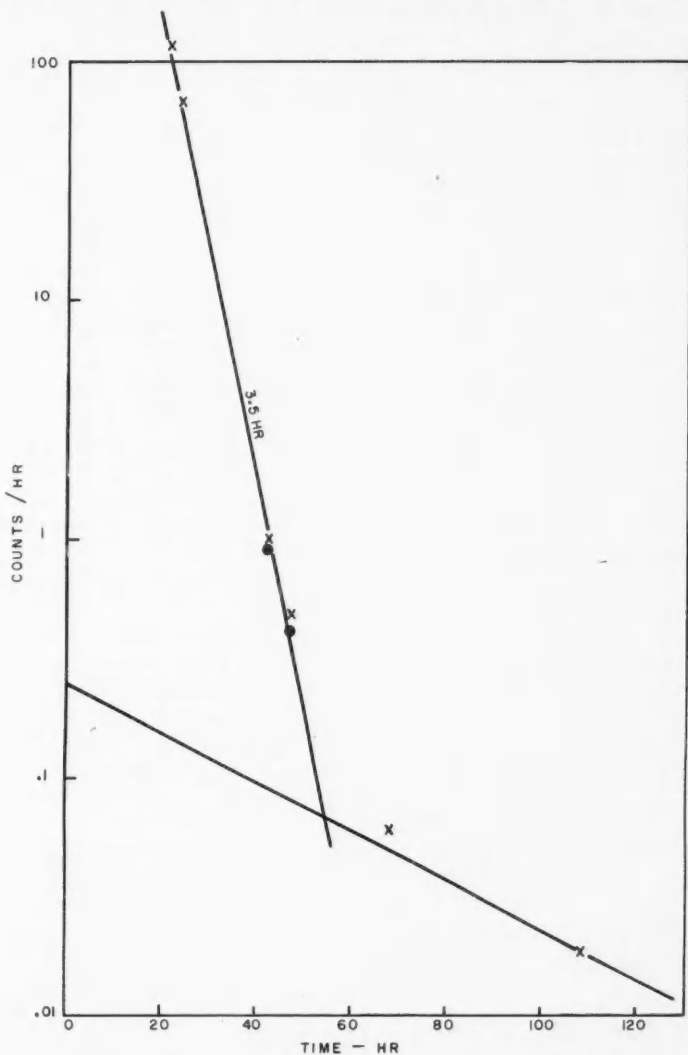


FIG. 2. Y^{92} calibration: X total counts/hour in channels 46-60; ● longer-lived component subtracted.

hours, with less than 0.13% longer-lived contamination seen. Three β -particles have been identified in the decay of Y^{92} (Ames, Bunker, and Starnier 1952). Little information is available on the relative abundances of the β -rays and as seen in Fig. 1(c), the Fermi-Kurie plot obtained from the scan of the spectrum showed only one end point above 1.3 Mev. However, Dzelepov and Peker (1958) list the 3.6-Mev β -branch from Y^{92} as 77% per disintegration and in the absence of further information it was decided to use this value for the purpose of calculation of the cross section.

B. Determination of the Uranium Content of the Irradiated Material

As pointed out earlier, any uranium present in the Y^{91} at the time of irradiation will undergo fission and contribute to the Y^{92} observed in this experiment. Attempts were made to determine this contribution by separating and counting Sr^{91} , Ba^{139} , and Np^{239} formed during the irradiation. Np^{239} gave the most unambiguous results, permitting the estimation of as little as 10^{-12} g of uranium in the sample plus capsule. The quantity of uranium which would produce the observed activity of neptunium (42 dis./hr) would also give rise to 90 dis./hr Y^{92} at the time of its separation from the parent Sr^{92} . This corresponds to $\sim 2\%$ of the total Y^{92} observed.

C. First Y^{91} Cross-section Measurement

A Fermi-Kurie plot prepared from the first 100-channel scan of the source (approximately 4 hours from the end of the 2-hour irradiation), using ϵ values determined from the Y^{91} calibration, Fig. 1(b), is shown in Fig. 1(d). Once the Y^{91} contribution is subtracted the remainder of the activity is easily separable into two components with cutoffs at channels 46 and 72, identifiable with reasonable certainty as Y^{90} and Y^{92} respectively.

In order to determine the decay of the component with end point in channel 72, that portion of the total counting rate appearing in channels 50-60 was summed for successive scans and plotted as a function of time, as shown in Fig. 3. (Channels 60-70 were not included in the totals because counting rates in that region were so low as to make unusual background fluctuations assume too great an importance.) As can be seen from the graph there was an appreciable long-lived component contributing to the counting rate in these channels, probably as a result of pile-up of Y^{91} to give an apparent 3.1-Mev particle, but when this component was subtracted a 3.7-hour activity remained. Extrapolating this curve to t_0 (210 counts/hr) and assuming a counting efficiency equal to that for the standard rhodium source (68% of the rhodium disintegrations by emission of a 3.53-Mev particle and 77% of the yttrium by a 3.6-Mev particle) in these same channels, a value of 6800 dis./hr Y^{92} at t_0 was obtained.

Substituting in the formula:

$$(1) \quad \sigma_{91} = (N\lambda)_{92}/N_{91} \cdot F$$

where F = average flux as determined by production of Co^{60} during the same period in an accurately weighed Co wire (Jervis 1957), relative to $\sigma_{2200} = 37.0$ barns,

$$(N\lambda)_{92} = \text{dis./hr of } Y^{92} \text{ at } t_0,$$

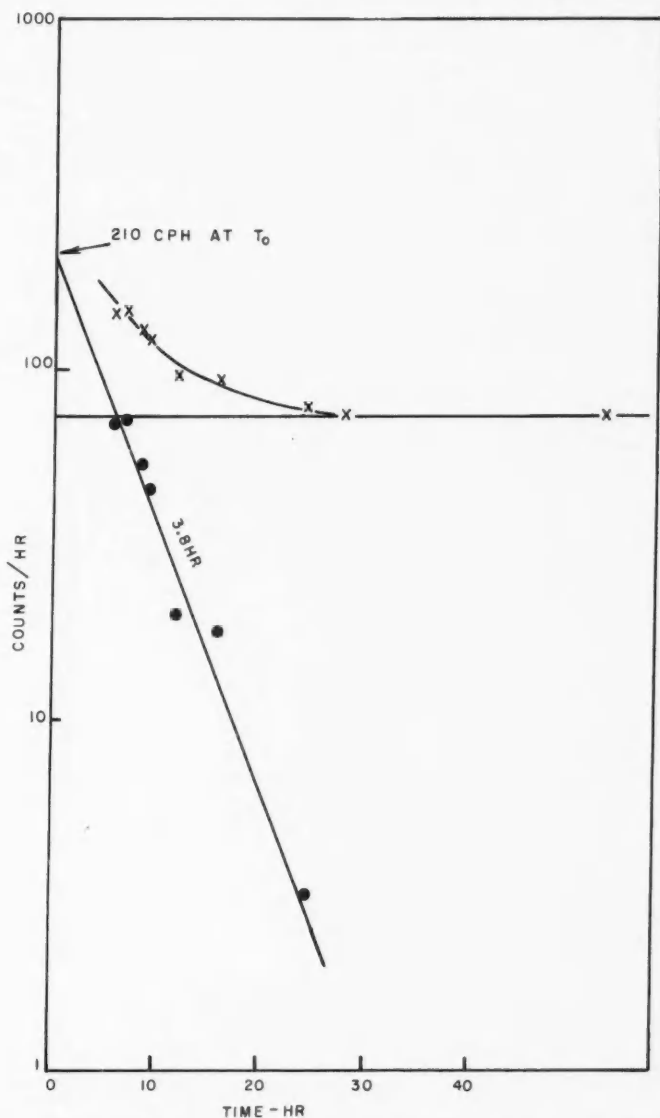


FIG. 3. First expt.: X counts/hour in channels 50-60; ● long-lived component subtracted.

N_{91} = total number of atoms of Y^{91} determined by comparison with a smaller source of the same sample whose activity was measured in a calibrated Geiger counter.

Then

$$\sigma_{91} = \frac{6800/0.327}{7.03 \times 10^{10} \times 6.45 \times 10^{13} \times 3600} = 1.27 \times 10^{-24} \text{ cm}^2,$$

where $F = 6.45 \times 10^{13}$ neutrons/cm² sec,

$$N_{91} = 7.03 \times 10^{16} \text{ atoms},$$

$(N\lambda)_{92} = 6800/0.327$ dis. per hr where the factor 0.327 represents the fraction of saturation reached during irradiation.

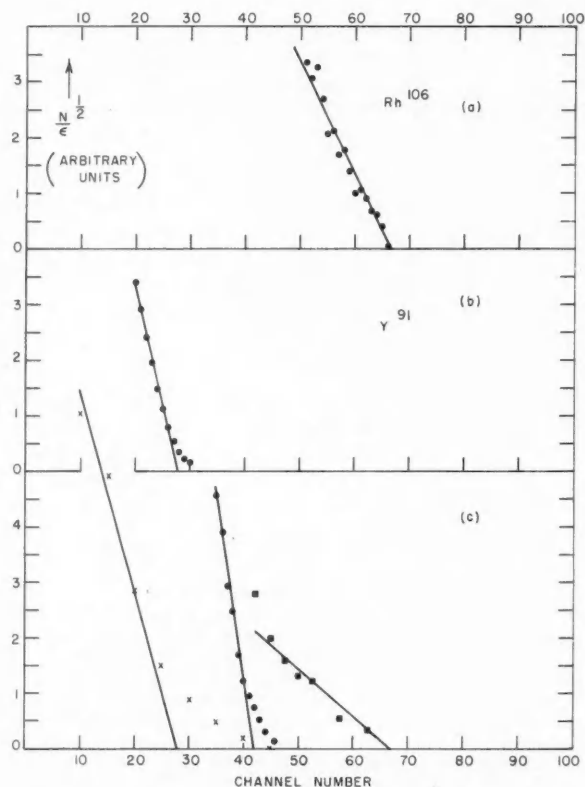


FIG. 4. (a) \bullet Rh^{106} at time of second expt.; cutoff channel 66.6; energy/channel = 53 kev. (b) \bullet Y^{91} spectrum prior to second expt.; cutoff channel 27.8; energy/channel = 55.4 kev (estimated cutoff for $Y^{90} = 41$). (c) Second expt.: \times original scan, Y^{91} cutoff channel 28, energy/channel = 55 kev; \bullet original scan $\times 10$, minus Y^{91} contribution, Y^{90} cutoff channel 42; \blacksquare original scan $\times 100$, minus Y^{91} and Y^{90} contributions, Y^{92} cutoff channel 68.

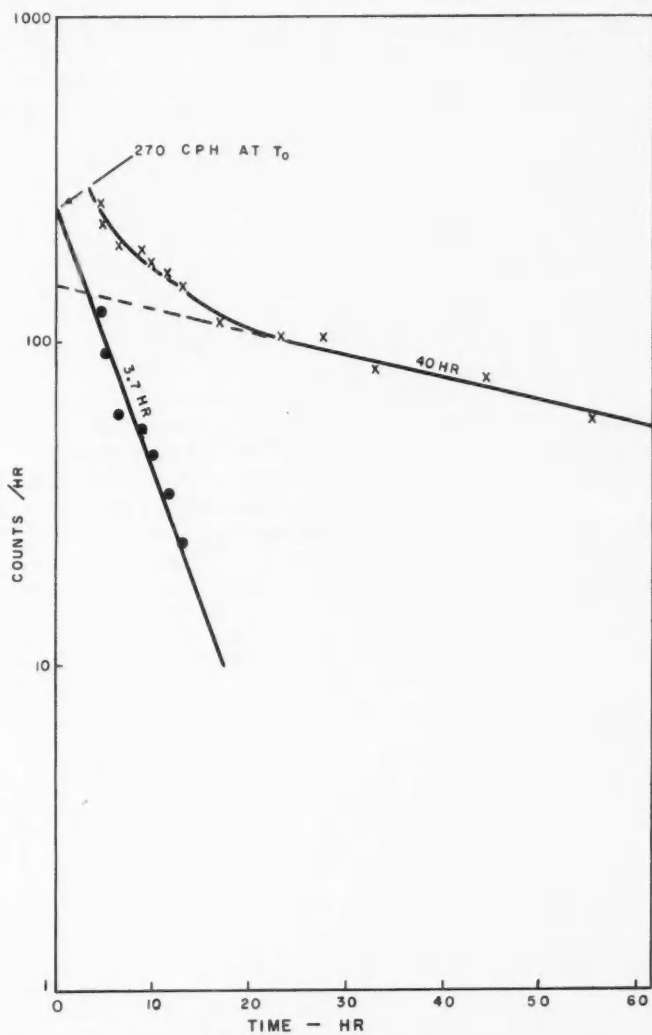


FIG. 5. Second expt.: X total counts/hour in channels 46-60; ● 40-hour component subtracted.

Unfortunately, as a result of the choice of too high a discriminator setting the counting rates obtained by the method 1 outlined earlier were so low that analysis of the data was impossible. A lower setting, yielding higher counting rates, but possibly including some longer-lived low energy components, was planned for the second experiment.

D. Second Y^{91} Cross-section Measurement

Figure 4(c) is a Fermi-Kurie plot of the first scan of the source (approximately 4.5 hours from the end of the 7-hour irradiation). As shown in Figs. 4(a) and (b) a shift in gain of the amplifier between experiments had been sufficient to make an appreciable change in the cutoff channels for the energies checked. Since the Y^{90} cutoff had moved down to channel 42 it was decided that channels 46-60 could safely be summed for the hard-component decay curve, thus partially compensating for the decreased counting efficiency measured in channels 50-60. Figure 5 shows the decay curve so obtained, and the 3.7-hour activity remaining after the subtraction of a 40-hour activity. This longer-lived component probably results from Y^{90} pile-up, plus Y^{91} (1.54 Mev), and Y^{90} (2.27 Mev) adding to give an apparent 3.8-Mev β -particle. (Since the sample of Y^{91} used was considerably smaller than that of the previous experiment the irradiation time had been increased by a factor of 3.5; hence the Y^{90} contamination was much larger in this instance.) By extrapolating the 3.7-hour component of the activity to t_0 (270 counts/hr) as in the previous case, and using the Rh efficiency obtained from this experiment, a value of 9200 dis./hr Y^{92} at t_0 was obtained.

Figure 6 shows the decay observed using a discriminator as outlined pre-

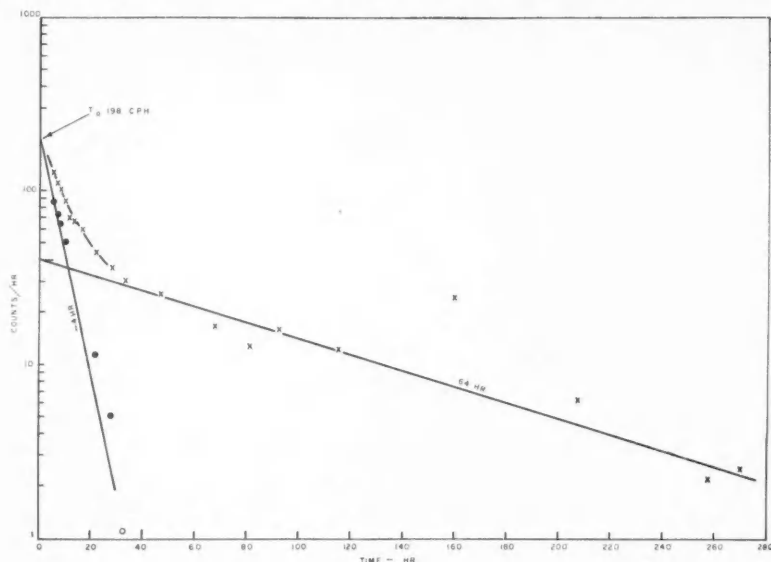


FIG. 6. Second expt.: X decay at discriminator setting yielding 2.35% efficiency for 3.6 Mev; ● 64-hour component subtracted.

viously. Subtraction of a 64-hour background (Y^{90}) left a component of ~ 4 -hour half-life, which may be inferred from the data to be Y^{92} . Extrapolation of this component activity to t_0 (198 counts/hr), and use of the Rh efficiency measured for this discriminator setting has led to a value of 11000 dis./hr Y^{92} at t_0 . This value is in reasonable agreement with that obtained by method 2, their average being 10,100 dis./hr.

Substituting this in equation (1), yields

$$\sigma_{92} = \frac{10,100/0.74}{4.1 \times 10^{10} \times 6.12 \times 10^{13} \times 3600} = 1.51 \times 10^{-24} \text{ cm}^2$$

where $F = 6.12 \times 10^{13}$ neutrons/cm² sec,

$N_{91} = 4.1 \times 10^{10}$ atoms,

$(N\lambda)_{92} = 10,100/0.74$.

Hence, for the two experiments the average value of the cross section of $Y^{91} = 1.4 \pm 0.3$ barns.

ACKNOWLEDGMENTS

The authors wish to thank Mr. W. D. Mackintosh of the Development Chemistry Branch for his assistance in the development of methods of source preparation prior to irradiation and Dr. J. C. D. Milton of the Physics Division, for his advice and assistance in both the design of the scintillation counter and its calibration.

REFERENCES

- AMES, D. P., BUNKER, M. E., and STARNER, J. W. 1952. Los Alamos Scientific Lab. Class. Report WASH 75. Unpublished.
 DZELEPOV, B. S. and PEKER, L. K. 1958. Decay schemes of radioactive nuclei (Academy of Sciences of the U.S.S.R. Press, Moscow).
 EASTWOOD, T. A., BAERG, A. P., BIGHAM, C. B., BROWN, F., CABELL, M. J., GRUMMITT, W. E., ROY, L. P., and SCHUMAN, R. P. 1958. Second United Nations International Conference on the Peaceful Uses of Atomic Energy. A/Conf. 15/P/203.
 JERVIS, R. E. 1957. A.E.C.L. Report CRDC-730.
 STROMINGER, D., HOLLANDER, J. M., and SEABORG, G. T. 1958. Revs. Modern Phys. **30**, 585.

NOTES

A NOTE ON HANSEN'S VECTOR WAVE FUNCTIONS

T. B. A. SENIOR

Almost a quarter of a century ago, Hansen (1935) proposed a method for generating solutions of the vector wave equation in any co-ordinate system in which the scalar wave equation is separable. The solutions are, essentially, a development of those employed by Mie (1908) in a study of scattering by a sphere, and were used by Hansen (1935, 1936, 1937) to analyze various problems dealing with the radiation from antennas. Because of these applications, Hansen was primarily concerned with spherical polar co-ordinates, and for the extension of the method to more general co-ordinate systems the credit is, perhaps, due to Stratton (1941).

The three vectors which Hansen proposed are

$$(1) \quad \mathbf{L} = \nabla \psi$$

$$(2) \quad \mathbf{M} = \nabla \wedge (\boldsymbol{\sigma} \psi)$$

$$(3) \quad \mathbf{N} = \frac{1}{k} \nabla \wedge \mathbf{M},$$

where ψ is a solution of the scalar wave equation

$$(4) \quad \nabla^2 \psi + k^2 \psi = 0$$

in the appropriate co-ordinate system, and $\boldsymbol{\sigma}$ is either a radial vector or, more generally, is such that \mathbf{M} and \mathbf{N} satisfy the vector wave equation

$$(5) \quad \nabla \wedge \nabla \wedge \mathbf{A} = k^2 \mathbf{A}.$$

It will be observed that \mathbf{L} has zero curl, and accordingly \mathbf{L} is suitable for the representation of an electrostatic or magnetostatic field. On the other hand, $\nabla \cdot \mathbf{L} = -k^2 \psi$, and therefore \mathbf{L} cannot appear in the representation of a solenoidal function except in the limit $k = 0$, whereas \mathbf{M} and \mathbf{N} can. Indeed, from equations (3) and (5), it follows that

$$(6) \quad \mathbf{M} = \frac{1}{k} \nabla \wedge \mathbf{N}$$

and since \mathbf{M} and \mathbf{N} are now related by curl operations, they are ideally suited to the representation of an electromagnetic field (\mathbf{E} , \mathbf{H}).

The above vectors have formed the basis for most attempts at the solution of vector scattering problems in electromagnetic theory. The ease with which a solution can be obtained in any given case is vitally effected by the choice of the vector $\boldsymbol{\sigma}$ in terms of which \mathbf{M} and \mathbf{N} are defined, and it is conceivable

that in some instances an unwise choice of δ could prevent the determination of a solution. When the co-ordinate system involved is more complicated than spherical, it therefore pays to devote some attention to the selection of δ before attempting the solution, and it is now of interest to know the possibilities which are available. Fortunately it is not difficult to find the most general form for δ .

For this purpose it is only necessary to consider the vector \mathbf{M} . From equation (2),

$$(7) \quad \mathbf{M} = \mathbf{L} \wedge \delta + \psi \nabla \wedge \delta,$$

giving

$$(8) \quad \nabla \wedge \mathbf{M} = k^2 \delta \psi + \mathbf{P},$$

where

$$(9) \quad \mathbf{P} = \nabla(\delta \cdot \mathbf{L}) - 2(\mathbf{L} \cdot \nabla)\delta + \mathbf{L} \nabla \cdot \delta + \psi \nabla \wedge \nabla \wedge \delta,$$

and hence

$$\nabla \wedge \nabla \wedge \mathbf{M} = k^2 \mathbf{M} + \nabla \wedge \mathbf{P}.$$

It now follows that if \mathbf{M} is to satisfy the vector wave equation, $\nabla \wedge \mathbf{P}$ must be zero, and since it is not identically zero for all δ , this condition, coupled with the fact that δ must be independent* of ψ , serves to determine the most general δ .

Since the vector \mathbf{P} is defined in terms of vector operators, it is sufficient to carry out the analysis using a particular set of co-ordinates and then use the invariance of these operators with respect to transformations of co-ordinates to give the specification of δ in general. For simplicity, Cartesian co-ordinates (x_1, x_2, x_3) are therefore chosen, and the independence of δ and ψ is employed by choosing in turn three simple forms for ψ .

If $\psi = \psi(x_1)$, the condition $\nabla \wedge \mathbf{P} = 0$ leads to six differential equations involving the rectangular components σ_i of δ . Similarly if $\psi = \psi(x_2)$ or $\psi = \psi(x_3)$, and the resulting set of 18 differential equations is compatible if and only if

$$\sigma_1 = \sigma_1(x_1), \text{ etc.}$$

and

$$\nabla^2 \delta = 0.$$

Hence

$$\sigma_1 = \alpha_1 x_1 + \beta_1,$$

$$\sigma_2 = \alpha_2 x_2 + \beta_2,$$

$$\sigma_3 = \alpha_3 x_3 + \beta_3,$$

where the α_i and β_i are constants, and each component of δ is now a first order linear function of the corresponding variable. Substituting into equation (9), we have

*Were δ not independent of ψ , the vectors \mathbf{M} and \mathbf{N} would have completely different forms for incident and scattered fields, and this would destroy much of their usefulness.

$$(10) \quad \mathbf{P} = \nabla(\boldsymbol{\delta} \cdot \mathbf{L}) + \sum_i \alpha_i (\mathbf{L} - 2L_i \hat{x}_i)$$

and since this is only irrotational if $\alpha_1 = \alpha_2 = \alpha_3 (= \alpha, \text{ say})$,

$$(11) \quad \boldsymbol{\delta} = \alpha(x_1 \hat{x}_1 + x_2 \hat{x}_2 + x_3 \hat{x}_3) + \beta_1 \hat{x}_1 + \beta_2 \hat{x}_2 + \beta_3 \hat{x}_3.$$

This represents the necessary and sufficient condition that \mathbf{M} (and therefore \mathbf{N}) satisfy the vector wave equation in Cartesian co-ordinates, and by using the invariance under transformation of co-ordinates it now follows that the most general form for $\boldsymbol{\delta}$ in any co-ordinate system consists of a radial vector \mathbf{R} , together with a set of constant (unit) vectors. It has been known for a long time that both radial and constant vectors are possible, but the above proof is valuable in showing that no other forms for $\boldsymbol{\delta}$ are permissible. It will be observed that only with Cartesian co-ordinates are the unit vectors in the direction of the co-ordinate axes.

If equation (11) is interpreted in terms of a general co-ordinate system, $\boldsymbol{\delta}$ is such that

$$\nabla \wedge \boldsymbol{\delta} = 0,$$

$$\nabla \cdot \boldsymbol{\delta} = 3\alpha$$

and

$$(\mathbf{L} \cdot \nabla) \boldsymbol{\delta} = \alpha \mathbf{L},$$

so that

$$\mathbf{P} = \nabla(\alpha\psi + \boldsymbol{\delta} \cdot \mathbf{L}).$$

Hence

$$(12) \quad \mathbf{M} = \mathbf{L} \wedge \boldsymbol{\delta},$$

$$(13) \quad k\mathbf{N} = k^2 \alpha\psi + \nabla(\alpha\psi + \boldsymbol{\delta} \cdot \mathbf{L}),$$

and the fact that the second group of terms on the right-hand side of (13) can be written as a single gradient is necessary if \mathbf{M} is to satisfy equation (5).

In any practical application of Hansen's vectors it is unlikely that $\boldsymbol{\delta}$ will be required in its most general form (11), and it is usual to take one of α , β_1 , β_2 , and β_3 unity with all the others zero. One of the most important cases is obtained by taking $\alpha = 1$ so that $\boldsymbol{\delta} = \mathbf{R}$. This is the standard choice for the scattering of an electromagnetic wave by a sphere (see, for example, Stratton 1941), and also proves convenient in the corresponding problem for an ellipsoid (Senior 1961).

A final point concerns the behavior of the vectors in the static limit. If $\psi \rightarrow \phi$ as $k \rightarrow 0$, where $\nabla^2 \phi = 0$, then

$$\mathbf{L} \rightarrow \mathbf{S}$$

where \mathbf{S} is the electrostatic (or magnetostatic) field defined as $\mathbf{S} = \nabla\phi$. Also

$$\mathbf{M} \rightarrow \mathbf{S} \wedge \boldsymbol{\delta}$$

and

$$k\mathbf{N} \rightarrow \alpha\mathbf{S} + \nabla(\boldsymbol{\delta} \cdot \mathbf{S}),$$

so that in the limit of zero frequency the field cannot be represented in terms of the vectors \mathbf{N} alone. This has important consequences in any attempt to determine the low frequency (or Rayleigh) expansion for the field, and implies that in a general co-ordinate system both \mathbf{M} and \mathbf{N} vectors are necessary to match the static field. On the other hand, if spherical polar co-ordinates are employed with $\mathbf{e} = \mathbf{R}$,

$$\psi + \mathbf{e} \cdot \mathbf{L} = \frac{\partial}{\partial R} (R\psi)$$

and since ψ is a function of R only in the combination kR ,

$$\frac{\partial}{\partial R} (R\psi) \rightarrow \text{const.} \times \phi$$

as $k \rightarrow 0$. In this co-ordinate system therefore,

$$k\mathbf{N} \rightarrow \text{const.} \times \mathbf{S}$$

and the static field can be represented entirely by the vectors \mathbf{N} .

ACKNOWLEDGMENT

The work described in this paper was carried out for the Air Force Cambridge Research Center under Contract AF 19(604)-6655.

HANSEN, W. W. 1935. *Phys. Rev.* **47**, 139.

— 1936. *Physics*, **7**, 460.

— 1937. *J. Appl. Phys.* **8**, 282.

MIE, G. 1908. *Ann. Phys.* **25**, 377.

SENIOR, T. B. A. 1961. To be published.

STRATTON, J. A. 1941. *Electromagnetic theory* (McGraw-Hill, New York).

RECEIVED AUGUST 12, 1960.

RADIATION LABORATORY,

UNIVERSITY OF MICHIGAN,

ANN ARBOR, MICHIGAN, U.S.A.

THE FRANCK-CONDON FACTOR ($q_{v'v''}$) ARRAY TO HIGH VIBRATIONAL QUANTUM NUMBERS FOR THE $\text{O}_2(\text{B}^2\Sigma_u^- - \text{X}^2\Sigma_g^+)$ SCHUMANN-RUNGE BAND SYSTEM

R. W. NICHOLLS*

The Schumann-Runge band system of O_2 is unusual in view of the relatively large ($\sim 0.4 \text{ \AA}$) difference between the equilibrium internuclear separations (r_e) of the two electronic states concerned. The Franck-Condon principle thus implies that for this system the strongest bands lie on a very wide quasi parabola in the $v'-v''$ plane. The limbs of the curve lie mainly at large values of v' and v'' along the $v'' = 0$ and $v' = 0$ progressions respectively, and the

*Temporarily on leave of absence from the University of Western Ontario.

curve avoids the (0,0) region. This primary "Condon parabola" and the subsidiary parabolae are indicated in Table II.

The accurate computation of arrays of Franck-Condon factors (vibrational overlap integral squares ($|\int \psi_v \psi_{v'} dr|^2$)) for such transitions which involve relatively large Δr_e and thus high values of v' and v'' presents two serious problems. The first, which is very common in quantum mechanics, is the severe cancellation between the often almost equal positive and negative parts of the integrand. The second is the inability of the empirical analytic models of molecular potentials, such as the Morse potential, to represent true molecular potentials particularly at the regions of very high vibrational quantum number. The form of the wave functions involved in the overlap integral is, of course, very much determined by the potential used.

The first of these problems has been overcome in some cases by direct computation (using desk calculators) carrying as many significant figures as is possible (Jarman and Nicholls 1954) and in others by the development of approximate methods (which are most accurate at low values of $v' + v''$) in which the remainder left after cancellation is evaluated (Fraser and Jarman 1953; Jarman and Fraser 1953; Fraser 1954). A large number of important band systems have been treated by such methods (Jarman, Fraser, and Nicholls 1953, 1955; Fraser, Jarman, and Nicholls 1954; Nicholls, Fraser, and Jarman 1959; Nicholls, Fraser, Jarman, and McEachran 1960). The second problem is harder to overcome as all of the current methods for evaluating Franck-Condon factors require analytic wave functions specific to some form of potential. Recent numerical studies of the form of molecular potentials using the Klein-Dunham method (Jarman 1959, 1960) or the very similar Rydberg-Klein-Rees method (Vanderslice, Mason, Maisch, and Lippincott 1959; Vanderslice, Mason, and Lippincott 1959; Vanderslice, Mason, and Maisch 1959, 1960) to delineate the profile of vibrational oscillator turning points show that the Morse potential is a very fair representation of molecular potentials at low quantum numbers in many cases, but that each case has to be considered on its own merits.

Ultimately, of course, it will be necessary to obtain numerically the wave functions appropriate to the numerical potentials for computation of exact Franck-Condon factors, and work on this is in progress.

Arrays of Franck-Condon factors for the O_2 Schumann-Runge system have been computed with various degrees of accuracy and completeness by a number of workers over the past few years using a variety of approximate methods. This work is summarized in Table I. Each of these calculations is subject to some inaccuracy arising from limitations of the method used, from inappropriateness of the potential employed, and incompleteness in the number of bands studied.

The facilities of the N.B.S. Computation Laboratory including an IBM-704 computer have therefore been used to compute a complete array ($0 < v' < 21$; $0 < v'' < 21$) of Franck-Condon factors for all the possible bands using a Morse model for potentials in each case. The straightforward method used has previously been used by Jarman and Nicholls (1954) for the N_2 first and

TABLE I
Franck-Condon factor arrays for the O₂ Schumann-Runge band system

Author	Method	Extent of table	Comments
Pillow (1950)	Distorted simple harmonic oscillator, numerical integration	$v' = 0$; $v'' = 6-15$ 1 5-16 2 4-16 3 3-16 4 3-10 5-7 2-10 8-10 0-10	Table of q/λ^4 intensities in emission at infinite temperature. Table of q/λ^4 also given at 3000° K. Tables of q/λ intensity in absorption given at 300° K, 1350° K, 2300° K, and infinite temperature. Hand-calculated
Pillow (1952)	Distorted simple harmonic oscillator, numerical integration	$v' = 0$; $v'' = 7-16$ 1 6-16 2 5-12, 14-16 3 5-11, 13-15	Table of q/λ^4 intensities in emission at infinite temperature. Hand-calculated
Fraser, Jarman, and Nicholls (1954)	Fraser-Jarman (1953) analytic integration method Morse model	$v' = 0-3$; $v'' = 0-25$ 4-15 0-2	Hand-calculated
Jarman, Fraser, and Nicholls (1955)	Fraser-Jarman (1953) analytic integration method Morse model	$v' = 0-15$ $v'' = 0-2$	Very small values of q in region of table of specific use in absorption studies. Hand-calculated
Nicholls, Fraser, and Jarman (1959)	Fraser-Jarman (1953) analytic integration method Morse model	$v' = 0-3$; $v'' = 0-21$ $v' = 4-15$; $v'' = 0-2$	Data also given on λ , q/λ^4 , p (relative vibrational transition probabilities). Electronically computed
Keck, Camm, Kivel, Wentinck (1959)	An empirical approximation used which employs Morse wave functions for $\psi_{v'}$ and delta functions $\delta(r'_{1,2})$ at the oscillator turning points $r'_{1,2}$ of the lower state for $\psi_{v'}$	No table specifically given, Frank-Condon factors used in other calculations	Method implies $q_{v',v''} = \text{const } \psi_{v'}^2(r'_{1,2})$

TABLE II

Franck-Condon factor array to high vibrational quantum numbers for the Schumann-Runge band system of O_2 . Primary and subsidiary Condon "parabola" are indicated, and entries at local maxima through which the parabola pass are italicized. The negative number in each entry is the power of 10 by which it is multiplied

v'	0	1	2	3	4	5	6	7	8	9	10
0	3.3636-0	9.1726-8	1.3505-6	1.2033-5	7.7140-5	3.7873-4	1.4800-3	4.7231-3	1.2534-2	2.8020-2	5.3261-2
1	3.9676-8	1.0381-6	1.2945-5	1.0219-4	5.7192-4	2.4074-3	7.8855-3	2.0493-2	4.2622-2	7.0841-2	9.2702-2
2	2.4404-7	5.7887-6	6.4721-5	4.5190-4	2.2003-3	7.8859-3	2.1377-2	4.4199-2	6.8987-2	7.8196-2	5.8045-2
3	1.0427-6	2.2432-5	2.2478-4	1.3859-3	5.8435-3	1.7073-2	3.8964-2	6.1890-2	6.7163-2	4.2565-2	8.0346-3
4	3.4788-6	6.7902-5	6.0943-4	3.3101-3	1.2022-2	3.0330-2	5.3060-2	6.1176-2	9.9368-2	6.5928-3	4.8018-3
5	9.6580-6	1.7110-4	1.3745-3	6.5583-3	2.0379-2	4.2238-2	6.6541-2	1.8779-2	1.0217-2	2.3054-3	2.9640-2
6	2.3224-5	3.7355-4	2.6835-3	1.1212-2	2.9558-2	4.9398-2	4.7668-2	1.8745-2	2.4519-2	2.0252-2	5.7544-2
7	4.9711-5	7.2621-4	4.6005-3	1.6983-2	3.7559-2	4.9002-2	3.0040-2	2.8849-2	8.9576-3	5.8909-2	2.0936-2
8	9.6625-5	7.3428-3	2.3230-2	3.2320-2	4.2587-2	4.1577-2	1.3901-2	7.4736-4	2.3072-2	2.8295-2	3.1437-3
9	1.7312-4	2.0880-3	1.0652-2	2.9007-2	4.3413-2	2.9670-2	2.8284-3	8.7805-3	2.9806-2	1.3134-2	1.4009-3
10	2.8930-4	3.1716-3	1.4394-2	3.3722-2	4.0000-2	1.7010-2	9.6842-5	1.9035-3	2.4320-2	1.7349-3	1.1930-2
11	4.5511-4	4.5507-3	1.8283-2	3.6448-2	3.3274-2	6.8669-3	4.1409-3	2.4509-2	1.3329-2	9.7568-4	2.1221-2
12	6.7919-4	6.1581-3	2.1993-2	3.6947-2	2.4773-2	1.1980-3	1.1258-2	2.3748-2	3.7310-3	8.0403-3	2.1145-2
13	9.0700-4	7.9824-3	3.5206-2	3.5264-2	1.6158-2	1.2053-4	1.7641-2	1.7500-2	1.4795-5	1.5820-2	1.3387-2
14	1.3229-3	9.5340-3	2.7064-2	3.1758-2	8.8051-3	2.5852-3	2.0894-2	9.5999-3	2.2594-3	1.8983-2	4.0266-3
15	1.7436-3	1.1923-2	2.9196-2	2.6995-2	3.5617-3	6.9014-3	2.0397-2	3.2778-3	7.6300-3	1.6489-2	2.0345-4
16	2.2239-3	1.3854-2	2.9744-2	2.1615-2	7.0127-4	1.1398-2	1.6938-2	2.3993-4	1.2745-2	1.0622-2	1.2745-3
17	2.7558-3	1.5639-2	2.9329-2	1.6222-2	1.8546-5	1.4841-2	1.1986-2	5.3370-4	1.5866-2	4.6352-3	5.6573-3
18	3.3202-3	1.7199-2	2.8097-2	1.1299-2	1.0010-3	1.6907-2	7.0243-3	3.0986-3	1.4912-2	8.6967-4	1.0193-2
19	3.9072-3	1.8475-2	2.6120-2	7.1750-3	3.0097-3	1.6607-2	3.1183-3	6.4905-3	1.2098-2	6.0498-5	1.6048-2
20	4.8973-3	1.9450-2	2.3685-2	4.0129-3	5.4277-3	1.5152-2	7.7446-3	9.5019-3	8.2156-3	1.6173-3	1.3263-2
21	5.0733-3	2.0044-2	2.0940-2	1.8339-3	7.7662-3	1.2743-2	2.2666-6	1.1559-2	4.4952-3	4.9257-3	9.9517-3

TABLE II (Concluded)

ν'	11	12	13	14	15	16	17	18	19	20	21
0	8.5671-2	1.2151-1	1.4648-1	1.5285-1	1.3786-1	1.0759-1	7.2104-2	4.1588-2	2.0512-2	8.5997-3	3.0411-3
1	9.1951-2	6.2856-2	2.1844-2	1.0257-4	1.8334-2	6.7037-2	1.1871-1	1.5009-1	1.1805-1	7.5084-2	4.1375-2
2	2.0000-2	7.3533-7	2.1395-2	6.0732-2	6.9694-2	3.5561-2	1.9243-3	1.5355-2	7.0036-2	1.1824-1	1.8452-1
3	3.6442-3	3.5436-2	5.6165-2	3.1874-2	1.1283-3	1.7764-2	6.9376-2	5.2714-2	1.7704-2	1.9012-3	4.9349-2
4	3.5497-2	4.5615-2	1.5187-2	1.5192-3	3.3574-2	4.9767-2	1.0873-2	2.1202-3	4.1768-2	6.4767-2	2.8002-2
5	4.0054-2	1.1488-2	3.1190-3	3.4247-2	3.6109-2	3.7200-3	1.3003-2	4.7616-2	2.8565-2	1.2399-5	3.5960-2
6	1.4153-2	1.5408-3	2.9194-2	3.0501-2	1.6898-3	1.6769-2	1.0045-2	1.1688-2	6.0358-3	4.8709-2	3.1371-2
7	3.5905-7	2.0682-2	3.0640-2	3.0113-3	1.3052-2	3.4378-2	8.0148-3	8.6070-3	3.8518-2	1.4719-2	4.9956-3
8	1.0329-2	2.9746-2	7.8961-3	6.2085-3	3.0316-2	1.0138-2	5.7265-3	5.2809-2	1.0979-2	6.9141-3	3.7762-2
9	2.4219-2	1.4508-2	5.8060-4	2.3815-2	1.6070-2	1.2937-3	2.6919-2	1.3395-2	3.9868-3	3.1802-2	9.4771-3
10	2.3860-2	1.9694-3	1.2715-2	2.4668-2	4.5480-4	1.7952-2	1.9016-2	4.1577-4	2.5446-2	1.2415-2	5.5010-3
11	1.3076-2	1.9041-3	2.2911-2	7.2076-3	6.4555-3	2.8039-2	1.4750-3	1.5844-2	1.8382-2	7.9941-4	2.6187-2
12	1.8049-3	1.1752-2	1.7579-2	1.0321-5	1.8677-2	9.7814-3	4.5501-3	2.2209-2	1.1380-3	1.7116-2	1.4938-2
13	7.2684-3	1.3755-2	6.1763-3	6.3663-3	1.8538-2	1.5729-4	1.6968-2	9.3470-3	5.3332-3	2.0722-2	1.1138-4
14	6.8563-3	1.6846-2	9.8265-5	1.5255-2	8.2706-3	4.6217-3	1.7841-2	7.5768-5	1.7568-2	6.5714-3	8.5787-3
15	1.3583-2	9.1074-3	2.8376-3	1.6752-2	5.8329-4	1.3659-2	7.9002-3	5.1825-3	1.6216-2	1.3173-4	1.5685-2
16	1.6971-2	2.1520-3	9.5466-3	1.0663-3	1.7071-3	1.6660-2	4.4515-4	1.3908-2	5.6509-3	7.7287-3	1.2930-2
17	1.3305-2	2.8063-5	1.5966-2	3.3389-3	7.9905-3	1.0195-2	2.0040-3	1.4765-2	1.4320-5	1.5060-3	2.3634-3
18	7.9653-3	2.5359-3	1.3277-2	3.8679-5	1.2740-2	3.0448-3	8.3632-3	8.2711-3	3.6269-3	1.2776-2	6.9412-4
19	2.9867-3	6.9176-3	8.9273-3	1.6452-3	1.2407-2	9.4048-6	1.4475-2	1.0953-3	1.0040-2	5.0972-3	8.8776-3
20	3.1174-4	1.0322-2	3.9232-3	5.7175-3	8.3954-3	1.8981-3	1.1365-2	1.4158-4	1.3599-2	2.0001-4	1.4044-2
21	2.8823-4	1.1276-2	6.9827-4	9.2104-5	3.5587-3	5.9906-3	6.8169-3	3.1689-3	9.4255-3	1.5109-3	1.1182-2

second positive systems. The zeroth vibrational wave function ψ_0 was computed at 0.01 Å intervals for each of the two potentials using the analytic form of this function given by Morse (1929). A recursion relation (Nicholls, Jarman, and Fraser 1953; Fraser, Jarman, and Henderson 1959) was then used to build up, step by step, numerical wave functions at 0.01 Å intervals for all known higher vibrational levels. Overlap integrals of all pairs of wave functions between the two states were then evaluated numerically using the trapezoidal and Simpson rules. Agreement between the results of these two methods of integration was excellent, which showed that the interval of integration was sufficiently small. The results of this computation are shown in Table II.

It is of course realized that the Morse potential is not a particularly realistic representation for the $B^3\Sigma_u^-$ state of O_2 specifically at high vibrational quantum numbers, in view of the relatively large value of w, y_e (Brix and Herzberg 1952), some evidence of predissociation in it (Carroll 1959), and a comparison between the Morse and "true" numerical potential (Vanderslice, Mason, and Maisch 1960; Jarman 1960). Nevertheless when used in conjunction with intensity measurements in emission (for which the $v' = 0, 1, 2, 3$ progressions are the most important) the data of Table II are reliable and realistic. They have been recently used by Hébert (1960) for the interpretation of intensity measurements in emission for this system. Full details of this work will be published shortly.

These calculations represent the first of a series for which the IBM-704 program is being used to evaluate arrays of Franck-Condon factors and r -centroids for important molecular transitions. Vibrational wave functions calculated during this work are on file on magnetic tape.

The author's sincere thanks are due to Miss I. Stegun and Miss R. Zucker of the N.B.S. Computation Laboratory for writing and testing the program and to Mr. W. R. Jarman for providing details of the method of computation in a form suitable for programming.

- BRIX, P. and HERZBERG, G. 1954. *Can. J. Phys.* **32**, 110.
 CARROLL, P. K. 1959. *Astrophys. J.* **129**, 794.
 FRASER, P. A. 1954. *Proc. Phys. Soc. A*, **67**, 939.
 FRASER, P. A. and JARMAN, W. R. 1953. *Proc. Phys. Soc. A*, **66**, 1145.
 FRASER, P. A., JARMAN, W. R., and NICHOLLS, R. W. 1954. *Astrophys. J.* **119**, 286.
 FRASER, P. A., JARMAN, W. R., and HENDERSON, G. 1959. Scientific Report No. 2, Contract AF 19(604)-4560, University of Western Ontario.
 HÉBERT, G. R. 1960. Ph.D. Thesis, University of Western Ontario.
 JARMAN, W. R. 1959. *J. Chem. Phys.* **31**, 1137.
 ——— 1960. *Can. J. Phys.* **38**, 217.
 JARMAN, W. R. and FRASER, P. A. 1953. *Proc. Phys. Soc. A*, **66**, 1153.
 JARMAN, W. R. and NICHOLLS, R. W. 1954. *Can. J. Phys.* **32**, 201.
 JARMAN, W. R., FRASER, P. A., and NICHOLLS, R. W. 1953. *Astrophys. J.* **118**, 228.
 ——— 1955. *Astrophys. J.* **122**, 55.
 KECK, J. C., CAMM, J. C., KIVEL, B., and WENTINCK, T., JR. 1959. *Ann. Phys.* **7**, 1.
 MORSE, P. M. 1929. *Phys. Rev.* **34**, 57.
 NICHOLLS, R. W., JARMAN, W. R., and FRASER, P. A. 1953. *Can. J. Phys.* **31**, 1019.
 NICHOLLS, R. W., FRASER, P. A., and JARMAN, W. R. 1959. *Combustion and Flame*, **3**, 13.
 NICHOLLS, R. W., FRASER, P. A., JARMAN, W. R., and MCEACHRAN, R. P. 1960. *Astrophys. J.* **131**, 399.

- PILLOW, M. E. 1950. *Proc. Phys. Soc. A*, **63**, 940.
——— 1952. *Proc. Phys. Soc. A*, **65**, 858.
VANDERSLICE, J. T., MASON, E. A., MAISCH, W. G., and LIPPINCOTT, E. R. 1959. *J. Mol. Spectroscopy*, **3**, 17.
VANDERSLICE, J. T., MASON, E. A., and LIPPINCOTT, E. R. 1959. *J. Chem. Phys.* **30**, 129.
VANDERSLICE, J. T., MASON, E. A., and MAISCH, W. G. 1959. *J. Chem. Phys.* **31**, 738.
——— 1960. *J. Chem. Phys.* **32**, 515.

RECEIVED AUGUST 12, 1960.
NATIONAL BUREAU OF STANDARDS,
WASHINGTON 25, D.C.

LETTERS TO THE EDITOR

Under this heading brief reports of important discoveries in physics may be published. These reports should not exceed 600 words and, for any issue, should be submitted not later than six weeks previous to the first day of the month of issue. No proof will be sent to the authors.

Frequency Measurement of Standard Frequency Transmissions^{1,2}

Measurements are made at Ottawa, Canada, using N.R.C. caesium-beam frequency resonator as reference standard (with an assumed frequency of 9 192 631 770 c.p.s.). Frequency deviations from nominal are quoted in parts per 10¹⁰. A negative sign indicates that the frequency is below nominal.

Date, September 1960	GBR, 16 kc/s				WWVB, 60 kc/s
	MSF, 60 kc/s	5-hour average*	24-hour average		
1	-159	-158	N.M.		-150
2	-161	N.M.	N.M.		-149
3	-159	-158	N.M.		N.M.
4	N.M.	N.M.	N.M.		N.M.
5	N.M.	N.M.	N.M.		N.M.
6	-160	N.M.	N.M.		-148
7	-150	-154	-155		-148
8	-157	-154	-156		-146
9	-154	-151	-155		N.M.
10	-156	-155	-155		N.M.
11	-159	-157	-157		N.M.
12	-154	-158	-151		-144
13	-153	N.M.	N.M.		-144
14	-162	-146	-144		-146
15	-147	-148	-146		-143
16	-148	-153	-149		-144
17	-150	-148	-151		N.M.
18	-161	-154	-154		N.M.
19	-147	N.M.	N.M.		-140
20	-146	-151	-150		-141
21	-148	-151	-151		-140
22	-145	-147	-147		-139
23	-148	-154	-150		-140
24	N.M.	-152	N.M.		N.M.
25	N.M.	N.M.	N.M.		N.M.
26	-149	N.M.	N.M.		-138
27	-145	-149	-149		-137
28	-148	-149	N.M.		-137
29	-146	-142	N.M.		-136
30	-145	-146	-148		-137
Midmonthly mean	-163	-152	-152		-142
Midmonthly mean of WWV	-142				

NOTE: N.M. no measurement.

*Time of observations: 0.100 to 04.30 and 11.30 to 13.00 U.T.

RECEIVED OCTOBER 17, 1960.
DIVISION OF APPLIED PHYSICS,
NATIONAL RESEARCH COUNCIL,
OTTAWA, CANADA.

S. N. KALRA

¹Issued as N.R.C. No. 6021.

²Cf. Kalra, S. N. 1959. Can. J. Phys. **37**, 1328.

Can. J. Phys. Vol. 38 (1960)

Spin Rate of the Satellite Echo I as Determined by a Tracking Radar

Echo I has been observed on nine occasions at the Prince Albert Radar Laboratory,¹ (PARL), since its launch on August 12, 1960. The radar signal reflected from the satellite is detected in two orthogonal channels, right and left circular polarization. Transmitted polarization is left circular. Since reflection of a circularly polarized radio signal changes the direction of rotation of the polarization, the main component of the received signal has right circular polarization. However, because of the finite isolation between the two channels, and some depolarization of the signal upon reflection, power is detected in the left circular channel as well.

On all passes tracked at PARL (Table I) a regular fast scintillation has been observed in the received signal reflected from the satellite. The scintillation rate remained constant at 134 fades per minute to pass number 131. On the next pass observed, number 217, the scintillation rate had changed to 154 fades per minute. During the early revolutions of Echo I the fades were small in amplitude (0-3 db). On pass 131, fades as great as 10 db were observed in both channels. However, on pass 217 the fading in the right circular channel had decreased to about 5 or 6 db. No fast fading was observed in the left circular channel. Instead slow deep fading with a period of about 30 seconds was observed. This period of fading is thought to correspond to the period of rotation of the satellite.

TABLE I

Date	Revolution No.	Scintillation rate (per minute)	Rotation rate (r.p.m.)
August 12	1	134	1.63
" 12	2	"	"
" 13	9	"	"
" 13	10	"	"
" 13	11	"	"
" 13	12	"	"
" 16	46	"	"
" 23	131	"	"
" 30	217	154	1.88

The rotational period, or spin rate, of the satellite may be determined by studying the scintillations of the received signal if the method of fabricating the balloon is taken into account. The balloon is made up of 82 gores. If it is assumed that

(a) the satellite is rotating about an axis which permits the sequential observation of all 82 gores each rotation,

(b) the scintillations in the received radar signal are caused by the motion of the gores,

(c) there is a one-to-one correspondence between each observed fade and the opposition of a gore,

then the spin rate of the satellite can be calculated. Scintillation rates of 134 fades per minute (pass 131) and 154 fades per minute (pass 217) correspond to periods of rotation of 36.8 seconds and 31.9 seconds respectively. The agreement between the calculated period of rotation for pass 217 and the observed period of deep fading in the right circular channel indicates that the assumptions made are valid.

Radar observations of Echo I indicate that between passes 131 and 217 the spin rate increased from 1.63 r.p.m. to 1.88 r.p.m. It is interesting to note that between these two observations the satellite first started passing into the earth's shadow. This may have caused the internal pressure of the gases inside the balloon to decrease, resulting in some shrinkage and/or deformation of the balloon. If it is assumed that angular momentum was conserved between the two observations, a decrease in radius of 7% required to account for the increased spin.

RECEIVED OCTOBER 19, 1960.
DEFENCE RESEARCH TELECOMMUNICATIONS ESTABLISHMENT,
PRINCE ALBERT RADAR LABORATORY,
PRINCE ALBERT, SASKATCHEWAN.

G. E. K. LOCKWOOD

¹Millstone-type radar.

Simultaneous Observations of Pulsations in the Geomagnetic Field and in Ionospheric Absorption

During the latter part of September 1959, a cosmic noise absorption monitor (sometimes called a riometer) and a magnetometer were operated at Saskatoon with the recording meters running at a sufficiently high chart speed (12 inches/hour) to permit fluctuations of a few seconds' duration to be resolved. The riometer, operating on a frequency of 34 Mc/s, is broadly similar to that described by Reid and Collins (1959) and the magnetometer is of the standard three-component fluxgate type described by Serson (1957) but only one (the H) component was recorded at high speed.

On the 20th and 21st of September, shortly after 7 a.m. local time, regular pulsations were recorded simultaneously on both of the records. The magnetic pulsations of amplitude 30–50 gamma, together with the simultaneously recorded pulsations in cosmic noise absorption, of amplitude 2.5–3 db, are shown in Figs. 1 and 2. The riometer record indicates the amount of absorption suffered by extraterrestrial radio waves as they traverse the ionosphere while the magnetometer record indicates the variations of the earth's magnetic field due, presumably, to currents located either in the lower ionosphere or at great distances from the earth. Cosmic noise absorption is usually attributed to abnormal increases in the electron density, collision frequency, or both at heights below about 95 km in the atmosphere.

It can be seen from the figures that for many cycles the geomagnetic pulsations remain in phase with the cosmic noise absorption fluctuations but there are occasions when the two phenomena appear to be exactly 180° out of phase. This occasional sudden change in phase would appear to rule out the possibility that the geomagnetic pulsations are a purely local phenomenon brought about by a local periodic increase of the conductivity of the lower ionosphere.

Jacobs and Obayashi (1958) have found experimental evidence in support of the suggestion that some magnetic pulsations are due to a toroidal hydromagnetic oscillation of the earth's outer atmosphere of the kind proposed by Dungey (1954). According to this picture the period of oscillation should change with geomagnetic latitude and for the geomagnetic latitude of Saskatoon (60.5° N.) should be about 2.5 minutes. The observed periods, ranging from 2.5 to 3.0 minutes, are in good agreement with the predicted value and suggest that the pulsations are, in fact, due to toroidal hydromagnetic oscillations of the outer atmosphere.

Akasofu (1959) has concluded on theoretical grounds that the energy dissipated in the ionosphere by hydromagnetic waves would cause only a negligible rise in temperature, so that it is necessary to look for some indirect connection between these two simultaneously occurring phenomena. One possibility that comes to mind is that extra ionization in the lower ionosphere (observed by the riometer) is being caused by the periodic influx of particles. These particles could, in turn, be accelerated during some part of each cycle of the hydromagnetic oscillation of the outer atmosphere.

The author is grateful to Dr. P. A. Forsyth for helpful suggestions and guidance in the course of this work and to Dr. A. Kavadas for useful discussions. This work is supported in part by the Defence Research Board under Grant 9511-25 and in part by the National Research Council under Grant T-123.

- AKASOFU, S. 1959. Proc. Symposium on Physical Processes in the Sun-Earth Environment, Defence Research Telecommunications Establishment, Ottawa.
DUNGEY, J. W. 1954. Pennsylvania State University Reports, Nos. 57 and 69.
JACOBS, J. A. and OBAYASHI, T. 1958. Geophys. J. **1**, 53.
REID, G. C. and COLLINS, C. 1959. J. Atmospheric and Terrest. Phys. **14**, 63.
SERSON, P. H. 1957. Can. J. Phys. **35**, 1387.

RECEIVED OCTOBER 24, 1960.
INSTITUTE OF UPPER ATMOSPHERIC PHYSICS,
UNIVERSITY OF SASKATCHEWAN,
SASKATOON, SASKATCHEWAN.

SYED ZIAUDDIN*

*On leave of absence from the University of Mysore, India.

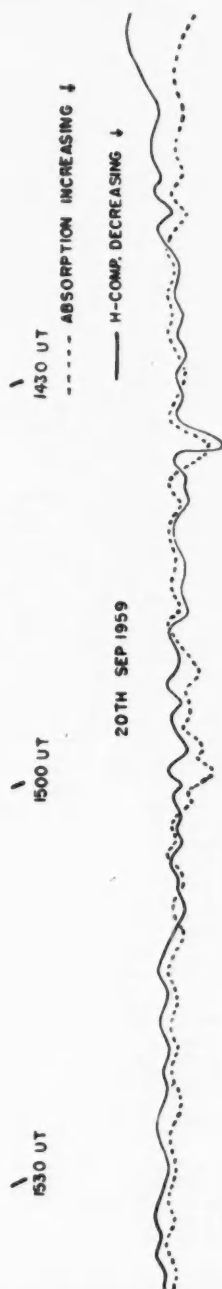


FIG. 1

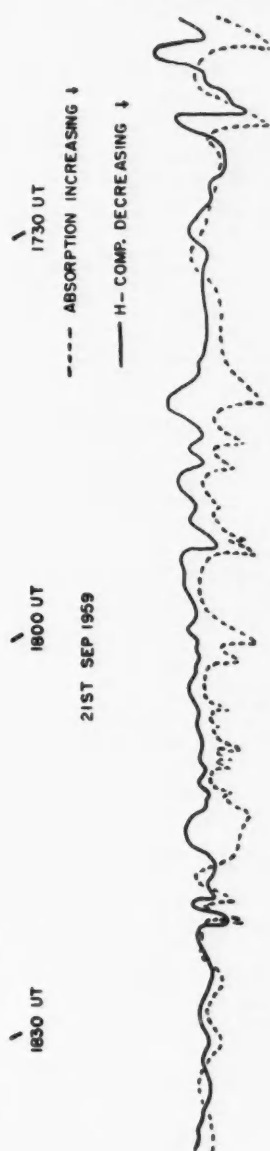


FIG. 2

CONTENTS OF VOLUME 38

- Adhav, R. S.** On the optical and electrical properties of semitransparent copper films, 1570.
- Alexander, T. K.** See Walker, W. H., 57.
- Allin, E. J.** See Gush, H. P., 176.
- Armstrong, R. A. and Szabo, A.** Relaxation in ruby, 1304.
- Artina, A. and Law, M. E.** The decay of Pm^{140} , 1577.
- Aust, K. T.** Relative energies of tilt-type subboundaries in aluminum, 547.
- Bailey, D. K. and Pomerantz, M. A.** The cosmic ray increase of 17 July 1959, 332.
- Barber, R. C.** See Isenor, N. R., 819.
- Barrington, R. E. and Nishizaki, T.** The hydrogen ion effect in whistler dispersion, 1642.
- Bartholomew, G. A.** Internal pair angular correlation spectrometer for determination of γ -ray multipolarities, 871.
- Bartholomew, G. A., Campion, P. J., and Robinson, K.** A study of methods for obtaining high resolution with a pair spectrometer, 194.
- Bedford, R. E.** A low temperature standard of total radiation, 1256.
- Bell, R. E. and Jørgensen, M. H.** Mean lives of positrons in aluminum and the alkali metals, 652.
- Benson, C. B. and Hollis Hallett, A. C.** Viscosity measurements in liquid helium II, 1376.
- Benson, G. C.** See Dempsey, E., 399.
- Bergsteinsson, J. L.** See Roalsvig, J. P., 320.
- Berry, R. J.** The reproducibility of the sulphur point, 1027.
- Bhattacharyya, B. K.** Correlation studies of radio-aurora, magnetic, and earth-current disturbances, 624.
- A study of auroral motions from all-sky camera records, 1279.
- Blackmore, W. R.** The source of noise in ebulliometry, 565.
- Bloom, M.** See Muller, B., 1318.
- Bolling, G. F.** See Sekerka, R. F., 883.
- Boucher, R. R.** See Michaud, G. G., 555.
- Bourret, R.** An hypothesis concerning turbulent diffusion, 665.
- Bourret, R. C.** Velocity autocorrelations of charged particles in a magnetoionic medium with applications to turbulent diffusion, 1213.
- Bresesti, M.** See Roy, J. C., 1428.
- Brysk, H.** The radar cross section of a semi-infinite body, 48.
- Burgess, R. E.** Negative resistance in semiconductor devices, 369.
- Campion, P. J.** See Bartholomew, G. A., 194.
- Carruthers, J. A.** See Clifford, C. E., 504.
- Chapman, J. H.** The polar radio black-out of the ionosphere of 7 July, 1958, 1195.
- Clark, M. A.** Transition intensities and conversion coefficients in Dy^{169} , 262.
- Clark, M. A. and Robson, J. M.** Asymmetries in the beta decay of polarized neutrons, 693.
- Clifford, C. E., Carruthers, J. A., and Cunningham, J. R.** γ -Radiation at air-ground interfaces with distributed Cs^{137} sources, 504.
- Cox, C. D.** Bulk photoeffects in inhomogeneous semiconductors, 1328.
- Crawford, J. E.** See Stryland, J. C., 1546.
- Cunningham, J. R.** See Clifford, C. E., 504.
- Currie, B. W.** See Kim, J. A., 1366.
- Daniels, J. M. and Farach, H. A.** "Spin-flip narrowing" of paramagnetic resonance lines, 151.
- Daniels, J. M. and Rieckhoff, K. E.** Spin lattice relaxation in neodymium ethylsulphate at liquid helium temperatures, 604.
- Das, S. C.** Comparison of flow lines in various types of rheological bodies, 32.
- Dauphinee, T. M.** See Preston-Thomas, H., 824.
- Davison, B.** On the rate of convergence of the spherical harmonics method (for the plane case, isotropic scattering), 1526.
- Demers, J.** See Fournaux, J., 1482.
- Demers, P.** See Fournaux, J., 1482.
- Dempsey, E. and Benson, G. C.** Tables of the modified Bessel functions of the second kind for particular types of argument, 399.
- Dixon, R. N.** A Π - Π electronic band system of the free NCO radical, 10.
- Duckworth, H. E.** See Isenor, N. R., 819.
- Durie, R. A. and Herzberg, G.** Forbidden transitions in diatomic molecules. V. The rotation-vibration spectrum of the hydrogen-deuteride (HD) molecule, 806.
- Durie, R. A., Legay, F., and Ramsay, D. A.** An emission system of the IO molecule, 444.
- Eastwood, T. A. and Werner, R. D.** The thermal neutron capture cross section and resonance capture integral of protactinium-233, 751.
- Eaton, D. R.** Infrared temperature and line strength measurements on carbon monoxide excited in a radio-frequency discharge, 390.

- Ebisuzaki, R.** See Jarman, W. R., 510.
- Edwards, M. H. and Woodbury, W. C.** Condensation of supersaturated He^4 vapor in a cloud chamber, 335.
- Edwards, W. D.** Liquid-solid interface shape observed in silicon crystals grown by the Czochralski method, 439.
- Englefield, M. J.** Use of Racah algebra in evaluating commutators, 315.
- Ewan, G. T., Graham, R. L., and Grodzins, L.** The $K\text{-}LL$ Auger spectrum of ^{152}Sm , 163.
- Ewan, G. T. and Merritt, J. S.** Relative intensities of $K\text{-}LL$ Auger lines in ^{152}Gd , 324.
- Farach, H. A.** See Daniels, J. M., 151.
- Farley, T. A.** Half-period of Th^{232} , 1059.
- Fejer, J. A.** Scattering of radio waves by an ionized gas in thermal equilibrium, 1114.
- Forsyth, P. A.** On the geometry of radio reflections from aurora, 593.
- Forsyth, P. A., Green, F. D., and Mah, W.** The distribution of radio-aurora in central Canada, 770.
- Fournaux, J., Demers, J., and Demers, P.** Fabrication et étude des propriétés des émulsions ionographiques, 1482.
- Fraser, P. A.** See McEachran, R. P., 317.
- Fritze, K. and Kennett, T. J.** The identification and half lives of fission-product Rb^{92} and Rb^{93} , 1614.
- Garber, M., Henry, W. G., and Hoeve, H. G.** A magnetic susceptibility balance and the temperature dependence of the magnetic susceptibility of copper, silver, and gold, $295^\circ\text{--}975^\circ\text{K}$, 1595.
- Garrett, C.** See Henry, W. H., 1677.
- Gaudet, G., Hedgcock, F. T., Lamarche, G., and Wallingford, E. W.** The electrical resistance maximum in dilute magnesium alloys, 1134.
- Geiger, K. W.** The status of the Canadian neutron standard, 569.
- Gold, L. W.** The cracking activity in ice during creep, 1137.
- Graham, R. L.** See Ewan, G. T., 163.
- Green, E.** See Preston-Thomas, H., 824.
- Green, F. D.** See Forsyth, P. A., 770.
- Green, G. W. and Lew, H.** Rotational spectrum of K^{39}F by the molecular beam electric resonance method, 482.
- Grodzins, L.** See Ewan, G. T., 163.
- Grummitt, W. E.** See Milton, G. M., 1690.
- Gush, H. P., Hare, W. F. J., Allin, E. J., and Welsh, H. L.** The infrared fundamental band of liquid and solid hydrogen, 176.
- Hare, W. F. J.** See Gush, H. P., 176.
- Harrower, G. A.** See Ryan, W. D., 883.
- Haslam, R. N. H.** See King, J. D., 231, 1069; Roalsvig, J. P., 320.
- Hawton, J. J.** See Roy, J. C., 1428.
- Hedgcock, F. T.** See Gaudet, G., 1134.
- Hedgcock, F. T., Muir, W. B., and Wallingford, E.** The electrical resistance of dilute magnesium and aluminum alloys at low temperatures, 376.
- van Heerden, I. J. and Judek, B.** The relative abundances of cosmic ray nuclei of charge $Z \geq 3$, 964.
- Held, G.** See Ishimaru, A., 78.
- Henry, W. G.** See Garber, M., 1595.
- Henry, W. G. and Rogers, J. L.** The magnetic susceptibilities of some diamagnetic alloys. The primary solid solutions of cadmium, indium, tin, and antimony in copper and in silver; zinc, gallium, germanium, and arsenic in silver; copper in silver and silver in copper, 908.
- Henry, W. H. and Garrett, C.** The Canadian standard free-air chamber for medium quality X-rays, 1677.
- Herzberg, G.** See Durie, R. A., 806.
- Herzberg, L.** The wavelength displacements of some infrared lines between limb and center of the sun. II, 853.
- Hines, C. O.** Internal atmospheric gravity waves at ionospheric heights, 1441.
- Hirth, J. P.** See Rapp, R. A., 709.
- Hoeve, H. G.** See Garber, M., 1595.
- Hollis Hallett, A. C.** See Benson, C. B., 1376; Jones, G. H. S., 696.
- Holuj, F. and Petch, H. E.** A nuclear magnetic resonance study of colemantite, 515.
- Hunten, D. M.** A condenser memory unit for improving signal-to-noise ratios, 346.
See also Lytle, E. A., 477; Vallance Jones, A., 458.
- Hurd, R. A.** Diffraction by a unidirectionally conducting half-plane, 168.
An electromagnetic diffraction problem involving unidirectionally conducting surfaces, 1229.
- Isenor, N. R., Barber, R. C., and Duckworth, H. E.** Some recent determinations of atomic masses in the strontium-zirconium region, 819.

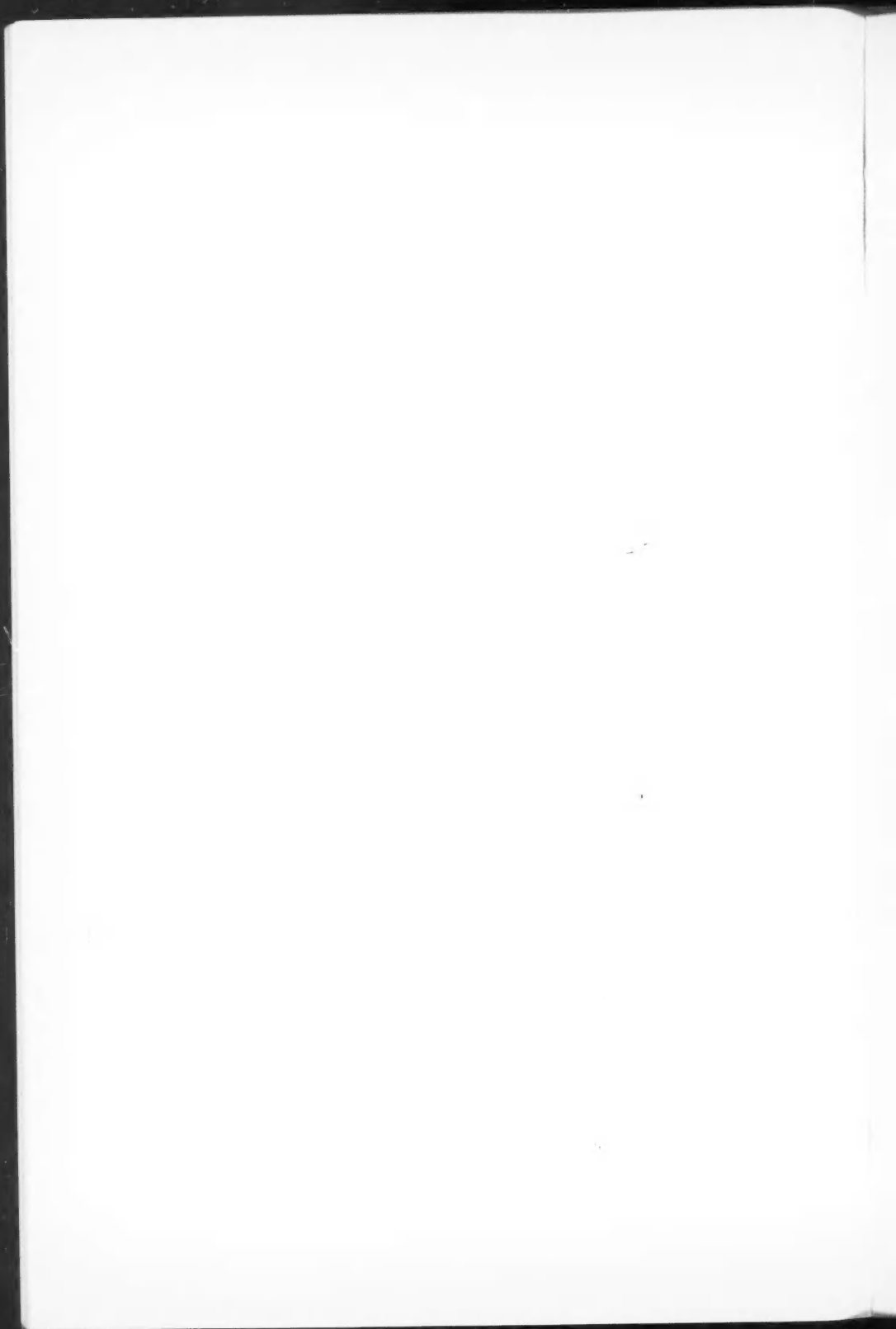
- Ishimaru, A. and Held, G.** Analysis and synthesis of radiation patterns from circular apertures, 78.
- Jarmain, W. R.** Klein-Dunham potential energy functions in simplified analytical form, 217.
- Jarmain, W. R., Ebisuzaki, R., and Nicholls, R. W.** Franck-Condon factors and r -centroids for some bands of the CO fourth positive ($A''\Pi-X''\Sigma$) band system, 510.
- Jones, G. H. S. and Hollis Hallett, A. C.** The specific heat of crystalline quartz between 2°K and 4°K , 696.
- Jørgensen, M. H.** See Bell, R. E., 652.
- Judek, B.** See van Heerden, I. J., 964.
- Kalra, S. N.** Frequency measurement of standard frequency transmissions, 150, 332, 513, 576, 713, 881, 971, 1136, 1228, 1395, 1552, 1712.
See also Preston-Thomas, H., 824.
- Katzman, J. and Venkatesan, D.** A world-wide study of the daily variation of the nucleonic component of cosmic rays, 1011.
- Kavanagh, T. M.** Decay of $\text{Au}^{198\text{m}}$, 1436.
- Keller, J. B.** See Levy, B. R., 128.
- Kennett, T. J.** See Fritze, K., 1614.
- Kennett, T. J. and Thode, H. G.** Diffusion phenomena and isotope effects in the extraction of fission-product xenon and krypton from irradiated U_3O_8 , 945.
- Kerwin, L.** See McGowan, Wm., 567, 642; Marmet, P., 787, 972.
- Kim, J. A. and Currie, B. W.** Further observations of the horizontal movements of aurora, 1366.
- King, J. D., Haslam, R. N. H., and McDonald, W. J.** The gamma-neutron cross section for F^{19} , 1069.
- King, J. D., Haslam, R. N. H., and Parsons, R. W.** The gamma-neutron cross section for N^{14} , 231.
- Kirkaldy, J. S.** The thermodynamic description of heterogeneous dissipative systems by variational methods. I. A formulation of the principle of minimum rate of entropy production with application to certain stationary heterogeneous convective systems, 1343.
The thermodynamic description of heterogeneous dissipative systems by variational methods. II. A variational principle applicable to non-stationary (unconstrained) heterogeneous dissipative systems, 1356.
- Kjelberg, A., Taniguchi, H., and Yaffe, L.** Gamma radiation in the decay of Ag^{113} , 866.
- Kollar, F.** See Russell, R. D., 616.
- Kovács, I.** Intensities in Σ - Δ and Π - Δ transitions of diatomic molecules, 955.
- Lamarche, G.** See Gaudet, G., 1134.
- Laubitz, M. J.** Thermal and electrical properties of Armco iron at high temperatures, 887.
- Law, M. E.** See Artua, A., 1577.
- Lee-Whiting, G. E.** A Compton-electron γ -spectrometer with two-directional focusing, 720.
- Legay, F.** Analyse de la bande 1-0 du système $^3\Pi_1-^3\Sigma^-$ de PH , 797.
See also Duric, R. A., 444.
- Levy, B. R. and Keller, J. B.** Diffraction by a spheroid, 128.
- Lew, H.** See Green, G. W., 482.
- Lew, H. and Title, R. S.** Note on the hyperfine structure of the $2s^22p^2P_1$ state of boron 10 and 11, 868.
- Litherland, A. E. and McCallum, G. J.** An illustration of a type of triple correlation measurement which can be easily interpreted, 927.
- Lockwood, G. E. K.** Spin rate of the satellite Echo I as determined by a tracking radar, 1713.
- Loh, S. C.** The radiation characteristics of a sinuate antenna, 119.
- Lyon, G. F.** The association of visible auroral forms with radar echoes, 385.
- Lytle, E. A. and Hunten, D. M.** Dawn enhancement of auroral N_2^+ emission, 477.
- McCallum, G. J.** See Litherland, A. E., 927.
- McDiarmid, I. B. and Rose, D. C.** High-altitude cosmic ray measurements at Fort Churchill, 638.
- McDonald, W. J.** See King, J. D., 1069.
- McEachran, R. P. and Fraser, P. A.** d -Wave contribution to electron-hydrogen atom scattering, 317.
- McGowan, Wm. and Kerwin, L.** Some sensitivities of ion gauges, 567.
Some oxygen ions formed at high pressures in a mass spectrometer, 642.
- McLaren, E. H. and Murdock, E. G.** The freezing points of high purity metals as precision temperature standards. V. Thermal analyses on 10 samples of tin with purities greater than 99.99+%, 100.
The freezing points of high purity metals as precision temperature standards. VI. Thermal analyses on five samples of lead with purities greater than 99.999+%, 577.
- McMillan, M. and Opechowski, W.** On the temperature dependence of the shape of paramagnetic resonance lines, 1168.
- McNamara, A. G.** An analysis of some statistical properties of auroral radar reflections and their relationships to the detection capabilities of the radar, 425.

- Mah, W.** See Forsyth, P. A., 770.
- Marmet, P. and Kerwin, L.** An improved electrostatic electron selector, 787.
Experimentally measured vibrational levels in H_2^+ , 972.
- Marr, G. V. and Swarup, P.** Spin-lattice relaxation effects observed in the continuous power saturation of paramagnetic lines, 495.
- Martin, D. L.** The specific heat of copper from 20° to 300° K, 17.
The specific heat of a lithium-magnesium alloy. The martensitic transformation, 25.
The specific heat of annealed and cold-worked copper from 0.4° to 1.5° K, 1390.
- Mastoor, M. A.** See Stryland, J. C., 1546.
- Merritt, J. S.** See Ewan, G. T., 324.
- Michaud, G. G. and Boucher, R. R.** Neutron sources from the beryllium reduction of plutonium dioxide, 555.
- Millar, R. F.** A note on diffraction by an infinite slit, 38.
The scattering of a plane wave by a row of small cylinders, 272.
- Milton, G. M. and Grummitt, W. E.** The "reactor" neutron capture cross section of Y^{91} , 1690.
- Moore, R. B. and White, W.** Tables of rotational energy levels of deformed even-even nuclei, 1149.
- Morris, D.** See Mungall, A. G., 779, 1510.
- Morris, D. and Mungall, A. G.** TE surface waves guided by a dielectric-covered metal plane, 1553.
- Muir, W. B.** See Hedgcock, F. T., 376.
- Müller, B. and Bloom, M.** On the study of diffusion using spin echoes, 1318.
- Mungall, A. G.** See Morris, D., 1553.
- Mungall, A. G. and Morris, D.** The group velocity of plane surface waves, 779.
Time delay and frequency response of resonant cavities, 1510.
- Murdock, E. G.** See McLaren, E. H., 100, 577.
- Newton, T. D.** On the axial symmetry of the Nilsson model nucleus, 700.
- Nicholls, R. W.** The Franck-Condon factor ($Q_{v'v''}$) array to high vibrational quantum numbers for the $O_2(B^2\Sigma^- - X^2\Sigma^+)$ Schumann-Runge band system, 1705.
See also Jarman, W. R., 510; Parkinson, W. H., 715.
- Nishizaki, T.** See Barrington, R. E., 1642.
- Opechowski, W.** See McMillan, M., 1168.
- Parkinson, W. H. and Nicholls, R. W.** Spectroscopic temperature measurements in a shock tube using CN as a thermometric molecule, 715.
- Parsons, R. W.** See King, J. D., 231.
- Pearson, J. M.** The nuclear matrix element ratio in the $0^- \rightarrow 0^+$ beta transition of Pr^{144} , 148.
- Pearson, W. B.** The thermoelectric power of annealed and cold-worked silver and gold at low temperatures, 1048.
- Petch, H. E.** See Holuj, F., 515.
- Plaskett, T. S. and Winegard, W. C.** Cell to dendrite transition in tin base alloys, 1077.
- Plonus, M. A.** Backscattering from a conducting cylinder with a surrounding shell, 1665.
- Pomerantz, M. A.** See Bailey, D. K., 332; Wilson, B. G., 328.
- Pound, G. M.** See Rapp, R. A., 709.
- Pounder, E. R.** See Smith, M., 354.
- Preston-Thomas, H., Turnbull, L. G., Green, E., Dauphinee, T. M., and Kalra, S. N.** An absolute measurement of the acceleration due to gravity at Ottawa, 824.
- Rabinovitch, W.** Exponential transfer and diffusion, 1406.
- Ramsay, D. A.** See Durie, R. A., 444.
- Rao, K. S., Stoicheff, B. P., and Turner, R.** High resolution Raman spectroscopy of gases. XIII. Rotational spectra and structures of the zinc-, cadmium-, and mercury-dimethyl molecules, 1516.
- Rapp, R. A., Hirth, J. P., and Pound, G. M.** On the condensation coefficient in the growth of silver from the vapor phase, 709.
- Rastall, P.** An approach to a theory of gravitation, 975.
A solution of the Einstein field equations, 1661.
- Rieckhoff, K. E.** See Daniels, J. M., 604.
- Roalsvig, J. P., Haslam, R. N. H., and Bergsteinsson, J. L.** A note of the reaction $Zn^{64}(\gamma, n)Zn^{63}$, 320.
- Robinson, K.** See Bartholomew, G. A., 194.
- Robson, J. M.** See Clark, M. A., 693.
- Rogers, J. L.** See Henry, W. G., 908.
- Rose, D. C.** The sudden increase in cosmic ray intensity of May 4, 1960, 1224.
See also McDiarmid, I. B., 638; Wilson, B. G., 328.
- Roy, J. C., Bresesti, M., and Hawton, J. J.** On the production of Be^7 in the NRX reactor by the $B^{10}(p, \alpha)Be^7$, $Li^7(p, n)Be^7$, and $Li^6(d, n)Be^7$ reactions, 1428.
- Russell, R. D. and Kollar, F.** Transistorized power supplies for a mass spectrometer, 616.

- Ryan, W. D.** and **Harrower, G. A.** An apparent solar periodicity in radio star scintillation, 883.
- Scheidegger, A. E.** On the stability of displacement fronts in porous media: A discussion of the Muskat-Aronofsky model, 153.
- Schoen, L. J.** Triboluminescence in a mercury bubbler, 967.
- Schwerdtfeger, P.** Observations on estuary ice, 1391.
- Scott, S. A.** See Taylor, H. W., 573.
- Sekerka, R. F., Bolling, G. F., and Tiller, W. A.** Observations of macromosaic substructures in lead, 883.
- Sen, D. K.** A complex non-analytic manifold and conformal Minkowski space-time, 145.
- Senior, T. B. A.** Scalar diffraction by a prolate spheroid at low frequencies, 1632.
A note on Hansen's vector wave functions, 1702.
- Seshadri, S. R.** Scattering by a narrow unidirectionally conducting infinite strip, 1623.
- Sharma, B.** See Whyte, G. N., 877.
- Sharma, R. C.** See Steenberg, N. R., 290.
- Sharp, R. T.** See Smith, R. C., 1154.
- Shenstone, A. G.** The third spectrum of cobalt (Co III), 677.
- Shepherd, G. G.** A Fabry-Perot spectrometer for auroral and airglow observations, 1560.
- Shukla, R. C.** See Varshni, Y. P., 1547.
- Skinner, R.** See Weaver, J. T., 1089, 1104.
- Smith, A. W. and Williams, G. W.** Domain structure in yttrium iron garnet, 1187.
- Smith, D. S.** A method of precise fringe pointing, 983.
- Smith, M. and Pounder, E. R.** Impurity concentration profiles in ice by an anthrone method, 354.
- Smith, R. C. and Sharp, R. T.** Central three-body forces in heavy nuclei, 1154.
- Smith, R. W.** The white tin \rightarrow grey tin transition in tin-mercury alloys, 588.
- Steenberg, N. R. and Sharma, R. C.** Alpha decay and fission of aligned nuclei, 290.
- Stevenson, R.** Magneto-optical rotation in very high fields, 941.
- Stoicheff, B. P.** See Rao, K. S., 1516.
- Stryland, J. C., Crawford, J. E., and Mastoor, M. A.** Melting temperatures of krypton, xenon, and methane at pressures up to 3000 atm, 1546.
- Swarup, P.** See Marr, G. V., 495.
- Szabo, A.** See Armstrong, R. A., 1304.
- Taniguchi, H.** See Kjelberg, A., 866.
- Taylor, H. W.** See Whyte, G. N., 877.
- Taylor, H. W. and Scott, S. A.** High-energy gamma radiation from $\text{Ag}^{110\text{m}}$, 573.
- Terentiuk, F.** See Wolfson, J. L., 991.
- Thode, H. G.** See Kennett, T. J., 945; Young, B. G., 1.
- Thomas, M. A. and Welsh, H. L.** The Raman spectrum of methane, 1291.
- Tiller, W. A.** See Sekerka, R. F., 883.
- Title, R. S.** See Lew, H., 868.
- Trainor, L. E. H.** Considerations on a meson-atomic model of the nucleon, 1245.
- Turnbull, L. G.** See Preston-Thomas, H., 824.
- Turner, R.** See Rao, K. S., 1516.
- Vallance Jones, A.** An analysis of a spectrogram of the red aurora of February 10/11, 1958, in the wavelength range 7300-8700 Å, 453.
- Vallance Jones, A. and Hunten, D. M.** Rotational and vibrational intensity distribution of the first negative N_2^+ bands in sunlit auroral rays, 458.
- Vanier, J.** Temperature dependence of the pure nuclear quadrupole resonance frequency in KClO_3 , 1397.
- Van Kranendonk, J.** Theory of the infrared and Raman spectra of solid parahydrogen, 240.
- Varshni, Y. P. and Shukla, R. C.** On James' type of wave functions for hydrogen molecular ion, 1547.
- Venkatesan, D.** See Katzman, J., 1011.
- Wait, J. R.** Propagation of electromagnetic waves along a thin plasma sheet, 1586.
- Walker, W. H., Westcott, C. H., and Alexander, T. K.** Measurement of radiative capture resonance integrals in a thermal reactor spectrum, and the thermal cross section of Pu-240, 57.
- Wallingford, E.** See Hedgcock, F. T., 376.
- Wallingford, E. W.** See Gaudet, G., 1134.
- Weaver, J. T. and Skinner, R.** A theory of ionospheric currents associated with aurorae. I, 1089.
A theory of ionospheric currents associated with aurorae. II, 1104.
- Welsh, H. L.** See Gush, H. P., 176; Thomas, M. A., 1291.
- Werner, R. D.** See Eastwood, T. A., 751.
- Westcott, C. H.** See Walker, W. H., 57.
- White, W.** See Moore, R. B., 1149.

- Whyte, G. N., Sharma, B., and Taylor, H. W.** A note on the decay of Cs^{132} , 877.
- Williams, G. W.** See Smith, A. W., 1187.
- Williams, W. E.** A note on diffraction by a half plane, 507.
- Wilson, B. G., Rose, D. C., and Pomerantz, M. A.** The unusual cosmic ray events of July 17-18, 1959, 328.
- Winegard, W. C.** See Plaskett, T. S., 1077.
- Wolfe, J. L.** Measurements of the last few periods of Sputnik III by a radio direction finder, 882.
- Wolfson, J. L. and Terentiuk, F.** Concentration of particulate air-borne fission products at ground level in Canada during I.G.Y., 991.
- Woodbury, W. C.** See Edwards, M. H., 335.
- Wu, T.-Y.** Electron - hydrogen atom scattering in Born approximation, 1654.
- Yaffe, L.** See Kjelberg, A., 866.
- Young, B. G. and Thode, H. G.** Absolute yields of the xenon and krypton isotopes in U^{235} spontaneous fission, 1.
- Ziauddin, S.** Simultaneous observations of pulsations in the geomagnetic field and in ionospheric absorption, 1714.





NOTES TO CONTRIBUTORS

Canadian Journal of Physics

MANUSCRIPTS

General.—Manuscripts, in English or French, should be typewritten, double spaced, on paper $8\frac{1}{2} \times 11$ in. **The original and one copy are to be submitted.** Tables and captions for the figures should be placed at the end of the manuscript. Every sheet of the manuscript should be numbered. Style, arrangement, spelling, and abbreviations should conform to the usage of recent numbers of this journal. Greek letters or unusual signs should be written plainly or explained by marginal notes. Characters to be set in boldface type should be indicated by a wavy line below each character. Superscripts and subscripts must be legible and carefully placed. Manuscripts and illustrations should be carefully checked before they are submitted. Authors will be charged for unnecessary deviations from the usual format and for changes made in the proof that are considered excessive or unnecessary.

Abstract.—An abstract of not more than about 200 words, indicating the scope of the work and the principal findings, is required, except in Notes.

References.—References should be listed **alphabetically by authors' names**, unnumbered, and typed after the text. The form of the citations should be that used in current issues of this journal; in references to papers in periodicals, titles should not be given and only initial page numbers are required. The names of periodicals should be abbreviated in the form given in the most recent *List of Periodicals Abstracted by Chemical Abstracts*. All citations should be checked with the original articles and each one referred to in the text by the authors' names and the year.

Tables.—Tables should be numbered in roman numerals and each table referred to in the text. Titles should always be given but should be brief; column headings should be brief and descriptive matter in the tables confined to a minimum. Vertical rules should not be used. Numerous small tables should be avoided.

ILLUSTRATIONS

General.—All figures (including each figure of the plates) should be numbered consecutively from 1 up, in arabic numerals, and each figure referred to in the text. The author's name, title of the paper, and figure number should be written in the lower left corner of the sheets on which the illustrations appear. Captions should not be written on the illustrations.

Line drawings.—Drawings should be carefully made with India ink on white drawing paper, blue tracing linen, or co-ordinate paper ruled in blue only; any co-ordinate lines that are to appear in the reproduction should be ruled in black ink. Paper ruled in green, yellow, or red should not be used. All lines must be of sufficient thickness to reproduce well. Decimal points, periods, and stippled dots must be solid black circles large enough to be reduced if necessary. Letters and numerals should be neatly made, preferably with a stencil (**do NOT use typewriting**) and be of such size that the smallest lettering will be not less than 1 mm high when the figure is reduced to a suitable size. Many drawings are made too large; originals should not be more than 2 or 3 times the size of the desired reproduction. Whenever possible two or more drawings should be grouped to reduce the number of cuts required. In such groups of drawings, or in large drawings, full use of the space available should be made; the ratio of height to width should conform to that of a journal page ($4\frac{1}{2} \times 7\frac{1}{4}$ in.), but allowance must be made for the captions. **The original drawings and one set of clear copies (e.g. small photographs) are to be submitted.**

Photographs.—Prints should be made on glossy paper, with strong contrasts. They should be trimmed so that essential features only are shown and mounted carefully, with rubber cement, on white cardboard, with no space between those arranged in groups. In mounting, full use of the space available should be made. **Photographs are to be submitted in duplicate; if they are to be reproduced in groups one set should be mounted, the duplicate set unmounted.**

REPRINTS

A total of 100 reprints of each paper, without covers, are supplied free. Additional reprints, with or without covers, may be purchased at the time of publication.

Charges for reprints are based on the number of printed pages, which may be calculated approximately by multiplying by 0.6 the number of manuscript pages (double-spaced typewritten sheets, $8\frac{1}{2} \times 11$ in.) and including the space occupied by illustrations. Prices and instructions for ordering reprints are sent out with the galley proof.

Contents

<i>D. Morris and A. G. Mungall</i> —TE surface waves guided by a dielectric-covered metal plane	1553
<i>G. G. Shepherd</i> —A Fabry-Perot spectrometer for auroral and airglow observations	1560
<i>R. S. Adhav</i> —On the optical and electrical properties of semitransparent copper films	1570
<i>Agda Artina and Margaret E. Law</i> —The decay of Pm^{149}	1577
<i>James R. Wait</i> —Propagation of electromagnetic waves along a thin plasma sheet	1586
<i>M. Garber, W. G. Henry, and H. G. Hoeve</i> —A magnetic susceptibility balance and the temperature dependence of the magnetic susceptibility of copper, silver, and gold, 295°–975° K	1595
<i>K. Fritze and T. J. Kennett</i> —The identification and half lives of fission-product Rb^{92} and Rb^{93}	1614
<i>S. R. Seshadri</i> —Scattering by a narrow unidirectionally conducting infinite strip	1623
<i>T. B. A. Senior</i> —Scalar diffraction by a prolate spheroid at low frequencies	1632
<i>R. E. Barrington and T. Nishizaki</i> —The hydrogen ion effect in whistler dispersion	1642
<i>Ta-You Wu</i> —Electron-hydrogen atom scattering in Born approximation	1654
<i>Peter Rastall</i> —A solution of the Einstein field equations	1661
<i>M. A. Plonus</i> —Backscattering from a conducting cylinder with a surrounding shell	1665
<i>W. H. Henry and C. Garrett</i> —The Canadian standard free-air chamber for medium quality X-rays	1677
<i>Gwen M. Milton and W. E. Grummitt</i> —The "reactor" neutron capture cross section of Y^{91}	1690
Notes:	
<i>T. B. A. Senior</i> —A note on Hansen's vector wave functions	1702
<i>R. W. Nicholls</i> —The Franck-Condon factor ($Q_{v',v''}$) array to high vibrational quantum numbers for the $\text{O}_2(B^2\Sigma^- - X^2\Sigma^+)$ Schumann-Runge band system	1705
Letters to the Editor:	
<i>S. N. Kalra</i> —Frequency measurement of standard frequency transmissions	1712
<i>G. E. K. Lockwood</i> —Spin rate of the satellite Echo I as determined by a tracking radar	1713
<i>Syed Ziauddin</i> —Simultaneous observations of pulsations in the geomagnetic field and in ionospheric absorption	1714
Contents of Volume 38	1717

